

DECEMBER 2023

AJNR

VOLUME 44 • PP 1357–1470

AJNR

AMERICAN JOURNAL OF NEURORADIOLOGY

Official Journal ASNR • ASFNR • ASHNR • ASPNR • ASSR
DECEMBER 2023 | VOLUME 44 | NUMBER 12 | WWW.AJNR.ORG

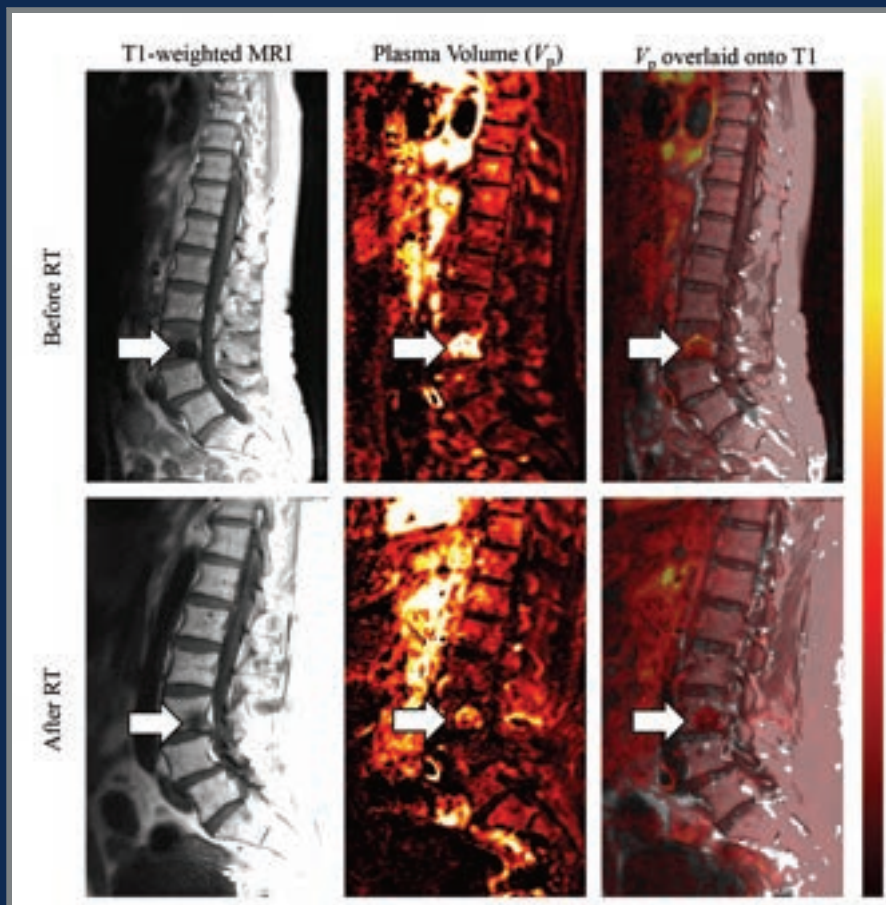
THE JOURNAL OF DIAGNOSTIC AND INTERVENTIONAL NEURORADIOLOGY

Imaging-related manifestations of monoclonal antibody–targeted therapies

Machine learning brain age prediction model using FLAIR MRI biomarkers

Osteomyelitis complication of neopharyngeal breakdown

Multiparametric MRI radiomics in pediatric myelin oligodendrocyte glycoprotein antibody-associated disorders



FRED™ X™

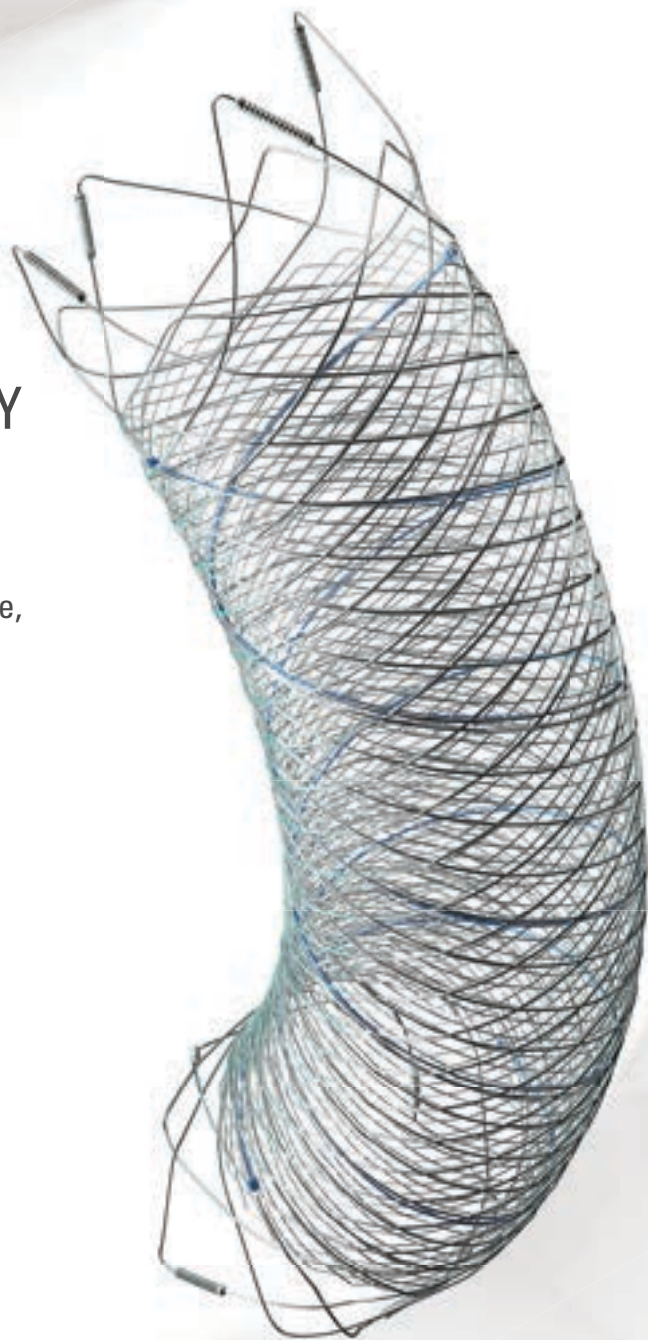
Flow Diverter Stent

THE NEXT ADVANCEMENT IN FLOW DIVERSION TECHNOLOGY

The FRED™ X Flow Diverter features the same precise placement and immediate opening of the FRED™ Device, now with X Technology. X Technology is a covalently bonded, nanoscale surface treatment, designed to:

- **REDUCE MATERIAL THROMBOGENICITY¹**
- **MAINTAIN NATURAL VESSEL HEALING RESPONSE^{2,3,4}**
- **IMPROVE DEVICE DELIVERABILITY AND RESHEATHING¹**

The only FDA PMA approved portfolio with a 0.021" delivery system for smaller device sizes, and no distal lead wire.



For more information, contact your local MicroVention sales representative or visit our website. www.microvention.com



^{*} Data is derived from in vivo and ex vitro testing and may not be representative of clinical performance.

¹ Data on file

² Tanaka M et al. Design of biocompatible and biodegradable polymers based on intermediate water concept. Polymer Journal. 2015;47:114-121.

³ Tanaka M et al. Blood compatible aspects of poly(2-methoxyethylacrylate) (PMEA) – relationship between protein adsorption and platelet adhesion on PMEA surface. Biomaterials. 2000;21:1471-1481.

⁴ Schiel L et al. X Coating™: A new biopassive polymer coating. Canadian Perfusion Canadienne. June 2001;11(2):9.

Indications for Use: The FRED X System is indicated for use in the internal carotid artery from the petrous segment to the terminus for the endovascular treatment of adult patients (22 years of age or older) with wide-necked (neck width 4 mm or dome-to-neck ratio < 2) saccular or fusiform intracranial aneurysms arising from a parent vessel with a diameter 2.0 mm and 5.0 mm.

Rx Only: Federal (United States) law restricts this device to sale by or on the order of a physician. For Healthcare professionals intended use only.

MICROVENTION, FRED and HEADWAY are registered trademarks of MicroVention, Inc. in the United States and other jurisdictions. Stylized X is a trademark of MicroVention, Inc. © 2022 MicroVention, Inc. MM1222 US 03/22

WEB™ 17

Aneurysm Embolization System

LOWER PROFILE



NEW SIZES



MORE ACCESS OPTIONS



INDICATIONS FOR USE:

The WEB Aneurysm Embolization System is intended for the endovascular embolization of ruptured and unruptured intracranial aneurysms and other neurovascular abnormalities such as arteriovenous fistulae (AVF). The WEB Aneurysm Embolization System is also intended for vascular occlusion of blood vessels within the neurovascular system to permanently obstruct blood flow to an aneurysm or other vascular malformation.

POTENTIAL COMPLICATIONS:

Potential complications include but are not limited to the following: hematoma at the site of entry, aneurysm rupture, emboli, vessel perforation, parent artery occlusion, hemorrhage, ischemia, vasospasm, clot formation, device migration or misplacement, premature or difficult device detachment, non-detachment, incomplete aneurysm filling, revascularization, post-embolization syndrome, and neurological deficits including stroke and death. For complete indications, potential complications, warnings, precautions, and instructions, see instructions for use (IFU provided with the device).

VIA 21, 27, 33 - The VIA Microcatheter is intended for the introduction of interventional devices (such as the WEB device/stents/flow diverters) and infusion of diagnostic agents (such as contrast media) into the neuro, peripheral, and coronary vasculature.

VIA 17, 17 Preshaped - The VIA Microcatheter is intended for the introduction of interventional devices (such as the WEB device/stents/flow diverters) and infusion of diagnostic agents (such as contrast media) into the neuro, peripheral, and coronary vasculature.

The VIA Microcatheter is contraindicated for use with liquid embolic materials, such as n-butyl 2-cyanoacrylate or ethylene vinyl alcohol & DMSO (dimethyl sulfoxide).

The device should only be used by physicians who have undergone training in all aspects of the WEB Aneurysm Embolization System procedure as prescribed by the manufacturer.

RX Only: Federal law restricts this device to sale by or on the order of a physician.

For healthcare professional intended use only.



MicroVention Worldwide
Innovator Center

PH +1.714.247.8000

35 Enterprise
Aliso Viejo, CA 92656 USA
MicroVention UK Limited
MicroVention Europe, S.A.R.L.
MicroVention Deutschland GmbH
Website

PH +44 (0) 191 258 6777
PH +33 (1) 39 21 77 46
PH +49 211 210 798-0
microvention.com



WEB™ and VIA™ are registered trademarks
of Sequent Medical, Inc. in the United States.

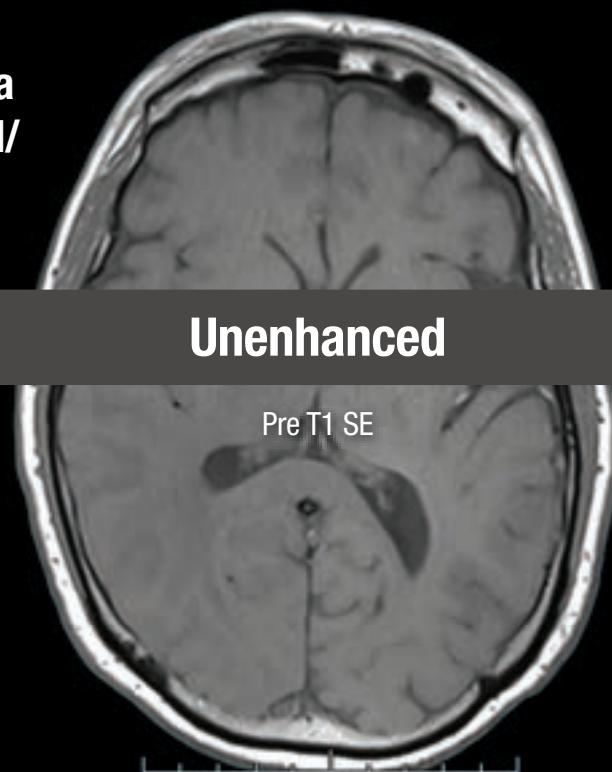
©2021 MicroVention, Inc. MM1184 WW 11/2021

THIS IS HALF Gd*

***Effective contrast enhancement at half the gadolinium dose (0.05 mmol/kg) vs a macrocyclic GBCA at a dose of 0.1 mmol/kg in approved indications in the U.S.^{1-6†}**


Vueway®
(gadopiclenol) injection
485.1 mg/mL

**NO COMPROMISE IN MRI FROM BRACCO,
YOUR TRUSTED PARTNER**



[†]Phase III CNS Study Design (Study GDX-44-010): Intra-individual, crossover comparison of 0.05 mmol/kg VUEWAY (gadopiclenol) injection vs. 0.1 mmol/kg Gadavist® in MRI of the CNS. Patients with known or suspected CNS lesions. Three primary visualization endpoints (lesion border delineation, lesion internal morphology, degree of contrast enhancement). The CNS study included 256 patients with known or highly suspected CNS lesion(s) with a mean age of 57 years (range: 18-84 years), and 53% female patients.

Please see Brief Summary of Prescribing Information including Boxed Warning on adjacent page.

VUEWAY® (gadopiclenol) solution for injection

Indications

VUEWAY injection is indicated in adults and children aged 2 years and older for use with magnetic resonance imaging (MRI) to detect and visualize lesions with abnormal vascularity in:

- the central nervous system (brain, spine and surrounding tissues),
- the body (head and neck, thorax, abdomen, pelvis, and musculoskeletal system).

IMPORTANT SAFETY INFORMATION

WARNING: NEPHROGENIC SYSTEMIC FIBROSIS (NSF)

Gadolinium-based contrast agents (GBCAs) increase the risk for NSF among patients with impaired elimination of the drugs. Avoid use of GBCAs in these patients unless the diagnostic information is essential and not available with non-contrasted MRI or other modalities. NSF may result in fatal or debilitating fibrosis affecting the skin, muscle and internal organs.

- The risk for NSF appears highest among patients with:
 - Chronic, severe kidney disease (GFR < 30 mL/min/1.73 m²), or
 - Acute kidney injury.

- Screen patients for acute kidney injury and other conditions that may reduce renal function. For patients at risk for chronically reduced renal function (e.g. age > 60 years, hypertension, diabetes), estimate the glomerular filtration rate (GFR) through laboratory testing.
- For patients at highest risk for NSF, do not exceed the recommended VUEWAY dose and allow a sufficient period of time for elimination of the drug from the body prior to any re-administration.

Contraindications

VUEWAY injection is contraindicated in patients with history of hypersensitivity reactions to VUEWAY.

Warnings

Risk of **nephrogenic systemic fibrosis** is increased in patients using GBCA agents that have impaired elimination of the drugs, with the highest risk in patients with chronic, severe kidney disease as well as patients with acute kidney injury. Avoid use of GBCAs among these patients unless the diagnostic information is essential and not available with non-contrast MRI or other modalities.

Hypersensitivity reactions, including serious hypersensitivity reactions, could occur during use or shortly following VUEWAY administration. Assess all patients for any history of a reaction to contrast media, bronchial asthma and/or allergic disorders, administer VUEWAY only in



LIFE FROM INSIDE

65-year-old man – 3.0 T Siemens
Brain metastasis from lung adenocarcinoma⁷

SE = Spin Echo. These are representative images from reference studies; individual results may vary.

Gadopichlenol 0.05 mmol/kg

Post T1 SE

Gadobutrol 0.1 mmol/kg

Post T1 SE

situations where trained personnel and therapies are promptly available for the treatment of hypersensitivity reactions, and observe patients for signs and symptoms of hypersensitivity reactions after administration.

Gadolinium retention can be for months or years in several organs after administration. The highest concentrations (nanomoles per gram of tissue) have been identified in the bone, followed by other organs (brain, skin, kidney, liver and spleen). Minimize repetitive GBCA imaging studies, particularly closely spaced studies, when possible.

Acute kidney injury requiring dialysis has occurred with the use of GBCAs in patients with chronically reduced renal function. The risk of acute kidney injury may increase with increasing dose of the contrast agent.

Ensure catheter and venous patency before injecting as **extravasation** may occur, and cause tissue irritation.

VUEWAY may **impair the visualization of lesions** seen on non-contrast MRI. Therefore, caution should be exercised when VUEWAY MRI scans are interpreted without a companion non-contrast MRI scan.

The most common adverse reactions (incidence $\geq 0.5\%$) are injection site pain (0.7%), and headache (0.7%).

You are encouraged to report negative side effects of prescription drugs to the FDA. Visit www.fda.gov/medwatch or call 1-800-FDA-1088.

Please see BRIEF SUMMARY of Prescribing Information for VUEWAY, including BOXED WARNING on Nephrogenic Systemic Fibrosis.

Manufactured for Bracco Diagnostics Inc. by Liebel-Flarsheim Company LLC - Raleigh, NC, USA 27616.

VUEWAY is a trademark of Bracco Imaging S.p.A.

All other trademarks and registered trademarks are the property of their respective owners.

References: 1. VUEWAY® (gadopichlenol) solution for injection, 485.1 mg/mL Full Prescribing Information and Patient Medication Guide. Monroe Twp., NJ: Bracco Diagnostics Inc.; September 2022. 2. Robic C, Port M, Rousseaux O, et al. Physicochemical and pharmacokinetic profiles of gadopichlenol: a new macrocyclic gadolinium chelate with high T1 relaxivity. *Invest Radiol.* 2019 Aug;54:475-484. 3. GADAVIST® (gadobutrol) Injection. Full Prescribing Information. Bayer HealthCare Pharmaceuticals Inc. Whippany, NJ; April 2022. 4. DOTAREM® (gadoterate meglumine) Injection. Full Prescribing Information. Guerbet LLC. Princeton, NJ; April 2022. 5. CLARISCAN™ (gadoterate meglumine) injection for intravenous use. Full Prescribing Information. GE Healthcare. Chicago, IL; February 2020. 6. ProHance® (Gadoteridol) Injection, 279.3 mg/mL Full Prescribing Information and Patient Medication Guide. Monroe Twp., NJ: Bracco Diagnostics Inc.; June 2022. 7. Loevner LA, Kolumban B, Hutóczki G, et al. Efficacy and safety of gadopichlenol for contrast-enhanced MRI of the central nervous system: the PICTURE randomized clinical trial. *Invest Radiol.* 2023 May;58(5):307-313.

Bracco Diagnostics Inc.
259 Prospect Plains Road, Building H
Monroe Township, NJ 08831 USA
Phone: 609-514-2200
Toll-Free: 1-877-272-2269 (U.S. only)
Fax: 609-514-2446

© 2023 Bracco Diagnostics Inc.
All Rights Reserved. US-VW-2300022 08/23



VISIT
VUEWAY.COM
FOR MORE
INFORMATION

Vueway™ (gadopiclenol) injection, for intravenous use

BRIEF SUMMARY: Please see package insert of full prescribing information.

WARNING: NEPHROGENIC SYSTEMIC FIBROSIS (NSF)

Gadolinium-based contrast agents (GBCAs) increase the risk for NSF among patients with impaired elimination of the drugs. Avoid use of GBCAs in these patients unless the diagnostic information is essential and not available with non-contrast MRI or other modalities. NSF may result in fatal or debilitating fibrosis affecting the skin, muscle and internal organs.

- The risk for NSF appears highest among patients with:
 - Chronic, severe kidney disease (GFR < 30 mL/min/1.73 m²), or
 - Acute kidney injury.
- Screen patients for acute kidney injury and other conditions that may reduce renal function. For patients at risk for chronically reduced renal function (e.g. age > 60 years, hypertension, diabetes), estimate the glomerular filtration rate (GFR) through laboratory testing.
- For patients at highest risk for NSF, do not exceed the recommended Vueway dose and allow a sufficient period of time for elimination of the drug from the body prior to any re-administration [see Warnings and Precautions (5.1) in the full Prescribing Information].

INDICATIONS AND USAGE

Vueway™ (gadopiclenol) is a gadolinium-based contrast agent indicated in adult and pediatric patients aged 2 years and older for use with magnetic resonance imaging (MRI) to detect and visualize lesions with abnormal vascularity in:

- the central nervous system (brain, spine, and associated tissues),
- the body (head and neck, thorax, abdomen, pelvis, and musculoskeletal system).

CONTRAINDICATIONS

Vueway is contraindicated in patients with history of hypersensitivity reactions to gadopicholol.

WARNINGS AND PRECAUTIONS

Nephrogenic Systemic Fibrosis Gadolinium-based contrast agents (GBCAs) increase the risk for nephrogenic systemic fibrosis (NSF) among patients with impaired elimination of the drugs. Avoid use of GBCAs among these patients unless the diagnostic information is essential and not available with non-contrast MRI or other modalities. The GBCA-associated NSF risk appears highest for patients with chronic, severe kidney disease (GFR < 30 mL/min/1.73 m²) as well as patients with acute kidney injury. The risk appears lower for patients with chronic, moderate kidney disease (GFR 30-59 mL/min/1.73 m²) and little, if any, for patients with chronic, mild kidney disease (GFR 60-89 mL/min/1.73 m²). NSF may result in fatal or debilitating fibrosis affecting the skin, muscle, and internal organs. Report any diagnosis of NSF following Vueway administration to Bracco Diagnostics Inc. (1-800-257-5181) or FDA (1-800-FDA-1088 or www.fda.gov/medwatch).

Screen patients for acute kidney injury and other conditions that may reduce renal function. Features of acute kidney injury consist of rapid (over hours to days) and usually reversible decrease in kidney function, commonly in the setting of surgery, severe infection, injury or drug-induced kidney toxicity. Serum creatinine levels and estimated GFR may not reliably assess renal function in the setting of acute kidney injury. For patients at risk for chronically reduced renal function (e.g., age > 60 years, diabetes mellitus or chronic hypertension), estimate the GFR through laboratory testing.

Among the factors that may increase the risk for NSF are repeated or higher than recommended doses of a GBCA and the degree of renal impairment at the time of exposure. Record the specific GBCA and the dose administered to a patient. For patients at highest risk for NSF, do not exceed the recommended Vueway dose and allow a sufficient period of time for elimination of the drug prior to re-administration. For patients receiving hemodialysis, physicians may consider the prompt initiation of hemodialysis following the administration of a GBCA in order to enhance the contrast agent's elimination [see Use in Specific Populations (8.6) and Clinical Pharmacology (12.3) in the full Prescribing Information]. The usefulness of hemodialysis in the prevention of NSF is unknown.

Hypersensitivity Reactions With GBCAs, serious hypersensitivity reactions have occurred. In most cases, initial symptoms occurred within minutes of GBCA administration and resolved with prompt emergency treatment.

- Before Vueway administration, assess all patients for any history of a reaction to contrast media, bronchial asthma and/or allergic disorders. These patients may have an increased risk for a hypersensitivity reaction to Vueway.
- Vueway is contraindicated in patients with history of hypersensitivity reactions to Vueway [see Contraindications (4) in the full Prescribing Information].
- Administer Vueway only in situations where trained personnel and therapies are promptly available for the treatment of hypersensitivity reactions, including personnel trained in resuscitation.
- During and following Vueway administration, observe patients for signs and symptoms of hypersensitivity reactions.

Gadolinium Retention Gadolinium is retained for months or years in several organs. The highest concentrations (nanomoles per gram of tissue) have been identified in the bone, followed by other organs (e.g. brain, skin, kidney, liver, and spleen). The duration of retention also varies by tissue and is longest in bone. Linear GBCAs cause more retention than macrocyclic GBCAs. At equivalent doses, gadolinium retention varies among the linear agents with gadodiamide causing greater retention than other linear agents such as gadoxetate disodium, and gadobenate dimeglumine. Retention is lowest and similar

among the macrocyclic GBCAs such as gadoterate meglumine, gadobutrol, gadoteridol, and gadopicholol.

Consequences of gadolinium retention in the brain have not been established. Pathologic and clinical consequences of GBCA administration and retention in skin and other organs have been established in patients with impaired renal function [see Warnings and Precautions (5.1) in the full Prescribing Information]. There are rare reports of pathologic skin changes in patients with normal renal function. Adverse events involving multiple organ systems have been reported in patients with normal renal function without an established causal link to gadolinium.

While clinical consequences of gadolinium retention have not been established in patients with normal renal function, certain patients might be at higher risk. These include patients requiring multiple lifetime doses, pregnant and pediatric patients, and patients with inflammatory conditions. Consider the retention characteristics of the agent when choosing a GBCA for these patients. Minimize repetitive GBCA imaging studies, particularly closely spaced studies, when possible.

Acute Kidney Injury In patients with chronically reduced renal function, acute kidney injury requiring dialysis has occurred with the use of GBCAs. The risk of acute kidney injury may increase with increasing dose of the contrast agent. Do not exceed the recommended dose.

Extravasation and Injection Site Reactions Injection site reactions such as injection site pain have been reported in the clinical studies with Vueway [see Adverse Reactions (6.1) in the full Prescribing Information]. Extravasation during Vueway administration may result in tissue irritation [see Nonclinical Toxicology (13.2) in the full Prescribing Information]. Ensure catheter and venous patency before the injection of Vueway.

Interference with Visualization of Lesions Visible with Non-Contrast MRI As with any GBCA, Vueway may impair the visualization of lesions seen on non-contrast MRI. Therefore, caution should be exercised when Vueway MRI scans are interpreted without a companion non-contrast MRI scan.

ADVERSE REACTIONS

The following serious adverse reactions are discussed elsewhere in labeling:

- Nephrogenic Systemic Fibrosis [see Warnings and Precautions (5.1) in the full Prescribing Information]
- Hypersensitivity Reactions [see Contraindications (4) and Warnings and Precautions (5.2) in the full Prescribing Information]

Clinical Trials Experience Because clinical trials are conducted under widely varying conditions, adverse reaction rates observed in the clinical trials of a drug cannot be directly compared to rates in the clinical trials of another drug and may not reflect the rates observed in clinical practice.

The safety of Vueway was evaluated in 1,047 patients who received Vueway at doses ranging from 0.025 mmol/kg (one half the recommended dose) to 0.3 mmol/kg (six times the recommended dose). A total of 708 patients received the recommended dose of 0.05 mmol/kg. Among patients who received the recommended dose, the average age was 51 years (range 2 years to 88 years) and 56% were female. The ethnic distribution was 79% White, 10% Asian, 7% American Indian or Alaska native, 2% Black, and 2% patients of other or unspecified ethnic groups.

Overall, approximately 4.7% of subjects receiving the labeled dose reported one or more adverse reactions.

Table 1 lists adverse reactions that occurred in > 0.2% of patients who received 0.05 mmol/kg Vueway.

TABLE 1. ADVERSE REACTIONS REPORTED IN > 0.2% OF PATIENTS RECEIVING VUEWAY IN CLINICAL TRIALS	
Adverse Reaction	Vueway 0.05 mmol/kg (n=708) (%)
Injection site pain	0.7
Headache	0.7
Nausea	0.4
Injection site warmth	0.4
Injection site coldness	0.3
Dizziness	0.3
Local swelling	0.3

Adverse reactions that occurred with a frequency < 0.2% in patients who received 0.05 mmol/kg Vueway included: maculopapular rash, vomiting, worsened renal impairment, feeling hot, pyrexia, oral paresthesia, dysgeusia, diarrhea, pruritus, allergic dermatitis, erythema, injection site paresthesia, Cystatin C increase, and blood creatinine increase.

Adverse Reactions in Pediatric Patients

One study with a single dose of Vueway (0.05 mmol/kg) was conducted in 80 pediatric patients aged 2 years to 17 years, including 60 patients who underwent a central nervous system (CNS) MRI and 20 patients who underwent a body MRI. One adverse reaction (maculopapular rash of moderate severity) in one patient (1.3%) was reported in the CNS cohort.

USE IN SPECIFIC POPULATIONS

Pregnancy Risk Summary There are no available data on Vueway use in pregnant women to evaluate for a drug-associated risk of major birth defects, miscarriage or other adverse maternal or fetal outcomes. GBCAs cross the human placenta and result in fetal exposure and gadolinium retention. The available human data on GBCA exposure during pregnancy and adverse fetal outcomes are limited and inconclusive (see Data). In animal reproduction studies, there were no adverse developmental effects observed in rats or rabbits with intravenous administration of Vueway during organogenesis (see Data). Because of the potential risks of gadolinium to the fetus, use Vueway only if imaging is essential during pregnancy and cannot be delayed. The estimated background risk of major birth defects and miscarriage for the indicated population(s) are unknown. All pregnancies have a background risk of birth defect, loss, or other adverse outcomes. In the U.S. general population, the estimated background risk of major birth defects and miscarriage in clinically recognized pregnancies is 2% to 4% and 15% to 20% respectively. Data Human Data Contrast enhancement is visualized in the placenta and fetal tissues after maternal GBCA administration. Cohort studies and case reports on exposure to GBCAs during pregnancy have not reported a clear association between GBCAs and adverse effects in the exposed neonates. However, a retrospective cohort study comparing pregnant women who had a GBCA MRI to pregnant women who did not have an MRI reported a higher occurrence of stillbirths and neonatal deaths in the group receiving GBCA MRI. Limitations of this study include a lack of comparison with non-contrast MRI and lack of information about the maternal indication for MRI. Overall, these data preclude

a reliable evaluation of the potential risk of adverse fetal outcomes with the use of GBCAs in pregnancy.

Animal Data Gadolinium Retention: GBCAs administered to pregnant non-human primates (0.1 mmol/kg on gestational days 85 and 135) result in measurable gadolinium concentration in the offspring in bone, brain, skin, liver, kidney, and spleen for at least 7 months. GBCAs administered to pregnant mice (2 mmol/kg daily on gestational days 16 through 19) result in measurable gadolinium concentrations in the pups in bone, brain, kidney, liver, blood, muscle, and spleen at one-month postnatal age.

Reproductive Toxicology: Animal reproduction studies conducted with gadopicholol showed some signs of maternal toxicity in rats at 10 mmol/kg and rabbits at 5 mmol/kg (corresponding to 52 times and 57 times the recommended human dose, respectively). This maternal toxicity was characterized in both species by swelling, decreased activity, and lower gestation weight gain and food consumption.

No effect on embryo-fetal development was observed in rats at 10 mmol/kg (corresponding to 52 times the recommended human dose). In rabbits, a lower mean fetal body weight was observed at 5 mmol/kg (corresponding to 57 times the recommended human dose) and this was attributed as a consequence of the lower gestation weight gain.

Lactation Risk Summary There are no data on the presence of gadopicholol in human milk, the effects on the breastfed infant, or the effects on milk production. However, published lactation data on other GBCAs indicate that 0.01% to 0.04% of the maternal gadolinium dose is excreted in breast milk. Additionally, there is limited GBCA gastrointestinal absorption in the breast-fed infant. Gadopicholol is present in rat milk. When a drug is present in animal milk, it is likely that the drug will be present in human milk (see Data). The developmental and health benefits of breastfeeding should be considered along with the mother's clinical need for Vueway and any potential adverse effects on the breastfed infant from Vueway or from the underlying maternal condition. Data In lactating rats receiving single intravenous injection of [¹⁵³Gd]-gadopiclenol, 0.3% and 0.2% of the total administered radioactivity was transferred to the pups via maternal milk at 6 hours and 24 hours after administration, respectively. Furthermore, in nursing rat pups, oral absorption of gadopicholol was 3.6%.

Pediatric Use The safety and effectiveness of Vueway for use with MRI to detect and visualize lesions with abnormal vascularity in the CNS (brain, spine, and associated tissues), and the body (head and neck, thorax, abdomen, pelvis, and musculoskeletal system) have been established in pediatric patients aged 2 years and older.

Use of Vueway in this age group is supported by evidence from adequate and well-controlled studies in adults with additional pharmacokinetic and safety data from an open-label, uncontrolled, multicenter, single dose study of Vueway (0.05 mmol/kg) in 80 pediatric patients aged 2 to 17 years. The 80 patients consisted of 60 patients who underwent a CNS MRI and 20 patients who underwent a body MRI [see Adverse Reactions (6.1) and Clinical Pharmacology (12.3) in the full Prescribing Information].

The safety and effectiveness of Vueway have not been established in pediatric patients younger than 2 years of age.

Geriatric Use Of the total number of Vueway-treated patients in clinical studies, 270 (26%) patients were 65 years of age and over, while 62 (6%) patients were 75 years of age and over. No overall differences in safety or efficacy were observed between these subjects and younger subjects.

This drug is known to be substantially excreted by the kidney, and the risk of adverse reactions to this drug may be greater in patients with impaired renal function. Because elderly patients are more likely to have decreased renal function, it may be useful to monitor renal function.

Renal Impairment In patients with renal impairment, the exposure of gadopicholol is increased compared to patients with normal renal function. This may increase the risk of adverse reactions such as nephrogenic systemic fibrosis (NSF). Avoid use of GBCAs among these patients unless the diagnostic information is essential and not available with non-contrast MRI or other modalities. No dose adjustment of Vueway is recommended for patients with renal impairment. Vueway can be removed from the body by hemodialysis [see Warnings and Precautions (5.1, 5.3, 5.4) and Clinical Pharmacology (12.3) in the full Prescribing Information].

OVERDOSAGE

Among subjects who received a single 0.3 mmol/kg intravenous dose of gadopicholol (6 times the recommended dose of Vueway), headache and nausea were the most frequently reported adverse reactions. Gadopicholol can be removed from the body by hemodialysis [see Clinical Pharmacology (12.3) in the full Prescribing Information].

PATIENT COUNSELING INFORMATION Advise the patient to read the FDA-approved patient labeling (Medication Guide).

Nephrogenic Systemic Fibrosis Inform the patient that Vueway may increase the risk for NSF among patients with impaired elimination of the drugs and that NSF may result in fatal or debilitating fibrosis affecting the skin, muscle and internal organs.

Instruct the patients to contact their physician if they develop signs or symptoms of NSF following Vueway administration, such as burning, itching, swelling, scaling, hardening and tightening of the skin; red or dark patches on the skin; stiffness in joints with trouble moving, bending or straightening the arms, hands, legs or feet; pain in the hip bones or ribs; or muscle weakness [see Warnings and Precautions (5.1) in the full Prescribing Information].

Gadolinium Retention Advise patients that gadolinium is retained for months or years in brain, bone, skin, and other organs following Vueway administration even in patients with normal renal function. The clinical consequences of retention are unknown. Retention depends on multiple factors and is greater following administration of linear GBCAs than following administration of macrocyclic GBCAs [see Warnings and Precautions (5.3) in the full Prescribing Information].

Injection Site Reactions Inform the patient that Vueway may cause reactions along the venous injection site, such as mild and transient burning or pain or feeling of warmth or coldness at the injection site [see Warnings and Precautions (5.5) in the full Prescribing Information].

Pregnancy Advise pregnant women of the potential risk of fetal exposure to Vueway [see Use in Specific Populations (8.1) in the full Prescribing Information].

Rx only

US Patent No. 10,973,934
Manufactured for Bracco Diagnostics Inc. by Liebel-Flarsheim Company LLC - Raleigh, NC, USA 27616.
Toll Free: 1-877-272-2269 (U.S. only)
Revised November 2022

JOIN US! COMPREHENSIVE NEURORADIOLOGY COURSE

February 1-3, 2024 • Cancun, Mexico / On-Demand

ASNR's Comprehensive Neuroradiology Course offers you three days of image-rich neuroradiology review focused on:

**Adult Brain Imaging | Head and Neck Imaging | Spine Imaging
Pediatric Neuroradiology | Advanced Imaging Techniques**

Join our award-winning faculty and engage in our interactive classroom environment, as well as during planned social and evening activities. Take advantage of a discounted, all-inclusive rate at the host hotel: the Hyatt Ziva Cancun!

Can't attend in person? An on-demand option is also available!

**Get all of the details and register now at
www.asnr.org/cnc24.**

Meet the Faculty

Joshua Nickerson, MD, FACR

Professor, Division Chief of Neuroradiology, Oregon Health & Science University

Tabassum Kennedy, MD

Professor, Division Chief of Neuroradiology, University of Wisconsin, Madison

Judith Gadde, DO, MBA

Associate Professor, Northwestern University Feinberg School of Medicine;
Pediatric Radiology Rotation Site Director, Lurie Children's Hospital of Chicago

Mahmud Mossa-Basha, MD

Professor of Radiology, Vice Chair of Clinical Research and Clinical Transformation,
University of Washington School of Medicine

Wende Gibbs, MD, MA

Associate Professor, Director of Spine Imaging and Intervention, Barrow
Neurological Institute

Ashley Aiken, MD,

Professor of Radiology and Imaging Sciences, Vice Chair of Faculty Advancement,
Emory University

**I am a global citizen.
I am patient-centered care.
I am an academic neuroradiologist.
I am a researcher.
I am a life-long learner.
I am determined.
I am curious.
I am a collaborative team player.
I am a volunteer.
I am ASNR.**

Don't miss out on the tools, resources and relationships you've come to rely on. Log in and renew your ASNR membership today! www.asnr.org

THE FOUNDATION OF THE ASNR



Apply Now! Foundation of the ASNR Grants 2024 Cycle Is Now Open

The Foundation of the ASNR's Grant Program is presented annually to support members of the ASNR who demonstrate great promise for future contributions to the field of neuroradiology.

Visit foundation.asnr.org for all of the details and deadlines.

Research projects will now be funded at \$120,000 each!

Foundation of the ASNR Grant Program 2022 Recipients Are Making an Impact

The primary goal of our study is to develop and evaluate a state-of-the-art automated pre- and postoperative glioblastoma volumetric segmentation algorithm at a high-volume brain tumor center. The significance of this study is that it will provide a new tool for automated, objective assessment of progression and/or treatment response in patients with glioblastoma. This grant has been instrumental in jumpstarting my research career as a junior academic neuroradiology faculty member. With this award I have been able to secure essential dedicated research time and personnel support to help achieve my early career research goals. All FASNR donors should know that these awards make a difference and help build successful radiology research careers.



**Evan Calabrese,
MD, PhD**
Duke University

Paramagnetic rim lesions (PRLs) may serve as an imaging marker for the work up of multiple sclerosis (MS) progression and treatment. With the help of the ASNR foundation grant, we are working to establish a radiologic-histological correlation for PRLs. The study of PRLs and this research could clinically impact MS diagnosis and monitoring, may better determine the efficacy of existing therapeutic agents or stimulate development of new therapeutics, and overall may help reduce disability associated with disease progression. This work would not have been possible without the generous support of the Foundation.



**Emmanuel Obusez,
MD**
Cleveland Clinic

AJNR

AMERICAN JOURNAL OF NEURORADIOLOGY


DECEMBER 2023
VOLUME 44
NUMBER 12
WWW.AJNR.ORG

Publication Preview at www.ajnr.org features articles released in advance of print.
Visit www.ajnrblog.org to comment on AJNR content and chat with colleagues.

EDITORIAL



- 1357 **Introducing AJNR SCANTastic and the AJNR Academy of Reviewers** *Max Wintermark, MD*

REVIEW ARTICLE

-  1358 **Monoclonal Antibodies: What the Diagnostic Neuroradiologist Needs to Know** *R. Alsufayan, et al.*

ADULT BRAIN

GENERAL CONTENTS

-  1367 **Prevalence and Characteristics of Intracranial Aneurysms in Hereditary Hemorrhagic Telangiectasia** *How-Chung Cheng, et al.*
- 1373 **Predicting Antiseizure Medication Treatment in Children with Rare Tuberous Sclerosis Complex–Related Epilepsy Using Deep Learning** *Haifeng Wang, et al.*
-  1384 **Brain Age Estimation on a Dementia Cohort Using FLAIR MRI Biomarkers** *Owen Crystal, et al.*
-  1391 **Deep Learning–Based Synthetic TOF-MRA Generation Using Time-Resolved MRA in Fast Stroke Imaging** *Sung-Hye You, et al.*
-  1399 **Quantification of Thalamic Atrophy in MS: From the Multicenter Italian Neuroimaging Network Initiative Data Set to Clinical Application** *Loredana Storelli, et al.*
-  1405 **Brain Abnormalities in Becker Muscular Dystrophy: Evaluation by Voxel-Based DTI and Morphometric Analysis** *Hiroyuki Maki, et al.*
-  1411 **Comparison of Quantitative Hippocampal Volumes and Structured Scoring Scales in Predicting Alzheimer Disease Diagnosis** *Michael Essien, et al.*
-  1418 **Cervical Osteomyelitis and Diskitis as a Complication of Neopharyngeal Breakdown: A Multisite Case Series Review** *Alok A. Bhatt, et al.*
-  1421 **CT of the Larynx: Is an Additional High-Resolution Acquisition Necessary for Diagnostic Accuracy?** *Eva Chau, et al.*
-  1425 **Diagnostic Value of Multiparameter MRI-Based Radiomics in Pediatric Myelin Oligodendrocyte Glycoprotein Antibody–Associated Disorders** *Ting Li, et al.*

NEUROVASCULAR/
STROKE IMAGING

ARTIFICIAL
INTELLIGENCE

ARTIFICIAL
INTELLIGENCE

ARTIFICIAL
INTELLIGENCE

ULTRA-HIGH-FIELD MRI/
IMAGING OF EPILEPSY/
DEMYELINATING DISEASES/
INFLAMMATION/INFECTION

NEURODEGENERATIVE
DISORDER IMAGING








NEURODEGENERATIVE
DISORDER IMAGING

HEAD AND NECK
IMAGING

HEAD AND NECK
IMAGING

PEDIATRIC
NEUROIMAGING

AJNR (Am J Neuroradiol ISSN 0195–6108) is a journal published monthly, owned and published by the American Society of Neuroradiology (ASNR), 820 Jorie Boulevard, Oak Brook, IL 60523. Annual dues for the ASNR include approximately 19% for a journal subscription. The journal is printed by Intellicor Communications, 330 Eden Road, Lancaster, PA 17601; Periodicals postage paid at Oak Brook, IL and additional mailing offices. Printed in the U.S.A. POSTMASTER: Please send address changes to American Journal of Neuroradiology, P.O. Box 3000, Denville, NJ 07834, U.S.A. Subscription rates: nonmember \$452 (\$530 foreign) print and online, \$320 online only; institutions \$520 (\$594 foreign) print and basic online, \$1029 (\$1103 foreign) print and extended online, \$380 online only (basic), \$825 online only (extended); single copies are \$35 each (\$40 foreign). Indexed by PubMed/MEDLINE, BIOSIS Previews, Current Contents (Clinical Medicine and Life Sciences), EMBASE, Google Scholar, HighWire Press, Q-Sensei, RefSeek, Science Citation Index, SCI Expanded, ReadCube, and Semantic Scholar. Copyright © American Society of Neuroradiology.

-   **1432 Automatic Quantification of Normal Brain Gyrfication Patterns and Changes in Fetuses with Polymicrogyria and Lissencephaly Based on MRI** *Bossmat Yehuda, et al.*
-  **1440 Fetal Brain Growth in the Early Second Trimester** *Maria Camila Cortes-Albornoz, et al.*
-  **1445 Diagnostic Performance of Decubitus Photon-Counting Detector CT Myelography for the Detection of CSF-Venous Fistulas** *Ajay A. Madhavan, et al.*
-   **1451 T1-Weighted, Dynamic Contrast-Enhanced MR Perfusion Imaging Can Differentiate between Treatment Success and Failure in Spine Metastases Undergoing Radiation Therapy** *Mark Behar, et al.*
- 1458 Accuracy of Noncontrast T2 SPACE in Active MS Cord Lesion Detection** *Anousheh Sayah, et al.*
-  **1464 Automated Determination of the H3 K27-Altered Status in Spinal Cord Diffuse Midline Glioma by Radiomics Based on T2-Weighted MR Images** *Junjie Li, et al.*

**PEDIATRIC
NEUROIMAGING**

**PEDIATRIC
NEUROIMAGING**

**SPINE IMAGING AND
SPINE IMAGE-GUIDED
INTERVENTIONS**

**SPINE IMAGING AND
SPINE IMAGE-GUIDED
INTERVENTIONS**

**SPINE IMAGING AND
SPINE IMAGE-GUIDED
INTERVENTIONS**

**SPINE IMAGING AND
SPINE IMAGE-GUIDED
INTERVENTIONS**

ONLINE FEATURES

ANNUAL MEETING

- E46 “Best of” ASNR 2023 (Chicago) and “Sneak Peek” of ASNR 2024 (Las Vegas)** *Paul M. Bunch, et al.*

MEMORIAL

- E52 Robert D. Zimmerman, MD** *E. Russell, et al.*

BOOK REVIEWS *R.M. Quencer, Section Editor*

Please visit www.ajnrblog.org to read and comment on Book Reviews.



In a dynamic contrast-enhanced MR imaging perfusion study of spinal metastatic disease, Behar et al found that perfusion parameters, specifically plasma volume, may be able to discriminate between treatment success and persistent disease.



Indicates Editor's Choices selection



Indicates Fellows' Journal Club selection



Indicates open access to non-subscribers at www.ajnr.org



Indicates article with supplemental online data



Indicates article with supplemental online video



Evidence-Based Medicine Level 1



Evidence-Based Medicine Level 2

EDITOR-IN-CHIEF

Max Wintermark, MD, MAS, FASFN, FICIS

*Frank T. McGraw Memorial Chair in the Study of Cancer
Professor and Chair of Neuroradiology
The University of Texas MD Anderson Center*

DEPUTY EDITOR

Lubdha M. Shah, MD, MS

Professor of Radiology and Director of Spine Imaging
Department of Radiology and Imaging Sciences
University of Utah

SPECIAL ADVISORS TO THE EDITOR-IN-CHIEF

Mauricio Castillo, MD, FACR

MA Mauro Distinguished Professor of Radiology
University of North Carolina-Chapel Hill

Robert Quencer, MD

Professor Emeritus
Department of Radiology
University of Miami

ARTIFICIAL INTELLIGENCE

Senior Editor

Reza Forghani, MD, PhD

Professor of Radiology & Artificial Intelligence
Vice Chair of AI
Director, Radiomics & Augmented Intelligence Laboratory (RAIL)
Department of Radiology
University of Florida College of Medicine

Associate Editors

Andreas Rauschecker, MD, PhD

Assistant Professor-in-Residence
Co-Executive Director and Clinical Director,
Center for Intelligent Imaging (ci²)
Department of Radiology & Biomedical Imaging
University of California, San Francisco

Sam (Sayedmehdi) Payabvash, MD

Assistant Professor of Radiology
Yale School of Medicine
Connecticut

BRAIN TUMOR IMAGING

Senior Editor

Ben Ellingson, MD

Professor and Director of MRI Research
Director, UCLA Brain Tumor Imaging Laboratory
Department of Radiological Sciences
David Geffen School of Medicine
University of California, Los Angeles

Associate Editors

Ali Nabavizadeh, MD

Assistant Professor of Radiology
Division of Neuroradiology
University of Pennsylvania

Mark S. Shiroishi, MD, MS, FASFN

Assistant Professor, Division of Neuroradiology,
Department of Radiology
Director of Neuro-Oncology Imaging - USC Brain Tumor Center
Chief of Pediatric Neuroradiology - Los Angeles General Medical Center
Affiliated Faculty - USC Imaging Genetics Center
Mark and Mary Stevens Neuroimaging and Informatics Institute
Keck School of Medicine of USC
University of Southern California

EMERGENCY NEURORADIOLOGY

Senior Editor

Karen Buch, MD

Assistant Professor of Radiology
Massachusetts General Hospital

Associate Editors

Melissa A. Davis, MD, MBA

Vice Chair of Medical Informatics
Associate Professor
Department of Radiology and Biomedical Imaging
Yale School of Medicine
Connecticut

Jason Talbott, MD, PhD

Associate Professor, Neuroradiology Section
Department of Radiology and Biomedical Imaging
University of California, San Francisco and
Zuckerberg San Francisco General Hospital

HEAD AND NECK IMAGING

Senior Editor

Amy Juliano, MD

Associate Professor of Radiology
Massachusetts Eye and Ear
Harvard Medical School

Associate Editors

Burce Ozgen, MD

Clinical Professor of Radiology
University of Illinois at Chicago

David Zander, MD

Assistant Professor, Radiology
University of Colorado School of Medicine

HEALTH POLICIES/QUALITY IMPROVEMENT/ EVIDENCE-BASED NEUROIMAGING

Senior Editor

Nadja Kadom, MD, FACR, FAAP

Professor, Department of Radiology and Imaging Sciences
Emory University School of Medicine
Pediatric Neuroradiologist, Department of Radiology
Children's Healthcare of Atlanta

Associate Editors

Melissa M. Chen, MD

Associate Professor,
Department of Neuroradiology, Division of Diagnostic Imaging
The University of Texas MD Anderson Center

Ajay Malhotra, MBBS, MD, MMM

Professor of Radiology and Biomedical Imaging and Neurosurgery
Yale School of Medicine
Connecticut

MOLECULAR NEUROIMAGING/NUCLEAR MEDICINE

Senior Editor

Ana M. Franceschi, MD, PhD

Associate Professor of Radiology
Donald and Barbara Zucker School of Medicine at Hofstra/Northwell
The Feinstein Institutes for Medical Research
Neuro-PET Imaging
Lenox Hill Hospital
New York

Associate Editors

Nadya Pyatigorskaya, MD, PhD

Neuroradiology Department, Pitié-Salpêtrière Hospital
Researcher, Brain Institute (ICM)
France

Marc Daniel Benayoun, PhD, MD

Assistant Professor of Radiology
Co-Section Head of Nuclear Medicine
Medical Director of Nuclear Medicine and PET
Vice Chair of Radiation Drug Research Committee
Atrium Wake Forest Health
North Carolina

NEURODEGENERATIVE DISORDER IMAGING

Senior Editor

Gloria Chiang, MD

Associate Professor, Co-Director of the Brain Health Imaging Institute
Department of Radiology
Weill Cornell Medicine/NewYork-Presbyterian Hospital

Associate Editors

Fang Frank Yu, MD

Assistant Professor of Radiology
Division of Neuroradiology, Department of Radiology
Advanced Imaging Research Center
University of Texas Southwestern Medical Center

Priya Rajagopalan, MBBS, MPH

Assistant Professor of Radiology, Division of
Neuroradiology
Associate Program Director, Neuroradiology
Fellowship
Medical Director, Center for Image Acquisition
Mark and Mary Stevens Neuroimaging and
Informatics Institute
Keck School of Medicine, University of Southern
California

**NEUROIMAGING PHYSICS/FUNCTIONAL
NEUROIMAGING/CT AND MRI TECHNOLOGY****Senior Editor****Hongyu An, DSc**

Professor, Mallinckrodt Institute of Radiology
Neurology, Biomedical Engineering, Electrical and
Systems Engineering, Division of Biology and
Biomedical Sciences
Director, Biomedical Magnetic Resonance Center
Associate Director, Center for Clinical Imaging Research
Washington University in St. Louis

Associate Editors**Timothy J. Carroll, PhD**

Professor, Department of Radiology
University of Chicago

Hugo de Jong, PhD

Professor of Medical Physics Radiology and
Nuclear Medicine
UMC Utrecht
the Netherlands

NEUROINTERVENTION**Senior Editor****Steven Hetts, MD, FACR**

Co-Chief, NeuroEndovascular Surgery Service Line
Chief of Interventional Neuroradiology, Mission
Bay Hospitals
Professor of Radiology, Biomedical Imaging, and
Neurological Surgery
University of California, San Francisco

Associate Editors**Kristine Blackham, MD**

Associate Professor
Diagnostic and Interventional Neuroradiology
Clinic for Radiology and Nuclear Medicine
University Hospital of Basel

Maksim Shapiro, MD

Clinical Associate Professor
Departments of Radiology, Neurosurgery, and
Neurology
Division of Neurointerventional Radiology
NYU Langone Health and Bellevue NYCH +
Hospitals
New York

NEUROPSYCHIATRIC IMAGING**Senior Editor****Jody Tanabe, MD**

Professor
Chief of Neuroradiology
University of Colorado-Anschutz Medical Campus

Associate Editors**John-Paul J. Yu, MD, PhD**

Assistant Professor of Radiology, Psychiatry, and
Biomedical Engineering
University of Wisconsin School of Medicine and
Public Health

J. Eric Schmitt, MD, PhD

Assistant Professor of Radiology and Psychiatry
Division of Neuroradiology
Perelman School of Medicine, University of
Pennsylvania

NEUROVASCULAR/STROKE IMAGING**Senior Editor****Ajay Gupta, MD, MS**

Alexander R. Margulis, MD, Distinguished
Professor in Radiology
Weill Cornell Medical College
New York

Associate Editors**Shalini Amukotuwa, MB BS, PhD,
FRANZCR**

Head of Neuroradiology and Director of MRI,
Monash Health
Associate Professor of Radiology, Monash University
Australia

Mahmud Mossa-Basha, MD

Professor of Radiology, Neurology and Electrical
Engineering
Vice Chair of Clinical Research and Clinical
Transformation
Co-Director of the Research Vascular Imaging Lab
University of Washington School of Medicine

PEDIATRIC NEUROIMAGING**Senior Editor****Caroline D. Robson, MBChB**

Division Chief & Endowed Chair, Neuroradiology
Director, Head & Neck Imaging
Department of Radiology
Department of Otolaryngology
Boston Children's Hospital
Harvard Medical School

Associate Editors**Anna Trofimova, MD, PhD**

Assistant Professor, Radiology and Imaging
Sciences, Emory University
Pediatric Neuroradiologist, Children's Healthcare
of Atlanta

Matthew Whitehead, MD

Department of Radiology, Division of
Neuroradiology
Children's Hospital of Philadelphia
Associate Professor of Radiology
Perelman School of Medicine, University of
Pennsylvania

**SPINE IMAGING AND SPINE IMAGE-GUIDED
INTERVENTIONS****Senior Editor****J. Levi Chazen, MD**

Associate Professor, Neuroradiology
Director, Spine Imaging
Hospital for Special Surgery
Weill Cornell Medicine
New York

Associate Editors**Jennifer McCarty, MD**

UTHealth Houston

Vinil Shah, MD

Associate Professor of Radiology Neuroradiology
Division Chief
University of California, San Francisco

**ULTRA-HIGH-FIELD MRI/IMAGING OF
EPILEPSY/DEMYELINATING DISEASES/
INFLAMMATION/INFECTION****Senior Editor****Erik Middlebrooks, MD**

Professor of Radiology
Mayo Clinic Florida

Associate Editors**Susie Y. Huang, MD, PhD**

Associate Professor of Radiology, Harvard
Medical School
Associate Chair, Faculty Affairs, Department of
Radiology
Director of Translational Neuro MR Imaging &
Connectomics, Athinoula A. Martinos Center for
Biomedical Imaging
Massachusetts General Hospital

Girish Bathla, MD, FRCR

Associate Professor, Neuroradiology
Mayo Clinic
Minnesota

OUTREACH AND EDUCATION**Senior Editor****Lea Alhilali, MD**

Radiology Partners, HonorHealth Research
Institute
Arizona

DIGITAL MEDIA AND ENGAGEMENT**Senior Editor****Kevin Hsu, MD**

Clinical Assistant Professor
Department of Radiology
NYU Grossman School of Medicine
New York

Case Collection Editors**Matylda Machnowska, BMedSc, MD,
FRCSC, ABR**

Assistant Professor of Radiology, University of
Toronto
Neuroradiologist, Sunnybrook Health Sciences
Centre

Anvita Pauranik, MD

Clinical Assistant Professor of Radiology
BC Children's Hospital
University of British Columbia

Sandy Cheng-Yu Chen, MD

Chair, Translational Imaging Research Center
Taipei Medical University Hospital
Vice President of Taipei Medical University

Social Media Editor**Kimberly Seifert, MD, MS**

Stanford University
California

Assistant Social Media Editors**Ani Hoxha, MD**

Mother Theresa UHC
Albania

Maxwell Opoku, MD

Novosibirsk State Research University
Russia

Podcast Editor

Kevin Hiatt, MD

Assistant Professor, Radiology
Wake Forest University School of Medicine
North Carolina

Deputy Podcast Editor

George K. Vilanilam, MD

PGY5 Resident Physician, Department of Radiology
University of Arkansas for Medical Sciences

STATISTICS

Senior Editor

Bryan A. Comstock, MS

Senior Biostatistician, Department of Biostatistics
University of Washington

EDITORIAL FELLOWS

Alexandre Boutet, MD, PhD

Neuroradiologist
Joint Department of Medical Imaging
University of Toronto

Nicholas S. Cho, MD/PhD Candidate

University of California, Los Angeles

Burak Berksu Ozkara, MD

Research Fellow
Department of Neuroradiology
The University of Texas MD Anderson Center

BOOK REVIEW EDITOR

Robert Quencer, MD

Professor Emeritus
Department of Radiology
University of Miami

Founding Editor
Juan M. Taveras

Editors Emeriti
Mauricio Castillo, Robert I. Grossman,
Michael S. Huckman, Robert M. Quencer,
Jeffrey S. Ross

Managing Editor
Karen Halm
Assistant Managing Editor
Laura Wilhelm
Executive Director, ASNR
Mary Beth Hepp

Introducing *AJNR* SCANTastic and the *AJNR* Academy of Reviewers

Max Wintermark, MD

Editor-in-Chief, *American Journal of Neuroradiology*

In this age of rapid technological progress, our capacity to communicate and share information has undergone remarkable transformation. The *American Journal of Neuroradiology* fully embraces this digital revolution, recognizing the diverse communication needs and preferences of our audiences. It underscores the importance of customizing our approaches to cater to these distinct requirements.

In the upcoming months, our readers will witness a series of initiatives designed to redefine how the *AJNR* engages with its audience. Leading this charge is *AJNR* SCANTastic, spearheaded by Dr Lea Alhilali, from Radiology Partners, Instagram, and the Research Institute in Arizona. *AJNR* SCANTastic represents a novel educational endeavor on social media, injecting a fresh perspective into the realm of neuroradiology research. Its mission is to make the high-quality content of *AJNR* more accessible and insightful, extending its impact to a broader readership and amplifying the influence of neuroradiology research. The potential applications of *AJNR* SCANTastic are far-reaching, benefiting trainees and patient education alike. We invite you to explore *AJNR* SCANTastic on platforms such as X (Twitter), Facebook, LinkedIn, and Instagram and help us spread the word!

<http://dx.doi.org/10.3174/ajnr.A8043>

In the dynamic landscape of academic publishing, peer review serves as a cornerstone of quality assurance and knowledge dissemination. It is the mechanism through which scholarly work is rigorously assessed and authors receive constructive feedback, fostering a culture of continuous improvement and collaboration. To bolster this essential process, the *AJNR* is proud to introduce its Academy of Reviewers, a program led by Dr Mauricio Castillo, Emeritus Editor, and Dr Alexandre Boutet, Editorial Fellow.

The *AJNR* Academy of Reviewers is an initiative aimed at elevating the quality of the peer review process. It establishes a structured framework for reviewer training, mentorship, and ongoing professional development. By providing rigorous training, guidance, and best practices through the Academy, we anticipate a significant enhancement in the quality of reviews, resulting in more dependable peer assessment of academic work. The Academy also serves to standardize review practices and ethical standards, ensuring fairness and consistency in the peer review process. Transparent and accountable reviews not only benefit authors but also enhance the credibility and integrity of academic publishing.

In an era marked by the swift flow of information and the relentless expansion of academic content, both publishing and peer review processes must adapt and progress. The groundbreaking initiatives of *AJNR* SCANTastic and the *AJNR* Academy of Reviewers offer the promise of cultivating a more resilient, well-informed, and widely disseminated scholarly publishing landscape. As these innovative concepts take hold, it becomes paramount to nurture and sustain them to grow and develop our neuroradiology community as a cohesive whole.

Monoclonal Antibodies: What the Diagnostic Neuroradiologist Needs to Know

R. Alsufayan, C. Hess, and T. Krings



ABSTRACT

SUMMARY: Monoclonal antibodies have become increasingly popular as novel therapeutics against a variety of diseases due to their specificity, affinity, and serum stability. Due to the nearly infinite repertoire of monoclonal antibodies, their therapeutic use is rapidly expanding, revolutionizing disease course and management, and what is now considered experimental therapy may soon become approved practice. Therefore, it is important for radiologists, neuroradiologists, and neurologists to be aware of these drugs and their possible different imaging-related manifestations, including expected and adverse effects of these novel drugs. Herein, we review the most commonly used monoclonal antibody–targeted therapeutic agents, their mechanism of action, clinical applications, and major adverse events with a focus on neurologic and neurographic effects and discuss differential considerations, to assist in the diagnosis of these conditions.

ABBREVIATIONS: Ab = antibody; AE = adverse event; Ag = antigen; ARIA = amyloid-related imaging abnormalities; CAA = cerebral amyloid angiopathy; CTLA-4 = cytotoxic T-lymphocyte Ag 4; Fc = constant fragment; IRAE = immune-related AE; IRIS = immune reconstitution inflammatory syndrome; mAb = monoclonal antibody; NTZ = natalizumab; PML = progressive multifocal leukoencephalopathy; PRES = posterior reversible encephalopathy syndrome; TNF = tumor necrosis factor

Antibodies (Abs) are produced by B cells and share the same basic structure, which is Y-shaped and allows Ab molecules to carry out their dual functions: antigen (Ag) binding and biologic activity mediation.

The base of the Ab is composed of a constant fragment (Fc), which imparts the effector properties of the molecule in the immune system, on its recognition by Fc receptors present on various cell types that determine the actual biologic effect. The opposing end is the variable fragment of the molecule that binds to unique Ags, imparting the specificity of each Ab. Each B-cell line produces Abs specific for 1 unique epitope, thus resulting in monoclonal Ab (mAb) production. At times, multiple B cells generate different Abs against multiple epitopes from different

regions of a full-length protein Ag. This feature allows immune responses to a highly specific target to disable/eliminate the Ag from the system, after which B cells remain in the bloodstream ready to produce Abs when the Ag is encountered again.¹

The method of producing various mAbs against a variety of targets, ranging from cancer to autoimmune diseases, is similar. The target Ag, or part thereof, is injected into a host animal, mounting an immune response and creating a pool of B cells specific to that Ag. The B cells are then harvested and cultured with myeloma cells, creating a hybridoma of a line of immortal mAb-producing cells that can divide to generate more of the desired mAbs. However, the Fcs of Abs produced in host animals are foreign to the human immune system, inducing a response that can neutralize the treatment or even lead to an anaphylactic reaction. Three options are available to overcome this hurdle: The mAbs can be humanized through the use of transgenic mice that create Abs with human Fcs. Products that use this method have names that end in -zumab.¹ A second approach is to split host-derived mAbs and then combine the created variable fragment with human Fc. The end products are chimeras and have names that end in -ximab.¹ A third approach is to create a fusion protein composed of a human Fc and an Ag-specific receptor. These do not resemble typical Abs but act in a similar manner and have names that end in -cept.¹ mAbs mediate their therapeutic effect by targeting cells for death via Ab-induced apoptosis, Ab-dependent cell cytotoxicity, or complement mediated cell lysis, or

Received June 19, 2023; accepted after revision July 17.

From the Division of Neuroradiology, Department of Medical Imaging (R.A., T.K.), University of Toronto, Toronto Western Hospital, University Health Network and University Medical Imaging, Toronto, Ontario, Canada; Department of Diagnostic Imaging (R.A.), Peterborough Regional Health Centre, Peterborough, Ontario, Canada; Department of Radiology and Biomedical Imaging (C.H.), University of California, San Francisco, San Francisco, California; and Division of Neurosurgery (T.K.), Sproul Department of Surgery, University of Toronto, Toronto, Ontario, Canada.

Please address correspondence to Timo Krings, MD, PhD, FRCP(C), Neuroradiology, University of Toronto, Toronto Western Hospital, 3MCL-431, 399 Bathurst St, Toronto, ON, M5T2S8, Canada; e-mail: timo.krings@uhn.ca

Indicates open access to non-subscribers at www.ajnr.org

Indicates article with online supplemental data.

<http://dx.doi.org/10.3174/ajnr.A7974>

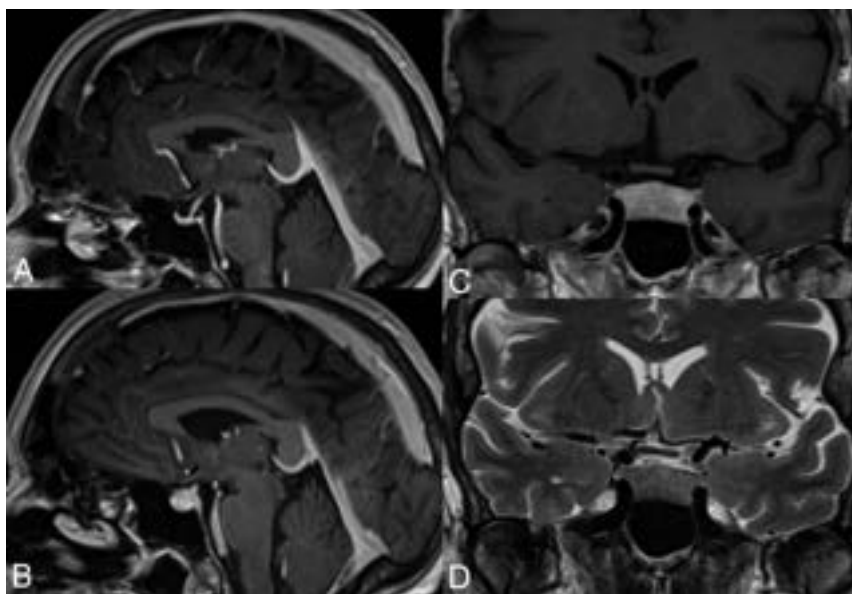


FIG 1. Hypophysitis induced by anti-CTLA-4 mAbs. This 61-year-old woman with metastatic melanoma underwent adjuvant treatment with ipilimumab. A, Sagittal T1 fast-spoiled gradient recalled image cut through the midline, postgadolinium, at initiation of treatment in the patient with a normal-for-age pituitary gland. MR imaging 6 months later (B–D) demonstrates a markedly thickened, densely enhancing pituitary gland in keeping with ipilimumab-induced hypophysitis.

mAbs can physically block a receptor ligand interaction,¹ with the ultimate goal of targeting a specific cell population or molecule relevant to disease pathogenesis.

Generally, only ~0.1% of the circulating Abs enter the brain, and they do so via either adsorptive-mediated endocytosis, carrier-mediated transport, or receptor-mediated transcytosis.² This process is discussed in greater detail in the Online Supplemental Data.

Immunostimulating mAbs: Ipilimumab and Tremelimumab

Ipilimumab and tremelimumab are mAbs that selectively block cytotoxic T-lymphocyte Ag 4 (CTLA-4), an immune-inhibitory protein expressed on activated T cells, thereby enhancing the immune response against tumors.³ In multiple trials, they have shown high efficacy in the treatment of metastatic melanoma.^{3,4} They are currently under study for the treatment of various other types of advanced malignancy, including metastatic renal cell carcinoma and prostate cancer.

The most common adverse events (AEs), affecting >10% of patients, are diarrhea, rash, pruritus, fatigue, nausea or vomiting, abdominal pain, insomnia, anorexia, hallucinations, and temperature intolerance.^{3,4} In addition, a novel spectrum of autoimmune-inflammatory toxicities surfaced, the pathogenic mechanism of which seems to be sustained by the positive modulation on the immune system known as immune-related AEs (IRAEs).⁵ The gastrointestinal tract, liver, skin, pituitary, and the musculoskeletal system are most frequently involved, leading to colitis, hepatitis, dermatitis, hypophysitis, and arthritis. Rarer IRAEs include uveitis, thyroiditis, primary adrenal insufficiency, polyneuritis, Guillain-Barré syndrome, optic ischemic or peripheral neuropathy, pneumonitis, pancreatitis, aseptic meningitis, nephritis, red blood cell aplasia, myocarditis, myasthenia gravis, sarcoidosis, and

myositis. The frequency and severity of IRAEs appear to be dose-dependent.^{6,7} Occasionally (~1%), deaths have occurred as a result of colonic perforation.⁸

From a neurologic and neuroradiologic point of view, hypophysitis is the most commonly encountered AE of these drugs and is estimated to occur in 10%–18% of patients treated.⁹ MR imaging features of hypophysitis are typically characterized by diffuse enlargement of the pituitary gland, with loss of normal posterior pituitary signal intensity on the precontrast T1WI and variable enlargement of the infundibulum. Enhancement is typically uniform but can be heterogeneous (Fig 1).¹⁰

Symptoms are variable, such as fatigue, insomnia, anorexia, hallucinations, and temperature intolerance. The laboratory findings may show a decline in values of biomarkers of the affected pituitary lobe, ie, thyroid-stimulating hormone, cortisol, and sex hormones compared with the normal ranges.

Several issues concerning anti-CTLA-4-induced hypophysitis remain to be fully elucidated, including the higher prevalence in males and the lower incidence in patients exposed to tremelimumab compared with ipilimumab.¹¹

Clinically, resolution of acute symptoms after discontinuation of mAb treatment and steroid therapy is typically seen; if required, hormone replacement therapies are initiated. It remains to be seen how many patients will have persistent partial hypopituitarism or panhypopituitarism requiring long-term hormone replacement. Most important, the treatment of IRAEs with immunosuppressive agents, such as corticosteroids, does not appear to affect the anti-tumor response.⁶

The most important differential diagnosis is that of a new pituitary metastatic deposit; this can only be evaluated with time with follow-up imaging after cessation of mAb treatment (Online Supplemental Data). Other causes of hypophysitis unrelated to anti-CTLA-4 mAbs may be considered, including polyglandular autoimmune syndromes and immunoglobulin G-related systemic disease, secondary hypophysitis due to local inflammation of the pituitary as a reaction to sellar disease, or systemic diseases (infectious or inflammatory disorders, eg, Wegener granulomatosis, sarcoidosis, tuberculosis, or syphilis).^{12,13}

Immunosuppressive mAbs: Natalizumab

Natalizumab (NTZ) is a humanized monoclonal antibody directed against the $\alpha 4\beta 1$ and $\alpha 4\beta 7$ integrins. It prevents inflammatory cells from binding to cerebrovascular endothelial cells, thereby preventing them from crossing the BBB,¹⁴ resulting in CNS immunosuppression. It is mainly used for relapsing-remitting MS but has also proved efficacy in Crohn disease and ankylosing spondylitis.¹⁵

The overall incidence of AEs associated with NTZ is low. However, 3 associated phenomena need to be kept in mind

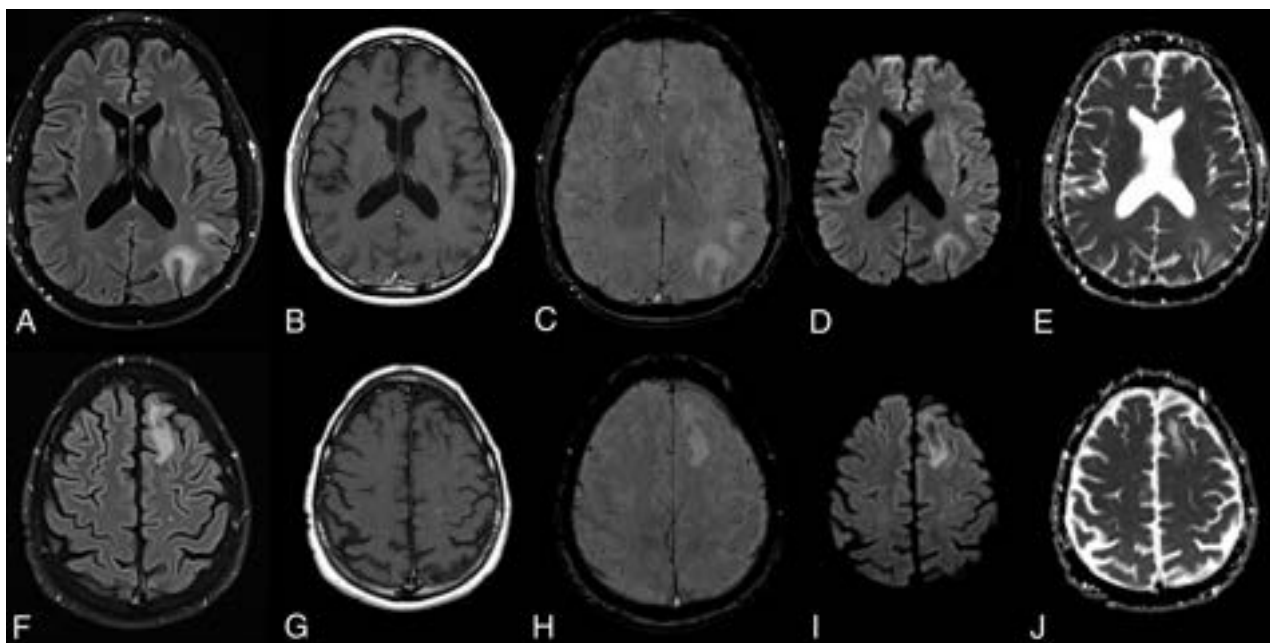


FIG 2. NTZ-induced PML. PML in a 52-year-old male patient with Crohn disease treated with NTZ. FLAIR (A and F), enhanced T1 (B and G), SWI (C and H), DWI (D and I), and ADC maps (E and J) at ganglionic (A–E) and supraganglionic (F–J) levels demonstrate the typical imaging features of PML with subcortical U-fiber involvement, lack of enhancement, and asymmetric involvement of the white matter.

because early recognition of their spectrum of clinical and imaging findings is crucial to limit morbidity: The primary AE is progressive multifocal leukoencephalopathy (PML). Secondly, on clearance of NTZ, a PML-associated immune reconstitution inflammatory syndrome (PML-IRIS) may occur, resulting in a paradoxical worsening of symptoms. Third, on cessation of NTZ, an exuberant rebound of MS may be observed.¹⁶

PML

The cause of PML is the neurotrophic polyoma JC virus. By causing lytic infection of brain oligodendrocytes and, to a lesser extent, astrocytes, widespread CNS demyelination ensues. Clinical signs and symptoms of PML vary. The most common symptoms in PML are confusion, hemiparesis, incoordination, speech disturbance, and visual problems.¹⁷

On MR imaging, PML presents with preferentially peripheral, variably sized and shaped white matter T2/FLAIR hyperintensities, classically involving subcortical U-fibers, which do not conform to cerebrovascular territories and do not enhance (Fig 2). They are bilateral, with an asymmetric distribution, growing larger and becoming confluent as the disease progresses, with no or only mild mass effect. Involvement of the overlying cortex, while originally thought to be rare, has been increasingly reported.^{18,19}

With time, lesions become increasingly hypointense on T1WI as irreversible white matter destruction occurs, and they may demonstrate a “microcyst” or “granular” pattern,²⁰ which may represent small areas of demyelination in the immediate vicinity of infected oligodendrocytes.¹⁸ These will lead with time to progressive brain atrophy (Online Supplemental Data).

Superficial and deep gray matter involvement (more commonly the thalami) has been reported in conjunction with white matter lesions in up to 5%–31% of patients.²¹ Posterior fossa

involvement is most commonly in the cerebellum and middle cerebellar peduncles, but the brainstem can also be involved with crescent-shaped lesions.²² The optic nerve and spinal cord are spared, and hemorrhage is a rare finding of PML but has been reported in patients with HIV taking NTZ.^{23,24}

Enhancement in NTZ-associated PML may indicate a worse prognosis and may be patchy, linear, nodular, or peripheral.²⁵

The DWI and DTI appearance of PML lesions varies depending on the stage of the disease. Early on, when lesions are relatively small, infected oligodendrocytes swell and die, resulting in high signal on DWI.¹⁶ Fractional anisotropy values are reduced, compatible with myelin injury. As the lesions enlarge, the signal on DWI remains high within the periphery as new oligodendrocytes become infected.²⁶ When lesions become quiescent, the rim loses its DWI hyperintensity. In later phases of tissue destruction, a relatively free diffusion of water within the irreversibly damaged tissue is observed.⁹

A confirmed diagnosis of PML is based on histologic examination or CSF polymerase chain reaction.

Differential diagnoses of PML include other opportunistic viral infections, including varicella zoster encephalomyelitis and herpes simplex encephalitis and various bacterial and fungal infections. Varicella zoster myelitis may demonstrate T2-hyperintense signal and enhancement in the spinal cord,²⁷ differentiating it from PML. Herpes zoster encephalitis demonstrates rapidly progressive cortical and subcortical T2 hyperintensity, swelling, and occasional enhancement involving the limbic regions.²⁸

MS relapse is presumably the most important differential for new lesions. New MS lesions tend to be small, focal, and well-delineated, favoring the periventricular and juxtacortical white matter and are typically round or ovoid.^{20,21} MS lesions may enhance homogeneously or peripherally, whereas PML generally

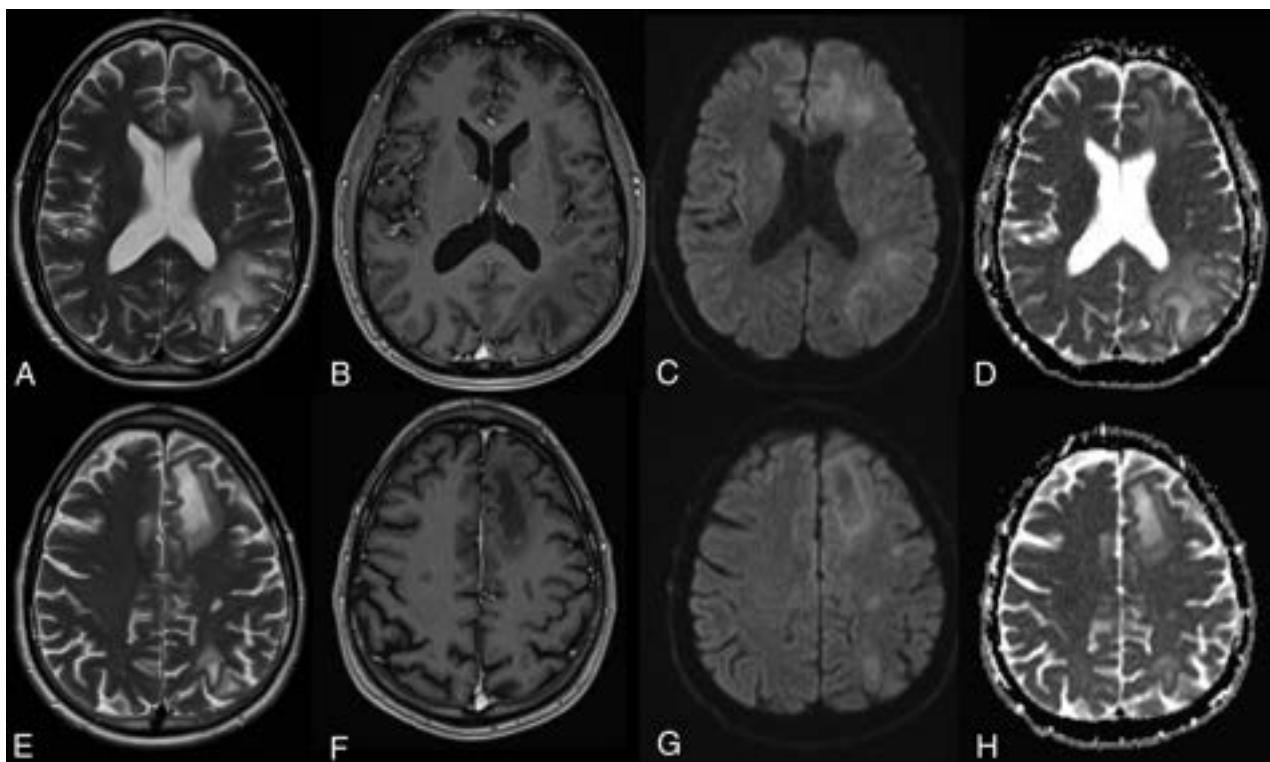


FIG 3. PML-IRIS after cessation of NTZ treatment. PML-IRIS in the same patient as depicted in Fig 2 following cessation of NTZ. The condition of the patient deteriorated clinically, prompting additional imaging that now demonstrates a “leading edge” of demyelination toward the white matter, mild enhancement, and DWI hypersignal, in keeping with cellular infiltration.

does not. MS lesions generally restrict diffusion only in the hyper-acute phase (<1 week).²⁹ Both tumefactive demyelinating and PML lesions demonstrate large areas of T2 hyperintensity and T1 hypointensity; however, mass effect is usually greater with the former, and T1 hypointensity improves with time in tumefactive lesions due to remyelination,³⁰ while improvement does not occur in PML.

Acute disseminated encephalomyelitis can appear similar to PML, with large areas of T2 signal abnormality in the white matter and deep gray structures, with minimal enhancement and variable mass effect.³¹

Posterior reversible encephalopathy syndrome (PRES) can appear similar to PML on initial examination, but lesions tend to be more symmetric than those in PML and predominantly involve the posterior aspects of the brain, and lesions typically resolve with treatment of the inciting etiology. In addition, PRES-associated T2/FLAIR hyperintensities classically present with facilitated diffusion.

The goal of treatment for NTZ-associated PML is the restoration of immune function by rapid removal of the drug, typically achieved with plasma exchange or immunoadsorption, to clear the drug from the $\alpha 4\beta 1$ receptors.³²

PML-IRIS

Once NTZ is cleared by plasma exchange, many (~70%)³³ patients with prior PML will experience rapid progression of neurologic symptoms, thought to be due to an exuberant immune response to viral Ags resulting in inflammation-mediated damage to infected and noninfected neuronal and glial tissue.

PML-IRIS may also occur following discontinuation of NTZ, usually ~90 days after the last dose, reflecting the longer time necessary to clear the drug without plasma exchange.¹⁶

On imaging, pseudoprogession of the PML imaging abnormalities with active inflammation and new peripheral and open rim enhancement is seen (Fig 3). Existing PML lesions may increase in size or coalesce as more white matter becomes involved, accompanied by increasing cerebral swelling and mass effect. Contrast enhancement develops or increases (variable patterns: patchy, punctate, irregular, and hazy, ill-defined).¹⁸ Across time, T1 hypointensity increases, indicating irreversible white matter damage with long-term atrophy of the overlying cortex due to retrograde neuronal degeneration. The therapy for PML-IRIS is high-dose corticosteroids.³⁴

NTZ Rebound

Discontinuation of NTZ therapy may be necessary for a variety of reasons, including fear of contracting PML after long-term usage, JC virus seroconversion, disease progression despite treatment, pregnancy or the intention to become pregnant, Abs to NTZ, or allergy.³⁵ In these patients, rebound of the primary disease (MS) may be encountered in 22%, with an unusually robust inflammatory response greater than a patient's typical relapse severity before starting NTZ therapy on MR imaging.³⁶

On MR imaging, the appearance of the rebound phenomenon is new enhancing and/or nonenhancing lesions, and the number of these lesions may be greater than in a typical relapse and can

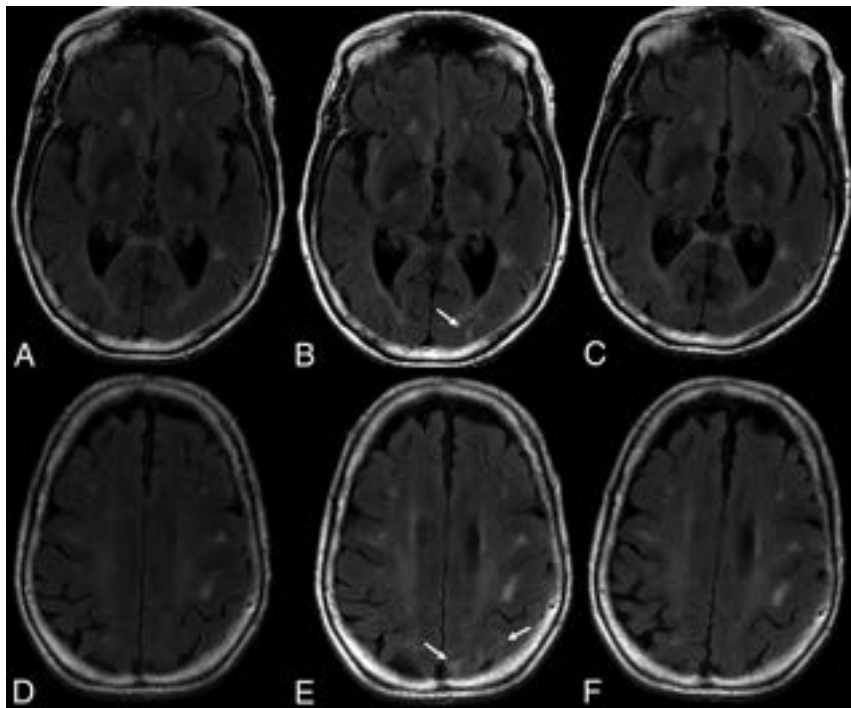


FIG 4. ARIA-E on follow-up. T2-weighted FLAIR scans at baseline (A and D), after 7 months of aducanumab treatment (B and E), and on follow-up 2 months later (C and F) demonstrate, in this 81-year-old patient who remained clinically stable, new development of edematous changes in the left occipital and parietal cortical and subcortical regions (arrows), which spontaneously resolved, in keeping with ARIA-E.

be quite severe. Development of enhancement at the margins of old lesions has also been reported.³⁷

Other immunosuppressive mAbs such as efalizumab, rituximab, brentuximab vedotin, alemtuzumab, and eculizumab share with NTZ potential primary and secondary AEs and are discussed in greater detail in the Online Supplemental Data.

Amyloid-Segregating mAbs: Aducanumab

Aducanumab is a human mAb that selectively targets amyloid β aggregates, including soluble oligomers and insoluble fibrils. It is used in the treatment of mild cognitive impairment and mild Alzheimer disease.³⁸ Even with the FDA approval of this drug, there is debate regarding its clinical efficacy in treating mild cognitive impairment and Alzheimer disease, to a certain extent due to the termination of the 2 pivotal Phase 3 clinical trials, 221AD301 Phase 3 Study of Aducanumab (BIIB037) in Early Alzheimer's Disease (ENGAGE) and 221AD302 Phase 3 Study of Aducanumab (BIIB037) in Early Alzheimer's Disease, following a futility analysis.³⁹ Despite the early termination of both trials, both demonstrated a favorable treatment effect of aducanumab at low doses, but they were discordant at the highest dose because the ENGAGE trial showed no beneficial treatment outcome compared with a placebo, while the EMERGE clinical trial showed a decrease in the rate of cognitive and functional decline. When the final 2 data sets were compared with their respective futility data sets, an improved treatment effect was evident in both studies as additional data were collected. The FDA cited EMERGE as having "substantial evidence of effectiveness to support approval."⁴⁰

Nonetheless, at best, the treatment may only slow cognitive and functional decline—raising the question of what pathologies drive continued functional decline as amyloid burden diminishes.

There has been a high rate of imaging-related abnormalities observed in patients treated with Aducanumab. These have been coined amyloid-related imaging abnormalities (ARIA) and occurred in >40% of individuals in the aducanumab 10 mg/kg group.³⁹ Clinically, new signs or symptoms suggestive of ARIA were present in a large number of patients, including headaches in 13%, dizziness in 4%, confusion/altered mental status in 5%, visual disturbance/eye disorders in 2%, and nausea in 2%.³⁹

In September 2022, the *American Journal of Neuroradiology* published a white paper on ARIA,⁴¹ focusing on imaging abnormalities and how to report these. In brief, the current hypothesis of ARIA formation is based on the assumption that amyloid deposition in vessel walls (cerebral amyloid angiopathy [CAA]) may result in loss of vascular integrity and reduced perivascular clearance and may be related

to spontaneously occurring microhemorrhages.⁴² When anti-amyloid mAb therapy is initiated, antibody-mediated breakdown of amyloid plaque and mobilization of parenchymal and vascular $A\beta$ increase the load of perivascular drainage.⁴³ This overload of the perivascular clearance pathways, ie, the glymphatic system, transiently increases amyloid deposition in the arterial wall, while at the same time, antibody-mediated inflammation and breakdown of amyloid occur in the vessel wall, all causing loss of vascular integrity and BBB breakdown.⁴⁴ As a result, proteinaceous fluid and/or red blood cells leak into the parenchyma and/or leptomeningeal space, and this issue results in edema/effusion (ARIA-E) or microhemorrhages/superficial siderosis (ARIA-H). High-risk factors for ARIA are the following: 1) initial treatment period, 2) higher drug doses, 3) *ApoE4* genotype—with *ApoE4* homozygotes having the highest risk,⁴⁵ and 4) pretreatment microhemorrhages most consistent with CAA, lobar microhemorrhages, and superficial siderosis.^{46,47}

ARIA-E

The E in ARIA-E stands for edema, effusion, and exudate that may be present, either parenchymal, sulcal, or both. The imaging appearance of parenchymal edema is similar to that of vasogenic edema, ie, absent diffusion restriction, and is best depicted on T2 FLAIR (Fig 4). It occurs mainly in the white matter, with some gray matter involvement. There may be associated local mass effect and gyral swelling. When the leak occurs in the leptomeningeal space, the result is a sulcal effusion or exudate, appreciated on T2 FLAIR sequences within the sulci/subpial spaces.⁴⁸

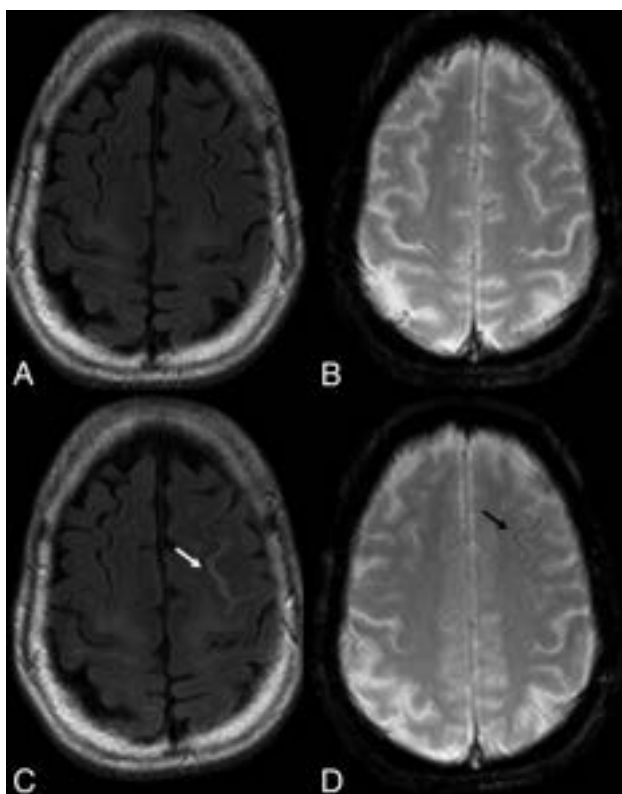


FIG 5. ARIA-H. In this 80-year old woman treated for amnesic mild cognitive impairment with aducanumab, serial imaging demonstrates, in the asymptomatic patient, new foci of blooming artifacts within the left frontal sulcus compared with the baseline scan (A and B; FLAIR and T2 gradient echo sequences). On follow-up 3 months later (C and D), note T2-weighted FLAIR hypersignal surrounding the left superior frontal sulcus (arrow in C), where mild pial siderosis is seen (arrow in D), in keeping with ARIA-H.

ARIA-E is most often found in dependent (posterior) brain regions—in the following order: occipital, parietal, frontal, and temporal lobes, and, least frequently, the cerebellum. Variable lesion intensity and size ranging from single subtle to multifocal and near-hemispheric⁴⁶ generally have ill-defined margins and infrequently have circumscribed margins.

ARIA-E is transient and typically persists on MR imaging for about 4–12 weeks, with self-limiting clinical symptoms lasting about 4 weeks after interruption or discontinuation of anti-amyloid therapy and has even been reported to resolve under continued dosing.⁴⁹

Differential diagnoses of ARIA-E include CAA, especially its inflammatory subtype (CAA-RI), PRES, sarcoidosis, or neoplasms, for example, angiocentric lymphoma.

The similarity of ARIA-E to PRES and inflammatory CAA, both on clinical presentation and MR imaging findings, is thought to be related to a similar CNS vascular endothelial dysfunction.⁴⁶ Differentiating these entities on the basis of imaging alone may, therefore, be difficult, and obtaining the clinical history of treatment with mAbs is crucial in making the diagnosis.

ARIA-H

ARIA-H, particularly in the form of microhemorrhages, is common in untreated, older individuals, and increases in incidence with age. Most cases of ARIA are asymptomatic, with the

incidence of symptomatic ARIA in the 10 mg/kg group being 7.5%. Overall, the incidence of ARIA-H was lower than that of ARIA-E, and *ApoE4* carriage has an increased risk.³⁹

The H in ARIA-H is hemorrhage, which includes microhemorrhages and superficial siderosis detected on heme-sensitive sequences, ie, T2* gradient recalled-echo and SWI (Fig 5). Intraparenchymal heme leakage results in microhemorrhages that are punctate and rounded, with markedly hypointense foci on T2* sequences, measuring <10 mm in diameter. A leak of heme products into the leptomeningeal or subpial space results in superficial siderosis, which manifests as curvilinear hypointensity along the brain surface.

Lobar macrohemorrhage (focus of hemorrhage identifiable on T1- or T2-weighted imaging, and usually >10 mm in diameter on gradient recalled-echo) rarely occurs with anti-amyloid agents, and when it does, it may be the result of an underlying disease process such as CAA.⁵⁰ The location of the microbleeds (superficial rather than deep), the type of bleeds (microbleeds as well as siderosis), and their occurrence in conjunction with mAb treatment will help the radiologist differentiate ARIA-H from other causes of microbleeds such as hypertensive angiopathy.

Clinical management is based on patient symptomatology and imaging criteria, with the radiologist playing a major role in the evaluation of patients treated with these new drugs as outlined by the white paper of Cogswell et al⁴¹ and summarized in the Online Supplemental Data.

In recent clinical trials, the incidence of ARIA was higher with mAbs that bind the N- (aducanumab, bapineuzumab, gantenerumab) versus C-terminal (ponezumab) and target aggregated-versus-soluble (ponezumab) forms of amyloid β .⁴¹ Newer FDA-approved mAbs such as lecanemab that target amyloid β soluble protofibrils appear to have a lower risk of ARIA (approximately 12%).⁵¹

Tumor Necrosis Factor–Inhibiting mAbs: Adalimumab

Adalimumab is a human mAb that inhibits tumor necrosis factor- α (TNF- α) by binding to TNF- α and blocking its interaction with surface TNF receptors, thus suppressing inflammation.⁵² It is used to treat inflammatory conditions including rheumatoid arthritis (RA), psoriasis, psoriatic arthritis, ankylosing spondylitis (AS), inflammatory bowel diseases, juvenile idiopathic arthritis, and hidradenitis suppurativa.⁵²

A variety of immune-mediated AEs have been reported and may manifest clinically as urticaria, psoriasis, lupus-like syndrome, and diabetes mellitus type 1.⁵³ In addition, numerous reports of neurologic AEs, including new development or exacerbation of demyelinating diseases, optic neuritis (Online Supplemental Data), chronic inflammatory demyelinating polyneuropathy, mononeuritis multiplex, Guillain-Barré syndrome, and others have been published.^{54,55}

The incidence of demyelinating disease in patients treated with TNF- α inhibitors is estimated to be 0.02%–0.2% of patients receiving this medication (Fig 6).⁵⁶

The relationship between the occurrence of demyelinating disease and TNF- α antagonists is poorly understood, though several theories have been proposed. One hypothesis is that TNF- α antagonists do not penetrate the BBB but peripherally prevent the destruction of autoreactive T cells. Thus, by increasing the number and activity of T cells, more will penetrate into the CNS and increase the autoimmune responses. Another hypothesis

states that the inability of TNF- α antagonists to enter the CNS would prevent the inhibition of TNF- α -mediated demyelination in MS. Third, as TNF- α antagonists decrease TNF- α levels systemically but not within the CNS, this could cause an upregulation of TNF- α expression in the CNS, further exacerbating TNF- α -mediated demyelination. Fourth, TNF- α antagonists may inhibit TNF- α -induced interleukin-10 and prostaglandin E2 production, resulting in upregulation of IL-12 and IFN- γ , which are associated with demyelinating disease processes. Fifth, down-regulation of TNF receptor 2 may occur. These receptors are

necessary for the proliferation of oligodendrocytes and damage repair. Finally, TNF- α antagonists may unmask a latent infection or neurologic disease, inciting an autoimmune demyelinating process.⁵⁶ Treatment requires discontinuation of mAb treatment, steroids, and, in severe cases, immunosuppressive drugs.⁵⁷

CONCLUSIONS

MAbs are currently and will in the future be increasingly used for the management of a wide variety of diseases including neoplastic, autoimmune, and degenerative processes. Knowledge of the type of treatment

the patient is undergoing is as important as understanding the potential pathologic mechanism involved in the development of imaging and neurologic sequelae.

While immunostimulating anti-cancer mAbs such as ipilimumab can lead to proinflammatory conditions such as hypophysitis, immunosuppressive drugs such as NTZ used in a variety of inflammatory conditions and severe MS forms can lead to activation of underlying opportunistic infections (with associated treatment-related IRIS and rebound phenomena). Amyloid-segregating mAbs can lead to amyloid-related imaging abnormalities in which the radiologist plays an instrumental role in patient management. The fourth group of mAbs that is frequently associated with neurologic and neuroradiologic findings is TNF-inhibiting mAbs that cause a higher incidence of demyelinating abnormalities both in the central and peripheral nervous system (Table).

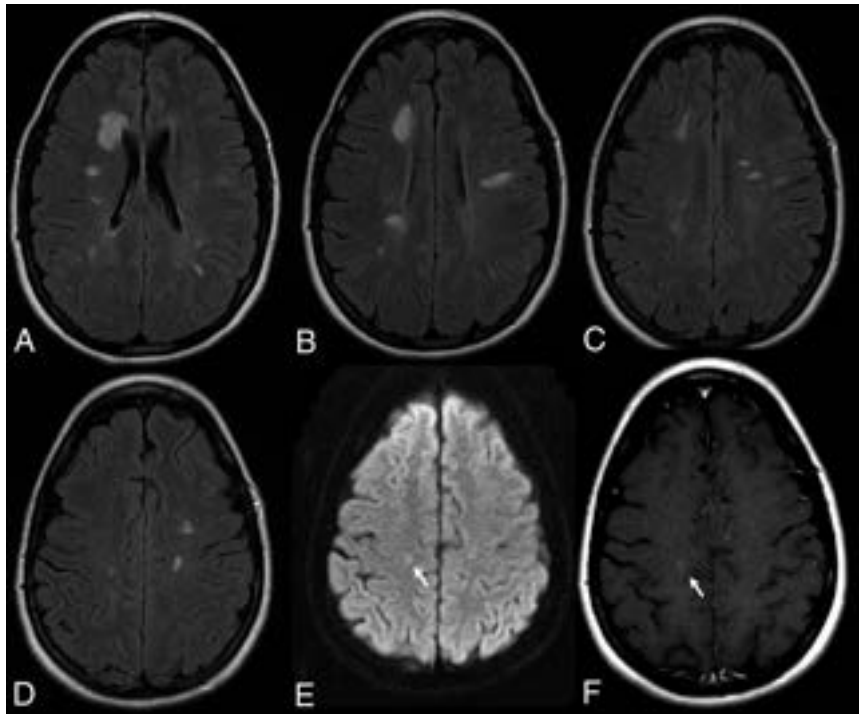


FIG 6. Demyelinating lesions after anti-TNF- α AE. This 36-year-old female patient with ankylosing spondylitis was treated with adalimumab and had cognitive decline. MR imaging (A–D: T2 weighted FLAIR, E: DWI, F: Contrast enhanced T1) demonstrates multiple demyelinating plaques with very subtle contrast enhancement (arrow, F).

ACKNOWLEDGMENTS

Dr Krings acknowledges the generous support from the Patricia Holt-Hornsby

Monoclonal antibody therapies and their use in neurologic diseases

Drug	Target	Mechanism of Action	Condition Used	Adverse Effects
Ipilimumab, tremelimumab	CTLA-4	Anti-CTLA-4 selectively blocking CTLA-4	Metastatic melanoma, several types of advanced malignancy	Immune-related AEs such as hypophysitis, colitis, uveitis, dermatitis, and arthritis
Aducanumab	Amyloid β aggregates, including soluble oligomers and insoluble fibrils	Decrease CNS amyloid burden	MCI and mild Alzheimer disease	ARIA
Adalimumab	TNF- α	Blocks TNF- α interaction with p55 and p75 cell surface TNF receptors	RA, PsA, AS, IBD, JIA, and HS	Neurologic AEs including demyelinating diseases, ON, CIDPN, MNM, and GB
NTZ	$\alpha 4 \beta 1$ Integrin	Blocks entry of T cells into the CNS	Multiple sclerosis (RRMS)	PML, PML-IRIS, NTZ rebound

Note:—ON indicates optic neuritis; CIDPN, chronic inflammatory demyelinating polyneuropathy; MNM, mononeuritis multiplex; GB, Guillain-Barré syndrome; RRMS, relapsing-remitting MS; AS, ankylosing spondylitis; MCI, mild cognitive impairment; RA, rheumatoid arthritis; PsA, psoriatic arthritis; IBD, inflammatory bowel diseases; JIA, juvenile idiopathic arthritis; HS, hidradenitis suppurativa.

and Dan Andreae Vascular Research Unit and University Medical Imaging Toronto.

Disclosure forms provided by the authors are available with the full text and PDF of this article at www.ajnr.org.

REFERENCES

- Novak JC, Lovett-Racke AE, Racke MK. **Monoclonal antibody therapies and neurologic disorders.** *Arch Neurol* 2008;65:1162–65 CrossRef Medline
- Yu YJ, Watts RJ. **Developing therapeutic antibodies for neurodegenerative disease.** *Neurotherapeutics* 2013;10:459–72 CrossRef Medline
- Keilholz U. **CTLA-4: negative regulator of the immune response and a target for cancer therapy.** *J Immunother* 2008;31:431–39 CrossRef Medline
- Cranmer LD, Hersh E. **The role of CTLA4 blockade in the treatment of malignant melanoma.** *Cancer Invest* 2007;25:613–31 CrossRef Medline
- Sanderson K, Scotland R, Lee P, et al. **Autoimmunity in a Phase I trial of a fully human anti-cytotoxic T-lymphocyte antigen-4 monoclonal antibody with multiple melanoma peptides and Montanide ISA 51 for patients with resected stages III and IV melanoma.** *J Clin Oncol* 2005;23:741–50 CrossRef Medline
- Boasberg P, Hamid O, O'Day S. **Ipilimumab: unleashing the power of the immune system through CTLA-4 blockade.** *Semin Oncol* 2010;37:440–49 CrossRef Medline
- Kaehler KC, Piel S, Livingstone E, et al. **Update on immunologic therapy with anti-CTLA-4 antibodies in melanoma: identification of clinical and biological response patterns, immune-related adverse events, and their management.** *Semin Oncol* 2010;37:485–98 CrossRef Medline
- Ribas A, Hauschild A, Kefford R, et al. **Phase III, open-label, randomized, comparative study of tremelimumab (CP-675,206) and chemotherapy (temozolomide [TMZ] or dacarbazine [DTIC]) in patients with advanced melanoma.** *J Clin Oncol* 2008;26:(Suppl 15):LBA9011–11.1 CrossRef
- Usiskin SI, Bainbridge A, Miller RF, et al. **Progressive multifocal leukoencephalopathy: serial high-b value diffusion-weighted MR imaging and apparent diffusion coefficient measurements to assess response to highly active antiretroviral therapy.** *AJNR Am J Neuroradiol* 2007;28:285–86 Medline
- Sato N, Sze G, Endo K. **Hypophysitis: endocrinologic and dynamic MR findings.** *AJNR Am J Neuroradiol* 1998;19:439–44 Medline
- Agarwala SS, Ribas A. **Current experience with CTLA4-blocking monoclonal antibodies for the treatment of solid tumors.** *J Immunother* 2010;33:557–69 CrossRef Medline
- Caturegli P, Newschaffer C, Olivi A, et al. **Autoimmune hypophysitis.** *Endocr Rev* 2005;26:599–614 CrossRef Medline
- Leporati P, Landek-Salgado MA, Lupi I, et al. **IgG4-related hypophysitis: a new addition to the hypophysitis spectrum.** *J Clin Endocrinol Metab* 2011;96:1971–80 CrossRef Medline
- Lutterotti A, Martin R. **Getting specific: monoclonal antibodies in multiple sclerosis.** *Lancet Neurol* 2008;7:538–47 CrossRef Medline
- Ciccio F, Rizzo A, Guggino G, et al. **Clinical efficacy of $\alpha 4$ integrin block with natalizumab in ankylosing spondylitis.** *Ann Rheum Dis* 2016;75:2053–54 CrossRef Medline
- Clifford DB, De Luca A, Simpson DM, et al. **NTZ-associated progressive multifocal leukoencephalopathy in patients with multiple sclerosis: lessons from 28 cases.** *Lancet Neurol* 2010;9:438–46 CrossRef Medline
- Carson KR, Evens AM, Richey EA, et al. **Progressive multifocal leukoencephalopathy after rituximab therapy in HIV negative patients: a report of 57 cases from the Research on Adverse Drug Events and Reports project.** *Blood* 2009;113:4834–40 CrossRef Medline
- Yousry TA, Pelletier D, Cadavid D, et al. **Magnetic resonance imaging pattern in NTZ-associated progressive multifocal leukoencephalopathy.** *Ann Neurol* 2012;72:779–87 CrossRef Medline
- Koralnik IJ. **Progressive multifocal leukoencephalopathy revisited: has the disease outgrown its name?** *Ann Neurol* 2006;60:162–73 CrossRef Medline
- Boster A, Hreha S, Berger JR, et al. **Progressive multifocal leukoencephalopathy and relapsing-remitting multiple sclerosis: a comparative study.** *Arch Neurol* 2009;66:593–99 CrossRef Medline
- Wattjes MP, Richert ND, Killestein J, et al. **The chameleon of neuroinflammation: magnetic resonance imaging characteristics of NTZ-associated progressive multifocal leukoencephalopathy.** *Mult Scler* 2013;19:1826–40 CrossRef Medline
- Kastrup O, Maschke M, Diener HC, et al. **Progressive multifocal leukoencephalopathy limited to the brain stem.** *Neuroradiology* 2002;44:227–29 CrossRef Medline
- Cordoliani S. **MRI aspects of progressive multifocal leukoencephalopathy.** *J Neuroradiol* 1995;22:172–79 Medline
- Langer-Gould A, Atlas SW, Green AJ, et al. **Progressive multifocal leukoencephalopathy in a patient treated with NTZ.** *N Engl J Med* 2005;353:375–81 CrossRef Medline
- Wattjes MP, Verhoeff L, Zentjens W, et al. **Punctate lesion pattern suggestive of perivascular inflammation in acute NTZ-associated progressive multifocal leukoencephalopathy: productive JC virus infection or preclinical PML IRIS manifestation?** *J Neurol Neurosurg Psychiatry* 2013;84:1176–77 CrossRef Medline
- Bergui M, Bradac GB, Oguz KK, et al. **Progressive multifocal leukoencephalopathy: diffusion-weighted imaging and pathological correlations.** *Neuroradiology* 2004;46:22–25 CrossRef Medline
- Fine AJ, Sorbello A, Kortepeter C, et al. **Central nervous system herpes simplex and varicella zoster virus infections in NTZ-treated patients.** *Clin Infect Dis* 2013;57:849–52 CrossRef Medline
- Kwiatkowski A, Gallois J, Bilbault N, et al. **Herpes encephalitis during NTZ treatment in multiple sclerosis.** *Mult Scler* 2012;18:909–11 CrossRef Medline
- Eisele P, Szabo K, Griebel M, et al. **Reduced diffusion in a subset of acute MS lesions: a serial multiparametric MRI study.** *AJNR Am J Neuroradiol* 2012;33:1369–73 CrossRef Medline
- Jander S, Turowski B, Kieseier BC, et al. **Emerging tumefactive multiple sclerosis after switching therapy from NTZ to fingolimod.** *Mult Scler* 2012;18:1650–52 CrossRef Medline
- Tenembaum S, Chitnis T, Ness J, et al; International Pediatric MS Study Group. **Acute disseminated encephalomyelitis.** *Neurology* 2007;68:S23–36 CrossRef Medline
- Khatri BO, Man S, Giovannoni G, et al. **Effect of plasma exchange in accelerating NTZ clearance and restoring leukocyte function.** *Neurology* 2009;72:402–09 CrossRef Medline
- Pavlovic D, Patera AC, Nyberg F, et al; Progressive Multifocal Leukoencephalopathy Consortium. **Progressive multifocal leukoencephalopathy: current treatment options and future perspectives.** *Ther Adv Neurol Disord* 2015;8:255–73 CrossRef Medline
- Kleinschmidt-Demasters BK, Miravalle A, Schowinsky J, et al. **Update on PML and PML-IRIS occurring in multiple sclerosis patients treated with NTZ.** *J Neuropathol Exp Neurol* 2012;71:604–17 CrossRef Medline
- Salhofer-Polanyi S, Baumgartner A, Kraus J, et al. **What to expect after NTZ cessation in a real-life setting.** *Acta Neurol Scand* 2014;130:97–102 CrossRef Medline
- West TW, Cree BA. **NTZ dosage suspension: are we helping or hurting?** *Ann Neurol* 2010;68:395–99 CrossRef Medline
- Sorensen PS, Koch-Henriksen N, Petersen T, et al. **Recurrence or rebound of clinical relapses after discontinuation of NTZ therapy in highly active MS patients.** *J Neurol* 2014;261:1170–77 CrossRef Medline
- ADUHELM® Prescribing Information. <https://biogen.com/us/aduhelm-pi.pdf>. Accessed June 7, 2023

39. Budd Haeberlein S, Aisen PS, Barkhof F, et al. **Two randomized Phase 3 studies of aducanumab in early Alzheimer's disease.** *J Prev Alzheimers Dis* 2022;9:197–210 CrossRef Medline
40. Food and Drug Administration. **November 6, 2020 BLA 761178: Peripheral and Central Nervous System Drugs Advisory Committee Meeting.** 2021. <https://www.fda.gov/media/143505/download>. Accessed July 12, 2023
41. Cogswell PM, Barakos JA, Barkhof F, et al. **Amyloid-related imaging abnormalities with emerging Alzheimer disease therapeutics: detection and reporting recommendations for clinical practice.** *AJNR Am J Neuroradiol* 2022;43:E19–35 CrossRef Medline
42. Kim SH, Ahn JH, Yang H, et al. **Cerebral amyloid angiopathy aggravates perivascular clearance impairment in an Alzheimer's disease mouse model.** *Acta Neuropathol Commun* 2020;8:181 CrossRef Medline
43. Greenberg SM, Bacsikai BJ, Hernandez-Guillamon M, et al. **Cerebral amyloid angiopathy and Alzheimer disease: one peptide, two pathways.** *Nat Rev Neurol* 2020;16:30–42 CrossRef Medline
44. Zago W, Schroeter S, Guido T, et al. **Vascular alterations in PDAPP mice after anti-Ab immunotherapy: implications for amyloid related imaging abnormalities.** *Alzheimers Dement* 2013;9:S105–15 CrossRef Medline
45. Ostrowitzki S, Lasser RA, Dorflinger E, et al; SCarlet RoAD Investigators. **A Phase III randomized trial of gantenerumab in prodromal Alzheimer's disease.** *Alzheimers Res Ther* 2017;9:95 CrossRef Medline
46. Sperling RA, Jack CR, Black SE, et al. **Amyloid related imaging abnormalities (ARIA) in amyloid modifying therapeutic trials: recommendations from the Alzheimer's Association Research Roundtable Workgroup.** *Alzheimers Dement* 2011;7:367–85 CrossRef Medline
47. Salloway S, Chalkias S, Barkhof F, et al. **Amyloid-related imaging abnormalities in 2 Phase 3 studies evaluating aducanumab in patients with early Alzheimer disease.** *JAMA Neurol* 2022;79:13–21 CrossRef Medline
48. Barakos J, Sperling R, Salloway S, et al. **MR imaging features of amyloid related imaging abnormalities.** *AJNR Am J Neuroradiol* 2013;34:1958–65 CrossRef Medline
49. Sperling R, Salloway S, Brooks DJ, et al. **Amyloid-related imaging abnormalities in patients with Alzheimer's disease treated with bapineuzumab: a retrospective analysis.** *Lancet Neurol* 2012;11:241–49 CrossRef Medline
50. Haller S, Haacke EM, Thurnher MM, et al. **Susceptibility-weighted imaging: technical essentials and clinical neurologic applications.** *Radiology* 2021;299:3–26 CrossRef Medline
51. van Dyck CH, Swanson CJ, Aisen P, et al. **Lecanemab in early Alzheimer's disease.** *N Engl J Med* 2023;388:9–21 CrossRef Medline
52. Burness CB, Deeks ED. **Adalimumab.** *Drugs* 2012;72:2385–95 CrossRef Medline
53. Borchers AT, Leibushor N, Cheema GS, et al. **Immune-mediated adverse effects of biologicals used in the treatment of rheumatic diseases.** *J Autoimmun* 2011;37:273–88 CrossRef Medline
54. Magnano MD, Robinson WH, Genovese MC. **Demyelination and inhibition of tumor necrosis factor (TNF).** *Clin Exp Rheumatol* 2004;22:S134–40 Medline
55. Ramos-Casals M, Roberto-Perez A, Diaz-Lagares C, et al; BIOGEAS Study Group. **Autoimmune diseases induced by biological agents: a double-edged sword?** *Autoimmun Rev* 2010;9:188–93 CrossRef Medline
56. Bosch X, Saiz A, Ramos-Casals M; BIOGEAS Study Group. **Monoclonal antibody therapy-associated neurological disorders.** *Nat Rev Neurol* 2011;7:165–72 CrossRef Medline
57. Kemanetoglou E, Andreadou E. **CNS demyelination with TNF- α blockers.** *Curr Neurol Neurosci Rep* 2017;17:36 CrossRef Medline

Prevalence and Characteristics of Intracranial Aneurysms in Hereditary Hemorrhagic Telangiectasia

How-Chung Cheng, Marie E. Faughnan, Karel G. terBrugge, Hon-Man Liu, Timo Krings, and the Brain Vascular Malformation Consortium Hereditary Hemorrhagic Telangiectasia Investigator Group



ABSTRACT

BACKGROUND AND PURPOSE: The association between hereditary hemorrhagic telangiectasia and intracranial aneurysms remains controversial. This study evaluated the prevalence and characteristics of intracranial aneurysms in patients with hereditary hemorrhagic telangiectasia with brain vascular malformations.

MATERIALS AND METHODS: Between 2007 and 2021, patients enrolled in the Brain Vascular Malformation Consortium with definite hereditary hemorrhagic telangiectasia, the presence of brain vascular malformations, and available angiographic studies of the brain were retrospectively reviewed. Angiographic features of intracranial aneurysms and their relationship to coexisting brain vascular malformations were analyzed. We also examined the association between baseline clinical features and the presence of intracranial aneurysms.

RESULTS: One hundred eighty patients were included. A total of 14 intracranial aneurysms were found in 9 (5%) patients, and 4 intracranial aneurysms were considered flow-related aneurysms. Patients with intracranial aneurysms were significantly older than patients without intracranial aneurysms (mean, 48.1 [SD, 18.2] years versus 33.5 [SD, 21.0] years; $P = .042$). If we excluded flow-related intracranial aneurysms, the prevalence of intracranial aneurysms was 3.3%. All intracranial aneurysms were in the anterior circulation, were unruptured, and had an average maximal diameter of 3.9 (SD, 1.5) mm. No intracranial aneurysms were found in pediatric patients with hereditary hemorrhagic telangiectasia. No statistically significant correlation was observed among other baseline demographics, hereditary hemorrhagic telangiectasia features, and the presence of intracranial aneurysms.

CONCLUSIONS: The prevalence of intracranial aneurysms in this large cohort study is comparable with that in the general population and might be increased slightly due to hemodynamic factors associated with shunting brain vascular malformations.

ABBREVIATIONS: HHT = hereditary hemorrhagic telangiectasia; IA = intracranial aneurysm; VM = vascular malformation

Hereditary hemorrhagic telangiectasia (HHT) or Osler-Weber-Rendu syndrome is an autosomal dominant disorder characterized by mucocutaneous telangiectasias and vascular malformations (VMs) in organs, including the liver, gastrointestinal tract,

lungs, brain, and spinal cord.^{1,2} It is caused by mutations in one of several genes involved in the transforming growth factor- β /bone morphogenetic protein signaling pathway. Loss-of-function mutations in HHT genes have been shown to impair endothelial cell proliferation and migration during angiogenesis and vascular remodeling.^{1,3,4} Approximately 96% of individuals with a definite clinical diagnosis of HHT have a mutation in the endoglin (*ENG*) gene or activin A receptor type II-like kinase 1 (*ACVRL1*) gene,⁵ and about 3% of patients have a mutation in the *SMAD4* gene. The diagnosis of HHT is made clinically using the Curaçao criteria, which include spontaneous and recurrent nose bleeds, multiple

Received July 24, 2023; accepted after revision October 6.

From the Division of Neuroradiology (H.-C.C., K.G.t., T.K.), Joint Department of Medical Imaging, Toronto Western Hospital, University Health Network, Toronto, Ontario, Canada; Division of Neurosurgery (H.-C.C.), Department of Surgery, and Department of Medical Imaging (H.-M.L.), Fu Jen Catholic University Hospital, Fu Jen Catholic University, New Taipei City, Taiwan; Toronto HHT Centre (M.E.F.), St. Michael's Hospital and Li Ka Shing Knowledge Institute, Toronto, Ontario, Canada; and Division of Respiriology (M.E.F.), Department of Medicine, University of Toronto, Toronto, Ontario, Canada.

The Brain Vascular Malformation Consortium is part of the Rare Diseases Clinical Research Network, which is funded by the National Institutes of Health and led by the National Center for Advancing Translational Sciences through its Office of Rare Diseases Research. The Brain Vascular Malformation Consortium is funded under grant No. U54NS065705 as a collaboration between the National Center for Advancing Translational Sciences and the National Institute of Neurological Disorders and Stroke. All Rare Diseases Clinical Research Network consortia are supported by the network's Data Management and Coordinating Center (U2CTR002818). Funding support for the Data Management and Coordinating Center is provided by National Center for Advancing Translational Sciences and the National Institute of Neurological Disorders and Stroke.

M.E.F. was also supported by the Li Ka Shing Knowledge Institute. This work was funded, in part, by the Holt-Hornsby and Andreae Fund and University Medical Imaging Toronto.

Please address correspondence to How-Chung Cheng, Division of Neuroradiology, Joint Department of Medical Imaging, Toronto Western Hospital, University Health Network, 399 Bathurst St, Toronto, ON, M5T 2S8, Canada; e-mail: vionishc@gmail.com



Indicates article with online supplemental data.

<http://dx.doi.org/10.3174/ajnr.A8058>

mucocutaneous telangiectasias (of the lips, oral cavity, nose, or fingers), visceral VMs (of the liver, lungs, or CNS), and a first-degree relative with HHT. Patients are diagnosed with “definite HHT” when 3 of these 4 criteria are met, whereas those who fulfill 2 criteria are considered to have “possible HHT.”⁶ For asymptomatic individuals from a family with known HHT, the International HHT Guidelines recommend genetic testing for diagnosis.⁵

Patients with HHT present with a wide variety of cerebrovascular diseases. Between 10% and 20% of patients have brain VMs, classified in previous studies as pial AVFs, nidus-type AVMs, or capillary vascular malformations.^{7–11} Other nonshunting vascular lesions such as cavernous malformations, developmental venous anomalies, and intracranial aneurysms (IAs) were also found in patients with HHT.^{8,11,12}

Although earlier studies reported the prevalence of IAs in the HHT population,^{8,11,13,14} no studies have addressed the characteristics of these aneurysms and their relationship to AVMs. The present study aimed to determine the prevalence of IAs in the HHT population, identify angiographic features of IAs, and examine the correlation between IAs and brain VMs in patients with HHT. Notably, a recent study found a strikingly high 14.5% prevalence of IAs in an HHT cohort, contrary to previous studies.¹⁴ Current screening recommendations may need refinement if this higher prevalence of IAs is confirmed in our data set.

MATERIALS AND METHODS

Study Population

We analyzed patient data from the HHT project of the Brain Vascular Malformation Consortium. Patients with either a confirmed genetic diagnosis or a definite clinical diagnosis of HHT, based on the presence of at least 3 of the Curaçao criteria,⁶ were enrolled in the Brain Vascular Malformation Consortium HHT project as previously reported.^{10,15} The Brain Vascular Malformation Consortium HHT cohort aimed for a 25% recruitment target for patients with brain VMs.¹⁵ From January 2007 to December 2021, we included all recruited patients with brain VMs and available angiographic studies (ie, CTA, MRA, and/or DSA). All patients provided written, informed consent. The study was approved by each participating center’s institutional review board.

Data Collection

For each patient, we collected data including age at enrollment, sex, clinical presentations, family history, and genetic testing results (*ENG*, *ACVRL1*, *SMAD4*) when available. Radiologic data included biplanar 6-vessel selective cerebral angiography, contrast-enhanced MRA or TOF-MRA using 1.5T or 3T scanners, and CTA. All images were retrospectively reviewed by 2 of the authors (H.-C.C. and T.K.) in consensus. Images were assessed for the presence of IAs and shunting lesions such as AVMs and AVFs, as classified in previous studies.^{10,16} The aneurysm location, the number of aneurysms per patient, their geometric measurements, and their relationship to the intracranial shunting lesions were recorded. We measured aneurysm neck width, dome-to-neck ratio, and aspect ratio on the PACS. Aneurysms with a neck diameter of ≥ 4 mm or a dome-to-neck ratio of < 2 were classified as wide-neck.^{17,18} A Spetzler-Martin grade was calculated for each AVM when the patient had a concurrent IA.¹⁹

Table 1: Basic demographics of 180 subjects with HHT and brain VMs

Characteristic	Summary ^a (%)
Age at enrollment (mean) (yr)	34.2 (SD, 21.1)
Women	111/180 (61.7%)
Curaçao criteria	
Epistaxis	168/180 (93.3%)
Mucosal telangiectasias	141/180 (78.3%)
Pulmonary AVMs	91/180 (50.6%)
Liver VMs	14/180 (7.8%)
Gastrointestinal bleeding	9/180 (5.0%)
Affected first-degree relative	135/180 (75%)
Genetic mutation	
<i>ENG</i>	109/131 (83.2%)
<i>ACVRL1</i>	21/131 (16.0%)
<i>SMAD4</i>	1/131 (0.7%)
DSA	116/180 (64.4%)
MRA	114/180 (63.3%)
CTA	5/180 (2.8%)
AVM	113/180 (62.8%)
AVF	16/180 (8.9%)
IAs	9/180 (5%)

^a Summary is the number of observations with each value over the total available numbers (and the percentage) or the mean (SD) for continuous variables.

IAs were considered unrelated aneurysms when they presented on vessels that were not AVM feeders, whereas those arising from vessels contributing to perfusion of the nidus were termed flow-related aneurysms.²⁰ Flow-related aneurysms were further classified as proximal when located at the circle of Willis up to the primary bifurcation, while those more distally located were considered distal.

Statistical Tests

We determined the prevalence of IAs by the number of patients having at least 1 IA divided by the total number of included patients with HHT. We tested for differences in age, sex, the presence of Curaçao criteria, and the presence of AVMs/AVFs between patients with IAs and those without. Continuous variables were compared using the Student *t* test, and categorical variables were compared using the Fisher exact test. We considered *P* values $< .05$ as statistically significant. All analyses used SPSS (IBM).

RESULTS

One hundred eighty patients with HHT and brain VMs as well as available angiographic studies were included in the study. The average age at enrollment was 34.2 (SD, 21.1) years, with 54 (30%) subjects younger than 18 years of age. Female patients accounted for 61.7% of the population. One hundred thirty-one patients had positive findings on genetic testing: One hundred nine (83.2%) had an *ENG* mutation, 21 (16.0%) had an *ACVRL1* mutation, and 1 (0.7%) had a *SMAD4* mutation. Basic demographics and clinical features of the study population are summarized in Table 1.

Fourteen IAs were noted in 9 (5%) patients, and 3 (33%) patients had multiple aneurysms. No pediatric patients with HHT in this cohort had an IA. All IAs were unruptured and were found in the anterior circulation, most commonly located in the ICA (64%), followed by the anterior cerebral artery (21%). The average neck size and maximal aneurysm diameter

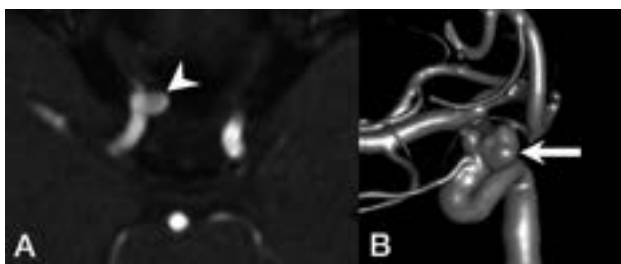


FIG 1. Representative images of a patient with HHT with an IA unrelated to AVMs. *A*, MRA demonstrates an ophthalmic segment aneurysm of the right ICA (arrowhead) projecting medially. *B*, 3D reconstruction of a DSA shows a bilobed, wide-neck, right ophthalmic segment aneurysm of the right ICA (arrow).

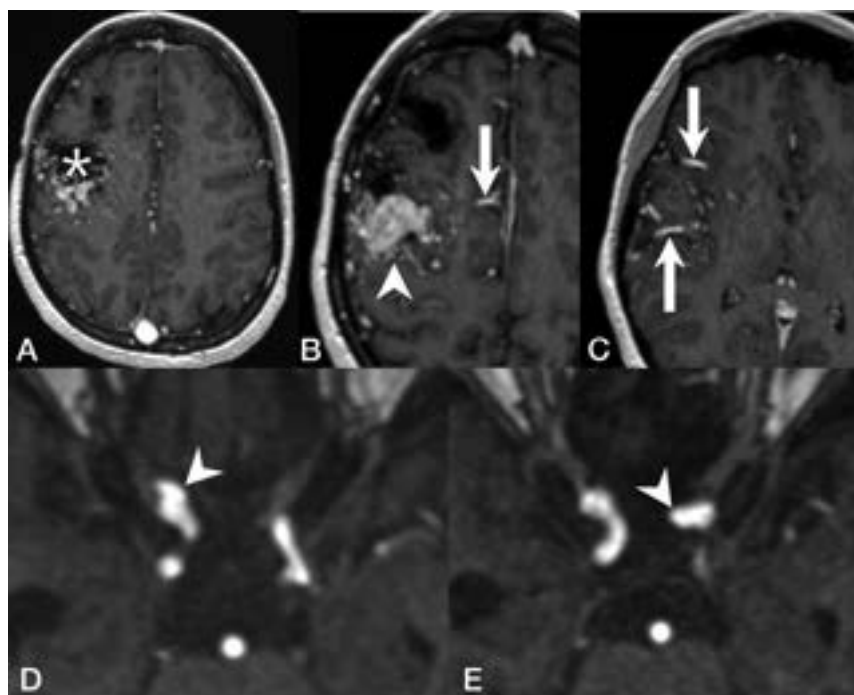


FIG 2. Representative images of a patient with HHT with flow-related cerebral aneurysms. T1 contrast-enhanced MR images demonstrate a Spetzler-Martin grade III right frontal AVM with a nidus size of 4 cm (*A*, asterisk) and venous varices (*B*, arrowhead), supplied by several dilated arterial feeders from the right anterior cerebral arteries (*B*, arrow) and the right middle cerebral arteries (*C*, arrow). MRA demonstrates a clinoid segment aneurysm of the right ICA (*D*, arrowhead) and another aneurysm arising from the ophthalmic segment of the left ICA (*E*, arrowhead).

were 3.7 (SD, 1.3) mm and 3.9 (SD, 1.5) mm, respectively. The average aspect ratio was 0.92 (SD, 0.30). All aneurysms had a dome-to-neck ratio of <2 . A representative example of IAs is shown in Fig 1.

Of the 9 patients with IAs, 6 had nidus-type brain AVMs, 1 had an AVF, and 2 had a capillary vascular malformation. Ten (71%) of the 14 IAs were considered unrelated to the VMs, whereas 4 (29%) were considered flow-related aneurysms arising from a feeding artery of a shunting VM. One patient with a right frontal Spetzler-Martin grade III AVM and a nidus size of 4 cm had 1 aneurysm on each of the ICAs (Fig 2). Another patient with a left frontal AVF and a large venous pouch had an aneurysm on the ipsilateral anterior cerebral artery. The last patient

had 2 Spetzler-Martin grade I AVMs in the same hemisphere as the aneurysm. The characteristics of IAs and angiographic features are summarized in the Online Supplemental Data. Patients with IAs were significantly older compared with patients without IAs (mean, 48.1 [SD, 18.2] years versus 33.5 [SD, 21.0] years; $P = .042$). No statistically significant association was found between patients with or without IAs regarding sex, the presence of the Curaçao criteria, or the presence of concurrent shunting brain VMs (AVMs and/or AVFs) (Table 2).

DISCUSSION

The association between HHT and IAs remains controversial. In a report on neurovascular manifestations of patients with HHT,

Brinjikji et al¹¹ demonstrated a 2.1% prevalence of IAs. Woodall et al⁸ evaluated 230 patients with HHT and found a 2.4% prevalence of IAs. Ring et al¹³ looked for arterial aneurysms in all locations in an HHT cohort and reported a 4.3% IA prevalence. A very recent study from Perez Akly et al¹⁴ found 33 (14.5%) patients with HHTs with IAs, >3 -fold higher than the prevalence rate of 3.2% in the general population,²¹ thus potentially changing the clinical practice regarding active screening for IAs in patients with HHT. This remarkable discrepancy and the potential impact of encountering a high prevalence of IAs in patients with HHT prompted the present study.

We report a prevalence of IAs of 5% in this largest series of patients with HHT with brain VMs. In the subgroup of patients not having flow-related IAs, the prevalence of IAs was 3.3%, very similar to that of the general population. Although we included specifically patients with HHT with brain VMs, our observation is in line with the reported prevalences by Brinjikji et al,¹¹ Woodall et al,⁸ and Ring et al.¹³ In addition, our study cohort shares similar prevalences of epistaxis,^{8,11,14} mucosal telangiectasias,^{1,11,22} and pulmonary AVMs^{1,11,23,24} with previous reports, and, therefore, is likely generalizable to unselected patients with HHT. Because children can develop complications of HHT,²⁵ we believe that it is necessary to include the pediatric population in this epidemiologic study to better understand the prevalence and natural history of IAs and, more important, to determine whether HHT is associated with an increased risk of IAs. Moreover, we are convinced that by including all patients with available angiographic studies of all types (ie, CTA, MRA, and/or DSA), our observed prevalence of IAs more accurately reflects the prevalence of IAs in the HHT population. According to our findings and those of the latter 3 studies,^{8,11,13} the prevalence of IAs in HHT is similar to that in the general

Table 2: Bivariate analysis between baseline demographics and IAs

Outcome	Patients with IAs (n = 9)	Patients without IAs (n = 171)	P Value
Age (mean) (yr)	48.1 (SD, 18.2)	33.5 (SD, 21.0)	.042
Women	7/9 (77.8%)	104/171 (60.8%)	.486
Curaçao criteria			
Epistaxis	9/9 (100%)	159/171 (93.0%)	1.000
Telangiectasias	8/9 (88.9%)	133/171 (77.8%)	.687
Pulmonary AVMs	6/9 (66.7%)	85/171 (49.7%)	.497
Liver VMs	2/9 (22.2%)	12/171 (7.0%)	.148
Gastrointestinal bleeding	0/9 (0%)	9/171 (5%)	1.000
Affected first-degree relative	5/9 (55.6%)	130/171 (76.0%)	.230
AVM	6/9 (66.7%)	107/171 (62.6%)	1.000
AVF	1/9 (11.1%)	15/171 (8.8%)	.576
AVM or AVF	7/9 (77.8%)	122/171 (71.3%)	1.000

population, with a small additional prevalence of IAs in patients with HHT with coexisting shunting brain VMs.

This observation is in keeping with pathogenetic concepts of HHT in several ways. First, it is postulated that in HHT, the targets of the dysfunction are the venules instead of the arteries.¹⁶ Early histopathologic studies demonstrated that the clinically detectable lesions of HHT start with focal dilation of postcapillary venules, which enlarge and connect with arterioles, eventually forming direct arteriovenous shuntings as capillaries disappear.^{1,26} More recent animal studies also suggest that the *ENG/ACVRL1* signaling pathway mediates the endothelial cell shear stress response and is essential for flow-induced endothelial cell migration against the direction of blood flow, starting from growing veins, ie, flow-migration coupling. Loss of *ENG* or *ACVRL1* expression in venous and capillary endothelial cells is sufficient to cause AVMs as a result of impaired flow-migration coupling, whereas *ENG* or *ACVRL1* deletion in arterial endothelial cells does not lead to AVM formation.^{4,27-30} Histopathologically, HHT is unlikely to be associated with a higher prevalence of IAs. Second, although several reports have associated the interruption of the transforming growth factor- β signaling pathway with a higher prevalence of visceral aneurysms in patients with HHT due to its important role in extracellular matrix remodeling,^{13,31} there is no genetic evidence to support applying the same hypothesis to IAs. *ENG*, one of the most commonly found mutated genes in patients with HHT, has repeatedly been reported to have no association with IAs.^{32,33}

In a study about sequencing transforming growth factor- β pathway genes in familial IA cases, Santiago-Sim et al³⁴ demonstrated that mutations in transforming growth factor- β receptor genes are not a major cause of IAs. Furthermore, a recently published genome-wide association study also demonstrated no evidence of polygenic overlap between other aortic aneurysms and IAs,³⁵ while another meta-analysis of genome-wide association study on genetic risk factors for IAs found no linkage between transforming growth factor- β -related genes and the development of IAs.³⁶ Finally, unlike some other clinical features of HHT that become apparent in early childhood and evolve, no IAs were found in the pediatric population of our cohort. In addition, the mean age of patients with IAs in this study was 48 years, comparable with the mean age of 47–55 years described in non-HHT populations with IAs.^{37,38} If IAs and VMs share the same

pathogenesis, there would presumably be more evidence of IAs in younger patients with HHT.

IAs in this study were most commonly found in the ICA and were small with a mean maximal diameter of 3.9 mm. Similar to findings in the previous studies,^{8,11,14} no patients in this cohort presented with SAH, which may hint at a benign nature of IAs in HHT. Although there were a few case reports describing ruptured IAs in patients with HHT,^{39,40} most were flow-related aneurysms associated with a shunting brain VM.

In this study, we found no association between IAs and shunting brain VMs. Because approximately 71% of included patients with HHT had at least 1 shunting brain VM, it is possible that we could not detect any significant difference in brain VM prevalence between patients with and without IAs, given this high prevalence of brain VMs in our cohort. Notably, merely 29% of the IAs in this study were related to the shunting brain VMs, and only 2% of the AVMs were found to have flow-related aneurysms, as opposed to 18% described previously by a meta-analysis on the natural history of brain AVMs and concurrent IAs in the non-HHT population.⁴¹ One possible explanation is that most of the AVMs found in patients with HHT are <3 cm;^{10,11,42} therefore, the hemodynamic factors related to the shunting in the AVM nidus, such as higher shear stress on the vessel wall, are less prominent among patients with HHT.

In conclusion, the prevalence of IAs in patients with HHT with brain VMs is similar to that in the general population. In addition, we observed that IAs in patients with HHT are seen in adults, but not children, and they are typically small with a low likelihood of hemorrhagic presentation. Thus, our observations do not support a recommendation for routine screening of patients with HHT specifically for IAs.

This study has limitations. First, it has some inherent selection bias because we included only patients with brain VMs. Although the genetic linkage between IAs and brain VMs, if any, remains undetermined, the prevalence of IAs in our study was in line with that reported in the literature. Second, genetic information was not available for one-third of the included individuals; therefore, there was an insufficient sample size to assess the association between IAs and genes mutated. Also, our study cohort included few patients with *ACVRL1* or *SMAD4* mutations, unsurprisingly, given the known association between brain VMs and *ENG* mutation, among patients with HHT. Additional studies will be required to clarify the association between these genes and IAs. Finally, the limited sample size of IAs may reduce the power of the study to detect statistically significant correlations such as the association between IAs and shunting brain VMs, but there was no evidence of even a trend association.

CONCLUSIONS

From this large cohort of patients with HHT and brain VMs, we demonstrate that the prevalence of IAs in HHT is similar to that

of the general population and is not clearly associated with the presence of shunting brain VMs. Further studies are required to explore the mechanistic linkage between HHT and IA formation and the natural history of IAs in the HHT population.

ACKNOWLEDGMENTS

We would like to thank Professor Shiao-Chi Wu of National Yang Ming Chiao Tung University for statistical analysis.

Brain Vascular Malformation Consortium Hereditary Hemorrhagic Telangiectasia Investigator Group:

Mary E. Atherton, Murali M. Chakinala, Marianne S. Clancy, Marie E. Faughnan, James R. Gossage, Adrienne M. Hammill, Katharine Henderson, Steven Hetts, Peter Hountras, Vivek Iyer, Raj S. Kasthuri, Helen Kim, Timo Krings, Michael T. Lawton, Doris Lin, Johannes Jurgen Mager, Douglas A. Marchuk, Justin P. McWilliams, Jamie McDonald, Ludmila Pawlikowska, Jeffrey Pollak, Felix Ratjen, Karen Swanson, Dilini Vethanayagam, Shantel Weinsheimer, Andrew J White, Pearce Wilcox.

Disclosure forms provided by the authors are available with the full text and PDF of this article at www.ajnr.org.

REFERENCES

- Shovlin CL. Hereditary haemorrhagic telangiectasia: pathophysiology, diagnosis and treatment. *Blood Rev* 2010;24:203–19 CrossRef Medline
- McDonald J, Bayrak-Toydemir P, Pyeritz RE. Hereditary hemorrhagic telangiectasia: an overview of diagnosis, management, and pathogenesis. *Genet Med* 2011;13:607–16 CrossRef Medline
- McDonald J, Wooderchak-Donahue W, VanSant Webb C, et al. Hereditary hemorrhagic telangiectasia: genetics and molecular diagnostics in a new era. *Front Genet* 2015;6:1 CrossRef Medline
- Jin Y, Muhl L, Burmakin M, et al. Endoglin prevents vascular malformation by regulating flow-induced cell migration and specification through VEGFR2 signaling. *Nat Cell Biol* 2017;19:639–52 CrossRef Medline
- Faughnan ME, Mager JJ, Hetts SW, et al. Second international guidelines for the diagnosis and management of hereditary hemorrhagic telangiectasia. *Ann Intern Med* 2020;173:989–1001 CrossRef Medline
- Shovlin CL, Guttmacher AE, Buscarini E, et al. Diagnostic criteria for hereditary hemorrhagic telangiectasia (Rendu-Osler-Weber syndrome). *Am J Med Genet* 2000;91:66–67 CrossRef Medline
- Nishida T, Faughnan ME, Krings T, et al. Brain arteriovenous malformations associated with hereditary hemorrhagic telangiectasia: gene-phenotype correlations. *Am J Med Genet A* 2012;158A:2829–34 CrossRef Medline
- Woodall MN, McGettigan M, Figueroa R, et al. Cerebral vascular malformations in hereditary hemorrhagic telangiectasia. *J Neurosurg* 2014;120:87–92 CrossRef Medline
- Brinjikji W, Iyer VN, Sorenson T, et al. Cerebrovascular manifestations of hereditary hemorrhagic telangiectasia. *Stroke* 2015;46:3329–37 CrossRef Medline
- Krings T, Kim H, Power S, et al; Brain Vascular Malformation Consortium HHT Investigator Group. Neurovascular manifestations in hereditary hemorrhagic telangiectasia: imaging features and genotype-phenotype correlations. *AJNR Am J Neuroradiol* 2015;36:863–70 CrossRef Medline
- Brinjikji W, Iyer VN, Yamaki V, et al. Neurovascular manifestations of hereditary hemorrhagic telangiectasia: a consecutive series of 376 patients during 15 years. *AJNR Am J Neuroradiol* 2016;37:1479–86 CrossRef Medline
- Gaetani E, Peppucci E, Agostini F, et al. Distribution of cerebrovascular phenotypes according to variants of the ENG and ACVRL1 genes in subjects with hereditary hemorrhagic telangiectasia. *J Clin Med* 2022;11:2685 CrossRef Medline
- Ring NY, Latif MA, Hafezi-Nejad N, et al. Prevalence of and factors associated with arterial aneurysms in patients with hereditary hemorrhagic telangiectasia: 17-year retrospective series of 418 patients. *J Vasc Interv Radiol* 2021;32:1661–69 CrossRef Medline
- Perez Akly MS, Vazquez C, Besada CH, et al. Prevalence of intracranial aneurysms in hereditary hemorrhagic telangiectasia: report from a single reference center. *AJNR Am J Neuroradiol* 2022;43:844–49 CrossRef Medline
- Akers AL, Ball KL, Clancy M, et al. Brain vascular malformation consortium: overview, progress and future directions. *J Rare Disord* 2013;1:5 Medline
- Krings T, Ozanne A, Chng SM, et al. Neurovascular phenotypes in hereditary haemorrhagic telangiectasia patients according to age. Review of 50 consecutive patients aged 1 day–60 years. *Neuroradiology* 2005;47:711–20 CrossRef Medline
- Fernandez Zubillaga A, Guglielmi G, Viñuela F, et al. Endovascular occlusion of intracranial aneurysms with electrically detachable coils: correlation of aneurysm neck size and treatment results. *AJNR Am J Neuroradiol* 1994;15:815–20 Medline
- Debrun GM, Aletich VA, Kehrli P, et al. Aneurysm geometry: an important criterion in selecting patients for Guglielmi detachable coiling. *Neurol Med Chir (Tokyo)* 1998;38(Suppl):1–20 CrossRef Medline
- Spetzler RF, Martin NA. A proposed grading system for arteriovenous malformations. *J Neurosurg* 1986;65:476–78 CrossRef Medline
- Ramos SK, Gardenghi B, Bortolotti C, et al. Aneurysms associated with brain arteriovenous malformations. *AJNR Am J Neuroradiol* 2016;37:1966–67 CrossRef Medline
- Thompson BG, Brown RD Jr, Amin-Hanjani S, et al; American Stroke Association. Guidelines for the management of patients with unruptured intracranial aneurysms: a Guideline for Healthcare Professionals from the American Heart Association/American Stroke Association. *Stroke* 2015;46:2368–400 CrossRef Medline
- Hyldahl SJ, El-Jaji MQ, Schuster A, et al. Skin and mucosal telangiectatic lesions in hereditary hemorrhagic telangiectasia patients. *Int J Dermatol* 2022;61:1497–505 CrossRef Medline
- Jaskolka J, Wu L, Chan RP, et al. Imaging of hereditary hemorrhagic telangiectasia. *AJR Am J Roentgenol* 2004;183:307–14 CrossRef Medline
- Fish A, Henderson K, Moushey A, et al. Incidence of spontaneous pulmonary AVM rupture in HHT patients. *J Clin Med* 2021;10:4714 CrossRef Medline
- Kilian A, Latino GA, White AJ, et al; the Brain Vascular Malformation Consortium HHT Investigator Group. Genotype-phenotype correlations in children with HHT. *J Clin Med* 2020;9:2714 CrossRef Medline
- Braverman IM, Keh A, Jacobson BS. Ultrastructure and three-dimensional organization of the telangiectases of hereditary hemorrhagic telangiectasia. *J Invest Dermatol* 1990;95:422–27 CrossRef Medline
- Crist AM, Lee AR, Patel NR, et al. Vascular deficiency of Smad4 causes arteriovenous malformations: a mouse model of hereditary hemorrhagic telangiectasia. *Angiogenesis* 2018;21:363–80 CrossRef Medline
- Bernabeu C, Bayrak-Toydemir P, McDonald J, et al. Potential second-hits in hereditary hemorrhagic telangiectasia. *J Clin Med* 2020;9:3571 CrossRef Medline
- Singh E, Redgrave RE, Phillips HM, et al. Arterial endoglin does not protect against arteriovenous malformations. *Angiogenesis* 2020;23:559–66 CrossRef Medline
- Park H, Furtado J, Poulet M, et al. Defective flow-migration coupling causes arteriovenous malformations in hereditary hemorrhagic telangiectasia. *Circulation* 2021;144:805–22 CrossRef Medline

31. Moulinet T, Mohamed S, Deibener-Kaminsky J, et al. **High prevalence of arterial aneurysms in hereditary hemorrhagic telangiectasia.** *Int J Cardiol* 2014;176:1414–16 CrossRef Medline
32. Krex D, Ziegler A, Schackert HK, et al. **Lack of association between endoglin intron 7 insertion polymorphism and intracranial aneurysms in a white population: evidence of racial/ethnic differences.** *Stroke* 2001;32:2689–94 CrossRef Medline
33. Onda H, Kasuya H, Yoneyama T, et al. **Endoglin is not a major susceptibility gene for intracranial aneurysm among Japanese.** *Stroke* 2003;34:1640–44 CrossRef Medline
34. Santiago-Sim T, Mathew-Joseph S, Pannu H, et al. **Sequencing of TGF-beta pathway genes in familial cases of intracranial aneurysm.** *Stroke* 2009;40:1604–11 CrossRef Medline
35. van 't Hof FN, Ruigrok YM, Lee CH, et al; Aneurysm Consortium; Vascular Research Consortium of New Zealand. **Shared genetic risk factors of intracranial, abdominal, and thoracic aneurysms.** *J Am Heart Assoc* 2016;5:e002603 CrossRef Medline
36. Alg VS, Sofat R, Houlden H, et al. **Genetic risk factors for intracranial aneurysms: a meta-analysis in more than 116,000 individuals.** *Neurology* 2013;80:2154–65 CrossRef Medline
37. Weir B, Disney L, Karrison T. **Sizes of ruptured and unruptured aneurysms in relation to their sites and the ages of patients.** *J Neurosurg* 2002;96:64–70 CrossRef Medline
38. Backes D, Vergouwen MD, Tiel Groenestege AT, et al. **PHASES score for prediction of intracranial aneurysm growth.** *Stroke* 2015;46:1221–26 CrossRef Medline
39. Helmchen C, Nahser HC, Yousry T, et al. **Therapy of cerebral aneurysms and arteriovenous vascular malformations in hereditary hemorrhagic telangiectasia (Rendu-Osler-Weber disease)** [in German]. *Nervenarzt* 1995;66:124–28 Medline
40. Ishii D, Takechi A, Seyama G, et al. **Ruptured large basilar artery aneurysm associated with an arteriovenous malformation in hereditary hemorrhagic telangiectasia.** *Neurol Med Chir (Tokyo)* 2012;52:502–05 CrossRef Medline
41. Gross BA, Du R. **Natural history of cerebral arteriovenous malformations: a meta-analysis.** *J Neurosurg* 2013;118:437–43 CrossRef Medline
42. Brinjikji W, Iyer VN, Wood CP, et al. **Prevalence and characteristics of brain arteriovenous malformations in hereditary hemorrhagic telangiectasia: a systematic review and meta-analysis.** *J Neurosurg* 2017;127:302–10 CrossRef Medline

Predicting Antiseizure Medication Treatment in Children with Rare Tuberous Sclerosis Complex–Related Epilepsy Using Deep Learning

Haifeng Wang, Zhanqi Hu, Dian Jiang, Rongbo Lin, Cailei Zhao, Xia Zhao, Yihang Zhou, Yanjie Zhu, Hongwu Zeng, Dong Liang, Jianxiang Liao, and Zhicheng Li

ABSTRACT

BACKGROUND AND PURPOSE: Tuberous sclerosis complex disease is a rare, multisystem genetic disease, but appropriate drug treatment allows many pediatric patients to have positive outcomes. The purpose of this study was to predict the effectiveness of antiseizure medication treatment in children with tuberous sclerosis complex–related epilepsy.

MATERIALS AND METHODS: We conducted a retrospective study involving 300 children with tuberous sclerosis complex–related epilepsy. The study included the analysis of clinical data and T2WI and FLAIR images. The clinical data consisted of sex, age of onset, age at imaging, infantile spasms, and antiseizure medication numbers. To forecast antiseizure medication treatment, we developed a multitechnique deep learning method called WAE-Net. This method used multicontrast MR imaging and clinical data. The T2WI and FLAIR images were combined as FLAIR3 to enhance the contrast between tuberous sclerosis complex lesions and normal brain tissues. We trained a clinical data-based model using a fully connected network with the above-mentioned variables. After that, a weighted-average ensemble network built from the ResNet3D architecture was created as the final model.

RESULTS: The experiments had shown that age of onset, age at imaging, infantile spasms, and antiseizure medication numbers were significantly different between the 2 drug-treatment outcomes ($P < .05$). The hybrid technique of FLAIR3 could accurately localize tuberous sclerosis complex lesions, and the proposed method achieved the best performance (area under the curve = 0.908 and accuracy of 0.847) in the testing cohort among the compared methods.

CONCLUSIONS: The proposed method could predict antiseizure medication treatment of children with rare tuberous sclerosis complex–related epilepsy and could be a strong baseline for future studies.

ABBREVIATIONS: ACC = accuracy; ASM = antiseizure medication; AUC = area under the curve; CNN = convolutional neural network; DCA = decision curve analysis; FCNN = fully connected neural network; FN = false-negative; FP = false-positive; ReLU = rectified linear unit; ROC = receiver operating characteristic; SEN = sensitivity; SPE = specificity; TN = true-negative; TP = true-positive; TSC = tuberous sclerosis complex; WAE = weighted-average ensemble

Tuberous sclerosis complex (TSC) is a rare genetic disease that affects multiple organs and is caused by mutations in the *TSC1* or *TSC2* genes.^{1–3} Its incidence is estimated to be 1 in 6000 live births,^{3,4} and it is commonly associated with seizures and related neuropsychiatric disorders.⁵ Epilepsy is the most prevalent symptom in pediatric patients with TSC,^{6,7}

affecting approximately 85% of them.^{2,8} The primary objective of epilepsy treatment in these patients is to control seizures and enhance their quality of life.³ However, >50% of pediatric patients with TSC develop drug resistance to antiseizure medication (ASM),^{9–11} and identifying this resistance can be a time-consuming process.¹² Therefore, investigating predictive

Received June 4, 2023; accepted after revision October 3.

From the Research Center for Medical Artificial Intelligence (H.W., D.J., Y. Zhou, D.L., Z.L.) and Paul C. Lauterbur Research Center for Biomedical Imaging (Y. Zhu, D.L.), Shenzhen Institutes of Advanced Technology, Chinese Academy of Sciences, Shenzhen, Guangdong, China; Shenzhen College of Advanced Technology (H.W., D.J., Y. Zhu, D.L., Z.L.), University of Chinese Academy of Sciences, Shenzhen, Guangdong, China; Departments of Neurology (Z.H., R.L., X.Z., J.L.) and Radiology (C.Z., H.Z.), Shenzhen Children's Hospital, Shenzhen, Guangdong, China; Department of Pediatric Neurology (Z.H.), Boston Children's Hospital, Boston, Massachusetts; and Research Department (Y. Zhou), Hong Kong Sanatorium and Hospital, Hong Kong, China.

Haifeng Wang, Zhanqi Hu, and Dian Jiang contributed equally to this work and share co-first authorship.

Some of the work was partially supported by the National Key R&D Program of China (2023YFB3811400), the Guangdong High-level Hospital Construction Fund (ynkt2021-zz11), the National Natural Science Foundation of Shenzhen Children's Hospital (ynkt2021-zz11), the Shenzhen Key Medical Discipline Construction Fund (SZXK033), the Shenzhen Fund for Guangdong Provincial High-Level Clinical Key Specialties (SZGSP012), the Sanming Project of Medicine in Shenzhen (SZSM201812005), the National Natural Science Foundation of China (62271474), the High-level Talent Program in Pearl River Talent Plan of Guangdong Province (2019QN01Y986) and the Shenzhen Science and Technology Program (KCCXF20211020163408012, KQTD20180413181834876 and JCYJ20210324115810030).

Please address correspondence to Jianxiang Liao, MD, Department of Neurology, Shenzhen Children's Hospital, Shenzhen, China; e-mail: liaojianxiang@vip.sina.com
<http://dx.doi.org/10.3174/ajnr.A8053>

biomarkers of drug-treatment outcomes for pediatric patients with epilepsy is an urgent need.

Currently, MR imaging provides excellent tissue contrast, which is a technique used routinely to diagnose TSC disease.¹³ Radiologists have difficulty distinguishing patients with pediatric refractory (resistant seizure) disease from those with seizure-controlled disease because these patients may have similar appearances in MR imaging. Recent artificial intelligence tools have been used to help radiologists assess the cortical tubers in rare pediatric TSC disease, including from MR images.¹⁴ Deep learning has promoted the progress of 3D volumetric classification.¹⁵⁻¹⁷ Previous studies have shown the ability of deep convolutional neural network (CNN) models to classify lung cancer and bone lesions on MR imaging with high accuracy.^{18,19} In addition, several studies have begun to combine images of multicontrast MR imaging, by using the complementary visual information from the multicontrast MR imaging to improve the performance of the classification.^{20,21} However, these studies required many images to train the CNNs, which were challenging to obtain in rare disorders like pediatric TSC disease. Until now, few studies have used deep learning methods to predict outcomes of drug treatment for epilepsy in rare pediatric TSC disease.

Because the quantity of patients with rare pediatric TSC is limited, some studies have only used some machine learning techniques for the prediction of epilepsy drug-treatment outcomes. For example, An et al²² predicted patients with drug-resistant epilepsy at the time of the first ASM prescription and achieved an area under curve (AUC) of 0.764 with random forests. However, their work mainly focused on patients with general epilepsy instead of pediatric patients with rare TSC. Recently, lesion location and type of information features of MR imaging have been identified to predict epilepsy drug-treatment outcomes in rare pediatric TSC disease with multilayer perceptron and achieved an AUC of 0.812.¹² However, the features of MR imaging were also typically extracted manually, possibly introducing errors, and the description of these features was usually qualitative, subjective, and nonspecific. With current state-of-the-art machine learning methods, it may be possible to achieve better performance in automated drug-treatment outcome prediction through analysis of advanced imaging. Until now, there are not any state-of-the-art machine learning methods that can achieve an AUC of approximately 0.90 to predict epilepsy drug-treatment outcomes in rare pediatric TSC applications. In this study, we aimed to develop a deep learning method for predicting the outcomes of epilepsy drug treatment in children with the rare TSC disease.

MATERIALS AND METHODS

Network Architectures of Imaging Data

Deep learning, especially CNNs, has been widely used in medical image processing.²³⁻²⁵ Among the different variants of CNNs, 2D Residual Network (ResNet: <https://keras.io/api/applications/resnet/>) has shown remarkable performance in image classification.²⁶ It is composed of residual blocks that are substantially deeper. In addition, the residual networks are easier to optimize and can gain accuracy from significantly increased depth. Additionally, although most imaging studies have used 2D CNNs as their model architecture, some studies have proposed 3D

CNNs that can fully use the spatial features of MR imaging and achieve better performance.²⁷⁻²⁹

Therefore, we have constructed a 3D CNN architecture based on the idea of ResNet,²⁶ which is a more developed model based on 2D-ResNet. The MR image-based models were the 3D version of the network modified on 2D-ResNet. ResNet3D models (<https://paperswithcode.com/lib/torchvision/resnet-3d>) were used for feature-extraction from imaging data. The ResNet3D classifying layer was replaced with an average pooling layer and a fully connected layer to perform the binary classification task. The neural network structure of ResNet3D is shown in Fig 1.

Network Architectures of Clinical Data

A fully connected neural network (FCNN) using clinical variables was separately developed for the classification task as in Table 1. FCNN consists of a series of fully connected layers of 1024, 512, 128, 64, 32, and 16 nodes with an interposing rectified linear unit (ReLU) activation and batch normalization layers. A final classification layer with a single node was used to perform the binary classification task of clinical variables.

Synthesis of T2WI and FLAIR

Cortical tubers and subcortical nodules are major brain manifestations of rare pediatric TSC disease. Improving the conspicuity of cortical tubers and subcortical nodules is very important for clinical radiologists to diagnose rare pediatric TSC disease.³⁰ T2WI provides higher lesion and brain contrast. However, there is a strong CSF signal in T2WI, which interferes with visualization of periventricular lesions. FLAIR images can suppress CSF. However, the lesion-brain contrast in FLAIR is not clear enough. No single sequence can generate all of the desired tissue-contrast features in 1 image due to the necessary trade-offs in the choice of MR imaging pulse sequence parameters. Recent work has shown that combining T2WI and FLAIR images can enhance the detection of MS lesions.^{31,32} However, methods to optimize combining T2WI and FLAIR in rare pediatric TSC disease have not been reported so far. Therefore, inspired by Wiggermann et al³¹ and Gabr et al,³² we propose to use FLAIR3 as a new synthetic technique to optimally combine T2WI and FLAIR in rare pediatric TSC disease as in the following equation,³²

$$\text{Equation 1} \quad \text{FLAIR3} = \text{FLAIR}^{1.55} \times \text{T2WI}^{1.45}.$$

This formula is used to balance the lesion and brain tissue contrast between T2WI and FLAIR images. Lesion-brain contrast levels were different in T2WI and FLAIR images, even at the same TE. Unlike T2WI, FLAIR introduces modest T1-weighting, which counteracts the effect of prolonged relaxation of T2 in the lesion, thereby reducing the lesion-to-brain contrast. In addition, only FLAIR produces CSF-nulled images. Therefore, combining the 2 images with optimized weights may yield the best lesion-to-brain contrast in patients with rare pediatric TSC.

Late Fusion Strategies

Recently, several studies³³⁻³⁵ reported that the late fusion model can most effectively grasp the data distribution and ultimately yielded the best prediction performances. Inspired from Eweje et al¹⁸ and Jonsson et al,²⁰ we developed a late fusion model to combine multiple sequences of MR imaging for a feature

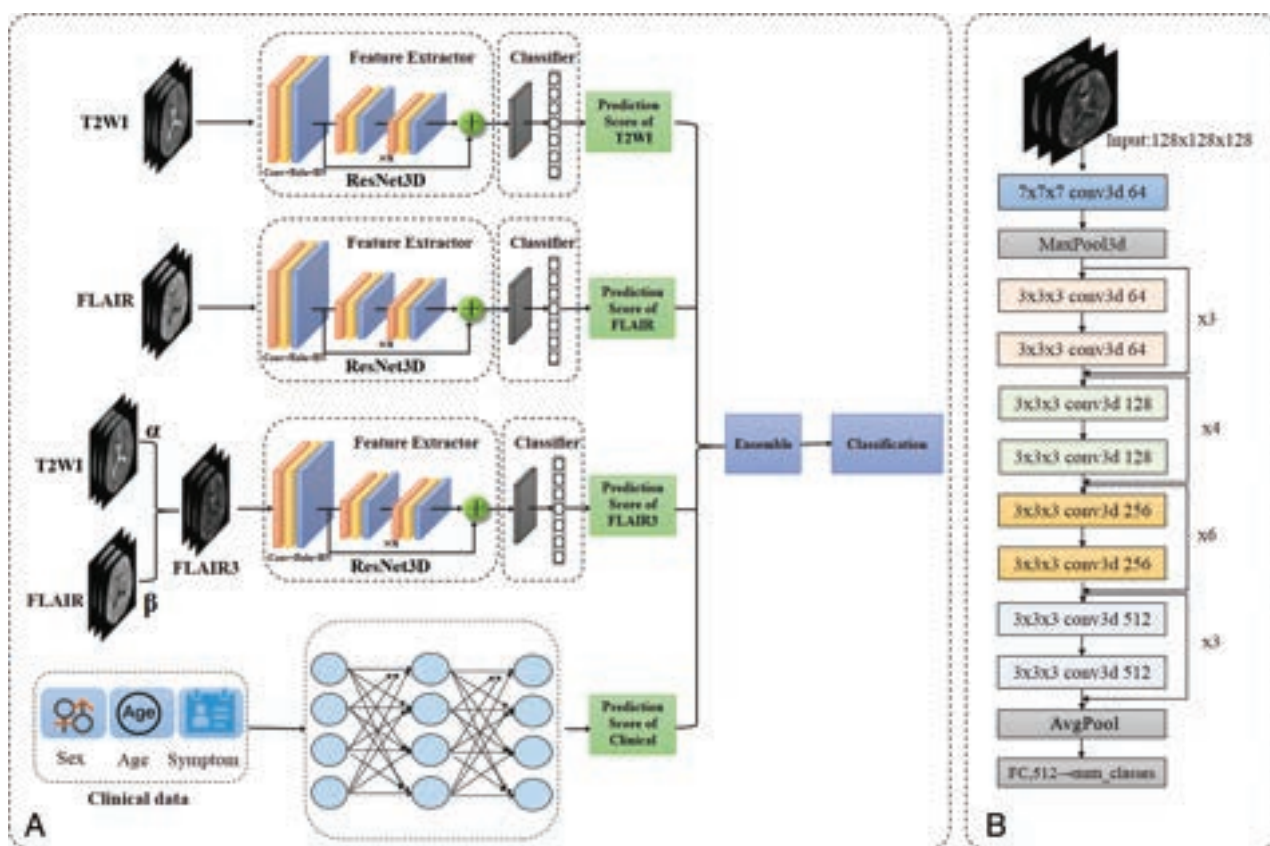


FIG 1. The net schematic of the proposed WAE-net method. **A**, Schematic of our proposed WAE-net pipeline. The ResNet3D took T2-weighted, FLAIR, and FLAIR3 images as input and output prediction scores, respectively. A FCNN model accepted age, sex, and TSC symptom variables as input and output a prediction score. A WAE-net used prediction scores from the T2-weighted, FLAIR, FLAIR3, and clinical models as input and output a final classification by a simple and effective direct weighted-averaging method. **B**, Network structure of ResNet3D. FC indicates fully connected layer; conv3d, 3D convolution.

Table 1: Network structure of FCNN using 1-dimensional clinical variables

Layer Name	Output Dims
Input layer	(1,4)
FC1	1024
FC2	512
FC3	128
FC4	64
FC5	32
FC6	16
Output layer	1

Note:—FC indicates fully connected layer; Dims, dimensions.

extractor. Then, clinical data were fed into an FCNN. The late fusion model used prediction scores from the T2WI, FLAIR, FLAIR3, and clinical models as input and output a final classification by a simple and effective weighted-average ensemble (WAE) method as follows,

$$\text{Equation 2} \quad \text{WAE} = W_1 \times \text{T2WI} + W_2 \times \text{FLAIR} + W_3 \times \text{FLAIR3} + W_4 \times \text{Clinical},$$

where $W_1 + W_2 + W_3 + W_4 = 1$. T2WI, FLAIR, FLAIR3 and Clinical represent the prediction scores of 3 input images and clinical data. WAE represents the output prediction scores W_1 , W_2 , W_3 , and W_4 are the weights of the prediction scores of the 4

input. The above multi-technique deep learning method is called as WAE-net, as shown in Fig 1.

For the pediatric TSC classification tasks with 1 single input image technique, 3D-ResNet34 architectures were applied. For the pediatric TSC classification tasks with 1 single-input clinical datum, FCNN architectures were applied. When WAE-net was used, 3 sequences of T2WI, FLAIR, FLAIR3 images, and clinical data were used as input. The late fusion model used prediction scores from the T2WI, FLAIR, FLAIR3, and the clinical model as input and output a final classification by a simple and effective weighted-average method. In our experiments, W_1 , W_2 , W_3 and W_4 , which were the weights of the prediction scores of the 4 inputs, are the same.

Participant Data

In this study, all pediatric patients came from Shenzhen Children's Hospital between January 2013 and September 2021, diagnosed with rare TSC-related epilepsy. Three hundred pediatric patients with ASM treatment for at least 1 year were enrolled in the retrospective study. Written informed consent was obtained from all subjects before the study, and the protocols and study were approved by the institutional review board of the Shenzhen Children's Hospital. Written informed consent was obtained from patients with rare TSC and/or their parents. All MR imaging scans included FLAIR images and T2WI before ASM treatment.

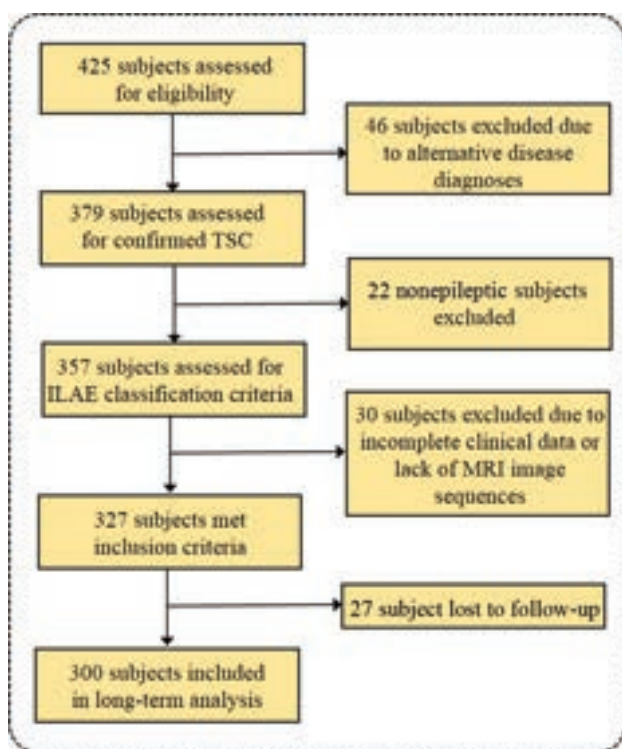


FIG 2. Study inclusion criteria. Flow chart details the identification of the study cohort. ILAE indicates International League Against Epilepsy.

Otherwise, drug-treatment outcomes were defined according to the 1981 International League Against Epilepsy classification,³⁶ which were recorded as a controlled group or an uncontrolled group. Pediatric patients were considered as the controlled group if they did not have clinical seizures for at least 1 year. Uncontrolled pediatric patients (refractory patients) had at least 1 seizure in the past year. Figure 2 shows the inclusion criteria.

Imaging Data

Binary classification models were trained to distinguish pediatric uncontrolled seizures from controlled seizures on T2-weighted, FLAIR, and FLAIR3 images. Five-fold cross-validation was used to evaluate the models. Using the ResNet3D architecture,³⁷ models were trained with a learning rate of 0.001, batch size of 4 for 100 epochs, Adam optimization (https://www.researchgate.net/publication/352497171_Adam_Optimization_Algorithm), and the loss function of focal loss. The area under the receiver operating characteristic (ROC) of cross-validation (AUC) as the metric for model evaluation, while preserving the model, achieved the best level of AUC during training. After training, we used the parameters of all 5 models, which originated from 5-fold cross-validation, to test. The prediction score of each pediatric patient was determined by the average of the prediction scores of the 5 models from 5-fold cross-validation. Figure 3B shows the training and evaluation scheme.

Pediatric data were randomly split into a training and validation data set ($n = 240$) and an independent test data set ($n = 60$). We trained all the models using an NVIDIA RTX A6000 GPU card (<https://www.techpowerup.com/gpu-specs/rtx-a6000.c3686>). Training, validation, and test of models were implemented with Python (Version 3.8.10) and PyTorch (Version 1.9.0) environments.

T2WI was registered into the FLAIR space using the FMRIB Linear Image Registration Tool (FLIRT; <http://www.fmrib.ox.ac.uk/fslwiki/FLIRT>) of FSL, which used mutual information as the cost function.³⁸ In neuroimaging studies, most lesions were located in the brain tissue. Therefore, we first used the deep learning tool HD-bet (<https://bio.tools/HD-BET#1>)³⁹ to dissect the skull in MR imaging.

The 3D MR images were resized to 128, 128, 128, and the image intensity was then normalized to the range between 0 and 1, using Equation 2 as follows,

$$\text{Equation 3} \quad \text{Normalized}(x) = \frac{x - \text{Min}(x)}{\text{Max}(x) - \text{Min}(x)},$$

where $\text{Max}(x)$ and $\text{Min}(x)$ are the maximum and minimum of the brain-extracted MR images and $\text{Normalized}(x)$ is the normalized MR images. Finally, T2WI and FLAIR were combined into FLAIR3. Figure 3A shows the schematic of the data-preprocessing pipeline.

Clinical Data

The FCNN model for clinical feature-based classification was also trained with a learning rate of 0.001, batch size of 4 for 100 epochs, Adam optimization, and the loss function of focal loss. Five-fold cross-validation was used to evaluate the models. The clinical features with statistical significance ($P < .05$) were selected as the final feature input of the FCNN model.

Evaluation Model

Here, AUC, accuracy (ACC), sensitivity (SEN), and specificity (SPE) were calculated to assess the classification performance for each model in each cohort. These metrics are defined in terms of true-positive (TP), which is the total number of positive classifications that are correct; true-negative (TN), which is the total number of negative classifications that are correct; false-positive (FP), which is the total number of positive classifications that are incorrect, and false-negative (FN) which is the total number of negative classifications that are incorrect. ACC, SEN, and SPE are calculated by using the following equations:

ACC: The percentage of the whole sample that is correctly classified.

$$\text{Equation 4} \quad \text{ACC} = \frac{TP + TN}{TP + TN + FP + FN}.$$

SEN: The percentage of the total sample that is true that is correctly classified.

$$\text{Equation 5} \quad \text{SEN} = \frac{TP}{TP + FN}.$$

SPE: The percentage of the total sample that is negative and correctly classified.

$$\text{Equation 6} \quad \text{SPE} = \frac{TN}{TN + FP}.$$

Statistical Analysis

Here, we used frequencies and percentages for categorical variables and mean (SD) for continuous variables. To compare pairs of groups, we used F -tests for continuous variables and χ^2 tests for categorical variables. $P < .05$ was defined as significant. All statistical

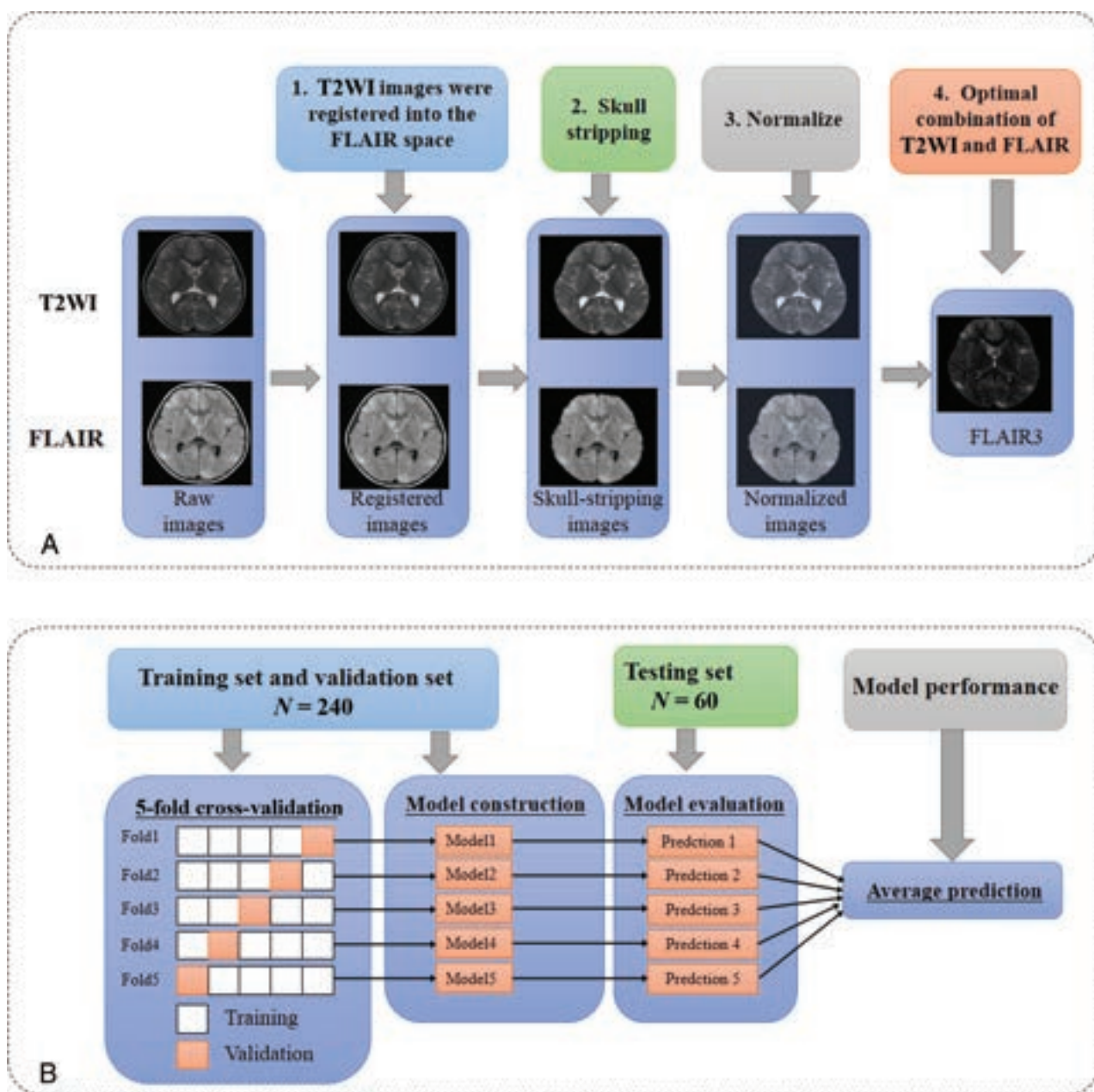


FIG 3. The applied operations of preprocessing pipeline, training, and evaluation. Schematic of the data preprocessing pipeline (A) and training and evaluation scheme (B). Five models were trained for each technique and used to predict drug-treatment outcome individually. The 5 predictions were averaged to give the final prediction of the model performances.

Table 2: The clinical characteristics of pediatric patients with rare TSC^a

Characteristics	Controlled (n = 97)	Uncontrolled (n = 203)	P Value
Male (No.) (%)	56 (57.7%)	107 (52.7%)	.416
Age at onset (mean) (months)	30.44 (SD, 33.17)	17.35 (SD, 26.22)	<.001 ^b
Age at imaging (mean) (months)	57.01 (SD, 45.18)	36.27 (SD, 40.37)	<.001 ^b
Infantile spasms (No.) (%)	21 (21.6%)	93 (45.8%)	<.001 ^b
Epilepsy (No.) (%)	97 (100.0%)	203 (100.0%)	
ASM numbers (≥ 3), n (%)	42 (43.3%)	171 (84.2%)	<.001 ^b
Focal epilepsy (No.) (%)	75 (77.3%)	165 (81.3%)	.424

Note:—Controlled indicates controlled seizures; Uncontrolled, uncontrolled seizures.

^a P values of continuous variables are the results of F-tests, and P values of categorical variables are the results of χ^2 tests.

^b The statistical significance between the groups.

analyses were performed using scikit-learn (<https://scikit-learn.org/stable/index.html>), scipy (<https://scipy.org/>), and stats (<https://pypi.org/project/statsmodels/>) models in Python 3.8.10.

RESULTS

Patient Characteristics

The main patient characteristics of all 300 patients with rare pediatric TSC-related disease are listed in Table 2. Of

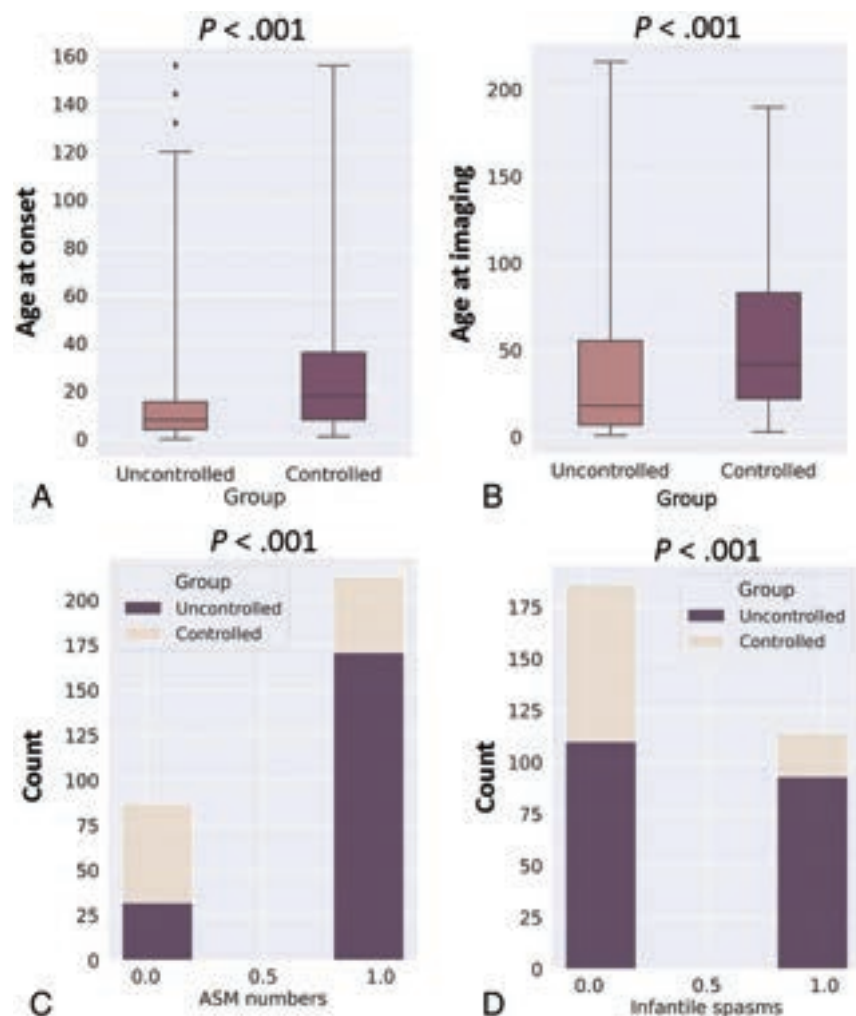


FIG 4. Statistical analysis of the clinical data set. A and B, Boxplots for continuous variables. A, Age at onset. B, Age at imaging. The horizontal axis represents groups, and the vertical axis represents features. The middle line of the boxplot is the median of the feature data. The upper and lower bounds of the boxplot are the upper and lower quartiles of the feature data, respectively. P values are the results of the Spearman correlation test. C and D, Stacked barplots for categorical variables. C, Infantile spasms. D, ASM numbers (≥ 3). The horizontal axis represents features (1.0 represents ASM numbers ≥ 3 or infantile spasms; 0.0 represents ASM numbers < 3 or no infantile spasms), and the vertical axis represents the number of patients in the 2 groups. P values of continuous variables are the results of F -tests, and P values of categorical variables are the results of χ^2 tests.

the 300 enrolled patients, 97 (41.1%) were controlled and 203 (58.9%) were uncontrolled by drug treatment. Thirty-one (41.3%) and 8 (40.0%) patients had controlled seizures, while 44 (58.7%) and 12 (60.0%) patients had uncontrolled seizures in the training and test cohorts, respectively. Of the 300 patients with TSC, 56 (57.7%) were male in the controlled seizures group and 107 (52.7%) were male in the uncontrolled group. The ages at onset in children with rare TSC were 30.44 (SD, 33.17) months and 17.35 (SD, 26.22) months in the controlled and uncontrolled groups, respectively. The ages at imaging of the children with TSC were 57.01 (SD, 45.18) months and 36.27 (SD, 40.37) months in the controlled and uncontrolled groups, respectively. There were no significant differences between the 2 drug-treatment outcomes based on sex and focal epilepsy features ($P > .05$). Age of onset, age at imaging, infantile spasms, and ASM numbers were significantly different between the 2 drug-treatment outcomes ($P < .05$).

Boxplots for age of onset and age at imaging and stacked barplots for infantile spasms and ASM numbers are shown in Fig 4. From the figure, we can see that the number of patients with

infantile spasms in the uncontrolled group was much larger than that in the controlled group. The number of pediatric patients with ASM numbers of 3 in the uncontrolled group was much higher than that in the controlled group.

Synthetic FLAIR3

Figure 5 shows FLAIR, T2WI, and synthetic FLAIR3 images in a representative child with rare TSC in the controlled group and a child with rare TSC in the uncontrolled group and a healthy child. Note the improved lesion contrast and visibility of the lesions on the synthetic FLAIR3 images of the child with rare TSC. The TSC lesion is shown by the white arrow.

Model Performance

The performance results compared with other networks on FLAIR is shown in Table 3. When the network inputs are FLAIR, ResNet3D achieved the best AUC performance. Performance of the final T2-weighted, FLAIR, FLAIR3, clinical data, and proposed WAE-net models on the test set are described in Table 4 and Fig 6.

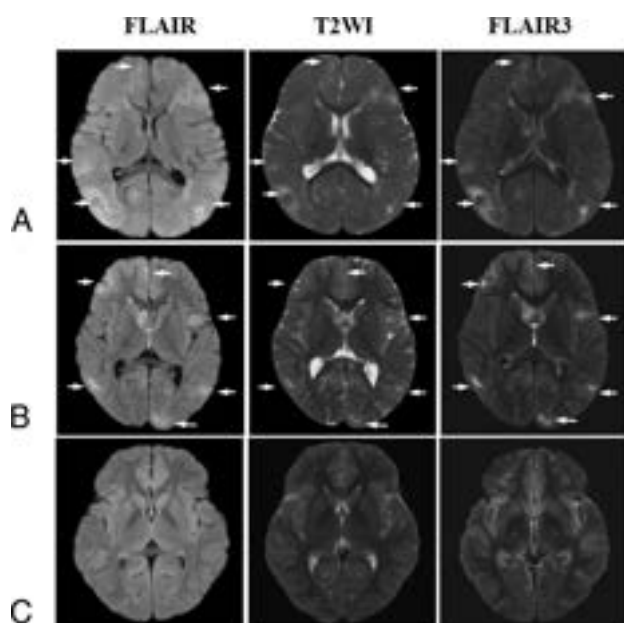


FIG 5. Representative images from a child with TSC in the controlled group, a child with TSC in the uncontrolled group, and a healthy child shown on T2WI, FLAIR, and the proposed synthetic FLAIR3 (TSC lesion, white arrow). Controlled group (A) uncontrolled group (B), and healthy child group (C).

Table 3: Performance results compared with other networks on FLAIR

Technique	Model	AUC	ACC	SEN	SPE
FLAIR	ResNet3D	0.783	0.695	0.650	0.790
FLAIR	LeNet3D	0.660	0.644	0.600	0.737
FLAIR	VGG3D	0.765	0.746	0.825	0.579

Note:—ResNet3D is derived from He et al;²⁶ LeNet3D is derived from Simonyan;⁴⁶ VGG3D is derived from Szegedy et al.⁴⁷

Table 4: The results of testing set

Technique	Model	AUC	ACC	SEN	SPE
FLAIR	ResNet3D	0.783	0.695	0.650	0.790
T2WI	ResNet3D	0.649	0.593	0.450	0.895
FLAIR3	ResNet3D	0.730	0.695	0.700	0.684
Clinical data	FCNN	0.774	0.831	0.950	0.579
FLAIR+ clinical data	WAE-net	0.826	0.847	0.974	0.580
FLAIR3+ clinical data	WAE-net	0.887	0.831	0.850	0.789
T2WI+ clinical data	WAE-net	0.809	0.847	0.975	0.579
Ensemble all	WAE-net	0.908	0.847	0.850	0.842

The clinical pediatric data-based model results were trained using age of onset, age at imaging, infantile spasms, and ASM numbers with an AUC of 0.774, ACC of 0.831, SEN of 0.950, and SPE of 0.579 in the testing cohort. The AUC performance of FLAIR3 was better than that of T2WI using the same network. When both FLAIR3 and clinical data are fed into the network, the network achieves an AUC performance of 0.887, which is higher than the AUC performance of T2-weighted data plus clinical data and FLAIR data plus clinical pediatric data. When T2-weighted (T2W), FLAIR, FLAIR3, and clinical pediatric data are all ensemble to input into the proposed network ('Ensemble all' in Table 4 and Fig 6), the best classification results were obtained for the proposed WAE-net model with an AUC of 0.908, ACC of 0.847, SEN

of 0.850, and SPE of 0.842 in the testing cohort. Figure 7A, -B shows the ROC curve for T2-weighted, FLAIR, FLAIR3, clinical pediatric data, and the performance of the proposed WAE-net models on the test set. Figure 7C, -D shows the decision curve analysis (DCA) for T2-weighted, FLAIR, FLAIR3, clinical pediatric data, and the performance of the proposed WAE-net models on the test set.

DISCUSSION

Reliable prediction of epilepsy drug-treatment outcomes allows more targeted treatment and can improve cure rates and may protect neurodevelopment.^{4,8,40} However, it is difficult for clinicians to determine epilepsy drug-treatment outcomes on the basis of clinical and treatment presentation. Therefore, there is an urgent need to develop a pediatric model that can predict epilepsy drug-treatment outcomes before treatment initiation.

Therefore, for the first time, we have developed a deep learning model to predict the drug-treatment outcome and have first introduced FLAIR3 as a new technique into the rare pediatric TSC diagnosis to improve lesion contrast. Our approach uses a deep neural network framework to extract descriptive factors from multicontrast MR images and clinical pediatric data. The proposed WAE-net model achieved the best AUC performance of 0.908 in the testing cohort when T2-weighted, FLAIR, FLAIR3, and clinical data are all input to the network. The structural MR images were complemented by demographic information (age at onset and age at imaging) and infantile spasms and ASM numbers collected at the baseline visit to compute a combined score used to predict epilepsy drug-treatment outcome. Compared with the single technique with ResNet3D approaches, the proposed WAE-net can improve the pediatric classification performance, meaning that combining multiple-contrast MR imaging and clinical pediatric data can use the complementary information between the two.^{20,21} Moreover, ResNet, with extremely high accuracies in the ImageNet data set (<https://image-net.org/>) has rapidly become a good choice for image-recognition tasks.²⁶ However, to the best of our knowledge, this article is the first to consider the ResNet3D of CNN architectures for diagnosis in rare pediatric TSC disease.

We specifically selected these structural MR imaging and clinical pediatric data to create a classification method that used the least invasive, lowest cost, and more commonly used diagnostic tools in clinical applications. In other words, the MR imaging and clinical pediatric data that we included here can typically be collected in nontertiary or highly specialized medical centers, greatly increasing the potential applicability of our method in clinical pediatric practice. For example, we did not use PET and fMRI as biomarkers because these imaging data are more expensive and less diffuse than the MR imaging and clinical pediatric data used here. In addition, a significant advantage of MR imaging over other imaging modalities such as CT and nuclear imaging is that it clearly shows soft tissues in multicontrasts.⁴¹

In addition, we found that FLAIR3 could improve lesion contrast and visibility of the lesions and that the AUC performance of FLAIR3 is better than that of T2WI by using the same neural network. In addition, the AUC performance of FLAIR3 data plus clinical data is higher than the AUC performance of T2-weighted

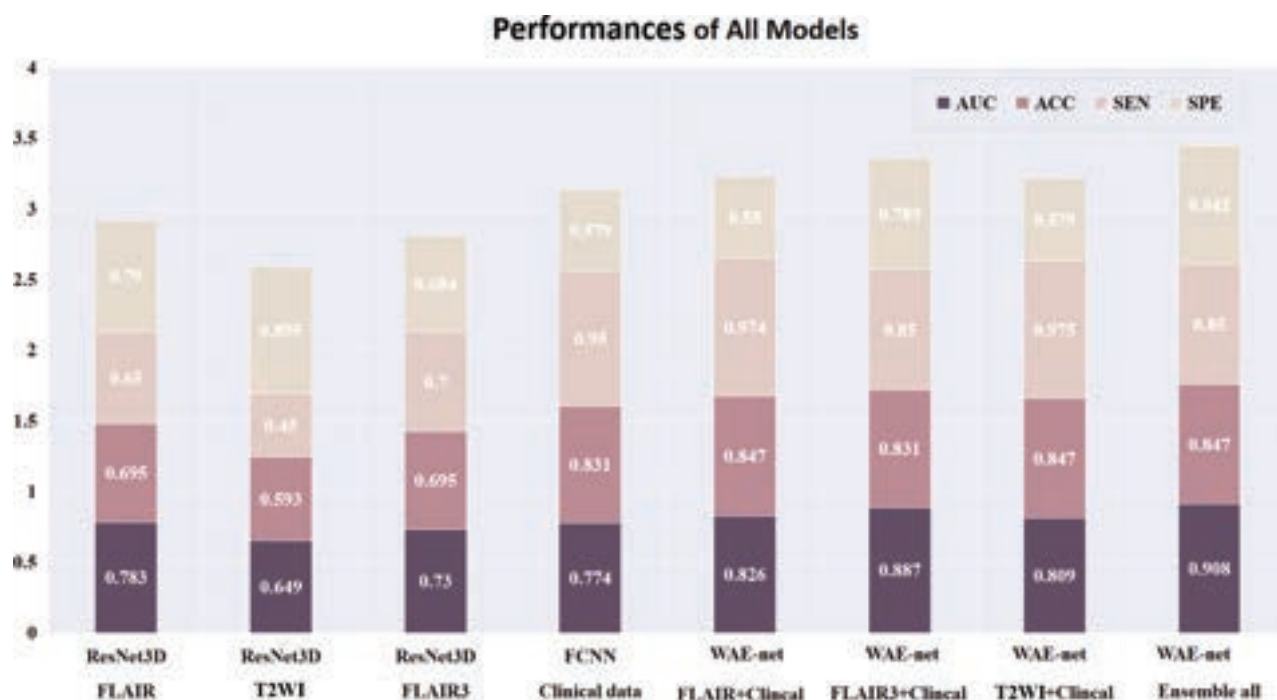


FIG 6. The performances of the final T2-weighted, FLAIR, FLAIR3, clinical pediatric data, and the proposed WAE-net models on the test set.

data plus clinical pediatric data and FLAIR data plus clinical pediatric data. One possible explanation is that FLAIR3 can improve the lesion-to-brain contrast and provide more low-dimensional visual lesion information for a rare pediatric TSC diagnosis, which may increase the interpretability of deep learning and support the idea that deep learning methods can identify the more relevant features from the input images.⁴² Previous studies^{43–45} have identified several risk factors affecting epilepsy prognosis in pediatric patients with TSC, including the age of onset of seizures, the presence of infantile spasm, and a history of using >3 antiepileptic drugs. In our study, we also observed the impact of age at onset and age at imaging on the prognosis of epilepsy. Specifically, we found that these factors were statistically different between the controlled and uncontrolled groups ($P < .05$), with the uncontrolled group being younger. Our findings suggest that pediatric patients with a younger age of onset and imaging are more likely to have a poorer prognoses. Pediatric patients with focal seizures before 1 year of age are more likely to develop resistance than patients with onset after 1 year of age.³ Jeong et al⁴⁵ also reported that pediatric patients with rare TSC epilepsy with previous infantile spasms are more likely to have drug resistance,³ which is consistent with our conclusion that the uncontrolled group has a higher proportion of infantile spasms.

In our study, we included pediatric patients with confirmed rare TSC-related epilepsy in Shenzhen Children's Hospital for 8 years, followed the patients for >1 year, and finally included 300 children with rare TSC-related epilepsy. During the experiments, we found that the proposed 3D CNN models can achieve better performance than the traditional machine learning approach from Yang et al.¹² They achieved an AUC of 0.812 with multilayer perceptron.¹² However, this study also had small sample sizes. We

did not find any studies involving deep learning techniques for the prediction of epilepsy drug-treatment outcome on MR imaging. Intuitively, neural network-based methods should perform better than conventional approaches for feature-extraction followed by a separate classifier, because the feature-selection process is directly driven by the performance-optimization procedures.¹⁶ Deep learning is required for a number of training samples to achieve good generalization performance. We believe the performance improvement of our method is primarily caused by fully using the spatial features of 3D MR imaging and complementary information of clinical pediatric data. The increase in the number of pediatric data sets may also be 1 reason.

The rarity of TSC presents a challenge in compiling a data set that could effectively power the training of a deep neural network for this task. Although the size of our data set is larger than that of many other data sets used for rare disease classification tasks, it is still orders of magnitude smaller than data sets used for other medical image characterization tasks. Larger data sets could also allow granular classification beyond binary, such as distinguishing infantile spasms or other histopathologic diagnoses.

Several limitations should be noted for the current pediatric study. First, we conducted this study in a retrospective manner without external validation, having the risk of bias and lack of generalizability. Second, the study participants belonged to a single ethnicity (Chinese), implying that our results might not be applicable to pediatric patients from other ethnic backgrounds. Collecting multicenter data sets is challenging due to the extremely low incidence of rare pediatric TSC disease and the need to follow pediatric patients with rare TSC for ≥ 1 year. Future prospective studies that incorporate data from other international centers and larger data samples can overcome this limitation.

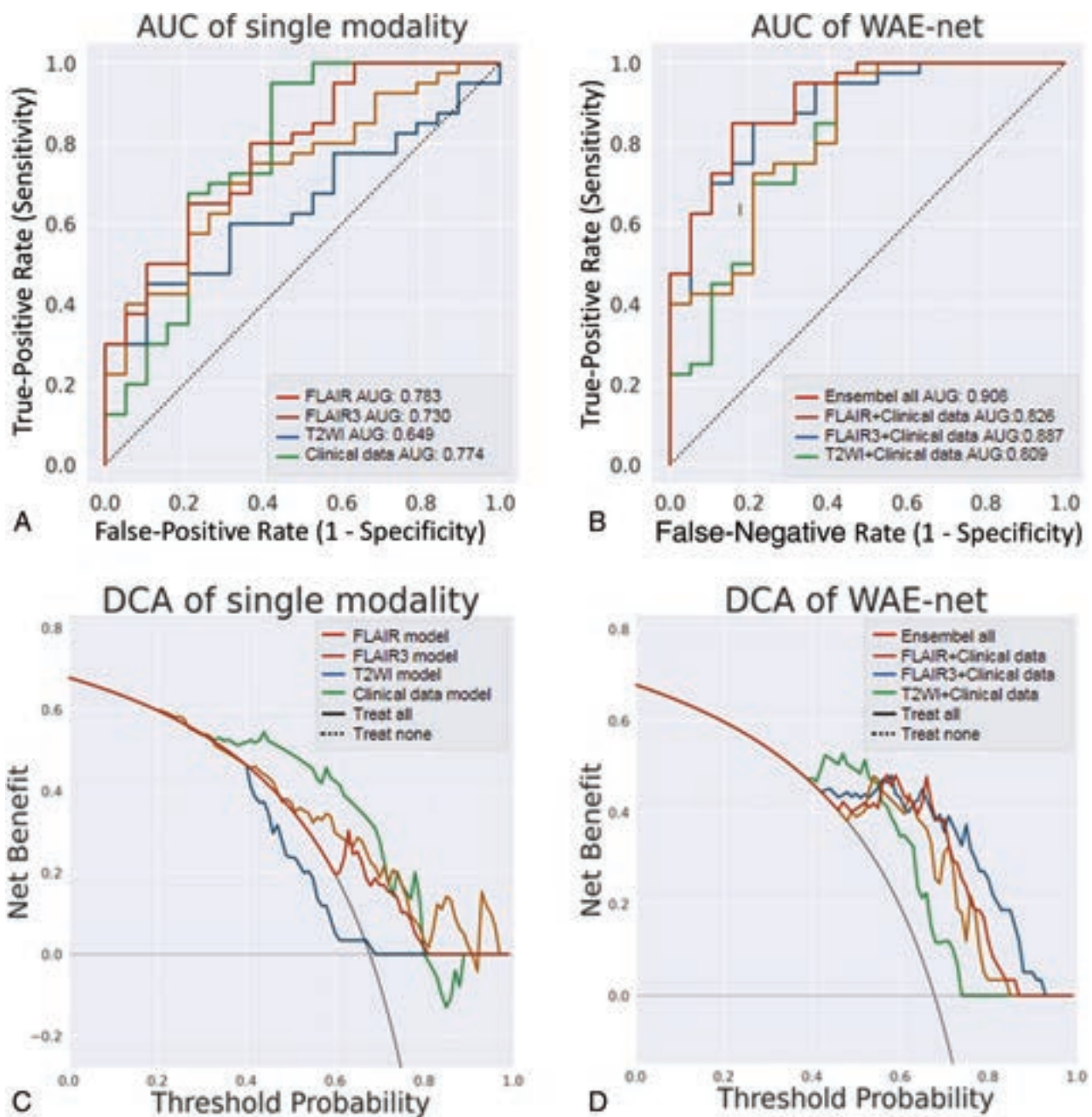


FIG 7. Analysis of the single technique and the proposed WAE-net methods. *A*, ROC curves in FLAIR, T2-weighted, FLAIR3, and the clinical model of the testing cohort. *B*, ROC curves in the proposed WAE-net of the testing cohort. *C*, DCA for FLAIR decision. T2-weighted, FLAIR3, and the clinical model of the testing cohort. *D*, DCA for the proposed WAE-net of the testing cohort. The black line represents the assumption that all patients have interventions. The colored lines represent the different models. The horizontal axis represents the threshold probability, and the vertical axis represents the net benefit.

In short, for the first time, we introduce FLAIR3 as a new technique in the rare pediatric TSC diagnosis to improve lesion contrast, and we have developed a deep learning model that can predict epilepsy drug-treatment outcomes with high AUC and accuracy. At present, this work demonstrates the promise of deep learning to aid radiologists in characterizing the refractory patients with improved certainty. FLAIR3 can provide clinicians with a new technique to accurately localize lesions in patients with rare pediatric TSC.

CONCLUSIONS

In general, age of onset, age at imaging, infantile spasms, and ASM numbers were shown to be related to epilepsy drug-treatment outcome in children with rare TSC. FLAIR3 can improve lesion contrast and visibility and provide more complementary information for our deep learning models to improve the prediction accuracy. The experiments have shown that the proposed deep learning method could successfully predict epilepsy drug-treatment outcomes in children with rare TSC-related disease.

The current test results have suggested that the proposed method could be a noninvasive, efficient, and reliable way to predict pediatric TSC-related drug-treatment outcomes and could be as a strong baseline for future pediatric researchers.

Disclosure forms provided by the authors are available with the full text and PDF of this article at www.ajnr.org.

REFERENCES

- Randle SC. **Tuberous sclerosis complex: a review.** *Pediatr Ann* 2017;46:e166–171 CrossRef Medline
- Holmes GL, Stafstrom CE; Tuberous Sclerosis Study Group. **Tuberous sclerosis complex and epilepsy: recent developments and future challenges.** *Epilepsia* 2007;48:617–30 CrossRef Medline
- Chu-Shore CJ, Major P, Camposano S, et al. **The natural history of epilepsy in tuberous sclerosis complex.** *Epilepsia* 2010;51:1236–41 CrossRef Medline
- Ślowińska M, Jóźwiak S, Peron A, et al. **Early diagnosis of tuberous sclerosis complex: a race against time—how to make the diagnosis before seizures?** *Orphanet J Rare Dis* 2018;13:25 CrossRef Medline
- Henske EP, Jóźwiak S, Kingswood JC, et al. **Tuberous sclerosis complex.** *Nat Rev Dis Primers* 2016;2:16035 CrossRef Medline
- Strzelczyk A, Rosenow F, Zollner JP, et al. **Epidemiology, healthcare resource use, and mortality in patients with tuberous sclerosis complex: a population-based study on German health insurance data.** *Seizure* 2021;91:287–95 CrossRef Medline
- Jansen FE, van Huffelen AC, Bourez-Swart M, et al. **Consistent localization of interictal epileptiform activity on EEGs of patients with tuberous sclerosis complex.** *Epilepsia* 2005;46:415–19 CrossRef Medline
- Curatolo P, Nabbout R, Lagae L, et al. **Management of epilepsy associated with tuberous sclerosis complex: updated clinical recommendations.** *Eur J Paediatr Neurol* 2018;22:738–48 CrossRef Medline
- van der Poest Clement E, Jansen FE, Braun KP, et al. **Update on drug management of refractory epilepsy in tuberous sclerosis complex.** *Paediatr Drugs* 2020;22:73–84 CrossRef Medline
- Jesmanas S, Norvaintė K, Gleiznienė R, et al. **Different MRI-defined tuber types in tuberous sclerosis complex: quantitative evaluation and association with disease manifestations.** *Brain Dev* 2018;40:196–204 CrossRef Medline
- Tong XZ, Wang XF, Qin L, et al. **Vagus nerve stimulation for drug-resistant epilepsy induced by tuberous sclerosis complex.** *Epilepsy Behav* 2022;126:108431 CrossRef Medline
- Yang J, Zhao C, Su S, et al. **Machine Learning in Epilepsy Drug Treatment Outcome Prediction Using Multi-modality Data in Children with Tuberous Sclerosis Complex.** In: *2020 6th International Conference on Big Data and Information Analytics (BigDIA)*. December 4–6, 2020. Shenzhen, China CrossRef
- Russo C, Nastro A, Cicala D, et al. **Neuroimaging in tuberous sclerosis complex.** *Childs Nerv Syst* 2020;36:2497–509 CrossRef Medline
- Sanchez Fernandez I, Yang E, Calvachi P, et al; TACERN Study Group. **Deep learning in rare disease: detection of tubers in tuberous sclerosis complex.** *PLoS One* 2020;15:e0232376 CrossRef Medline
- Hu J, Qing Z, Liu R, et al. **Deep learning-based classification and voxel-based visualization of frontotemporal dementia and Alzheimer's disease.** *Front Neurosci* 2020;14:626154 CrossRef Medline
- Spasov S, Passamonti L, Duggento A, et al; Alzheimer's Disease Neuroimaging Initiative. **A parameter-efficient deep learning approach to predict conversion from mild cognitive impairment to Alzheimer's disease.** *Neuroimage* 2019;189:276–87 CrossRef Medline
- Kim H, Lee Y, Kim YH, et al. **Deep learning-based method to differentiate neuromyelitis optica spectrum disorder from multiple sclerosis.** *Front Neurol* 2020;11:599042 CrossRef Medline
- Eweje FR, Bao B, Wu J, et al. **Deep learning for classification of bone lesions on routine MRI.** *EBioMedicine* 2021;68:103402 CrossRef Medline
- Grossman R, Haim O, Abramov S, et al. **Differentiating small-cell lung cancer from non-small-cell lung cancer brain metastases based on MRI using efficientnet and transfer learning approach.** *Technol Cancer Res Treat* 2021;20:153303382110049 CrossRef Medline
- Jonsson BA, Bjornsdottir G, Thorgeirsson TE, et al. **Brain age prediction using deep learning uncovers associated sequence variants.** *Nat Commun* 2019;10:5409 CrossRef Medline
- Peng H, Gong W, Beckmann CF, et al. **Accurate brain age prediction with lightweight deep neural networks.** *Med Image Anal* 2021;68:101871 CrossRef Medline
- An S, Malhotra K, Dilley C, et al. **Predicting drug-resistant epilepsy: a machine learning approach based on administrative claims data.** *Epilepsy Behav* 2018;89:118–25 CrossRef Medline
- Luckett PH, Maccotta L, Lee JJ, et al. **Deep learning resting state fMRI lateralization of temporal lobe epilepsy.** *Epilepsia* 2022;63:1542–52 CrossRef Medline
- Gleichgerricht E, Munsell B, Bhatia S, et al. **Deep learning applied to whole-brain connectome to determine seizure control after epilepsy surgery.** *Epilepsia* 2018;59:1643–54 CrossRef Medline
- Zhang Q, He Y, Qu T, et al. **Delayed brain development of Rolandic epilepsy profiled by deep learning-based neuroanatomic imaging.** *Eur Radiol* 2021;31:9628–37 CrossRef Medline
- He K, Zhang X, Ren S, et al. **Deep residual learning for image recognition.** In: *Proceedings of the IEEE Conference on Computer Vision and Pattern Recognition*. June 27–30, 2016. Las Vegas, Nevada
- Cole JH, Poudel RP, Tsagkrasoulis D, et al. **Predicting brain age with deep learning from raw imaging data results in a reliable and heritable biomarker.** *Neuroimage* 2017;163:115–24 CrossRef Medline
- Meyer A, Chlebus G, Rak M, et al. **Anisotropic 3D multi-stream CNN for accurate prostate segmentation from multi-planar MRI.** *Comput Methods Programs Biomed* 2021;200:105821 CrossRef Medline
- Folego G, Weiler M, Casseb RF, et al. **Alzheimer's disease detection through whole-brain 3D-CNN MRI.** *Front Bioeng Biotechnol* 2020;8:534592 CrossRef Medline
- Grilli G, Moffa AP, Perfetto F, et al. **Neuroimaging features of tuberous sclerosis complex and Chiari type I malformation: a rare association.** *J Pediatr Neurosci* 2018;13:224–28 CrossRef Medline
- Wiggermann V, Hernandez-Torres E, Traboulsee A, et al. **FLAIR2: a combination of FLAIR and T2 for improved MS lesion detection.** *AJNR Am J Neuroradiol* 2016;37:259–65 CrossRef Medline
- Gabr RE, Hasan KM, Haque ME, et al. **Optimal combination of FLAIR and T2-weighted MRI for improved lesion contrast in multiple sclerosis.** *J Magn Reson Imaging* 2016;44:1293–300 CrossRef Medline
- Liang G, Xing X, Liu L, et al. **Alzheimer's disease classification using 2D convolutional neural networks.** *Annu Int Conf IEEE Eng Med Biol Soc* 2021;2021:3008–12 CrossRef Medline
- Jiang D, Liao J, Zhao C, et al. **Recognizing pediatric tuberous sclerosis complex based on multi-contrast MRI and deep weighted fusion network.** *Bioengineering (Basel)* 2023;10:870 CrossRef Medline
- Hu Z, Jiang D, Zhao X, et al. **Predicting drug treatment outcomes in children with tuberous sclerosis complex-related epilepsy: a clinical radiomics study.** *AJNR Am J Neuroradiol* 2023;44:853–60 CrossRef Medline
- Shinnar S. **The new ILAE classification.** *Epilepsia* 2010;51:715–17 CrossRef Medline
- Tan M, Efficientnet LQ. **Rethinking model scaling for convolutional neural networks.** In: *Thirty-Sixth International Conference on Machine Learning*. June 9–15, 2019. Long Beach, California
- Jenkinson M, Beckmann CF, Behrens TE, et al. **FSL.** *Neuroimage* 2012;62:782–90 CrossRef Medline
- Isensee F, Schell M, Pfleger I, et al. **Automated brain extraction of multisequence MRI using artificial neural networks.** *Hum Brain Mapp* 2019;40:4952–64 CrossRef Medline
- Hsieh DT, Jennesson MM, Thiele EA. **Epileptic spasms in tuberous sclerosis complex.** *Epilepsy Res* 2013;106:200–10 CrossRef Medline
- Lyu Q, Shan H, Steber C, et al. **Multi-contrast super-resolution MRI through a progressive network.** *IEEE Trans Med Imaging* 2020;39:2738–49 CrossRef Medline
- Jaworek-Korjakowska J, Brodzicki A, Cassidy B, et al. **Interpretability of a deep learning based approach for the classification of skin**

- lesions into main anatomic body sites.** *Cancers (Basel)* 2021;13:6048 CrossRef Medline
43. Gül Mert G, Altunbaşak Ş, Hergüner Ö, et al. **Factors affecting epilepsy prognosis in patients with tuberous sclerosis.** *Childs Nerv Syst* 2019;35:463–68 CrossRef Medline
44. Kwan P, Brodie MJ. **Early identification of refractory epilepsy.** *N Engl J Med* 2000;342:314–19 CrossRef Medline
45. Jeong A, Nakagawa JA, Wong M. **Predictors of drug-resistant epilepsy in tuberous sclerosis complex.** *J Child Neurol* 2017;32:1092–98 CrossRef Medline
46. Simonyan K, Zisserman A. **Very deep convolutional networks for large-scale image recognition.** *arXiv* 2014;1409:1556 CrossRef
47. Szegedy C, Liu W, Jia Y, et al. **Going deeper with convolutions.** *arXiv* 2014;1409:4802–98 CrossRef

Brain Age Estimation on a Dementia Cohort Using FLAIR MRI Biomarkers

 Owen Crystal,  Pejman J. Maralani, Sandra Black, Corinne Fischer,  Alan R. Moody, and  April Khademi



ABSTRACT

BACKGROUND AND PURPOSE: The prodromal stage of Alzheimer's disease presents an imperative intervention window. This work focuses on using brain age prediction models and biomarkers from FLAIR MR imaging to identify subjects who progress to Alzheimer's disease (converting mild cognitive impairment) or those who remain stable (stable mild cognitive impairment).

MATERIALS AND METHODS: A machine learning model was trained to predict the age of normal control subjects on the basis of volume, intensity, and texture features from 3239 FLAIR MRI volumes. The brain age gap estimation (BrainAGE) was computed as the difference between the predicted and true age, and it was used as a biomarker for both cross-sectional and longitudinal analyses. Differences in biomarker means, slopes, and intercepts were investigated using ANOVA and Tukey post hoc test. Correlation analysis was performed between brain age gap estimation and established Alzheimer's disease indicators.

RESULTS: The brain age prediction model showed accurate results (mean absolute error = 2.89 years) when testing on held out normal control data. The computed BrainAGE metric showed significant differences between the stable mild cognitive impairment and converting mild cognitive impairment groups in cross-sectional and longitudinal analyses, most notably showing significant differences up to 4 years before conversion to Alzheimer's disease. A significant correlation was found between BrainAGE and previously established Alzheimer's disease conversion biomarkers.

CONCLUSIONS: The BrainAGE metric can allow clinicians to consider a single explainable value that summarizes all the biomarkers because it considers many dimensions of disease and can determine whether the subject has normal aging patterns or if he or she is trending into a high-risk category using a single value.

ABBREVIATIONS: AD = Alzheimer's disease; $A\beta$ = amyloid- β ; BrainAGE = brain age gap estimation; cMCI = converting mild cognitive impairment; NC = normal control; LVV = lateral ventricular volume; MAE = mean absolute error; MCI = mild cognitive impairment; MoCA = Montreal Cognitive Assessment; NABM = normal-appearing brain matter; p-tau = phosphorylated-tau; RFC = Random Forest Classifier; RFR = random forest regressor; sMCI = stable mild cognitive impairment; SVM = support vector machine

Alzheimer's disease (AD) causes accelerated loss of cognition and memory, and is the most common type of dementia.^{1,2} AD is expected to impact 1 in 85 persons worldwide within the

next 30 years.³ Mild cognitive impairment (MCI) is the prodromal phase of AD, characterized by abnormal changes in cognitive domains that have not reached the severity of AD.^{4,5} This prodromal phase represents a window in which interventions can be applied to reduce the risk of progressing to AD. The MCI phase is important to target because >50% of individuals with MCI eventually progress to AD.⁶ Subjects with MCI who convert to AD are referred to as converting MCI (cMCI) as opposed to subjects with stable MCI (sMCI) who have cognitive issues but do not progress to AD. Distinguishing between subjects with cMCI and sMCI can aid in early disease detection, as well as patient stratification in large clinical trials. Incorrect patient grouping is one of the most common causes of failed AD treatment trials.⁷ Quantitative biomarkers from MR imaging can help improve diagnostic accuracy and increase cohort homogeneity in AD treatment trials.

Aging is a time-dependent process in which humans undergo functional decline due to an accumulation of cellular damage.⁸

Received May 26, 2023; accepted after revision October 13.

From the Department of Electrical, Computer and Biomedical Engineering (O.C., A.K.), Toronto Metropolitan University, Toronto, Ontario, Canada; Department of Medical Imaging (P.J.M., A.R.M., A.K.), Institute of Medical Science (S.B., C.F.), and Department of Neurology (S.B.), University of Toronto, Toronto, Ontario, Canada; Hurvitz Brain Sciences Research Program (S.B.), Sunnybrook Research Institute, Toronto, Ontario, Canada; Division of Neurology (S.B.), Department of Medicine, and L.C. Campbell Cognitive Neurology Research Unit (S.B.), Sunnybrook Health Sciences Centre, Toronto, Ontario, Canada; Department of Psychiatry (C.F.), and Keenan Research Center (C.F., A.K.), St. Michael's Hospital, Toronto, Ontario, Canada; Institute of Biomedical Engineering, Science and Technology (O.C., A.K.), Toronto, Ontario, Canada; and Vector Institute for Artificial Intelligence (A.K.), Toronto, Ontario, Canada.

Please address correspondence to Owen Crystal, MC, Electrical, Computer and Biomedical Engineering, Toronto Metropolitan University, Toronto, ON, Canada; e-mail: ocrystal@torontomu.ca



Indicates article with online supplemental data.

<http://dx.doi.org/10.3174/ajnr.A8059>

Table 1: FLAIR MR imaging data sets^a

Diagnosis	Patient Information					
	Volumes	Images	Patients	Male:Female	Centers	Mean Age (yr)
NC	1033	37,706	435	187:248	57	71.54 (SD, 6.26)
sMCI	1662	57,322	632	345:287	58	74.17 (SD, 7.17)
cMCI	161	2315	62	37:25	34	74.49 (SD, 7.23)
AD	383	10,714	149	85:64	46	75.24 (SD, 7.66)
Total	3239	108,057	1278	654:624	58	73.42 (SD, 7.07)

^a All data were acquired at 1.5/3T and 3- to 5-mm section thickness.

When this process is accelerated due to AD, individuals have rapid cognitive decline and neurodegeneration. There is a growing interest in the community to measure this accelerated aging through brain age techniques. Brain age is the predicted chronological age of a subject estimated by using a machine learning model trained on normative data. This model is used to test disease data, and a large gap between the predicted age and true age is a sign of accelerated aging. Leveraging the benefits of machine learning can allow precision and preventative medicine when it comes to early AD diagnosis.

Previous brain age estimation techniques have used established T1-weighted MR imaging biomarkers and cognitive measures⁹ to categorize subjects into cognitive groups and identify subjects with cMCI.¹⁰

This work investigated brain age on the basis of FLAIR MR imaging biomarkers and a Random Forest Classifier (RFC) to differentiate between sMCI and cMCI in cross-sectional and longitudinal analyses. FLAIR MR imaging is routinely acquired in clinical settings, and FLAIR biomarkers have high translation potential. The FLAIR sequence highlights white matter disease and white matter lesions, which are related to many neurologic disorders,¹¹⁻¹³ cognitive impairment, age, and CSF biomarkers.^{11,14-17} Twelve FLAIR biomarkers related to intensity, texture, and volumes of objects in the brain were extracted using fully automated and validated algorithms and were used to train a machine learning algorithm to predict the brain age of subjects with cognitive impairment.

Four types of analysis were conducted. The first was a regression analysis to investigate the relationship between the predicted age and true age for each cognitive group. The second was a cross-sectional analysis, which compared the mean brain age gap estimate (BrainAGE) among the normal control (NC), sMCI, cMCI, and AD groups using ANOVA and the Tukey post hoc test. Longitudinal analysis was performed to compare regression slopes and intercepts of BrainAGE versus time among cognitive groups. Finally, the correlation between BrainAGE and CSF biomarkers and the APOE-4 genotype was investigated. The BrainAGE metric has benefits as a single, explainable biomarker that can be used for monitoring and diagnostic purposes or for generating homogeneous cohorts for clinical trials.

MATERIALS AND METHODS

Experimental Data

The Alzheimer's Disease Neuroimaging Initiative, an international data set with longitudinal imaging for studying AD, was used throughout all analyses.¹⁸ A total of 3072 imaging volumes from 978 patients was used for cross-sectional and longitudinal analysis.

The Montreal Cognitive Assessment (MoCA) score was used to label subjects as NC (MoCA > 26), MCI (19 < MoCA < 25), and AD (MoCA < 18). The MCI class is divided into sMCI and cMCI, depending on the analysis.

For cross-sectional analysis, a subject with MCI was labeled as cMCI if their MoCA score progressed from the MCI range to the AD range. The scan

immediately prior (approximately 1 year) to AD conversion was labeled cMCI. Only the cMCI scan before conversion was retained for the analysis to avoid data leakage. If a subject remained within the MCI MoCA range for all time points, they were labeled sMCI. For longitudinal analysis, subjects labeled MCI who converted to AD in later scans were assigned a cMCI label for up to 6 years before AD conversion and were included to analyze disease progression across time. All scans after progressing to AD were considered AD. For subjects with cMCI, the longitudinal time points were normalized so that time point 5 is 1 year before converting to AD. This normalization was implemented to investigate how the subjects with cMCI progressed leading up to AD conversion. A summary of the sample sizes used for the cross-sectional and longitudinal analyses by the cognitive group is shown in Table 1.

MR Imaging

FLAIR MR images were acquired from 58 centers worldwide on 3T machines from GE Healthcare, Siemens, and Philips Healthcare. Pixel spacing was 0.8594 mm, TR = 9000–11,000 ms, TE = 90–154 ms, TI = 2200–2500 ms.

Biomarker Measurement

FLAIR MR imaging volumes underwent bias field correction and intensity standardization to align intensity ranges of each tissue across data sets.¹⁹ Intracranial volume segmentation was performed using a convolutional neural network to extract brain tissue.²⁰ Note that 31 volumes were excluded due to poor intracranial volume segmentations significantly impacting downstream biomarker extraction. Using the standardized imaging volumes, 6 volume, 3 texture, and 3 intensity biomarkers were extracted. Thresholding was used to extract total brain volume and CSF volume,¹⁹ while lateral ventricular volume (LVV) and white matter lesions were extracted using deep learning techniques.^{12,21} Subarachnoid CSF volume was computed as the difference between the CSF and LVV masks. The texture biomarkers, macrostructural damage, microstructural damage, and microstructural integrity were computed using spatial correlation and local binary patterns of intensities within regions of the normal-appearing brain matter (NABM), which is defined as the entire intracranial volume excluding the CSF and white matter lesion.¹⁴ Using NABM, we calculated the mean intensity, skewness, and kurtosis of the intensity distribution as the intensity features.

Brain Age Model

A brain age prediction model was developed to examine differences among NC, sMCI, cMCI, and AD using FLAIR biomarkers.

Table 2: Brain age prediction model comparison based on MAE and correlation between true and predicted age^a

Model	MAE Raw	MAE Corr.	Correlation Raw	Correlation Corr.
RFC	3.16	2.89	0.70 ($P < .001$)	0.84 ($P < .001$)
SVM (reg.)	3.54	2.66	0.66 ($P < .001$)	0.86 ($P < .001$)
Log. Reg.	4.06	3.10	0.56 ($P < .001$)	0.79 ($P < .001$)
RFR	3.21	2.46	0.74 ($P < .001$)	0.87 ($P < .001$)

Note:—corr. indicates corrected; reg., regression; Log. Reg, Logistic Regression.

^aResults using the raw and corr. brain ages are shown for comparison.

Four different machine learning models were implemented, and their performance was compared using an RFC, logistic regression, support vector machine (SVM), and a random forest regressor (RFR). Note that for the discontinuous classifiers, the ages must be rounded to the nearest integer. A 70/30 ($n = 1187 / n = 509$) training/testing split was used. All normative (cross-sectional) data were used to train the model, which included FLAIR biomarkers and chronological age. Because all data are from a normative sample, the RFC is modeling healthy brain aging. A held out NC subset was used to verify model performance by measuring the mean absolute error (MAE) between the predicted brain age and ground truth chronological age. A common bias is frequently observed in brain age prediction in which models often overestimate the brain age of younger subjects, underestimate the brain age of older subjects, and predict subjects near the mean age more accurately.²²⁻²⁴ Common practice is to apply the following statistical bias correction to account for this:

$$\text{Corrected Brain Age} = \text{Predicted Age} + [\text{True Age} - (\text{Slope} \times \text{True Age} + \text{Intercept})].$$

1)

While other methods have been attempted for bias correction of brain age, this technique has been found optimal.²⁵ Note that the slope and intercept used in Equation 1 are from the true age versus predicted age of the NC group. Corrected brain age versus true age scatterplots and regression lines were analyzed using the Pearson correlation coefficient.

BrainAGE Computation

By means of the optimal normative model, the remaining held out data that included subjects with sMCI ($n = 1976$), cMCI ($n = 68$), and AD ($n = 1707$) were used to predict brain age. Franke et al²⁶ showed how a relevant metric called BrainAGE, which is the difference between predicted brain age and true chronological age, can be used as a biomarker in many applications, including the assessment of neurologic, neuropsychiatric, and neurodegenerative diseases (Equation 2). The authors found a significant BrainAGE difference between NC/sMCI and cMCI/AD groups, demonstrating the viability of a BrainAGE biomarker.

$$\text{Brain AGE} = \text{Brain Age} - \text{True Age (years)}$$

2)

Higher positive values indicate accelerated aging. The mean BrainAGE for each cognitive group was compared via ANOVA and Tukey post hoc analysis to investigate group differences.

Longitudinal BrainAGE

To analyze BrainAGE further, we used it as a biomarker to investigate disease progression across time for each disease group. The

held out longitudinal data for this experiment included sMCI ($n = 1976$), cMCI ($n = 161$), and AD ($n = 1707$). Compared with the cross-sectional analysis which considers only the scan before conversion to AD as cMCI, in this analysis, the longitudinal labeling includes volumes from subjects who converted up to 6 years prior. The normative model was used to predict the brain age from each subject

and time point. BrainAGE versus time regression lines were generated using the following equation: $\text{BrainAGE} \sim \text{time} + \text{diagnosis} + \text{time} \times \text{diagnosis}$. The slopes and intercepts of the regression lines for each diagnostic category were compared via ANOVA and Tukey post hoc. Cohen's d was computed for the slopes and intercepts of the groups to determine the effect size. In order to determine how much time before conversion cMCI subjects show significant differences compared to sMCI subjects, t tests were performed comparing the BrainAGE of cMCI subjects from each time point with the entire sMCI group.

Biomarker Correlation

The BrainAGE metric and its relation to cognitive decline were further analyzed by correlation with phosphorylated-tau (p-tau) and amyloid- β ($A\beta$) CSF biomarkers and the *APOE-4* genotype on cross-sectional data. These variables are known as criterion standard indicators of AD and cognitive impairment.^{27,28} Elevated p-tau and high levels of $A\beta$ in the CSF are both strong indicators of AD. The presence of the *APOE-4* allele is strongly associated with an elevated risk of developing AD.

RESULTS

All 12 FLAIR MR imaging biomarkers were extracted from the data set, and subjects were labeled as NC, sMCI, cMCI, or AD as in the subsection "Experimental Data." Analyses were completed on an NVIDIA GeForce RTX 3090 Ti GPU with 32GB of RAM.

An RFC, SVM, logistic regression model, and an RFR were trained using all biomarkers from the NCs to create a brain age prediction model. On a held out NC test set, the MAE and correlation coefficient between the predicted brain age and the true age when using each model were reported (Table 2).

The results show the RFR is the optimal brain age prediction model because the model achieved an MAE of 2.46 years, which is among the lowest reported in the literature, which typically ranged from 4 to 9 years.^{9,29} The RFR model also yielded a strong correlation coefficient of 0.87 ($P < .001$) when comparing the predicted and true chronological ages of the NCs. The positive impact of the correction can be seen as the MAE and correlations improve for each of the 4 models after correction. Corrected predicted brain age versus true chronological age plots for NC, sMCI, cMCI, and AD when using the optimal model (RFR) are shown in Fig 1. True age-versus-predicted age plots before bias correction are shown in the Online Supplemental Data.

BrainAGE was calculated by using Equation 2, and the distributions for each cognitive group are shown in Fig 2. With a worsening cognitive state, the mean BrainAGE increases. Results from ANOVA and Tukey post hoc demonstrated that all

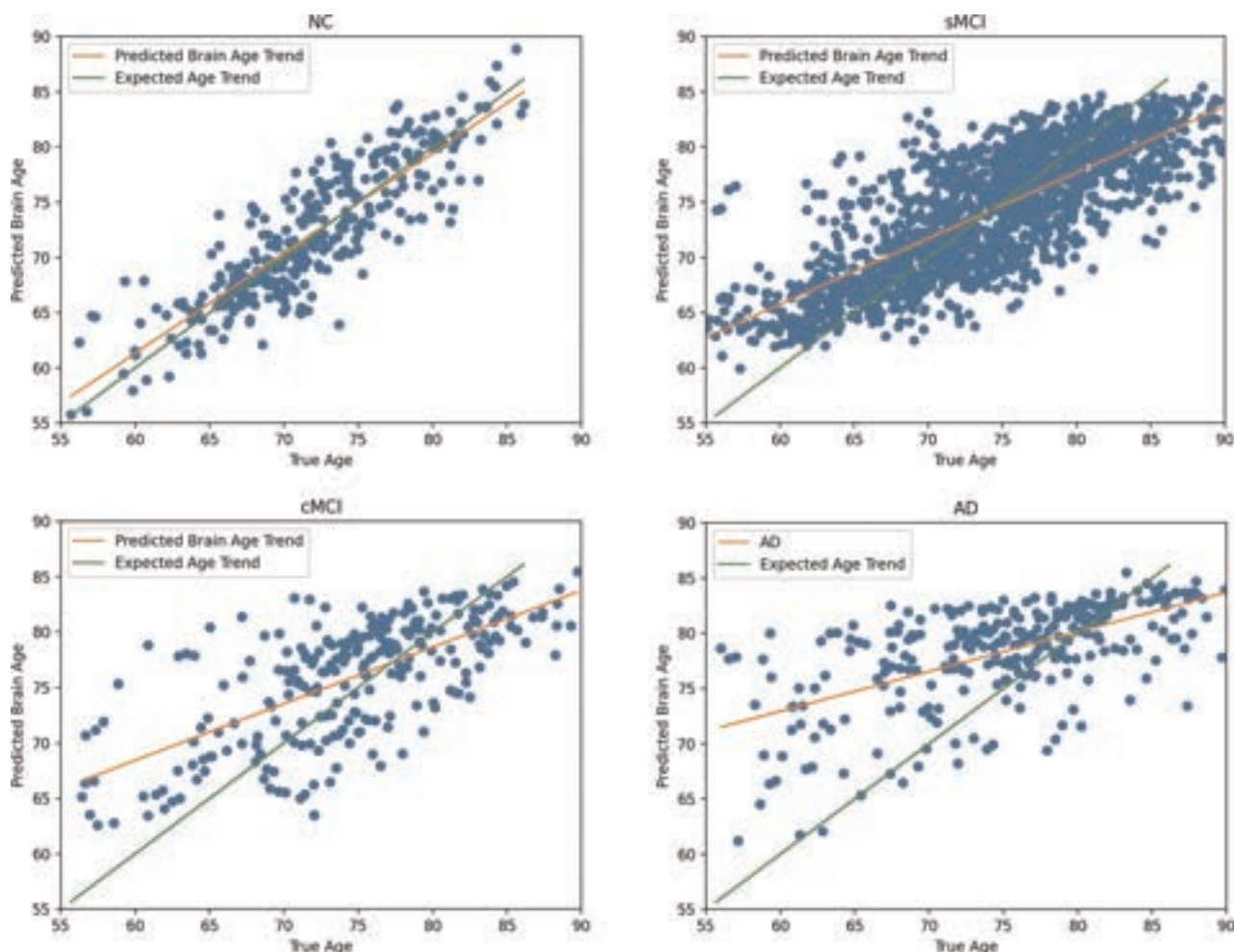


FIG 1. Corrected predicted brain age versus true age for NC, sMCI, cMCI, and AD using the RFR.

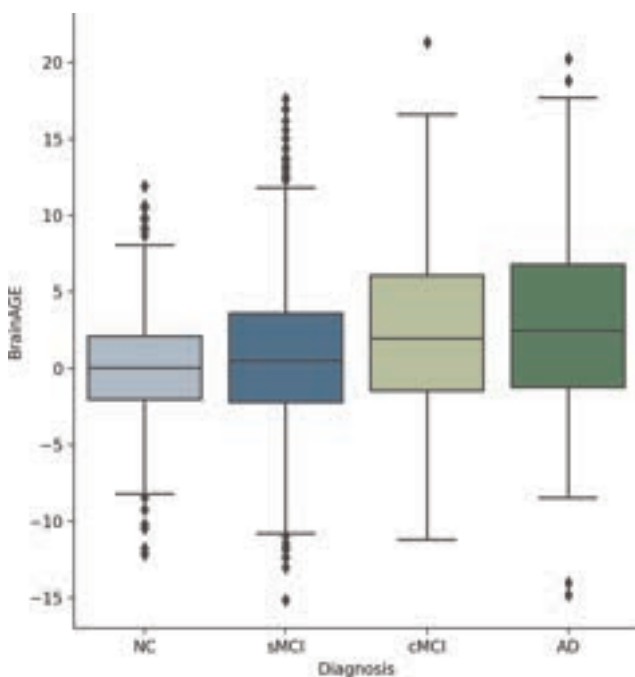


FIG 2. BrainAGE distributions.

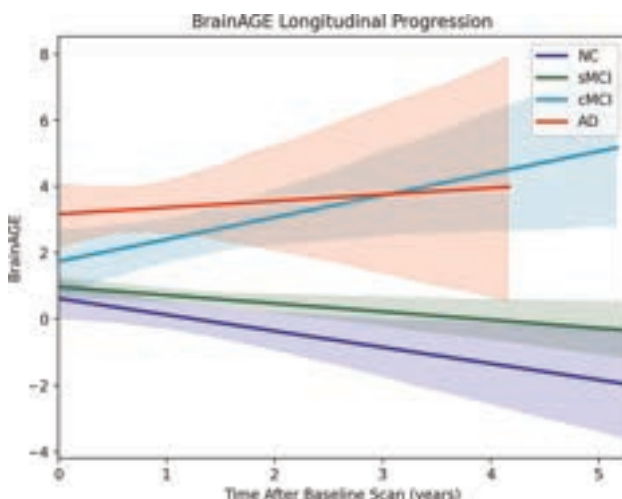
comparisons had significantly different BrainAGE except for the NC and sMCI comparison (Table 3).

BrainAGE versus time from baseline for each cognitive group is shown in Fig 3. ANOVA and Tukey post hoc tests were performed to investigate differences between slopes and intercepts of the BrainAGE-versus-time regressions across all cognitive groups. The only significant differences ($P < .05$) in BrainAGE slopes were found between cMCI and NC and cMCI and sMCI. All intercept comparisons with AD showed significant differences ($P < .01$). All slope comparisons showed a large effect size and practical significance ($d > 0.80$) except for the NC/sMCI and cMCI/AD comparisons. All AD intercept comparisons showed large effect sizes ($d > 0.80$). ANOVA and Tukey's post hoc results comparing slopes and intercepts are summarized in Table 4.

Table 5 shows the t test results comparing the mean BrainAGE of the cMCI group at 1-year time intervals with the entire sMCI data set. There were significant BrainAGE differences ($P < .05$) between sMCI and cMCI starting at time interval 2–3, which indicate that the biomarkers can detect cMCI 3–4 years before AD conversion (time point 5 represents 1 year before AD conversion, time point 4 is 2 years before conversion, and so forth). Significant differences ($P < .05$) also exist in time 3–4 and time 4–5 intervals for the sMCI–cMCI BrainAGE comparison. Correlation analysis

Table 3: ANOVA comparisons of BrainAGE

Comparison	P Value (Cohen's <i>d</i>)
NC vs sMCI	.30 (0.08)
NC vs cMCI	.03 (0.50)
NC vs AD	<.01 (0.91)
sMCI vs cMCI	<.01 (0.32)
sMCI vs AD	<.01 (0.63)
cMCI vs AD	<.01 (0.42)

**FIG 3.** BrainAGE comparison across time after baseline scans for all cognitive groups.**Table 4: ANOVA comparing slope and intercept of BrainAGE versus time^a**

Comparison	Slope Analysis (P Value) (Cohen's <i>d</i>)	Intercept Analysis (P Value) (Cohen's <i>d</i>)
NC vs sMCI	.66 (0.43)	.77 (0.30)
NC vs cMCI	.02 (2.29)	.29 (0.26)
NC vs AD	.16 (1.42)	<.01 (8.65)
sMCI vs cMCI	.04 (3.00)	.50 (0.18)
sMCI vs AD	.06 (1.90)	<.01 (9.03)
cMCI vs AD	.69 (0.42)	<.01 (7.02)

^a Cohen's *d* is the effect size.**Table 5: T test comparing BrainAGE of subjects with cMCI at 1-year intervals with sMCI data set^a**

Time before Conversion	P Value (Cohen's <i>d</i>)
5–6 yr	.19 (1.30)
4–5 yr	.35 (0.94)
3–4 yr	.04 (2.44)
2–3 yr	.02 (2.13)
1–2 yr	<.001 (3.47)

^a Cohen's *d* is the effect size.**Table 6: Results summary from the brain age prediction model**

Experiment	Results	Notes
Model validation	MAE = 2.46 yr	Existing work MAE = 4–13.5 yr
Cross-sectional ANOVA	$P < .01$	All comparisons except NC/sMCI
Longitudinal ANOVA (slopes)	$P < .05$	All cMCI comparisons except cMCI-AD
Longitudinal ANOVA (intercepts)	$P < .01$	All AD comparisons
1-year interval <i>t</i> tests	$P < .01$	sMCI/cMCI up to 4 years before conversion
Correlation analysis	$P < .05$	p-tau, $\alpha\beta$, APOE-4

was performed between the computed BrainAGE metric and the existing criterion standard AD conversion indicators p-tau and $\alpha\beta$ CSF biomarkers and the APOE-4 genotype. Significant correlation ($P < .05$) was found between each comparison. A complete summary of the results of each experiment is shown in Table 6.

DISCUSSION

This is the first work that uses FLAIR MR imaging biomarkers to predict the brain age of cognitively impaired subjects because T1-weighted MR imaging has been most commonly used in the past.^{9,29} Twelve biomarkers related to volume, intensity, and texture were extracted using previously validated tools.^{12,19–21} An RFC trained and validated on held out NC subjects was developed to distinguish between cognitive groups cross-sectionally and longitudinally.

The BrainAGE metric quantifies signs of accelerated aging using the 12 FLAIR-only biomarkers, which encapsulate various aging mechanisms. The volume biomarkers summarize global changes in volume as well as specific ROIs. The texture features measure the microstructural properties of the GM and WM, which are correlated with mean diffusivity and fractional anisotropy in DTI,¹⁴ while intensity features show signs of demyelination, edema, and ischemia.³⁰ The BrainAGE metric reduces the dimensionality of multiple features and summarizes the pathologic processes into a single value that successfully quantifies the amount of accelerated aging. Combining 12 different biomarkers accounts for the intersubject heterogeneity of AD progression.

The brain age prediction model validation yielded an MAE of 2.46 years between the corrected brain age and true age on a held out NC set, which is the lowest found in the literature when testing a dementia cohort. This finding demonstrates that the proposed FLAIR biomarkers provide a more accurate model compared with traditional approaches based on T1-weighted MR imaging. This result may be attributed to the unique insights FLAIR MR imaging provides, such as the ability to highlight white matter disease or increase LVV segmentation accuracy due to increased CSF-to-tissue contrast. There were significant differences in BrainAGE in all cross-sectional comparisons except NC/sMCI. Most notably, BrainAGE showed significant differences between sMCI and cMCI groups, demonstrating that FLAIR BrainAGE can identify high-risk subjects with MCI.

In the longitudinal analysis, the BrainAGE slope of the cMCI group showed significant differences compared with the NC and sMCI groups and no significant differences with the intercepts of NCs and subjects with sMCI. Therefore, at baseline, subjects with cMCI have profiles similar those of NCs and those with sMCI, but they neurodegenerate at an accelerated rate. Franke et al²⁶ demonstrated significant differences ($P < .050$) between the slope

of the BrainAGE-versus-time regression of NC/sMCI (group 1) and cMCI/AD (group 2), whereas the proposed model shows significant differences between the sMCI and cMCI groups specifically. This model is more applicable clinically because distinguishing between “low-risk” subjects with MCI (sMCI) and “high-risk” subjects with

MCI (cMCI) offers more value because appropriate intervention can prevent AD conversion. Interestingly, the cMCI group had a greater rate of change of BrainAGE in compared to the AD group. This further highlights the ability of this metric to identify high-risk subjects because they are progressing at a faster rate than subjects with AD.

These results coincide with findings in Bahsoun et al¹⁴ that the MCI cohort shows more rapid changes in some NABM texture and intensity features with age in compared to subjects with AD. While previous studies using T1-weighted MR imaging showed subjects with AD progressing at a faster rate than those with cMCI,²⁶ it is hypothesized that the increased rate of change of cMCI BrainAGE could be attributed to the unique biomarkers from FLAIR MR imaging. Using FLAIR NABM features in addition to established volume-based biomarkers uncovered the trend that subjects with cMCI have a greater rate of change in BrainAGE with time in compared to those with AD. Contrasted to NCs, sMCI, and cMCI, subjects with AD had a significantly higher baseline disease ($P < .05$). The BrainAGE of the AD group did not show significant slope differences between NC and sMCI groups, but there were significant differences when comparing intercepts. This finding indicates that baseline disease is higher in subjects with AD but that degeneration is at a rate similar to that of NCs and subjects with sMCI. No significant differences were found in any NC/sMCI comparisons, demonstrating that subjects with sMCI have neurodegenerative profiles similar to those of NCs. BrainAGE can perform longitudinal monitoring using a single value that encapsulates various dimensions of disease (volume, intensity, and texture). Otherwise, each individual biomarker would have to be monitored individually across time, and disease heterogeneity among patients would make it difficult to identify high-risk subjects on the basis of 12 different values.

To determine how far in advance the FLAIR-based BrainAGE showed differences between subjects with sMCI and cMCI, t tests were performed at 1-year intervals. There were significant differences between the sMCI and cMCI groups up to 4 years before conversion to AD. The earlier high-risk subjects are identified, the sooner a patient-specific neuroprotective treatment plan can be implemented. Existing brain age prediction models were able to predict AD conversion with adequate accuracy within 12 months' follow-up,⁹ but none reported the ability to distinguish between sMCI and cMCI in terms of years before conversion. Given the emergence of new AD therapies such as anti-amyloid antibodies³¹ and peptide-based biotherapeutics,³² using biomarkers to stratify patients into more homogeneous groups can help determine whom to treat on a preclinical level. On a clinical level, this stratification could lead to a reduction in the incidence of AD and an improvement in the quality of life of individuals with cognitive impairment.

Differences in BrainAGE between subjects with cMCI and sMCI, both cross-sectionally and longitudinally, demonstrate the value and potential of BrainAGE as a biomarker. To understand the relationship of the proposed BrainAGE biomarker to known pathologic mechanisms of AD, we correlated BrainAGE with p-tau and A β CSF biomarkers and the APOE-4 genotype. BrainAGE showed significant correlation ($P < .05$) with p-tau,

A β , and APOE-4. AD is characterized by an accumulation of p-tau and A β in various cortical regions of the brain,³³ while the APOE-4 protein helps transport different types of fat throughout the bloodstream. Recent studies have suggested that problems related to the ability of brain cells to process lipids may play a key role in the development of AD.³⁴ The significant correlations of the BrainAGE metric with all 3 of these criterion standard AD indicators demonstrate its strength in identifying these high-risk subjects.

Time normalization of the cMCI group may be considered a limitation of the longitudinal analysis as it is needed to align and analyze the progression of high-risk subjects as they approach AD conversion. Furthermore, the proposed metric should be analyzed with respect to clinical variables such as sex, lifestyle, socioeconomic status, and ethnicity. Although sex variables were available, the small cMCI sample size for the cMCI group would make it difficult to analyze sex-specific trends. In the future, we will consider adding data sets to further investigate these trends.

CONCLUSIONS

The BrainAGE metric demonstrates the ability to distinguish between subjects with sMCI and cMCI both cross-sectionally and longitudinally. The training of the brain age prediction model was performed on a held out NC data set. Doing so allowed the classifier to successfully identify subtle deviations from normal aging on diseased test samples and yielded BrainAGE values that showed significant differences among cognitive groups, most importantly between subjects with sMCI and cMCI. The brain age prediction model offers the ability to easily quantify the extent of the atypical aging into a single-valued metric while providing another method to distinguish among cognitive groups cross-sectionally and monitor accelerated aging longitudinally to identify, up to 4 years before conversion, subjects with MCI who are at an increased risk of developing AD. It can be concluded that this single-value metric successfully summarized the neuroanatomic state of the subjects, thus offering a maximally explainable and interpretable measure for the cognitive state of subjects both cross-sectionally and longitudinally. The BrainAGE metric showing significant differences between sMCI and cMCI up to 4 years before AD conversion is a major finding of this work. It would provide clinicians with the ability to make earlier diagnoses, thus giving them more time to intervene and help prevent further neurodegeneration toward the permanent damage caused by AD, leading to improving the quality of life for aging individuals and a reduction in AD prevalence.









Disclosure forms provided by the authors are available with the full text and PDF of this article at www.ajnr.org.

REFERENCES

1. Alzheimer's Association. **2017 Alzheimer's disease facts and figures.** *Alzheimers Dement* 2017;1:459–509 CrossRef
2. Mayeux R, Stern Y. **Epidemiology of Alzheimer disease.** *Cold Spring Harb Perspect Med* CrossRef
3. Brookmeyer R, Johnson E, Ziegler-Graham K, et al. **Forecasting the global burden of Alzheimer's disease.** *Alzheimers Dement* 2007;3:186–91 CrossRef Medline

4. Thung K, Yap P, Adeli E, et al; Alzheimer's Disease Neuroimaging Initiative. **Conversion and time-to-conversion predictions of mild cognitive impairment using low-rank affinity pursuit denoising and matrix completion.** *Med Image Anal* 2018;45:68–82 CrossRef Medline
5. Petersen R. **Mild cognitive impairment as a diagnostic entity.** *J Intern Med* 2004;256:183–94 CrossRef Medline
6. Gauthier S, Reisberg B, Zaudig M, et al; International Psychogeriatric Association Expert Conference on Mild Cognitive Impairment. **Mild cognitive impairment.** *Lancet* 2006;367:1262–70 CrossRef Medline
7. Marinescu RV, Bron EE, Oxtoby NP, et al. **Predicting Alzheimer's disease progression: results from the TADPOLE Challenge.** *Alzheimers Dement* 2020;16:1–6 CrossRef
8. Lopez-Otin C, Blasco MA, Partridge L, et al. **The hallmarks of aging.** *Cell* 2013;153:1194–217 CrossRef Medline
9. Franke K, Gaser C. **Ten years of BrainAGE as a neuroimaging biomarker of brain aging: what insights have we gained?** *Front Neurol* 2019;10:1–26 CrossRef Medline
10. Gaser C, Franke K, Klöppel S, et al; Alzheimer's Disease Neuroimaging Initiative. **BrainAGE in mild cognitive impaired patients: predicting the conversion to Alzheimer's disease.** *PLoS One* 2013;8:e67346 CrossRef Medline
11. DiGregorio J, Gibicar A, Khosravani H, et al. **Cross-sectional and longitudinal biomarker extraction and analysis for multicentre FLAIR brain MRI.** *Neuroimage: Reports* 2022;2:100091 CrossRef
12. Khademi A, Gibicar A, Arezza G, et al. **Segmentation of white matter lesions in multicentre FLAIR MRI.** *Neuroimage: Reports* 2021;1:1–29 CrossRef
13. Rocca MA, Battaglini M, Benedict RH, et al. **Brain MRI atrophy quantification in MS: from methods to clinical application.** *Neurology* 2017;88:403–13 CrossRef Medline
14. Bahsoun MA, Khan MU, Mitha S, et al. **FLAIR MRI biomarkers of the normal-appearing brain matter are related to cognition.** *Neuroimage Clin* 2022;34:102955 CrossRef Medline
15. Crystal O, Chan K, Khosravani H, et al. **Characterizing dementia using cross-sectional biomarkers from multicenter FLAIR MRI.** In: *Proceedings of the Annual Meeting of the American Society of Neuroradiology.* May 16–18, 2022. New York, New York
16. Chan K, Crystal O, Khosravani H, et al. **Texture biomarkers of the normal appearing brain matter in FLAIR are related to cognition.** In: *Proceedings of the Annual Meeting of the American Society of Neuroradiology.* May 16–18, 2022. New York, New York
17. Chan K, Fischer C, Khosravani H, et al. **FLAIR MRI biomarkers are related to APOE-4 status and A β 42 and Tau CSF markers.** In: *Proceedings of the Alzheimer's Association International Conference (AAIC).* August 3, 2022. San Diego, California
18. Jack CR Jr, Bernstein MA, Fox NC, et al. **The Alzheimer's Disease Neuroimaging Initiative (ADNI): MRI methods.** *J Magn Reson Imaging* 2008;27:685–91 CrossRef Medline
19. Reiche B, Moody AR, Khademi A. **Pathology-preserving intensity standardization framework for multi-institutional FLAIR MRI datasets.** *Magn Reson Imaging* 2019;62:59–69 CrossRef Medline
20. DiGregorio J, Arezza G, Gibicar A, et al. **Intracranial volume segmentation for neurodegenerative populations using multicentre FLAIR MRI.** *Neuroimage: Reports* 2021;1:100006 CrossRef
21. Crystal O, Maralani P, Black S, et al. **Domain adaptation using silver standard masks for lateral ventricle segmentation in FLAIR MRI.** In: *Proceedings of the International Conference on Machine Learning.* July 23–29, 2023. Honolulu, Hawaii
22. Cole JH. **Multimodality neuroimaging brain age in UK biobank: relationship to biomedical, lifestyle, and cognitive factors.** *Neurobiol Aging* 2020;92:34–42 CrossRef Medline
23. Le TT, Kuplicki RT, McKinney BA, et al; Tulsa 1000 Investigators. **A nonlinear simulation framework supports adjusting for age when analyzing BrainAGE.** *Front Aging Neurosci* 2018;10:317 CrossRef Medline
24. Liang H, Zhang F, Niu X. **Investigating systematic bias in brain age estimation with application to post-traumatic stress disorders.** *Hum Brain Mapp* 2019;40:3143–52 CrossRef Medline
25. de Lange AG, Cole JH. **Commentary: correction procedures in brain age prediction.** *Neuroimage Clin* 2020;26:102229 CrossRef Medline
26. Franke K, Gaser C; For the Alzheimer's Disease Neuroimaging Initiative. **Longitudinal changes in individual BrainAGE in healthy aging, mild cognitive impairment, and Alzheimer's disease.** *GeroPsych* 2012;25:235–45 CrossRef
27. Andersson C, Blennow K, Almkvist O, et al. **Increasing CSF phospho-tau levels during cognitive decline and progression to dementia.** *Neurobiol Aging* 2008;29:1466–73 CrossRef Medline
28. DeTure MA, Dickson DW. **The neuropathological diagnosis of Alzheimer's disease.** *Mol Neurodegener* 2019;14:32 CrossRef Medline
29. More S, Antonopoulos G, Hoffstaedter F, et al; Alzheimer's Disease Neuroimaging Initiative. **Brain age prediction: a systematic comparison of machine learning workflows.** *Neuroimage* 2023;270:119947 CrossRef Medline
30. Black S, Gao F, Bilbao J. **Understanding white matter disease: imaging-pathological correlations in vascular cognitive impairment.** *Stroke* 2009;40:S48–52 CrossRef Medline
31. Perneczky R, Jessen F, Grimmer T, et al. **Anti-amyloid antibody therapies in Alzheimer's disease.** *Brain* 2023;146:842–49 CrossRef Medline
32. Zhang X, Zhang X, Gao H, et al. **Phage display derived peptides for Alzheimer's disease therapy and diagnosis.** *Theranostics* 2022;12:2041–62 CrossRef Medline
33. Thal DR, Rüb U, Orantes M, et al. **Phases of A β -deposition in the human brain and its relevance for the development of AD.** *Neurology* 2002;58:1791–800 CrossRef Medline
34. Sienski G, Narayan P, Bonner JM, et al. **APOE-4 disrupts intracellular lipid homeostasis in human iPSC-derived glia.** *Sci Transl Med* 2021;13:eaaz4564 CrossRef Medline

Deep Learning–Based Synthetic TOF-MRA Generation Using Time-Resolved MRA in Fast Stroke Imaging

 Sung-Hye You,  Yongwon Cho,  Byungjun Kim,  Kyung-Sook Yang,  InSeong Kim,  Bo Kyu Kim,  Arim Pak, and  Sang Eun Park



ABSTRACT

BACKGROUND AND PURPOSE: Time-resolved MRA enables collateral evaluation in acute ischemic stroke with large-vessel occlusion; however, a low SNR and spatial resolution impede the diagnosis of vascular occlusion. We developed a CycleGAN-based deep learning model to generate high-resolution synthetic TOF-MRA images using time-resolved MRA and evaluated its image quality and clinical efficacy.

MATERIALS AND METHODS: This retrospective, single-center study included 397 patients who underwent both TOF- and time-resolved MRA between April 2021 and January 2022. Patients were divided into 2 groups for model development and image-quality validation. Image quality was evaluated qualitatively and quantitatively with 3 sequences. A multireader diagnostic optimality evaluation was performed by 16 radiologists. For clinical validation, we evaluated 123 patients who underwent fast stroke MR imaging to assess acute ischemic stroke. The diagnostic confidence level and decision time for large-vessel occlusion were also evaluated.

RESULTS: Median values of overall image quality, noise, sharpness, venous contamination, and SNR for M1, M2, the basilar artery, and posterior cerebral artery are better with synthetic TOF than with time-resolved MRA. However, with respect to real TOF, synthetic TOF presents worse median values of overall image quality, sharpness, vascular conspicuity, and SNR for M3, the basilar artery, and the posterior cerebral artery. During the multireader evaluation, radiologists could not discriminate synthetic TOF images from TOF images. During clinical validation, both readers demonstrated increases in diagnostic confidence levels and decreases in decision time.

CONCLUSIONS: A CycleGAN-based deep learning model was developed to generate synthetic TOF from time-resolved MRA. Synthetic TOF can potentially assist in the detection of large-vessel occlusion in stroke centers using time-resolved MRA.

ABBREVIATIONS: AdaLIN = Adaptive Layer-Instance Normalization; AIS = acute ischemic stroke; BA = basilar artery; EMT = endovascular mechanical thrombectomy; GAN = generative adversarial network; IQR = interquartile range; LVO = large-vessel occlusion; PCA = posterior cerebral artery; PSNR = peak SNR; synTOF = synthetic TOF; SSIM = structural similarity index measurement; TR = time-resolved

The primary goal of performing MRA in acute ischemic stroke (AIS) is to identify the presence of large-vessel occlusion


Received April 12, 2023; accepted after revision October 17.

From the Department of Radiology, (S.-H.Y., B.K., B.K.K., A.P., S.E.P.), Anam Hospital, Korea University College of Medicine, Seoul, Korea; Biomedical Research Center (Y.C.) and Department of Biostatistics (K.-S.Y.), Korea University College of Medicine, Seoul, Korea; and Siemens Healthineers (I.K.), Seoul, Korea.

S.-H. You and Y. Cho contributed equally to this study.

This study was supported by the Basic Science Research Program through the National Research Foundation of Korea, funded by the Ministry of Education (grant No. 2021R11A1A01050316); a grant from the Korea Health Technology R&D Project through the Korea Health Industry Development Institute, funded by Ministry of Health and Welfare, Republic of Korea (grant No. HR22CI302); and a Korea University grant (grant No. K2225761).

Please address correspondence to Byungjun Kim, MD, PhD, Department of Radiology, Anam Hospital, Korea University College of Medicine, 126-1, 5-Ka Anam-dong, Sungbuk ku, Seoul 136-705, Korea; e-mail: bjl492.kim@gmail.com

 Indicates article with online supplemental data.

<http://dx.doi.org/10.3174/ajnr.A8063>

(LVO), while the secondary objective is to assess the collateral status. Collateral status is the main factor determining how rapidly the penumbral tissue progresses to an irreversible infarct core.¹ Recent studies have revealed the significance of collateral imaging in selecting eligible patients for endovascular mechanical thrombectomy (EMT) in the late window, determining the need for transferring the patient to an EMT-capable hospital, predicting prognosis, and determining stroke etiology.^{1–6} Therefore, the American Heart Association/American Stroke Association 2019 guidelines suggest that incorporating collateral flow status into the clinical decision-making process for eligible candidates may help determine their eligibility for EMT.⁷

Time-resolved (TR) MRA enables the noninvasive evaluation of collateral status. A set of images is sequentially acquired at multiple time points while the contrast agent passes through the target vessel (Online Supplemental Data).^{8–11} Several existing techniques for TR-MRA, including time-resolved imaging of

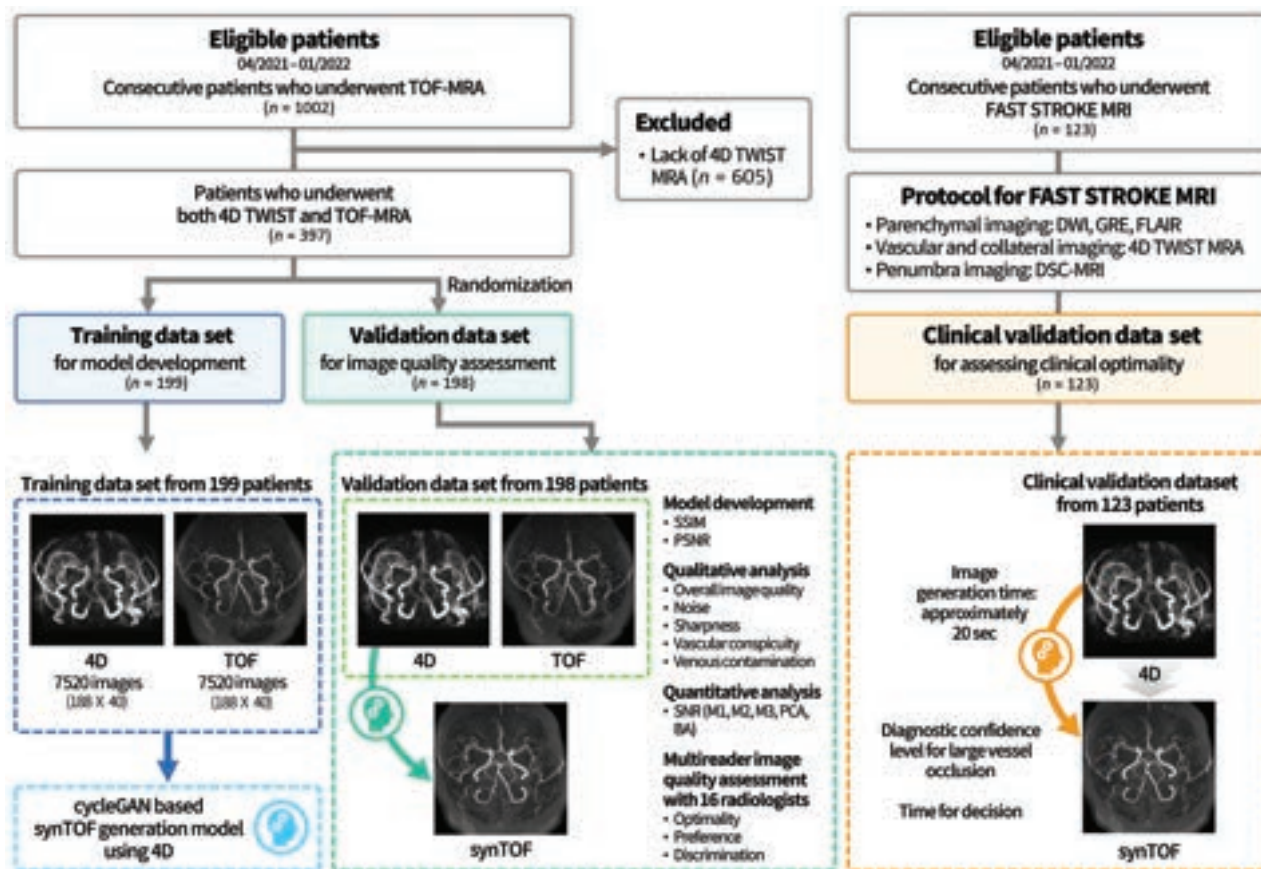


FIG 1. Study design. GRE indicates gradient recalled-echo.

contrast kinetics (TRICKS; GE Healthcare) and time-resolved imaging with stochastic trajectories (TWIST; Siemens), use center-weighted keyhole imaging and peripheral undersampling.¹² This method is particularly useful for evaluating the collateral or retrograde flow that occurs around stenoses. Nevertheless, compared with TOF-MRA, the inherent SNR penalties associated with undersampling and acceleration techniques further hinder the attainable spatial resolution of TR-MRA, thereby diminishing its usefulness in the assessment of LVO.^{9,13}

The cycle-consistent generative adversarial network (GAN) (CycleGAN; <https://github.com/junyanz/CycleGAN>), which is a deep learning algorithm, aims to improve image quality through learning between high-quality and low-quality images.¹⁴⁻¹⁹ The purpose of this study was to develop a CycleGAN model that generates high-quality synthetic TOF (synTOF) images from low-quality TR-MRA peak arterial phase images and to verify the clinical efficacy of synTOF in diagnosing LVO.

MATERIALS AND METHODS

Patient Selection

This retrospective study was approved by the institutional review board (Korea University Anam Hospital), and the need for informed consent was waived due to its retrospective design. Our study cohort included 1002 patients who underwent TOF-MRA from April 2021 to January 2022. Among them, 397 patients (mean age, 66.94 [SD, 13.79] years, 43.6% women [173/397]) underwent both TOF- and TR-MRA to evaluate their collateral

statuses (Fig 1). These 397 patients were divided into a training data set for model development (50.1%, [199/397]; mean age, 66.36 [SD, 14.02] years; 43.7% women [87/199]) and a validation data set for image-quality assessment [49.9%, [198/397]; mean age, 67.58 [SD, 13.56] years; 43.4% women (86/198)]. For clinical validation, 123 patients (mean age, 72.85 [SD, 11.24] years; 41.5% women [51/123]) who underwent fast stroke MR imaging (FLAIR, DWI, perfusion MR imaging, and TR-MRA) to evaluate AIS during the same period were included in this study. Clinical information, such as sex, age, reason for fast stroke MR imaging, location of the AIS, and the LVO site, was collected.

Image Acquisition

MR imaging was performed with two 3T MR imaging scanners (Magnetom Skyra and Magnetom Prisma; Siemens) using a 64-channel head and neck coil. The specific imaging parameters for TOF- and TR-MRA (TWIST) are listed in the Online Supplementary Data. After we obtained a pre-enhancement image, 30 consecutive T1WI 3D data sets were acquired in the coronal plane after automatic injection of 0.2 mL/kg of gadoteridol (ProHance; Bracco), followed by 30 mL of saline. Both sequences were performed in the same session.

Among the dynamic images, the peak arterial phase images were selected to evaluate LVO. MIP images (40 images [anteroposterior 20, lateral 20]) of TOF- and TR-MRA were automatically created under the same conditions by Siemens 3D software (Syngo.via; Siemens Healthineers, Forchheim, Germany).

Model Development

Training Stage. A schematic diagram of the network architecture and model details are shown in the Online Supplementary Data. This model was developed with paired TR-TOF MIP imaging sets from 199 patients. It includes 2 generators and discriminators, 4 loss functions, and a gradient-weighted class activation map (GradCAM; <https://medium.com/the-owl/gradcam-in-pytorch-7b700caa79e5>). The basic architecture was based on an unsupervised generative attention network with Adaptive Layer-Instance Normalization (AdaLIN) for image-to-image translation and was customized to improve model performance (<https://github.com/taki0112/UGATIT>). The encoder is composed of 2 convolution layers (2D, kernel size: 3) with a stride size of 2 for downsampling and 4 residual blocks. The decoder consists of 4 residual blocks and 2 upsampling convolution layers (2D, kernel size: 3) with a stride size of 1. We used instance normalization for the encoder and AdaLIN for the decoder. Hyperparameters used in various training settings are listed in the Online Supplementary Data. GradCAM was incorporated into the foundational CycleGAN model to enable selective attention on specific areas of the image after testing improvement in terms of the structural similarity index measurement (SSIM) in 10 patients randomly selected from the validation data set (Online Supplementary Data). The same 150 training epochs were applied to all cases.

Validation Stage. The performance of the developed model to generate synTOF (GTOF) was assessed using the peak SNR (PSNR) and SSIM as metrics, defined as follows:²⁰

$$\text{PSNR}(x, y) = 20 \log_{10} \frac{\text{MAX}_x}{\|x - y\|_2}.$$
$$\text{SSIM}(x, y) = \frac{(2\mu_x\mu_y + C_1)(2\sigma_{xy} + C_2)}{(\mu_x^2 + \mu_y^2 + C_1)(\sigma_x^2 + \sigma_y^2 + C_2)}.$$

Image Interpretation

Image-Quality Evaluation (Qualitative and Quantitative Analysis). Two neuroradiologists (S.E.P and S.-H.Y., with 6 and 11 years of neuroradiologic experience) evaluated the image quality of the validation data set: 594 imaging sets (198 × 3 [TR-MRA, synTOF, and TOF]) from 198 patients (Online Supplementary Data). Each image set consisted of 40 anonymized MIP images and was evaluated through a PACS. Regarding disagreements in the qualitative evaluation, the final result was determined through a consensus meeting with 3 neuroradiologists, including another experienced neuroradiologist (B.K., with 17 years of experience in neuroradiology). The mean value from the 2 readers was used in the quantitative analysis. A 5-point Likert scale was used to evaluate each kind of image-quality parameter (Online Supplementary Data). For quantitative analysis, crucial ROIs were manually located at each vessel, demonstrating the highest signal intensity in the MIP image anterior-posterior view. The SNRs were calculated in the M1, M2, M3, posterior cerebral artery (PCA), and basilar arteries (BAs) (mean signal intensity/SD of the background SI).

Diagnostic Performance for Intracranial Aneurysm and Stenosis Detection. The same neuroradiologists who performed image-quality evaluation assessed the presence of aneurysms (largest

lesion) and intracranial arterial stenoses (most stenotic lesion, exceeding a moderate degree). Another neuroradiologist (B.K., with 17 years of experience in neuroradiology) evaluated both diseases using TOF and VICAST criteria.²¹

Multireader Image-Optimality Test with 16 Radiologists. Sixteen radiologists (7 and 9 neuroradiologists with 1–18 years of radiologic experience) evaluated imaging sets from 20 randomly chosen patients in the validation data set. Three image sequences of a patient were randomly arranged and shown simultaneously; then, we asked the following 3 tasks: 1) imaging optimality: select all the imaging sequences suitable for interpretation; 2) image preference: select the best MRA sequence subjectively perceived as optimal for interpretation; and 3) image discrimination: choose 1 MRA sequence that is highly likely to be a genuine TOF.

Assessment of Diagnostic Confidence Level and Decision Time for LVO in Fast Stroke MR Imaging. For the 123 patients who underwent fast stroke MR imaging, 2 neuroradiologists (B.K.K. and S.E.P., with 12 and 6 years of experience in neuroradiology, respectively) independently graded the diagnostic confidence level for intracranial LVO on the basis of a 5-point Likert scale. The time for the decision was defined as the difference between the time when each MRA image was opened and the time when the decision for LVO was made by the neuroradiologist. In the first session, 2 neuroradiologists evaluated the diagnostic confidence level and decision time using only TR-MRA. After 1 month, both were assessed using TR-MRA and synTOF-MRA simultaneously by the same neuroradiologist.

Statistical Analysis. The normality of the data distribution was assessed for each parameter using the Kolmogorov-Smirnov test. Patient data are reported as percentage (%), mean (SD), or median (interquartile range, [IQR]). The significance level of $P < .05$ was used to consider statistical significance. A Bonferroni correction was applied for post hoc analysis, in which the adjusted P value was multiplied by the number of comparisons made. The Friedman test was used to compare >3 non-normally distributed continuous variables, including qualitative and quantitative image-quality analyses and the diagnostic optimality tests. The McNemar-Bowker test was used to compare the distribution of confidence levels between the 2 different imaging sets and the diagnostic performance of 3 imaging sets. The Wilcoxon test was used to compare the nonparametric equivalents of the paired samples, specifically the median values of the diagnostic confidence level and time for decision. Interobserver agreement was assessed on the basis of the analysis of weighted κ values (qualitative analysis) or intraclass correlation coefficients (quantitative analysis).

MedCalc for Windows (Version 20.218; MedCalc Software) and SPSS Statistics software (Version 22.0; IBM) were used for all statistical analyses.

RESULTS

Patient Characteristics

Baseline patient characteristics of the model development and clinical validation data sets are listed in Table 1. In the clinical validation data set, 56 patients (45.5%, 56/123) showed acute ischemic infarction on DWI. Intracranial LVO was present in 25 patients (20.33%).

Table 1: Clinical characteristics of the patients

	Model Development		
	Training Data Set	Validation Data Set	Total
No. of patients	199	198	397
Age (mean) (yr)	66.36 (SD, 14.02)	67.58 (SD, 13.56)	66.97 (SD, 13.79)
Female	87 (43.7%)	86 (43.4%)	173 (43.6%)
Clinical validation			
No. of patients		123	
Age (mean) (yr)		72.85 (SD, 11.24)	
No. women		51 (41.5%)	
Reason for fast stroke MR imaging			
Mental change		53 (43.1%)	
Right-sided weakness		12 (9.8%)	
Left-sided weakness		18 (14.6%)	
Dysarthria		23 (18.7%)	
Dizziness		3 (2.4%)	
Facial palsy		4 (3.3%)	
Visual disturbance		3 (2.4%)	
Seizure		5 (4.1%)	
Syncope		2 (1.6%)	
Acute ischemic stroke			
None		67 (54.5%)	
ACA territory		4 (3.3%)	
MCA territory		30 (24.4%)	
PCA territory		2 (1.6%)	
BA/VA territory		12 (9.8%)	
Multiterritorial		8 (6.5%)	
LVO			
None		98 (79.7%)	
ICA		9 (7.3%)	
ACA		1 (0.8%)	
MCA (M1)		6 (4.9%)	
MCA (M2)		6 (4.9%)	
PCA		1 (0.8%)	
BA/VA		2 (1.6%)	
No. performing DSA		10 (8.1%)	

Note:—ACA indicates anterior cerebral artery; VA, vertebral artery.

Model Development

The median values and IQR of SSIM and PSNR between synTOF and TOF were 0.67 (0.65–0.69) and 15.56 (14.82–16.42) dB, respectively (Online Supplemental Data).

Qualitative Assessment

Qualitative analysis results are presented in the Online Supplemental Data. The synTOF showed significantly higher median values on the 5-point Likert scale compared with TR in all the following parameters: overall image quality, noise, sharpness, and venous contamination ($P < .001$). In comparison with real TOF, synTOF has lower median values in overall image quality, sharpness, and vascular conspicuity ($P < .001$). The interobserver agreement for all 5 parameters was substantial or excellent (weighted $\kappa > 0.700$) (Online Supplemental Data).

Quantitative Assessment

The Online Supplemental Data demonstrate the results of the quantitative analysis. The SNRs of the synTOF in the MCA (M1 and M2 segments) and BA were significantly higher than those in the TR ($P < .001$) in contrast to the M3 segment ($P = 1.000$). Compared with TOF, the SNRs of synTOF were significantly lower for the M3, BA, and PCA ($P < .001$), with no significant differences for M1 ($P = 1.000$) and M2 ($P = .358$). The interobserver

agreement for all values was excellent (intraclass correlation coefficient > 0.800) (Online Supplemental Data).

Diagnostic Performance for Intracranial Aneurysm and Stenosis Detection

The sensitivity in aneurysm detection for both 4D and synTOF was 50% (Online Supplemental Data). The aneurysm height for all false-negative cases was < 2 mm. The sensitivity in stenosis detection for 4D and synTOF was 75% and 86%, respectively. The diagnostic performance of both diseases was significantly lower than that of TOF ($P < .05$). No significant differences existed between 4D and synTOF (P values; aneurysm = 1.000; stenosis = .063). Representative images are shown in the Online Supplemental Data.

Multireader Imaging-Optimality Evaluation

The results for multireader image-optimality assessment for the 3 questions are presented in the Online Supplemental Data. For the first question, which pertained to imaging optimality for reading, no statistically significant difference was observed between the values for synTOF and real TOF imaging techniques, and both were significantly higher than those obtained using TR (TR versus synTOF

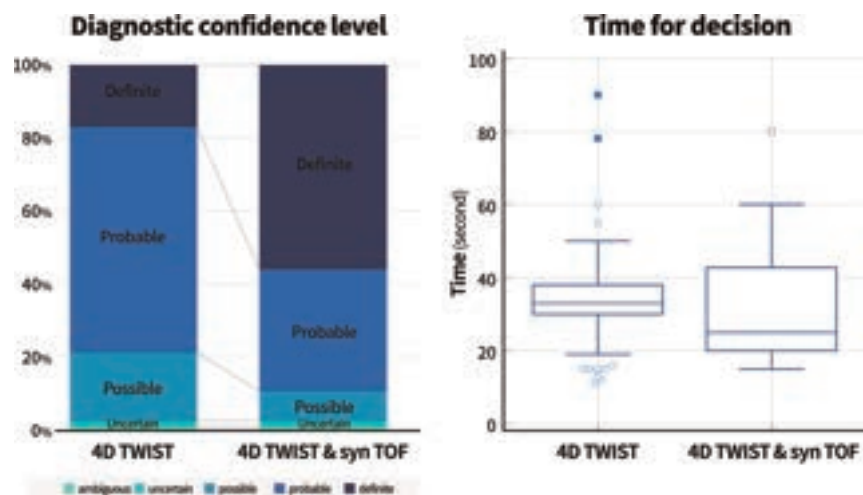
versus TOF; median [IQR]; 0.50 [0.00–2.00] versus 20.00 [18.00–20.00] versus 20.00 [18.50–20.00], $P = 1.000$). With respect to imaging preference, no statistically significant difference was observed between the values for synTOF (median, 4.50 [IQR, 4.00–9.50]) and TOF (median, 15.50 [IQR, 10.00–16.00]) ($P = .279$). Finally, for the last question, which aimed to select real TOF images, no statistically significant difference was observed between the values for synTOF (median, 10.00 [IQR, 3.50–16.00]) and TOF (median, 9.00 [IQR, 3.00–16.50]) ($P = 1.000$).

Diagnostic Confidence Level and Decision Time for LVO in Fast Stroke MR Imaging

Table 2 and Fig 2 present the results of the diagnostic confidence level and decision time for LVO. The diagnostic confidence levels were significantly higher for readers 1 and 2 when they determined LVO with both TR and synTOF images than with TR-only (TR and synTOF versus TR-only; reader 1: median, 5.00 [IQR, 4.00–5.00] versus 4.00 [IQR, 4.00–4.00]; reader 2: median, 5.00 [IQR, 4.00–5.00] versus 4.00 [IQR, 3.00–4.00], $P < .001$). The median values of decision time were significantly shorter in the TR and synTOF reading sessions than in the TR session (TR and synTOF versus TR-only; reader one: 25.00 [IQR, 20.00–42.75] versus 33.00 [IQR, 30.00–38.00], $P = .004$; reader two: 25.00 [IQR, 22.00–38.00] versus 39.00 [IQR, 30.00–50.00], $P < .001$).

Table 2: Diagnostic confidence level of TR-alone versus TR and synTOF

	TR	TR and synTOF	P Value
No. of patients	123	123	
Reader 1			
Confidence level			<.001 ^a
5 (Definite)	21 (17.1%)	69 (56.1%)	
4 (Probable)	76 (61.8%)	41 (33.3%)	
3 (Possible)	23 (18.7%)	10 (8.1%)	
2 (Uncertain)	2 (1.6%)	2 (1.6%)	
1 (Ambiguous)	1 (0.8%)	1 (0.8%)	
Median (IQR)	4.00 (4.00–4.00)	5.00 (4.00–5.00)	<.001 ^b
Time for decision (median) (IQR) (sec)	33.00 (30.00–38.00)	25.00 (20.00–42.75)	.004 ^b
Reader 2			
Confidence level			<.001 ^a
5 (Definite)	17 (13.8%)	69 (56.1%)	
4 (Probable)	71 (57.7%)	44 (35.8%)	
3 (Possible)	25 (20.3%)	7 (5.7%)	
2 (Uncertain)	7 (5.7%)	2 (1.6%)	
1 (Ambiguous)	3 (2.4%)	1 (0.8%)	
Median (IQR)	4.00 (3.00–4.00)	5.00 (4.00–5.00)	<.001 ^b
Time for decision (median) (IQR) (sec)	39.00 (30.00–50.00)	25.00 (22.00–38.00)	<.001 ^b

^a McNemar-Bowker test was performed.^b Wilcoxon test was performed.**FIG 2.** Diagnostic confidence level of TR-MRA-only versus TR-MRA and synTOF.

Representative TR-MRA, synTOF, and TOF images are shown in Fig 3.

DISCUSSION

The major findings of this study are summarized as follows. 1) A high-resolution synTOF generation model based on CycleGAN was developed for the diagnosis of LVO in AIS. 2) In comparison with TR-MRA, synTOF achieves a statistically significant reduction in noise and improvement in sharpness. 3) The model performance is excellent in terms of SNR improvement for M1, M2, BA, and PCA. 4) SynTOF does not accomplish equivalent image quality compared with TOF except for noise, venous contamination, and SNR of M1/M2. 5) SynTOF features limited the performance in detecting intracranial aneurysms and stenoses. 6) The combined use of both synTOF and TR-MRA has the potential to enhance diagnostic confidence and decrease decision time for the diagnosis of LVO in AIS for distal ICA to M2 occlusion.

CycleGAN: Deep Learning Algorithm for Intersequence Image Transfer

Our deep learning model improved the image quality of TR-MRA. This may have been influenced by 2 factors: the use of proper target images (TOF-MRA) and the effectiveness of the CycleGAN algorithm. TOF-MRA is the most commonly used intracranial MRA sequence with high image quality, and neuroradiologists are familiar with its image contrast.²² Therefore, we hypothesized that paired TOF images serve as a valuable guide for enhancing the image quality of TR-MRA. CycleGAN was selected for training because of its recognized capability of intersequence transfer. The GAN was designed to generate new images through simultaneous training of the generator and discriminator networks.^{19,23} In our study, CycleGAN, a modified version of the GAN with 2 generators and discriminators, was used to prevent mode collapse. Additionally, GradCAM was introduced into the model to drive the focus of the generator and discriminator toward meaningful regions of the images. An effective algorithm and an appropriate target image may have contributed to the favorable performance of the model.

Clinical Application of synTOF in AIS

The use of MRA has 2 objectives in AIS: diagnosis of LVO and assessment of collateral status.⁷ Considering the first objective and image quality, TOF-MRA was deemed the most suitable method. However, it may not be possible to perform owing to the long scan

time. Furthermore, TOF-MRA does not provide adequate information regarding the aortic and proximal cervical arteries, which are technically important for EMT. Single-phase contrast-enhanced MRA offers the advantage of a large FOV and short scan time; however, it is also known to underestimate the collateral status.^{24,25} TR-MRA is considered the most suitable option for the secondary objective of AIS evaluation, but challenges in attaining maximum efficiency for the primary purpose, owing to limitations in both spatial resolution and SNR, are unavoidable. Our results indicate that the use of synTOF significantly improved the diagnostic confidence level for LVO and reduced the decision time. Thus, in instances in which real TOF acquisition is impeded by time constraints, synTOF images from TR-MRA may serve as valuable additional high-resolution images for the initial evaluation of AIS. However, the diagnostic performance of synTOF in aneurysm and stenosis detection is still limited.

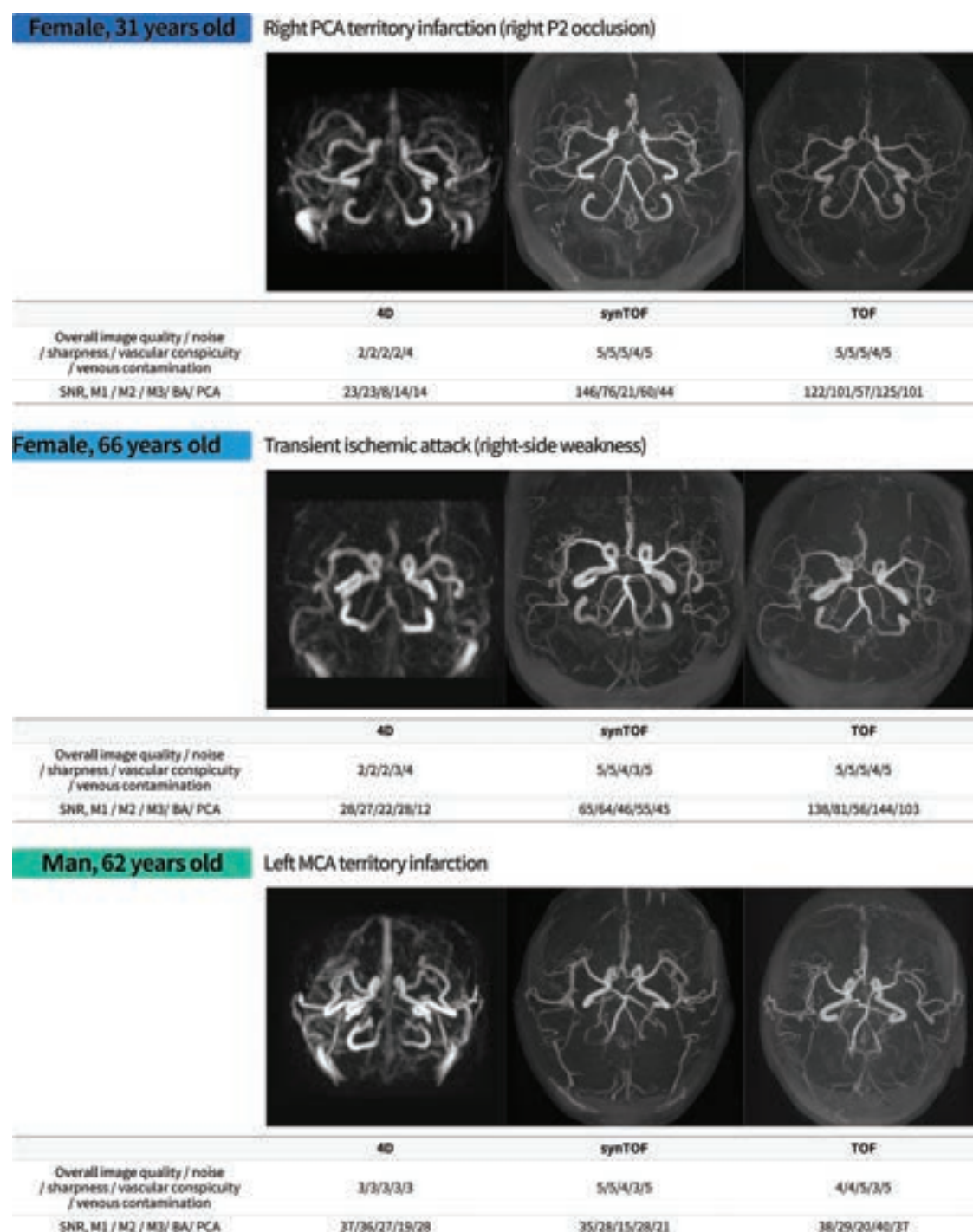


FIG 3. Representative images of TR-MRA, synTOF, and TOF.

CT versus an MR Imaging–Based Protocol for AIS

Two distinct imaging protocols, namely CT and MR imaging, are used for AIS evaluation. The preference in most stroke centers is CT for AIS evaluation, driven by its predominant advantages over MR imaging, such as rapid acquisition, widespread availability, and cost-effectiveness. A previous study with 36 tertiary hospitals reported that approximately 70% of stroke centers have adopted CT-based protocols.²⁶ Additionally, CTA, including the delayed phase, offers the highest image resolution for evaluating

LVO and collateral status. Nevertheless, some centers have explored the use of MR imaging owing to its unique strengths: 1) high accuracy for core infarction, 2) estimation of the onset time in wake-up strokes, 3) effective identification of stroke-mimic conditions, and 4) lack of radiation. In our center, we use a 6-minute MR imaging–based protocol for patients with presumed in-hospital stroke, and the results of our study may benefit MR imaging–based stroke centers. Considering the different goals of deep learning–based image-quality improvement

in MR imaging and CT, namely scan time reduction and radiation reduction, respectively, the advantage of CT-based protocols will be boosted by further deep learning-based studies to reduce the radiation and contrast dose while maintaining the image quality.

Limitations

First, the study was a retrospective single-center one. Second, multiobserver imaging evaluation was performed on limited patients, which could have impacted the generalizability of the results. Third, this study had a limitation in that it focused only on a single field strength (3T) and a single vendor sequence (TWIST). Fourth, the number of patients in the clinical validation group with AIS on DWI and LVO on MRA was relatively low, because our hospital only uses an MR imaging-based stroke protocol for inpatient strokes and a CT-based protocol at the emergency stroke center. Additionally, only 3 cases of LVO were included for the posterior circulation. Thus, further studies that include a larger number of patients are needed to determine the usefulness of synTOF in posterior circulation occlusion. Fifth, this model was developed using MIP images rather than raw data. This model is effective for LVO detection. However, raw-data images are essential for a confirmative diagnosis of stenoses and aneurysms. Further studies using raw data and another algorithm should be conducted. Sixth, owing to the widespread use of CT-based protocols in AIS evaluation, the applicability of our research findings is limited. They could be applied only to stroke centers that follow an MR imaging-based protocol. Further studies regarding image-quality improvement through reduction of the radiation dose in CT-based protocols will be needed. Seventh, we did not perform quantitative analysis for vascular sharpness. A reliable quantitative measuring method for sharpness should be developed because resolution enhancement may, essentially, affect image-quality improvement. Finally, DSA was performed on a limited number of patients, precluding a thorough evaluation of the diagnostic accuracy of synTOF- and TR-MRA.

CONCLUSIONS

In this study, we developed a CycleGAN-based deep learning model aimed at generating a synTOF with improved resolution and SNR. Despite the good image quality of TOF, it is often not performed for AIS because of the long scan time. TR-MRA with additional deep learning-based synTOF has the potential to effectively achieve both goals of initial stroke evaluation: accurate and rapid diagnosis of LVO and proper evaluation of collateral circulation.








Disclosure forms provided by the authors are available with the full text and PDF of this article at www.ajnr.org.

REFERENCES

- Berkhemer OA, Jansen IG, Beumer D, et al; MR CLEAN Investigators. Collateral status on baseline computed tomographic angiography and intra-arterial treatment effect in patients with proximal anterior circulation stroke. *Stroke* 2016;47:768–76 CrossRef Medline
- Menon BK, Qazi E, Nambiar V, et al; Interventional Management of Stroke III Investigators. Differential effect of baseline computed tomographic angiography collaterals on clinical outcome in patients enrolled in the Interventional Management of Stroke III trial. *Stroke* 2015;46:1239–44 CrossRef Medline
- Goyal M, Demchuk AM, Menon BK, et al; ESCAPE Trial Investigators. Randomized assessment of rapid endovascular treatment of ischemic stroke. *N Engl J Med* 2015;372:1019–30 CrossRef Medline
- Menon BK, d'Este CD, Qazi EM, et al. Multiphase CT angiography: a new tool for the imaging triage of patients with acute ischemic stroke. *Radiology* 2015;275:510–20 CrossRef Medline
- van den Wijngaard IR, Holswilder G, Wermer MJ, et al. Assessment of collateral status by dynamic CT angiography in acute MCA stroke: timing of acquisition and relationship with final infarct volume. *AJNR Am J Neuroradiol* 2016;37:1231–36 CrossRef Medline
- van den Wijngaard IR, Boiten J, Holswilder G, et al. Impact of collateral status evaluated by dynamic computed tomographic angiography on clinical outcome in patients with ischemic stroke. *Stroke* 2015;46:3398–404 CrossRef Medline
- Powers WJ, Rabinstein AA, Ackerson T, et al. Guidelines for the Early Management of Patients With Acute Ischemic Stroke: 2019 Update to the 2018 Guidelines for the Early Management of Acute Ischemic Stroke: A Guideline for Healthcare Professionals From the American Heart Association/American Stroke Association. *Stroke* 2019;50:e344–418 CrossRef Medline
- Hernández-Pérez M, Puig J, Blasco G, et al. Dynamic magnetic resonance angiography provides collateral circulation and hemodynamic information in acute ischemic stroke. *Stroke* 2016;47:531–34 CrossRef Medline
- Nael K, Sakai Y, Khatri P, et al. Imaging-based selection for endovascular treatment in stroke. *Radiographics* 2019;39:1696–713 CrossRef Medline
- Roh HG, Kim EY, Kim IS, et al. A novel collateral imaging method derived from time-resolved dynamic contrast-enhanced MR angiography in acute ischemic stroke: a pilot study. *AJNR Am J Neuroradiol* 2019;40:946–53 CrossRef Medline
- Kim HJ, Lee SB, Choi JW, et al. Multiphase MR angiography collateral map: functional outcome after acute anterior circulation ischemic stroke. *Radiology* 2020;295:192–201 CrossRef Medline
- Sakata A, Sakamoto R, Fushimi Y, et al. Low-dose contrast-enhanced time-resolved angiography with stochastic trajectories with iterative reconstruction (IT-TWIST-MRA) in brain arteriovenous shunt. *Eur Radiol* 2022;32:5392–401 CrossRef Medline
- Goldman-Yassen AE, Raz E, Borja MJ, et al. Highly time-resolved 4D MR angiography using golden-angle radial sparse parallel (GRASP) MRI. *Sci Rep* 2022;12:15099 CrossRef Medline
- Sorin V, Barash Y, Konen E, et al. Creating artificial images for radiology applications using generative adversarial networks (GANs): a systematic review. *Acad Radiol* 2020;27:1175–85 CrossRef Medline
- Finck T, Li H, Grundl L, et al. Deep-learning generated synthetic double inversion recovery images improve multiple sclerosis lesion detection. *Invest Radiol* 2020;55:318–23 CrossRef Medline
- Pang H, Qi S, Wu Y, et al. NCCT-CECT image synthesizers and their application to pulmonary vessel segmentation. *Comput Methods Programs Biomed* 2023;231:107389 CrossRef Medline
- You SH, Cho Y, Kim B, et al. Synthetic time of flight magnetic resonance angiography generation model based on cycle-consistent generative adversarial network using PETRA-MRA in the patients with treated intracranial aneurysm. *J Magn Reson Imaging* 2022;56:1513–28 CrossRef Medline
- Matsuo H, Nishio M, Nogami M, et al. Unsupervised-learning-based method for chest MRI-CT transformation using structure constrained unsupervised generative attention networks. *Sci Rep* 2022;12:11090 CrossRef Medline
- Wang R, Bashyam V, Yang Z, et al. Applications of generative adversarial networks in neuroimaging and clinical neuroscience. *Neuroimage* 2023;269:119898 CrossRef Medline
- Wang Z, Bovik AC, Sheikh HR, et al. Image quality assessment: from error visibility to structural similarity. *IEEE Trans Image Process* 2004;13:600–12 CrossRef Medline

21. You SH, Kim B, Yang K-S, et al. **Development and validation of visual grading system for stenosis in intracranial atherosclerotic disease on time-of-flight magnetic resonance angiography.** *Eur Radiol* 2022;32:2781–90 CrossRef Medline
22. Johnson KM. **Neurovascular magnetic resonance angiography.** In: *Advances in Magnetic Resonance Technology and Applications*. Volume 4, Chap 30. Elsevier; 2021:469–83
23. Goodfellow I, Pouget-Abadie J, Mirza M, et al. **Generative adversarial nets.** In: Ghahramani Z Welling M Cortes C, eds, et al. *Advances in Neural Information Processing Systems (NIPS 2014)*. December 8–13, 2014. Montreal, Quebec, Canada
24. Ravindran AV, Killingsworth MC, Bhaskar S. **Cerebral collaterals in acute ischaemia: Implications for acute ischaemic stroke patients receiving reperfusion therapy.** *Eur J Neurosci* 2021;53:1238–61 CrossRef Medline
25. Wieggers EJ, Mulder MJ, Jansen IG, et al; MR CLEAN Trial and MR CLEAN Registry Investigators. **Clinical and imaging determinants of collateral status in patients with acute ischemic stroke in MR CLEAN trial and registry.** *Stroke* 2020;51:1493–502 CrossRef Medline
26. Kim B, You SH, Jung SC. **A multicenter survey of acute stroke imaging protocols for endovascular thrombectomy.** *Neurointervention* 2021;16:20–28 CrossRef Medline

Quantification of Thalamic Atrophy in MS: From the Multicenter Italian Neuroimaging Network Initiative Data Set to Clinical Application

 Loredana Storelli,  Elisabetta Pagani,  Patrizia Pantano,  Antonio Gallo,  Nicola De Stefano,  Maria A. Rocca, and  Massimo Filippi, for the INNI Network



ABSTRACT

BACKGROUND AND PURPOSE: Thalamic atrophy occurs from the earliest phases of MS; however, this measure is not included in clinical practice. Our purpose was to obtain a reliable segmentation of the thalamus in MS by comparing existing automatic methods cross-sectionally and longitudinally.

MATERIALS AND METHODS: MR images of 141 patients with relapsing-remitting MS (mean age, 38 years; range, 19–58 years; 95 women) and 69 healthy controls (mean age, 36 years; range, 22–69 years; 47 women) were retrieved from the Italian Neuroimaging Network Initiative repository: T1WI, T2WI, and DWI at baseline and after 1 year (136 patients, 31 healthy controls). Three segmentation software programs (FSL-FIRST, FSL-MIST, FreeSurfer) were compared. At baseline, agreement among pipelines, correlations with age, disease duration, clinical score, and T2-hyperintense lesion volume were evaluated. Effect sizes in differentiating patients and controls were assessed cross-sectionally and longitudinally. Variability of longitudinal changes in controls and sample sizes were assessed. False discovery rate—adjusted $P < .05$ was considered significant.

RESULTS: At baseline, FSL-FIRST and FSL-MIST showed the highest agreement in the results of thalamic volume ($R = 0.87$, $P < .001$), with the highest effect size for FSL-MIST (Cohen $d = 1.11$); correlations with demographic and clinical variables were comparable for all software. Longitudinally, FSL-MIST showed the lowest variability in estimating thalamic volume changes for healthy controls ($SD = 1.07\%$), the highest effect size (Cohen $d = 0.44$), and the smallest sample size at 80% power level (15 subjects per group).

CONCLUSIONS: Multimodal segmentation by FSL-MIST increased the robustness of the results with better capability to detect small variations in thalamic volumes.

ABBREVIATIONS: EDSS = Expanded Disability Status Scale; FA = fractional anisotropy; HC = healthy controls; ICC = intraclass correlation coefficient; INNI = Italian Neuroimaging Network Initiative; LV = lesion volumes; RR = relapsing-remitting

The thalamus is a highly organized structure of gray matter nuclei that contains only a modest component of myelinated and unmyelinated white matter. It has a critical role in linking cortical and subcortical circuits, which subserve many neurologic functions.¹

In patients with MS, a high vulnerability to damage to this strategic structure has been consistently demonstrated.² Many studies have reported a volume reduction of the thalamus not only in all clinical MS phenotypes but also in the early phases of the disease. Thalamic atrophy has been found in patients with clinically isolated syndrome,³ early relapsing-remitting (RR)⁴ and primary-progressive MS,⁵ and also in pediatric patients with MS.⁶ Thalamic atrophy is related not only to the presence of thalamic lesions but also to the global burden of brain T2-hyperintense and


Received May 17, 2023; accepted after revision September 29.

From the Neuroimaging Research Unit (L.S., E.P., M.A.R., M.F.), Division of Neuroscience, Neurology Unit (M.A.R., M.F.), Neurorehabilitation Unit (M.F.), and Neurophysiology Service (M.F.), Istituto Di Ricovero e Cura a Carattere Scientifico San Raffaele Scientific Institute, Milan, Italy; Department of Human Neurosciences (P.P.), Sapienza University of Rome, Rome, Italy; Istituto Di Ricovero e Cura a Carattere Scientifico NEUROMED (P.P.), Pozzilli, Isernia, Italy; Department of Advanced Medical and Surgical Sciences and 3T MRI-Center (A.G.), University of Campania “Luigi Vanvitelli,” Naples, Italy; Department of Medicine, Surgery and Neuroscience (N.D.S.), University of Siena, Siena, Italy; and Vita-Salute San Raffaele University (M.A.R., M.F.), Milan, Italy.

Italian Neuroimaging Network Initiative—Milan: Paola Valsasina, Paolo Preziosa, Stefania Sala; Naples: Alvino Bisecco, Alessandro d'Ambrosio, Fabrizio Esposito, Alessandro Pasquale De Rosa; Rome: Silvia Tommasin, Claudia Piervincenzi, Costanza Gianni, Nikolaos Petsas; Siena: Marco Battaglini, Maria Laura Stromillo, Rosa Cortese; Italian Multiple Sclerosis Foundation: Paola Zaratin.

This study was partially supported by Fondazione Italiana Sclerosi Multipla with a research fellowship (FISM 2019/BR/009) and a research grant (FISM2018/S/3) and financed or co-financed with the ‘5 per mille’ public funding.

Please address correspondence to Massimo Filippi, MD, FEAN, FAAN, Neuroimaging Research Unit, Division of Neuroscience, IRCCS San Raffaele Scientific Institute, Via Olgettina, 60, 20132 Milan, Italy; e-mail: filippi.massimo@hsr.it; @rocca_mara; @IngStorelli_L; @NRU_SanRaffaele

 Indicates article with online supplemental data.
<http://dx.doi.org/10.3174/ajnr.A8050>

T1-hypointense lesions, supporting its potential to reflect changes secondary to axonal transection of white matter fibers. Notably, the quantification of thalamic damage in MS is also informative for disease evolution, overcoming, for instance, measures of global gray matter involvement and those that reflect intrinsic lesional microstructural damage in explaining changes in Expanded Disability Status Scale (EDSS) after an 8-year follow-up.^{7,8} For all these reasons, thalamic atrophy is a candidate biomarker in MS. Thus, it has been already included as an exploratory end point in clinical trials.⁹⁻¹³

In the clinical setting, this measure is, however, still not obtained, mainly because of the time-consuming procedure required for its manual segmentation. On the other hand, the existing automatic methods do not provide good enough reproducibility that allows monitoring atrophy changes at a single patient level. This drawback was shown in a recent article¹⁴ using data from the Alzheimer's Disease Neuroimaging Initiative data set and in another study¹⁵ in which the variation from repeated measurements ranged from 1% to 3%, depending on the method used. Although this variability can be considered sufficient for group comparisons, it is not suitable enough for individualized assessments.

A major issue for thalamic segmentation is the precise contouring of lateral boundaries toward the internal capsule, because contrast smoothly degrades due to the presence of white matter fibers terminating in the thalamus. In a previous article,¹⁶ we tried to control for this issue by using the contrast offered by fractional anisotropy (FA) maps from DWI for improving the segmentation. Recently, a multimodal approach for subcortical nuclei segmentation was included in the FSL library.^{17,18} Although the published article does not specifically discuss thalamic segmentation, the results obtained for other subcortical structures, such as the striatum and the globus pallidus, encourage the inclusion of FA for a better delineation of these structures.¹⁸

The Italian Neuroimaging Network Initiative (INNI) supports the creation of a repository in which MR imaging, clinical, and neuropsychological data from patients with MS and healthy controls (HC) are collected from 4 Italian research centers with internationally recognized expertise in MR imaging applied to MS.¹⁹

Using the large multicenter MR imaging data set from INNI, we aimed to obtain a reliable, automatic segmentation of the thalamus in MS by comparing the results obtained with existing automatic approaches both cross-sectionally and longitudinally. Final suggestions are provided for the application of these pipelines in large studies in MS.

MATERIALS AND METHODS

Ethics Committee Approval

Approval was received from the local ethics standards committee on human experimentation at each Research Center, and written informed consent was obtained from all subjects.

Subjects

We retrospectively analyzed data from 141 patients (center A: 35, center B: 34, center C: 36, center D: 36) with RRMS²⁰ and 69 HC (center A: 20, center B: 14, center C: 20, center D: 15) collected by

INNI from 4 centers identified here as A (where subjects were scanned with 2 different T1-weighted sequences) and B, C, and D (MR imaging data were acquired between January 2008 and July 2017) for pipeline comparison (validation set). A cross-sectional training set was needed for one of the compared pipelines. Thus, we collected from the INNI repository an additional data set including 50 patients with MS (center A: 20, center B: 10, center C: 10, center D: 10) and 50 HC (center A: 20, center B: 10, center C: 11, center D: 9). Inclusion/exclusion criteria for all patients and HC were the following: no contraindications to MR imaging, no history of alcohol or substance abuse, no neurologic diseases (other than MS), and no psychiatric diseases. All participants underwent a clinical and MR imaging evaluation at baseline with rating using the EDSS score and disease duration.

Of the validation set, 136 patients with MS and 31 HC underwent a follow-up re-evaluation 1 year after the baseline visit. At follow-up, all patients had been relapse-free and steroid-free for at least 1 month.

MR Imaging Acquisition

Baseline and follow-up 3D T1-weighted, T2-weighted, and DWI scans were acquired at each center using a local standardized protocol and 3T scanners. Pulse sequence parameters are reported in the Online Supplemental Data and are more extensively described in a previous publication.²¹

Image Analyses

All INNI MR imaging data underwent a standardized preprocessing, including a procedure for quality control described in detail elsewhere.²¹ Focal T2-hyperintense white matter lesions had already been manually identified and segmented by each participating center and made available for the quality control to the analyzer center (center A).

DWIs were corrected for movement and eddy current-induced distortions using the FDT tool (<https://fsl.fmrib.ox.ac.uk/fsl/fslwiki/FDT>) within the FSL Library.^{22,23} The Diffusion Toolbox was estimated by linear regression using DWI data at $b=0$, 900, or 1000 s/mm². Subsequently, FA maps were derived.²⁴

The pipelines selected for this study were all freely available and fully-automatic methods for cross-sectional volumetric segmentation of subcortical brain structures on MR images. None of these are specifically proposed and optimized for longitudinal quantification of subcortical tissue volume changes. Thus, 3 software programs were compared:

- FSL-FIRST, Version 5.0.10. (<https://fsl.fmrib.ox.ac.uk/fsl/fslwiki/FIRST/UserGuide>)²⁵
- FSL-MIST (β release) (<https://fsl.fmrib.ox.ac.uk/fsl/fslwiki/MIST>)²⁶
- FreeSurfer, Version 6.0 (<http://surfer.nmr.mgh.harvard.edu>).^{27,28}

The selected approaches were applied on the validation data set at baseline and follow-up for estimation of longitudinal volume change.

3D T1-weighted images after applying the lesion-filling technique²⁹ were given as input to all the toolboxes. FSL-MIST can also include the FA map coregistered into the T1-weighted space

Main demographic and clinical findings in HC and patients with RRMS at baseline for the training set required by FSL-MIST toolbox

	HC (n = 50)	RRMS (n = 50)	P Value
Female/male	30:20	32:18	.68 ^a
Mean age (range) (yr)	38 (19–56)	36 (19–62)	.3 ^b
Median disease duration (range) (yr)	–	8 (1–25)	–
Median EDSS (range)	–	1.5 (0–4.5)	–
Median T2 LV (range) (mL)	0.1 (0–0.5)	3.2 (0.3–33.0)	<.001 ^b

Note:—The en dash (–) indicates null values.

^a Pearson χ^2 test;

^b Mann-Whitney test.

as an optional input to the segmentation method to improve the results of the subcortical masks. Thus, for each subject, FA maps were registered to the T1-weighted space (FLIRT, FSL) and given as an additional input for the FSL-MIST pipeline. Moreover, FSL-MIST is a 2-step approach: one for the training of the model and the second for the test.

For longitudinal thalamic atrophy quantification, the changes between baseline and follow-up cross-sectional volumes obtained by the compared pipelines were assessed as the percentage difference between the 2 MR imaging acquisitions corrected for the baseline volume.

Here is a brief description of the methods:

FSL-FIRST. FIRST is a freely available toolbox for subcortical structure segmentation included within the FSL Library.²⁵ The method models shapes and appearance of 15 brain structures starting from 336 manually segmented T1-weighted MR images. In particular, FIRST uses the active shape and appearance models³⁰ that associate the intensities around a deformable shape with the spatial configuration of the shape.

FSL-MIST. MIST is a toolbox included in FSL Library for multimodal subcortical structure segmentation, taking advantage of the different image contrasts.²⁶ Unlike FIRST, it can use additional information from different MR imaging modalities and is less dependent on manual segmentation learning in an unsupervised fashion from a set of unlabeled training data.

FreeSurfer. FreeSurfer is a freely available software package for the analyses of structural MR imaging data and cortical thickness estimation.^{27,28} For subcortical structure segmentation, a probabilistic atlas, which is derived from a number of manual segmentations, is still used, but in this case, the procedure is based on modeling the segmentation as a nonstationary anisotropic Markov random field.

Statistical Analysis

Statistical analysis was performed using the R software package (Version 3.1.1; <https://www.r-project.org/>). Demographic data and T2 lesion volumes (LV) were compared between groups using the χ^2 Pearson test for categorical variables and the Mann-Whitney U or *t* test for continuous variables. We evaluated the intraclass correlation coefficient (ICC) to assess the strength of the agreement among the different software packages on the basis of thalamic volume measures. Between-group differences (center-corrected) in thalamic volumes and their longitudinal changes for the different software packages were expressed as effect size,

calculated according to the Cohen *d* definition.³¹ Pearson correlations of thalamic volume with age (separately for MS and HC) and partial correlations (adjusted for age) with clinical and MR imaging variables (EDSS, disease duration, T2 LV) for MS at baseline for each method were estimated. Finally, the variability of the results of the longitudinal changes in thalamic volumes in HC at follow-up for the different

pipelines was assessed. The sample size requirements at 80% power level for detecting a significant difference in the rate of thalamic atrophy between HC and MS at the .05 α level was estimated for each software package.

False discovery rate (Benjamini-Hochberg procedure) correction was applied. A *P* value < .05 was considered statistically significant.

A visual inspection of the thalamic segmentations for all the pipelines was also performed.

RESULTS

Demographic and Clinical Features

The Online Supplemental Data summarize the main demographic and clinical characteristics of the validation set at baseline. Patients with MS and HC were age- and sex-matched, with a higher prevalence of women in both groups. As expected, T2-hyperintense LV were significantly higher in the RRMS group compared with HC.

At follow-up (mean follow-up interval = 1.00 [SD, 0.25] year for MS, 1.06 [SD, 0.20] years for HC; *P* = .7), the median EDSS score was 1.5 (range, 0–4.5; *P* = .2 versus baseline) and 7 patients with MS had worsened clinically (EDSS score increase of ≥ 1.5 when the baseline EDSS was 0, ≥ 1.0 when the EDSS at baseline was <6.0, and ≥ 0.5 when EDSS at baseline was ≥ 6.0).³²

The Table shows the main demographic and clinical characteristics of the training set used for the FSL-MIST toolbox. Again, patients with MS and HC were age- and sex-matched, with a higher prevalence of women in both groups and higher T2-hyperintense LV in RRMS compared with HC. The validation and training data sets showed the same characteristics.

Baseline Results

At baseline, all software showed a good significant agreement in the results of thalamic volume, with the highest agreement between FSL-FIRST and FSL-MIST (ICC = 0.87, *P* < .001) and the lowest between FSL-MIST and FreeSurfer (ICC = 0.80, *P* < .001), for both MS and HC. Online Supplemental Fig 1 shows an example of thalamic segmentations for each software program on a healthy volunteer. However, from a visual inspection of the accuracy of the segmentations, we found that thalamic delineations obtained by FSL-MIST are always underestimated with respect to FSL-FIRST and FreeSurfer, also noticeable from the thalamic volumes at baseline.

All pipelines significantly differentiated patients with MS from HC (*P* < .001 for all software, Online Supplemental Fig 2), with the highest effect size found for FSL-MIST (Cohen *d* = 1.11)

and FSL-FIRST (Cohen $d=1.07$) compared with FreeSurfer (Cohen $d=0.79$). When we looked at the data, FSL-MIST showed the lowest variability with an increased robustness of the results at baseline (SD for the thalamic volume distribution in HC = 1.36 mL, in MS = 1.48 mL) with respect to the other 2 pipelines (SD for the thalamic volume distribution in HC = 1.74 mL and 1.95 mL, respectively for FSL-FIRST and FreeSurfer).

At baseline, the Pearson correlations between thalamic volumes and subjects' ages were similar and significant for all the compared pipelines, for both MS ($r = -0.33$ for FSL-MIST, $r = -0.32$ for FSL-FIRST, $r = -0.29$ for FreeSurfer, all $P < .001$) and HC ($r = -0.38$ for FSL-MIST, $r = -0.40$ for FSL-FIRST, $r = -0.45$ for FreeSurfer, all $P < .001$).

At baseline in patients with MS, partial correlations (adjusted for age) between thalamic volumes and EDSS were very low or not significant for all the compared pipelines ($r = -0.16$, $P = .06$ for FSL-MIST, $r = -0.3$, $P < .001$ for FSL-FIRST, $r = -0.17$, $P = .04$ for FreeSurfer). Again, at baseline in patients with MS, partial correlations (adjusted for age) between thalamic volumes and disease duration were significant only for FSL-FIRST ($r = -0.2$, $P = .02$), while these were not significant for FSL-MIST ($r = -0.10$, $P = .3$) and FreeSurfer ($r = -0.12$, $P = .1$).

Pearson correlations between thalamic volumes at baseline and T2 LV were all significant and comparable among the different software ($r = -0.46$, $P < .05$ for FSL-MIST, $r = -0.51$, $P < .05$ for FSL-FIRST, and $r = -0.46$, $P < .05$ for FreeSurfer).

Longitudinal Results

At follow-up, in HC, FSL-MIST showed the lowest variability of percentage thalamic volume change (SD = 1.07%) in comparison with the other pipelines (SD = 1.53% for FSL-FIRST and 4.96% for FreeSurfer). Online Supplemental Fig 3 shows the results of thalamic volume changes in HC and patients with MS for the different pipelines.

At follow-up, for percentage thalamic volume changes, FSL-MIST showed a small effect size but a better capability to significantly differentiate between HC and patients with MS (Cohen $d=0.44$) compared with FSL-FIRST (Cohen $d=0.09$) and FreeSurfer (Cohen $d=0.21$).

FSL-MIST and FSL-FIRST showed the smallest sample size requirement for assessment of longitudinal thalamic atrophy at an 80% power level: 15 subjects per arm for FSL-MIST and 29 subjects per arm for FSL-FIRST, while the highest sample size was found for FreeSurfer (105 subjects per group at an 80% level).

DISCUSSION

In this work, we aimed to compare 3 available fully automatic methods for thalamic segmentation and volume quantification on a multicenter data set to obtain a reliable segmentation of the thalamus for a possible future clinical introduction of this measure in MS. Using the INNI data set, we found that the inclusion of FA maps facilitated the automatic identification of thalamic boundaries, increasing the robustness of the results. In particular, the multimodal approach (FSL-MIST) showed a better capability to detect small longitudinal variations of thalamic volumes in patients with MS.

At baseline, we found a good agreement (ICCs ≥ 0.8) among the software for automatic thalamic segmentations analyzed. However, a slightly higher agreement was found between FSL-MIST and FSL-FIRST. This could be because both methods are implemented within the same FSL Library and have some basic methodologic similarities. In detail, both methods use a probabilistic Bayesian approach to fully exploit the relationship between intensity and shape/boundaries and use a generative model for the intensity profiles perpendicular to a deformable mesh. However, for FSL-FIRST, intensities and possible shape variations are derived from a set of 336 manually labeled training segmentations for 15 different subcortical structures based on a T1-weighted scan only, while FSL-MIST can learn in an unsupervised fashion from unlabeled training data, being less dependent on manual segmentations, and can simultaneously combine complementary information from different MR imaging modalities, which also increases the contrast-to-noise ratio. On the other hand, FreeSurfer similarly starts from a probabilistic atlas (as in FSL-MIST and FSL-FIRST), which is derived from a data set of 12 manually labeled segmentations, but it is used as a prior on a Markov random field model. The prior information included both the global spatial information, independent from other information, and the local spatial relationship between anatomic classes. These spatial constraints allow the Markov random field model to segment the image into a large number of classes required to segment the subcortical structures. These technical and implemental differences among the compared software could have been reflected on the observed discrepancies in terms of thalamic volume agreement.

All software could significantly differentiate thalamic volumes of patients with MS from those in HC at baseline, with a slightly higher effect size found for FSL-MIST in comparison with the other tools. Thus, all analyzed pipelines are suitable for analyses at a group level to detect thalamic volume differences between patients with MS and HC. From the standpoint of moving the application of these software programs to the single patient level and personalized medicine, our assessment should also take into account the variability of the results obtained and the measurement errors. Because there are no ground truth segmentations, we could not infer anything about measurement errors. However, by looking at the distributions of thalamic volumes at baseline in HC, we found the lowest variability of the results for FSL-MIST, suggesting more robustness of the measures.

Longitudinal analyses are extremely important to inspect the reliability of a measure and to assess the possibility of applying a tool for measurements on a single-subject level. In this study, after 1 year of follow-up, we expect very small changes in thalamic volumes in HC.^{7-9,33} Given these considerations, our longitudinal results on the percentage thalamic volume change in HC confirmed a higher robustness of the measurement for FSL-MIST (showing the lowest variability) in comparison with FSL-FIRST and FreeSurfer. This is also evident at a group level by looking at the results of the effect sizes among the different pipelines on the longitudinal measures of thalamic volume changes. Moreover, we found that thalamic volume changes obtained from FSL-MIST required the smallest sample size compared with the other 2 software programs, making this tool particularly appealing for MS

studies but also for possible use at the individual level and when evaluating treatment effects.

From a visual inspection of the accuracy of the segmentations, we found that thalamic delineations obtained by FSL-MIST are always underestimated with respect to FSL-FIRST and FreeSurfer, also noticeable from the thalamic volumes at baseline. In fact, FSL-MIST segmentation always tends not to include the thalamic region of pulvinar, probably because this subregion is well-contrasted in the FA contrast and is important information used for the FSL-MIST multimodal segmentation. Thus, the tool delineates the final boundary of the thalamus before this region, as shown in Online Supplemental Fig 1. This characteristic is certainly a limitation of the method. However, at a single-patient level, an essential value for a software is the capability to detect small thalamic volume changes with time, and the longitudinal reproducibility demonstrated by FSL-MIST is the most important result in this sense.

Our findings on the association between demographic and clinical variables with baseline thalamic volumes did not show relevant differences among the compared tools. At baseline, correlations of thalamic volumes with age, EDSS, and T2 LV, though significant, were very low and similar among the pipelines, while the association between thalamic volumes and disease duration was slightly significant only for the FSL-FIRST measures. Thus, considering baseline correlation results, none of the software seemed to perform better compared with the others.

Therefore, given the difficulty of modeling structures such as the thalamus, with darker-appearing tissue at the midline and a gradient of brighter intensities as one moves more laterally, the use of a multimodal approach could facilitate this automatic task. From our findings, the inclusion of FA contrast for thalamic segmentation seemed to increase the robustness of the results and demonstrated a better capability to detect small longitudinal variations of thalamic volumes, as shown by FSL-MIST results. However, due to the lack of data on the accuracy and precision in the selection of the appropriate pipeline for automatic thalamic segmentation, it would be important to take into account even other practical aspects. Considering the application context, the lack of FA maps, for example, could prevent the use of multimodal approaches like FSL-MIST in favor of faster approaches (FSL-FIRST). However, an increased complexity could be tolerable for a better longitudinal reproducibility of the results (FSL-MIST).

Limitations

As previously stated, one of the main limitations of this comparative study is the lack of ground truth thalamic segmentation for a fair validation of the software on the accuracy of thalamic volumes. However, manual segmentation of the thalamus is an extremely time-consuming task, especially on high-resolution 3D T1-weighted sequences, and its precise delineation is very difficult to achieve, even for an expert MR imaging reader. Moreover, test-retest data would be helpful to assess precision and measurement errors for the compared software, and further investigations are needed. As already stated, FSL-MIST segmentation always tends not to include the thalamic region of pulvinar, and this exclusion is certainly a limitation in the accuracy of the segmentation at a single visit. Finally, a more clinical setting in terms of

variability and lower quality of input MR imaging data could have allowed us to evaluate the performance and applicability of the methods, even in a clinical framework. However, the large multicenter cohort with no standardized MR imaging sequences and protocols collected for the purpose of this study is a good starting point to evaluate the available pipelines for automatic thalamic segmentation.

CONCLUSIONS

Thalamic atrophy is under investigation as a biomarker in MS. However, its applicability in the clinical setting is still not possible, mainly because of the lack of an automatic and robust segmentation method. Automatic methods are now available that could be optimized and tested in a multicenter context. Because the delimitation of the internal boundary toward the internal capsule is a limiting factor, a multimodal approach that includes FA maps could improve the overall reproducibility of thalamic segmentation. By comparing cross-sectional and longitudinal thalamic segmentations from 3 available automatic methods in a multicenter data set from INNI, we found that the inclusion of FA contrast increased the robustness of the longitudinal results and had a better capability to detect small variations of thalamic volumes, as shown by FSL-MIST results.

Disclosure forms provided by the authors are available with the full text and PDF of this article at www.ajnr.org.

REFERENCES

1. Haber SN. **The primate basal ganglia: parallel and integrative networks.** *J Chem Neuroanat* 2003;26:317–30 CrossRef Medline
2. Henry RG, Shieh M, Okuda DT, et al. **Regional grey matter atrophy in clinically isolated syndromes at presentation.** *J Neurol Neurosurg Psychiatry* 2008;79:1236–44 CrossRef Medline
3. Audoin B, Ranjeva JP, Au Duong MV, et al. **Voxel-based analysis of MTR images: a method to locate gray matter abnormalities in patients at the earliest stage of multiple sclerosis.** *J Magn Reson Imaging* 2004;20:765–71 CrossRef Medline
4. Audoin B, Davies GR, Finisku L, et al. **Localization of grey matter atrophy in early RRMS: a longitudinal study.** *J Neurol* 2006;253:1495–501 CrossRef Medline
5. Sepulcre J, Sastre-Garriga J, Cercignani M, et al. **Regional gray matter atrophy in early primary progressive multiple sclerosis: a voxel-based morphometry study.** *Arch Neurol* 2006;63:1175–80 CrossRef Medline
6. Mesaros S, Rocca MA, Absinta M, et al. **Evidence of thalamic gray matter loss in pediatric multiple sclerosis.** *Neurology* 2008;70:1107–12 CrossRef Medline
7. Mesaros S, Rocca MA, Pagani E, et al. **Thalamic damage predicts the evolution of primary-progressive multiple sclerosis at 5 years.** *AJNR Am J Neuroradiol* 2011;32:1016–20 CrossRef Medline
8. Rocca MA, Mesaros S, Pagani E, et al. **Thalamic damage and long-term progression of disability in multiple sclerosis.** *Radiology* 2010;257:463–69 CrossRef Medline
9. Azevedo CJ, Cen SY, Khadka S, et al. **Thalamic atrophy in multiple sclerosis: a magnetic resonance imaging marker of neurodegeneration throughout disease.** *Ann Neurol* 2018;83:223–34 CrossRef Medline
10. Filippi M, Rocca MA, Pagani E, et al. **ALLEGRO Study Group. Placebo-controlled trial of oral laquinimod in multiple sclerosis: MRI evidence of an effect on brain tissue damage.** *J Neurol Neurosurg Psychiatry* 2014;85:851–58 CrossRef Medline
11. Gaetano L, Haring DA, Radue EW, et al. **Fingolimod effect on gray matter, thalamus, and white matter in patients with multiple sclerosis.** *Neurology* 2018;90:e1324–32 CrossRef Medline

12. Hanninen K, Viitala M, Paavilainen T, et al. **Thalamic atrophy predicts 5-year disability progression in multiple sclerosis.** *Front Neurol* 2020;11:606 CrossRef Medline
13. Schoonheim MM, Ciccarelli O. **The value of including thalamic atrophy as a clinical trial endpoint in multiple sclerosis.** *Neurology* 2018;90:677–78 CrossRef Medline
14. Meijerman A, Amiri H, Steenwijk MD, et al; Alzheimer's Disease Neuroimaging Initiative. **Reproducibility of deep gray matter atrophy rate measurement in a large multicenter dataset.** *AJNR Am J Neuroradiol* 2018;39:46–53 CrossRef Medline
15. Velasco-Annis C, Akhondi-Asl A, Stamm A, et al. **Reproducibility of brain MRI segmentation algorithms: empirical comparison of local MAP PSTAPLE, FreeSurfer, and FSL-FIRST.** *J Neuroimaging* 2018;28:162–72 CrossRef Medline
16. Biseco A, Rocca MA, Pagani E, et al; MAGNIMS Network. **Connectivity-based parcellation of the thalamus in multiple sclerosis and its implications for cognitive impairment: a multicenter study.** *Hum Brain Mapp* 2015;36:2809–25 CrossRef Medline
17. FSL MIST. <https://fsl.fmrib.ox.ac.uk/fsl/fslwiki/MIST>. Accessed May 10, 2023
18. Visser E, Keuken MC, Forstmann BU, et al. **Automated segmentation of the substantia nigra, subthalamic nucleus and red nucleus in 7T data at young and old age.** *Neuroimage* 2016;139:324–36 CrossRef Medline
19. Filippi M, Tedeschi G, Pantano P, et al; INNI Network. **The Italian Neuroimaging Network Initiative (INNI): enabling the use of advanced MRI techniques in patients with MS.** *Neurol Sci* 2017;38:1029–38 CrossRef Medline
20. Lublin FD, Reingold SC. **Defining the clinical course of multiple sclerosis: results of an international survey: National Multiple Sclerosis Society (USA) Advisory Committee on Clinical Trials of New Agents in Multiple Sclerosis.** *Neurology* 1996;46:907–11 CrossRef Medline
21. Storelli L, Rocca MA, Pantano P, et al; INNI Network. **MRI quality control for the Italian Neuroimaging Network Initiative: moving towards big data in multiple sclerosis.** *J Neurol* 2019;266:2848–58 CrossRef Medline
22. Andersson JL, Graham MS, Drobnjak I, et al. **Towards a comprehensive framework for movement and distortion correction of diffusion MR images: within volume movement.** *Neuroimage* 2017;152:450–66 CrossRef Medline
23. Andersson JL, Sotiropoulos SN. **An integrated approach to correction for off-resonance effects and subject movement in diffusion MR imaging.** *Neuroimage* 2016;125:1063–78 CrossRef Medline
24. Behrens TE, Woolrich MW, Jenkinson M, et al. **Characterization and propagation of uncertainty in diffusion-weighted MR imaging.** *Magn Reson Med* 2003;50:1077–88 CrossRef Medline
25. Patenaude B, Smith SM, Kennedy DN, et al. **A Bayesian model of shape and appearance for subcortical brain segmentation.** *Neuroimage* 2011;56:907–22 CrossRef Medline
26. Visser E, Keuken MC, Douaud G, et al. **Automatic segmentation of the striatum and globus pallidus using MIST: multimodal image segmentation tool.** *Neuroimage* 2016;125:479–97 CrossRef Medline
27. Fischl B, Salat DH, Busa E, et al. **Whole brain segmentation: automated labeling of neuroanatomical structures in the human brain.** *Neuron* 2002;33:341–55 CrossRef Medline
28. Fischl B, Salat DH, van der Kouwe AJ, et al. **Sequence-independent segmentation of magnetic resonance images.** *Neuroimage* 2004;23 (Suppl 1):S69–84 CrossRef Medline
29. Battaglini M, Jenkinson M, De Stefano N. **Evaluating and reducing the impact of white matter lesions on brain volume measurements.** *Hum Brain Mapp* 2012;33:2062–71 CrossRef Medline
30. Cootes TF, Taylor CJ, Cooper DH, et al. **Active shape models: their training and application.** *Comput Vis Image Underst* 1995;61:38–59 CrossRef
31. Jacob C. *Statistical Power Analysis for the Behavioral Sciences.* Routledge; 1988:579
32. Rio J, Nos C, Tintore M, et al. **Defining the response to interferon-beta in relapsing-remitting multiple sclerosis patients.** *Ann Neurol* 2006;59:344–52 CrossRef Medline
33. Choi EY, Tian L, Su JH, et al. **Thalamic nuclei atrophy at high and heterogenous rates during cognitively unimpaired human aging.** *Neuroimage* 2022;262:119584 CrossRef Medline

Brain Abnormalities in Becker Muscular Dystrophy: Evaluation by Voxel-Based DTI and Morphometric Analysis

¹Hiroyuki Maki, ²Madoka Mori-Yoshimura, Hiroshi Matsuda, Yasumasa Hashimoto, ³Miho Ota, ⁴Yukio Kimura, ⁵Yoko Shigemoto, Naoko Ishihara, ⁶Hirohito Kan, ⁷Emiko Chiba, ⁸Elly Arizono, Sumiko Yoshida, ⁹Yuji Takahashi, and ¹⁰Noriko Sato



ABSTRACT

BACKGROUND AND PURPOSE: Although various neuropsychological problems in Becker muscular dystrophy have attracted attention, there have been few related neuroimaging studies. We investigated brain abnormalities in patients with Becker muscular dystrophy using 3D TIWI and DTI.

MATERIALS AND METHODS: MR images were obtained for 30 male patients and 30 age-matched healthy male controls. We classified patients into Dp140+ and Dp140− subgroups based on their predicted dystrophin Dp140 isoform expression and performed voxel-based comparisons of gray and white matter volumes and DTI metrics among the patients, patient subgroups, and controls. ROI-based DTI analyses were also performed.

RESULTS: Significantly decreased fractional anisotropy was observed in the left planum temporale and right superior parietal lobule compared between the Becker muscular dystrophy and control groups. In the Dp140− subgroup, decreased fractional anisotropy was observed in the left planum temporale, but no significant changes were seen in the Dp140+ subgroup. The ROI-based analysis obtained the same results. No significant differences were evident in the gray or white matter volumes or the DTI metrics other than fractional anisotropy between the groups.

CONCLUSIONS: A DTI metric analysis is useful to detect white-matter microstructural abnormalities in Becker muscular dystrophy that may be affected by the Dp140 isoform expression.

ABBREVIATIONS: AD = axial diffusivity; BMD = Becker muscular dystrophy; DARTEL = Diffeomorphic Anatomical Registration Through Exponentiated Lie Algebra; DMD = Duchenne muscular dystrophy; FA = fractional anisotropy; IQ = intelligence quotient; MD = mean diffusivity; RD = radial diffusivity; VBM = voxel-based morphometry; WAIS = Wechsler Adult Intelligence Scale

Becker muscular dystrophy (BMD) is an X-linked recessive form of muscular dystrophy caused by mutations in the

dystrophin gene that lead to the production of variable levels of partially functioning dystrophin.¹ Compared with the more severe allelic disorder Duchenne muscular dystrophy (DMD), individuals with BMD have a much longer normal life expectancy.² In addition to muscle weakness, mutations in the dystrophin gene have been linked to cognitive impairment. For example, learning and behavioral problems are well-revealed in individuals with DMD.³ Although it has not been established whether similar neuropsychological problems are part of the BMD disease spectrum, several studies have described attention problems, language/speech delays, and mental problems such as depression and neurosis in individuals with BMD.⁴⁻⁶

The dystrophin gene is the largest gene, containing 79 exons and tightly regulated tissue-specific promoters that make a range of protein isoforms known to reflect their relative sizes. These include the longest dystrophin isoform, Dp427, and the shorter products: Dp71, Dp116, Dp140, and Dp260.⁷ A genotype-phenotype relationship between mutations in the dystrophin gene and cognitive function has been described.⁸ Intellectual impairment is

Received December 15, 2022; accepted after revision September 28, 2023.

From the Departments of Radiology (H. Maki, Y.K., Y.S., E.C., E.A., N.S.), Neurology (M.M.-Y., Y.T.), and Psychiatric Rehabilitation (S.Y.), National Center Hospital, National Center of Neurology and Psychiatry, Tokyo, Japan; Department of Biofunctional Imaging (H. Matsuda), Fukushima Medical University, Fukushima, Japan; Department of Neurology (Y.H.), Kansai Medical University, Osaka, Japan; Department of Molecular Therapy (Y.H.), National Institute of Neuroscience, National Center of Neurology and Psychiatry, Tokyo, Japan; Department of Neuropsychiatry (M.O.), University of Tsukuba, Ibaraki, Japan; Medical Genome Center (N.I., S.Y.), National Center of Neurology and Psychiatry, Tokyo, Japan; and Department of Integrated Health Sciences (H.K.), Nagoya University Graduate School of Medicine, Aichi, Japan.

This work was supported by the Intramural Research Grant (2-4, 2-6, 3-10) for Neurological and Psychiatric Disorders from the National Center of Neurology and Psychiatry Hospital (Tokyo, Japan).

Please address correspondence to Noriko Sato, MD, PhD, Department of Radiology, National Center Hospital, National Center of Neurology and Psychiatry, 4-1-1, Ogawahigashi-cho, Kodaira-shi, Tokyo, 187-8551, Japan; e-mail: snoriko@ncnp.go.jp

Indicates open access to non-subscribers at www.ajnr.org

Indicates article with online supplemental data.

<http://dx.doi.org/10.3174/ajnr.A8041>

more prominent in patients with DMD with mutations in the distal part of the dystrophin gene (distal to exon 44) that are associated with the loss of expression of the Dp140 isoform.⁸ The role of Dp140 in BMD has been reported to be important.⁹

Functional and quantitative neuroimaging studies of DMD have revealed multiple abnormalities, including gray matter volume differences, altered white matter microstructural integrity as measured using DTI, and metabolic derangement shown by PET.^{10,11} DTI analyses have demonstrated widespread and significant white matter abnormalities in individuals with DMD lacking Dp140 expression compared with those with retained Dp140 expression and healthy controls.^{10,12} However, the existing neuroimaging studies of BMD are limited to a visual-assessment study on brain atrophy and a DTI study using ROI methodology.^{6,13} No quantitative evaluation of whole-brain morphology and microstructures in BMD has been reported.

Voxel-based morphometry (VBM) and DTI are commonly used methods in studies of neurodegenerative and psychiatric diseases. VBM visualizes morphologic brain differences, and DTI estimates microstructural parameters such as fractional anisotropy (FA), mean diffusivity (MD), axial diffusivity (AD), and radial diffusivity (RD), mainly in the white matter.^{14,15} In the present study, we conducted both VBM and DTI analyses to clarify the morphologic and microstructural features in patients with BMD and the group-level differences in BMD subtypes based on Dp140 expression.

MATERIALS AND METHODS

This retrospective study was approved by the Ethics Committee of Japan's National Center of Neurology and Psychiatry Hospital (Tokyo). The requirement for patients' informed consent was waived due to the retrospective nature of the study. We enrolled 39 male patients with BMD who visited our hospital and underwent MR imaging between January 2014 and December 2021. The diagnosis of BMD was based on typical symptoms (eg, delayed motor milestones, proximal weakness, hypertrophied calves, and elevated creatine kinase levels) and deletions of the dystrophin gene or reduced dystrophin levels confirmed by a muscle biopsy.¹ All the patients' diagnoses of BMD were reviewed and confirmed by an experienced neurologist.

Seven patients were excluded from this study because of a lack of 3D T1WI or DTI data. We also excluded 2 patients with multiple lacunar infarcts on MR imaging. A final total of 30 men with BMD was included in the study. We also recruited 30 age-matched healthy male controls on the basis of the following criteria: no history of neurologic or psychiatric diseases, no contact with psychiatric services, and no use of medication that affects the central nervous system. Written informed consent was obtained from each healthy control participant.

We retrospectively collected information regarding the disease duration of patients with BMD, ambulatory performance, and steroid treatment from their medical records. Information regarding intelligence test scores on the Wechsler Adult Intelligence Scale III (WAIS-III) was also collected. The WAIS-III was used to measure verbal intelligence quotient (IQ), performance IQ, and full-scale IQ.

Genetic Diagnoses

Information regarding the patients' genetic diagnoses was collected from their medical records. We classified the patients with BMD into 2 subgroups according to mutations that might alter Dp140 expression. Duplication, deletion, or small mutations in the genic region between the Dp140 promoter and the N-terminal and frameshift or nonsense mutations involving intron 44 or downstream were deemed to be Dp140 expression modifiers. Among these possible modifiers, we considered harmful Dp140 mutations (Dp140-) as deletion mutations, which included the Dp140 start codon and/or coding region or coding region nonsense or splice site variants.⁶

MR Imaging Acquisition

In all participants, MR imaging was performed using a 3T clinical scanner (Achieva; Philips Healthcare) with a 32-channel head coil. 3D sagittal T1-weighted images were acquired (TR/TE, 7.18/3.46; flip angle, 10°; effective section thickness, 0.6 mm; slab thickness, 180 mm; matrix, 384 × 384; FOV, 261 × 261 mm; number of excitations, 1), yielding 300 contiguous slices through the brain. Single-shot spin-echo echo-planar DWIs were obtained with the following parameters: TR/TE, 6700/58 ms; flip angle, 90°; effective section thickness, 3.0 mm with no gap; slices, 60; matrix, 80 × 78; FOV, 240 × 240 mm; number of excitations, 2; noncoplanar diffusion directions, 15; b-values, 0 and 1000 s/mm². This study used a cross-sectional design, and the MR imaging for each subject was performed only once.

VBM Analysis

To investigate morphologic differences in gray and white matter volumes, we segmented and spatially normalized the 3D T1-weighted images using the Statistical Parametric Mapping 12 software program (SPM12; <http://www.fil.ion.ucl.ac.uk/spm/>) running in Matlab (MathWorks) with the Diffeomorphic Anatomical Registration through Exponentiated Lie Algebra (DARTEL; part of SPM) technique.¹⁶ The segmented gray and white matter images were normalized to the Montreal Neurological Institute space using the DARTEL technique and smoothed with an 8-mm full width at half maximum Gaussian kernel.

ROI-Based Analysis of Gray and White Matter Volumes

The potential disparities of gray and white matter volumes between the patients with BMD and controls were also investigated using the FreeSurfer program (Version 6.0; <http://surfer.nmr.mgh.harvard.edu/>). The 3D T1-weighted images were processed using the recon-all processing stream (<https://surfer.nmr.mgh.harvard.edu/fswiki/recon-all>), and the gray and white matter volumes were parcellated into 34 bilateral ROIs as defined by the Desikan-Killiany atlas.¹⁷ The total intracranial volumes were also measured.

Postprocessing and Analysis of the DTI Data

We performed a voxel-based whole-brain comparison for DTI analyses that has been validated.¹⁸ First, we added the denoising step and Gibbs-ringing correction using MRtrix3 (<https://www.mrtrix.org/>).^{19,20} After eddy current correction and brain

extraction using FSL, Version 5.0 (<https://fsl.fmrib.ox.ac.uk/fsl/fslwiki>), we fitted the diffusion tensor model in each voxel derived from the data with a b -value of 1000 using the DTIFit function (<https://fsl.fmrib.ox.ac.uk/fsl/fslwiki/FDT/UserGuide>) to estimate the FA, MD, AD, and RD maps.^{15,21}

For the investigation of DTI metrics on a voxel-by-voxel basis, we spatially normalized these images using the DARTEL registration method. Each 3D T1-weighted image was coregistered and resliced to its $b=0$ image. Subsequently, the coregistered 3D T1-weighted images were spatially normalized using the DARTEL template. Finally, the transformation matrix was applied to DTI metric maps. Each image was then smoothed using an 8-mm full width at half maximum Gaussian kernel. To restrict the analysis to regions of white matter, we masked the DTI metrics maps with the binary mask image made by the segmented white matter images derived from each individual 3D T1-weighted image that was coregistered and resliced to its $b=0$ image.

ROI-Based DTI Analysis

In addition to the voxel-based analyses, we performed an ROI-based analysis. The ROI of each significant cluster in the voxel-based analysis derived from SPM12 was automatically mapped to normalized DTI metrics images using MRIcron software (<https://people.cas.sc.edu/rorden/mricron/>). We investigated the left-right asymmetry of the measured DTI metrics values by reflecting the ROI of each significant cluster to the corresponding hemisphere—if it included the planum temporale or planum polare—because these areas are reported to be highly asymmetric.²² Each ROI was flipped to the other hemisphere using MRIcro software (<https://people.cas.sc.edu/rorden/mricro/>). The flipped ROIs were then evaluated with the MRIcron software. To assess the asymmetry of the DTI metrics values, we evaluated the ratio of left and right ROIs between the patients with BMD and controls.

Statistical Analyses

Demographic data are presented as mean (SD), range, or percentage, as indicated. The Mann-Whitney U test was used to analyze continuous data, and the Fisher exact test was used to analyze binary data. All statistical analyses were performed using Bell-Curve (Social Survey Research Information) for Excel software (Microsoft), and a 2-tailed P value $< .05$ was regarded as significant.

To determine the differences among the patients with BMD, the BMD subgroups classified by the expression of the Dp140 isoform, and the control group, we subjected the normalized gray and white matter volumes and DTI values to a 2-sample t test analysis using SPM12. The significance of the differences in gray and white matter volumes was tested with patient age and the total intracranial volume (calculated by SPM12) as confounding covariates. The DTI values were statistically analyzed using patient age as a confounding variable. For all SPM analyses, the significance level was set at a family-wise error-corrected $P < .05$ at voxel-level and a cluster size of >100 voxels. A normalized template provided by SPM12 (single_subj_T1.nii) was used for visualization. We used Bell-Curve for Excel software to perform a 2-sample t test to examine the difference of each ROI and the

ratio of left and right ROIs between the patients with BMD and the controls. A 2-tailed P value $< .05$ was regarded as significant. We performed an ANCOVA to evaluate differences in the volume of each ROI between the BMD and control groups, controlling for patient age and total intracranial volume. The significance level of the statistical analysis was set at Bonferroni corrected $P < .05$.

RESULTS

Clinical Characteristics

The clinical characteristics of each subject group are summarized in the Online Supplemental Data. The mean ages of the patients with BMD and controls were 37.8 (SD, 12.5) and 38.9 (SD, 12.2) years, respectively. No significant differences in age were observed among the groups (BMD versus controls, $P = .78$; BMD_Dp140− versus controls, $P = .81$; BMD_Dp140+ versus controls, $P = .45$; and BMD_Dp140− versus BMD_Dp140+, $P = .41$). Among the 30 patients with BMD, the genetic diagnoses identified deletion mutations ($n = 20$, 66.7%), duplication mutations ($n = 2$, 6.7%), small mutations ($n = 6$, 20.0%), and others (diagnosed by immunohistochemistry; $n = 2$, 6.7%). Eighteen patients had deleterious Dp140 mutations (BMD_Dp140−), and 10 patients did not have deleterious Dp140 mutations (BMD_Dp140+). Among the 30 patients with BMD, 21 (70%) patients were ambulant and 9 (30%) were wheelchair-bound; the mean age at loss of ambulation was 32.2 (SD, 9.3) years. Four patients were on steroid treatment, with a mean treatment duration of 3.6 years (range, 2–9 years). No significant differences were noted in the duration of steroid treatment between the Dp140 expression subgroups ($P = .68$).

The WAIS-III data were available for 16 patients, and the scores are listed in the Online Supplemental Data. The full-scale IQ of the patients was within the normal range (≥ 70). No significant differences were observed in the WAIS-III scores between the BMD_Dp140+ and BMD_Dp140− subgroups.

Voxel-Based Morphometric and DTI Analyses

The results of the VBM analysis revealed no significant differences in either gray or white matter between the groups, ie, BMD versus controls; BMD_Dp140− versus controls; BMD_Dp140+ versus controls; and BMD_Dp140− versus patients with BMD_Dp140+. In the voxel-based DTI analysis, the 30 patients with BMD showed areas with significantly decreased FA in the left planum temporale and right superior parietal lobule compared with the healthy controls (Table 1 and Fig 1). Eighteen patients with BMD_Dp140− presented with significant FA reductions in the left planum temporale compared with controls (Table 1 and Fig 2). In contrast, the 10 patients with BMD_Dp140+ presented with no significant differences in FA compared with the BMD_Dp140− group and controls (data not shown). MD, AD, and RD values showed no significant differences in all group comparisons (data not shown).

ROI-Based Analysis of Gray and White Matter Volumes

No significant difference was observed in the gray or white matter volumes between the patients with BMD and the controls ($P > .05$).

Table 1: Results of the voxel-based FA analysis of white matter between the 30 patients with BMD and 30 controls and between the patients with BMD_Dp140– (*n* = 18) and healthy controls (*n* = 30)^a

Analysis	<i>df</i>	Cluster Size	<i>T</i> Value	MNI Coordinates			Regions of Peaks
				<i>x</i>	<i>y</i>	<i>z</i>	
Controls > BMD	57	222	7.67	–45	–34	15	Left planum temporale
		204	7.34	24	–62	42	Right superior parietal lobule
Controls > BMD_Dp140–	45	151	6.63	–46	–34	15	Left planum temporale

Note:—MNI indicates Montreal Neurological Institute.

^a All clusters are significant at a voxel level of *P* < .05 (family-wise error–corrected) and a cluster size of >100 voxels.

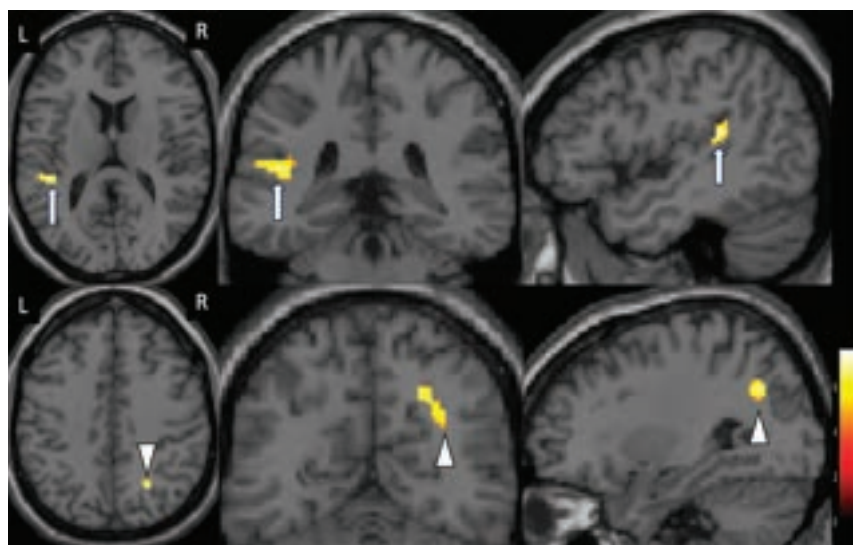


FIG 1. Results of the voxel-based FA analysis between the patients with BMD (*n* = 30) and controls (*n* = 30) (*P* < .05, family-wise error–corrected, voxel level). The FA was significantly decreased in the left planum temporale (arrows) and right superior parietal lobule (arrowheads) of the patients with BMD. The background images are single_subj_T1 images, which are regarded as one of the anatomically standardized images in the SPM12 toolbox. The color scale represents *t* values. L indicates left; R, right.

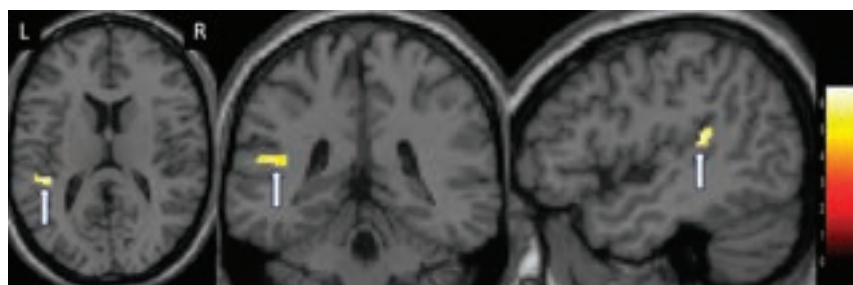


FIG 2. Results of the voxel-based FA analysis between the patients with BMD_Dp140– (*n* = 18) and controls (*n* = 30) (*P* < .05, family-wise error–corrected, voxel-level). The FA was significantly decreased in the left planum temporale (arrows) of the patients with BMD_Dp140–. The color scale represents *t* values. L indicates left; R, right.

ROI-Based DTI Analysis

As shown in Table 2, there was a significant difference in FA values in both the left planum temporale and the right superior parietal lobule between the BMD and control groups (*P* < .01 respectively). Between the 18 patients with BMD_Dp140– and the 30 controls, significant differences in FA values were observed in the left planum temporale (*P* < .01) (Table 3). The ratio of the left-right ROIs of FA values in the planum temporale showed significant differences between the BMD and control group and between the 18

patients with BMD_Dp140– and the control group (*P* < .01 respectively) (Tables 2 and 3).

DISCUSSION

We investigated VBM and DTI metrics in patients with BMD and observed significant FA reductions in the patients' left planum temporale and right superior parietal lobule compared with the healthy controls. The subgroup analyses revealed that the patients with BMD_Dp140– (but not the patients with BMD_Dp140+) had reduced FA in the left planum temporale. To our knowledge, this is the first published investigation of the microstructural differences between individuals with BMD and healthy controls using VBM and DTI analyses. Our findings suggest that the Dp140 dystrophin isoform may play an important role in microstructural abnormalities of the left planum temporale in individuals with BMD.

Neuroimaging studies in large cohorts of patients with DMD have revealed FA reductions in both the supratentorial and infratentorial white matter and indicated that Dp140 expression contributed to the FA changes in patients with DMD.^{10,12} Our present findings demonstrate impaired white matter integrity in the BMD group, and the range of abnormality is more limited than that of patients with DMD. This finding may indicate that BMD manifests with less severity compared with DMD.⁷ Our

comparison of BMD subtypes with the healthy controls revealed significant FA abnormalities in the Dp140– group but not in the Dp140+ group. The differences between the BMD_Dp140– subgroup and controls indicated that the expression of the Dp140 isoform could affect microstructural abnormalities in individuals with BMD and those with DMD. No significant difference was detected in Dp140 expression based on IQ scores; this may be because the intelligence test scores of some of the patients with more severe conditions may not have been available.

Table 2: Comparison of FA values of the ROIs located in the left planum temporale and those flipped to the right hemisphere between the 30 patients with BMD and 30 controls, and the ratio of FA values for the left and right ROIs^a

	Controls (n = 30)			BMD (n = 30)			P Value
	Mean	SD	Range	Mean	SD	Range	
Left planum temporale	0.29	0.04	0.21–0.40	0.23	0.04	0.16–0.30	<.01
ROIs flipped to the right	0.32	0.05	0.23–0.42	0.29	0.05	0.22–0.41	
Ratio of left-right ROIs	0.9	0.13	0.68–1.14	0.8	0.16	0.47–1.09	<.01
Right superior parietal lobule	0.34	0.03	0.28–0.42	0.29	0.04	0.25–0.34	<.01

^a A comparison of FA values of the ROIs located in the right superior parietal lobule is also shown.

Table 3: The FA values of the ROIs located in the left planum temporale and the ROIs flipped to the other hemisphere in 18 patients with BMD_Dp140– and 30 controls

	Controls (n = 30)			BMD_Dp140– (n = 18)			P Value
	Mean	SD	Range	Mean	SD	Range	
Left planum temporale	0.3	0.04	0.22–0.41	0.23	0.03	0.17–0.27	P < .01
ROIs flipped to the right	0.33	0.05	0.24–0.43	0.31	0.02	0.23–0.36	
Ratio of left-right ROIs	0.91	0.13	0.69–1.2	0.78	0.17	0.49–1.09	P < .01

Earlier DTI investigations of patients with DMD reported a significant increase in MD values in the white matter compared with controls.^{10,12} Contrary to this result, we observed no significant differences in MD between the present BMD and control groups. MD is a measure that can be affected by the barriers that restrict the movement of water, such as cell membranes.²³ The loss of the shorter isoforms of dystrophin was reported to be associated with reduced levels of aquaporin-4, a protein involved in membrane permeability.^{24,25} The difference in MD between individuals with DMD and those with BMD may be related to the differential cumulative loss of brain-expressed isoforms, affected by the mutation site along the gene. Axonal degeneration was described as sensitive to AD, whereas demyelination was deemed to be sensitive to RD.²⁶ We observed no significant differences in AD or RD between the present patients with BMD and controls, similar to our findings regarding MD. This result suggests that individuals with BMD may exhibit less-severe axonal and myelin abnormalities.

The present patients with BMD showed reduced FA in the left planum temporale. The established functional lateralization of the left cerebral hemisphere for language functions in most individuals has been confirmed, and the planum temporale has been presumed to be involved in auditory processing.²² Patients with BMD have been reported to have poor verbal working memory despite intact long-term memory and acquired knowledge.⁵ Verbal working memory is thought to reflect a distributed brain network consisting of the frontal lobe and hippocampus.²⁷ Functional MR imaging and electroencephalography studies have indicated an important role of the primary auditory area in the active maintenance of verbal memory and the support of verbal working memory.^{28,29} We thus speculate that the temporal areas with decreased FA in our present patients with BMD may have caused their poor verbal working memory.

In contrast to the alterations in FA, no significant differences in gray or white matter volumes were noted between the BMD and control groups in this study. An investigation of patients with DMD by a VBM analysis showed local gray matter reductions compared with healthy controls.¹⁰ Both the muscles and

brains of individuals with DMD have been reported to be completely missing the full-length 427 kDa dystrophin protein (Dp427), which is normally located in the cerebral cortex.³⁰ Dp427 may be present in small amounts or partially functioning in the brains and muscles of patients with BMD, thus resulting in the absence of significant differences in brain volumes between the present BMD and control groups.

There are some study limitations to consider. A voxel-based analysis is useful for identifying very subtle anatomic changes but is sensitive to registration accuracy. To reduce the effect of misregistration on the statistical analysis, we applied smoothing to the normalized images. We used the conventionally used default smoothing kernel (8-mm Gaussian filter). However, smoothing might aggravate the partial volume problem.¹⁵ Our study was further limited by the small sample size of subgroups of patients with BMD, and the study should, therefore, be viewed as a preliminary study and requires confirmation in larger samples. Because this was a retrospective study, the cognitive profiles of some of the participants were not evaluated by neuropsychological tests. Prospective studies that include more detailed neuropsychological examinations are necessary to investigate the correlation between brain abnormalities and cognitive impairment in patients with BMD.

CONCLUSIONS

We conducted VBM and DTI analyses in patients with BMD, and we observed significantly reduced FA in the left planum temporale in all patients with BMD and in the BMD_Dp140– subgroup compared with the healthy controls, but not in the BMD_Dp140+ subgroup. These results indicate that the Dp140 dystrophin isoform may contribute to temporal microstructural abnormalities in BMD.

ACKNOWLEDGMENTS

We thank the National Center of Neurology and Psychiatry Hospital's Biobank, a member of the National Center Biobank Network (Omae Y, Goto YI, Tokunaga K. National Center Biobank Network. *Human Genome Variation* 2022;9:38,

10.1038/s41439-022-00217-6), for supporting the psychological assessment and data handling.

Disclosure forms provided by the authors are available with the full text and PDF of this article at www.ajnr.org.

REFERENCES

1. Bushby KM, Gardner-Medwin D. **The clinical, genetic and dystrophin characteristics of Becker muscular dystrophy, I: natural history.** *J Neurol* 1993;240:98–104 CrossRef Medline
2. Monaco AP, Bertelson CJ, Liechti-Gallati S, et al. **An explanation for the phenotypic differences between patients bearing partial deletions of the DMD locus.** *Genomics* 1988;2:90–95 CrossRef Medline
3. Hinton VJ, De Vivo DC, Nereo NE, et al. **Poor verbal working memory across intellectual level in boys with Duchenne dystrophy.** *Neurology* 2000;54:2127–32 CrossRef Medline
4. Koeks Z, Hellebrekers DM, van de Velde NM, et al. **The neurocognitive profile of adults with Becker muscular dystrophy in the Netherlands.** *J Neuromuscul Dis* 2022;9:543–53 CrossRef Medline
5. Young HK, Barton BA, Waisbren S, et al. **Cognitive and psychological profile of males with Becker muscular dystrophy.** *J Child Neurol* 2008;23:155–62 CrossRef Medline
6. Mori-Yoshimura M, Mizuno Y, Yoshida S, et al. **Psychiatric and neurodevelopmental aspects of Becker muscular dystrophy.** *Neuromuscul Disord* 2019;29:930–39 CrossRef Medline
7. Muntoni F, Torelli S, Ferlini A. **Dystrophin and mutations: one gene, several proteins, multiple phenotypes.** *Lancet Neurol* 2003;2:731–40 CrossRef Medline
8. Felisari G, Martinelli Boneschi F, Bardoni A, et al. **Loss of dp140 dystrophin isoform and intellectual impairment in Duchenne dystrophy.** *Neurology* 2000;55:559–64 CrossRef Medline
9. Chamova T, Guergueltcheva V, Raycheva M, et al. **Association between loss of dp140 and cognitive impairment in Duchenne and Becker dystrophies.** *Balkan J Med Genet* 2013;16:21–30 CrossRef Medline
10. Doorenweerd N, Straathof CS, Dumas EM, et al. **Reduced cerebral gray matter and altered white matter in boys with Duchenne muscular dystrophy.** *Ann Neurol* 2014;76:403–11 CrossRef Medline
11. Lee JS, Pfund Z, Juhász C, et al. **Altered regional brain glucose metabolism in Duchenne muscular dystrophy: a PET study.** *Muscle Nerve* 2002;26:506–12 CrossRef Medline
12. Preethish-Kumar V, Shah A, Kumar M, et al. **In vivo evaluation of white matter abnormalities in children with Duchenne muscular dystrophy using DTI.** *AJNR Am J Neuroradiol* 2020;41:1271–78 CrossRef Medline
13. Biagi L, Lenzi S, Cipriano E, et al. **Neural substrates of neuropsychological profiles in dystrophinopathies: a pilot study of diffusion tractography imaging.** *PLoS One* 2021;16:e0250420 CrossRef Medline
14. Ashburner J, Friston KJ. **Voxel-based morphometry: the methods.** *Neuroimage* 2000;11:805–21 CrossRef Medline
15. Abe O, Takao H, Gonoi W, et al. **Voxel-based analysis of the diffusion tensor.** *Neuroradiology* 2010;52:699–710 CrossRef Medline
16. Ashburner J. **A fast diffeomorphic image registration algorithm.** *Neuroimage* 2007;38:95–113 CrossRef Medline
17. Seiger R, Ganger S, Kranz GS, et al. **Cortical thickness estimations of FreeSurfer and the CAT12 toolbox in patients with Alzheimer's disease and healthy controls.** *J Neuroimaging* 2018;28:515–23 CrossRef Medline
18. Ota M, Sato N, Maikusa N, et al. **Whole brain analyses of age-related microstructural changes quantified using different diffusional magnetic resonance imaging methods.** *Jpn J Radiol* 2017;35:584–89 CrossRef Medline
19. Kellner E, Dhital B, Kiselev VG, et al. **Gibbs-ringing artifact removal based on local subvoxel-shifts.** *Magn Reson Med* 2016;76:1574–81 CrossRef Medline
20. Veraart J, Novikov DS, Christiaens D, et al. **Denoising of diffusion MRI using random matrix theory.** *Neuroimage* 2016;142:394–406 CrossRef Medline
21. Smith SM. **Fast robust automated brain extraction.** *Hum Brain Mapp* 2002;17:143–55 CrossRef Medline
22. Dorsaint-Pierre R, Penhune VB, Watkins KE, et al. **Asymmetries of the planum temporale and Heschl's gyrus: relationship to language lateralization.** *Brain* 2006;129:1164–76 CrossRef Medline
23. Clark KA, Nuechterlein KH, Asarnow RF, et al. **Mean diffusivity and fractional anisotropy as indicators of disease and genetic liability to schizophrenia.** *J Psychiatr Res* 2011;45:980–88 CrossRef Medline
24. Frigeri A, Nicchia GP, Nico B, et al. **Aquaporin-4 deficiency in skeletal muscle and brain of dystrophic mdx mice.** *FASEB j* 2001;15:90–98 CrossRef Medline
25. Ricotti V, Roberts RG, Muntoni F. **Dystrophin and the brain.** *Dev Med Child Neurol* 2011;53:12 CrossRef Medline
26. Shizukuishi T, Abe O, Aoki S. **Diffusion tensor imaging analysis for psychiatric disorders.** *Magn Reson Med Sci* 2013;12:153–59 CrossRef Medline
27. Bidelman GM, Brown JA, Bashivan P. **Auditory cortex supports verbal working memory capacity.** *Neuroreport* 2021;32:163–68 CrossRef Medline
28. Emch M, von Bastian CC, Koch K. **Neural correlates of verbal working memory: an fMRI meta-analysis.** *Front Hum Neurosci* 2019;13:180 CrossRef Medline
29. Ferrero A, Rossi M. **Cognitive profile and neuropsychiatric disorders in Becker muscular dystrophy: a systematic review of literature.** *Neurosci Biobehav Rev* 2022;137:104648 CrossRef Medline
30. Kim TW, Wu K, Black IB. **Deficiency of brain synaptic dystrophin in human Duchenne muscular dystrophy.** *Ann Neurol* 1995;38:446–49 CrossRef Medline

Comparison of Quantitative Hippocampal Volumes and Structured Scoring Scales in Predicting Alzheimer Disease Diagnosis

Michael Essien, James Lah, Brent D. Weinberg, Jason W. Allen, and Ranliang Hu



ABSTRACT

BACKGROUND AND PURPOSE: Brain imaging plays an important role in investigating patients with cognitive decline and ruling out secondary causes of dementia. This study compares the diagnostic value of quantitative hippocampal volumes derived from automated volumetric software and structured scoring scales in differentiating Alzheimer disease, mild cognitive impairment, and subjective cognitive decline.

MATERIALS AND METHODS: Retrospectively, we reviewed images and medical records of adult patients who underwent MR imaging with a dementia protocol (2018–2021). Patients with postscanning diagnoses of Alzheimer disease, mild cognitive impairment, and subjective cognitive decline based on the International Statistical Classification of Diseases and Related Health Problems, 10th revision, were included. Diagnostic performances of automated normalized total hippocampal volume and structured manually assigned medial temporal atrophy and entorhinal cortical atrophy scores were assessed using multivariate logistic regression and receiver operating characteristic curve analysis.

RESULTS: We evaluated 328 patients (Alzheimer disease, $n=118$; mild cognitive impairment, $n=172$; subjective cognitive decline, $n=38$). Patients with Alzheimer disease had lower normalized total hippocampal volume (median, 0.35%), higher medial temporal atrophy (median, 3), and higher entorhinal cortical atrophy (median, 2) scores than those with subjective cognitive decline ($P<.001$) and mild cognitive impairment ($P<.001$). For discriminating Alzheimer disease from subjective cognitive decline, an entorhinal cortical atrophy cutoff value of 2 had a higher specificity (87%) compared with normalized total hippocampal volume (74%) and medial temporal atrophy (66%), but a lower sensitivity (69%) than normalized total hippocampal volume (84%) and medial temporal atrophy (84%). In discriminating Alzheimer disease from mild cognitive impairment, an entorhinal cortical atrophy cutoff value of 3 had a specificity (66%), similar to that of normalized total hippocampal volume (67%) but higher than medial temporal atrophy (54%), and its sensitivity (69%) was also similar to that of normalized total hippocampal volume (71%) but lower than that of medial temporal atrophy (84%).

CONCLUSIONS: Entorhinal cortical atrophy and medial temporal atrophy may be useful adjuncts in discriminating Alzheimer disease from subjective cognitive decline, with reduced cost and implementation challenges compared with automated volumetric software.

ABBREVIATIONS: AD = Alzheimer disease; ERICA = entorhinal cortical atrophy; ICD-10 = International Statistical Classification of Diseases and Related Health Problems, 10th revision; IQR = interquartile range; MCI = mild cognitive impairment; MTA = medial temporal lobe atrophy; NTHV = normalized total hippocampal volume; ROC = receiver-operating characteristic; SCD = subjective cognitive decline

Dementia is characterized by progressive loss of brain structure and function, resulting in a loss of intellectual abilities and

interference with social or occupational functions.¹ It is estimated that about 50 million people worldwide are affected by dementia, and this number is expected to triple to 150 million by 2050.² The most common cause of dementia is Alzheimer disease (AD).

The diagnosis of AD is often based on clinical history, neuropsychological evaluation, CSF markers, and imaging tests such as PET and MR imaging. Brain MR imaging is routinely performed in patients being evaluated for cognitive decline, and it is helpful in ruling out secondary causes of dementia. Subjective cognitive decline (SCD), mild cognitive impairment (MCI), and AD are not mutually

Received May 2, 2023; accepted after revision October 4.

From the Departments of Radiology and Imaging Sciences (M.E., B.D.W., J.W.A., R.H.), and Neurology (J.L.), Emory University School of Medicine, Atlanta, Georgia.

Please address correspondence to Ranliang Hu, MD, Emory University School of Medicine, Division of Neuroradiology, 1364 Clifton Rd NE, Ste BG20, Atlanta, GA 30322; e-mail: Ranliang.hu@emory.edu



Indicates article with online supplemental data.

<http://dx.doi.org/10.3174/ajnr.A8049>

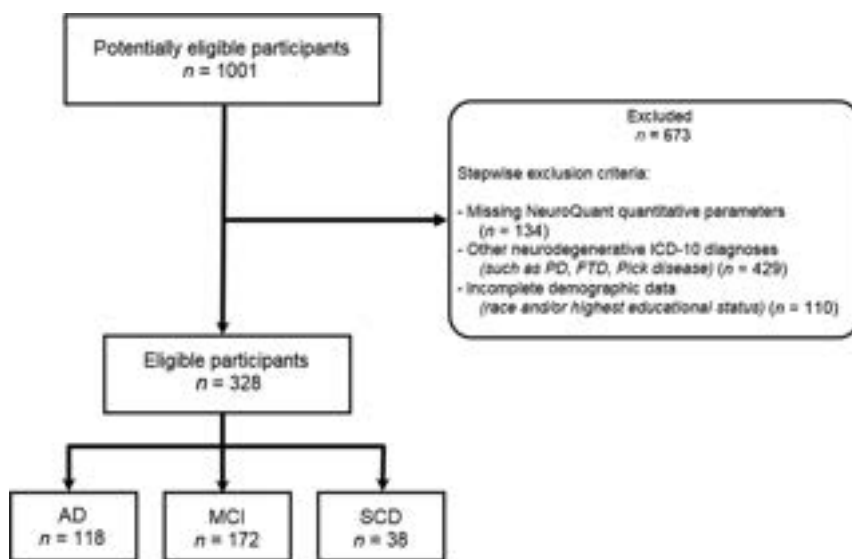


FIG 1. Flow chart of study participants. Only diagnoses made after MR imaging were considered for this study. PD indicates Parkinson disease; FTD, frontotemporal dementia.

exclusive states, and MCI has been described as a transitional phase between SCD and AD, with overlapping boundaries; some patients eventually convert to AD, while others remain stable.³

Recently, there has been increased clinical availability of automated software tools such as NeuroQuant (Version 2.3.0; Cortechs, San Diego, California) and icobrain (icomatrix, Leuven, Belgium) that measure overall and regional brain volumes and compare them with those of age-matched healthy controls. These tools provide an abundance of volumetric data and the potential for longitudinal tracking, but their diagnostic value in the clinical evaluation of dementia has not been widely adopted in clinical practice due to the wide variation in their technical and clinical validations for clinical practice, the lack of access to software algorithms, and the difficulty in integrating these tools into the clinical reporting workflow.^{4,5}

Attempts have been made to develop validated semiquantitative visual assessment tools that use clear definitions of what constitutes atrophy along with visual examples of each score, including the medial temporal atrophy (MTA)⁶ and entorhinal cortical atrophy (ERiCA) scores.⁷ These scores can reduce reporting variability and facilitate communication between radiologists and referring clinicians, and they have been shown, in some studies, to have high diagnostic accuracy.⁷

The primary purpose of our study was to compare the diagnostic value of quantitative regional brain volumes derived from NeuroQuant and structured scoring scales in the evaluation of AD.

MATERIALS AND METHODS

Study Design and Patient Selection

This was a Health Insurance Portability and Accountability Act-compliant retrospective review that was approved by our institutional review board. The need for patient-informed consent was waived. We reviewed imaging studies and medical records of adult patients from 2018 to 2021 at 5 centers that fall under the umbrella of a single health care institution.

The inclusion criteria were adult patients who had undergone MR imaging with the dementia protocol within the search period and who had postscanning International Statistical Classification of Diseases and Related Health Problems, 10th revision (ICD-10) diagnoses of AD or MCI, including those having SCD. Exclusion criteria were patients with missing NeuroQuant quantitative parameters, patients with other neurodegenerative ICD-10 diagnoses (such as Parkinson disease, frontotemporal dementia, Pick disease), and those with incomplete demographic data (race and/or highest education). The study participants' flow chart is shown in Fig 1.

Clinical Scenarios and Diagnoses

Requests for MR imaging with the dementia protocol were received from neurologists and primary care physicians within the institution's health care network and also from providers outside the network. These included requests from first-line memory clinics, doctor's offices, and tertiary referral centers. All patients were eventually reviewed by board-certified neurologists with additional subspecialty certification in Behavioral Neurology and Neuropsychiatry from the United Council for Neurologic Subspecialties. The final diagnosis was based on a comprehensive neurologic examination, detailed cognitive testing, review of laboratory tests and brain MR imaging scans, and additional CSF biomarker testing as appropriate. The diagnostic guidelines used are consistent with the 2011 National Institute on Aging-Alzheimer's Association revised diagnostic criteria for AD.⁸ In the selection of patients, we considered only those diagnoses made postscanning to be valid for our research.

Imaging Acquisition and Analysis

Brain MR imaging was performed on one of several 1.5T or 3T MR imaging scanners using our institutional dementia MR imaging protocol. All examinations included a volumetric T1-weighted sequence with 1-mm isotropic voxels in addition to standard brain MR imaging sequences. The exact sequence parameters varied among scanners due to scanner differences, but a representative MPRAGE sequence was performed with 1-mm section thickness, 1-mm in-plane resolution, FOV = 256 × 256 mm, TR = 2.3 seconds, TE = 3.17 ms, bandwidth = 210 Hz. Images were acquired in the sagittal plane and reformatted to the axial and coronal planes. Assessment of MTA and ERiCA scores was performed on coronal images by the interpreting board-certified and Certificate of Added Qualification-certified neuroradiologists according to published guides.^{6,7} To summarize, the MTA score is a quantification of temporal atrophy using the hippocampal height and width of neighboring CSF space, with scores ranging from 0 (no atrophy) to 4 (severe atrophy).⁶ The ERiCA score is a quantification of entorhinal cortex

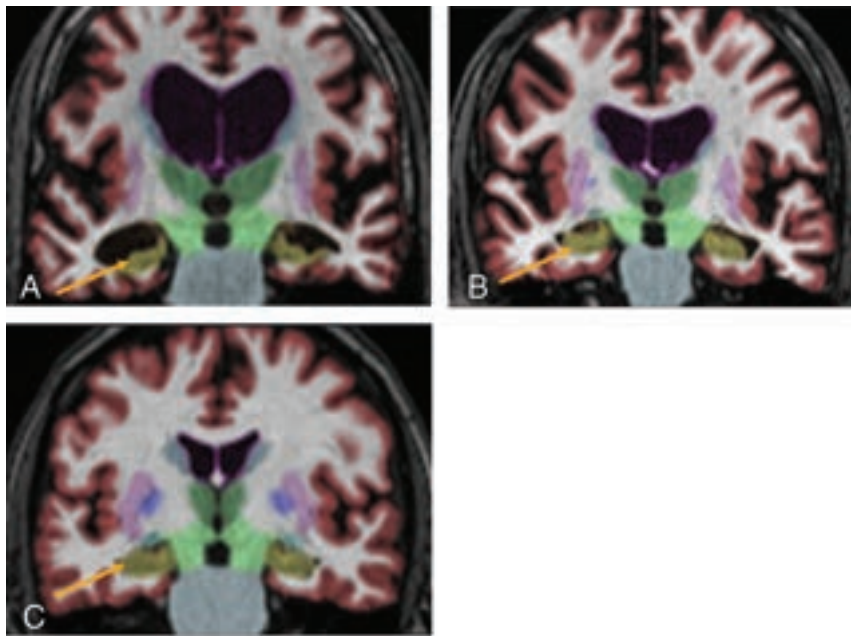


FIG 2. Coronal T1 noncontrast MR images with automated segmentation overlay obtained from NeuroQuant showing hippocampal volumes (yellow arrow) for patients with AD (A), mild cognitive impairment (B), and SCD (C). Note the marked hippocampal atrophy for AD compared with MCI and SCD.

atrophy assessed at the level of the mammillary bodies, with scores ranging from 0 (normal) to 3 (severe atrophy).⁷ Quantitative assessment was performed using NeuroQuant, which performed volumetric segmentation on the volumetric T1-weighted series and output quantitative volumes and ratios to the PACS. All imaging analyses were performed at the time of clinical interpretation, and no post hoc analysis was performed, to simulate a realistic clinical environment. Figure 2 shows examples of MR images obtained from NeuroQuant for patients with AD, MCI, and SCD.

Outcome and Predictor Variables

The outcome variables used were AD, MCI, and SCD. Normalized total hippocampal volume (NTHV), maximum MTA scores, and maximum ERiCA scores were used as predictor variables. NTHV was calculated by assessing the right and left hippocampal volumes generated separately by NeuroQuant, summing the 2 values, and expressing the resultant value as a percentage of each patient's intracranial volume [(right hippocampal volume + left hippocampal volume)/ICV]. Values generated by NeuroQuant are normalized to an age-specific cohort. MTA and ERiCA scores were assigned to each temporal lobe separately by the interpreting radiologists at the time of clinical interpretation using a structured visual scoring routine. Scores were obtained retrospectively from the radiology report. The higher value of the right and left MTA or ERiCA scores, which we termed maximum MTA or maximum ERiCA, was used for analysis.

Covariates

Covariates were sex, race, highest education attained, age at diagnosis, a history of arterial hypertension, and a history of diabetes mellitus.

Statistical Analysis

The χ^2 test was used to determine associations between categorical variables and the disease outcomes. The Kruskal-Wallis test was used to determine associations between continuous variables and disease outcomes because observations in these variables assumed a non-normal distribution based on the Shapiro-Wilk test for normality. Differences between comparison groups (AD versus MCI, AD versus SCD, and MCI versus SCD) were calculated in a post hoc analysis. Linear correlational analysis of quantitative and qualitative measures was assessed using the Spearman correlation. Multivariate logistic regression analyses were performed with a stepwise addition of predictors. Diagnostic performances of predictor variables were assessed by receiver operating characteristic (ROC) analyses, and the cutoff value for each parameter was calculated using the maximum Youden index. An α level of .05 was

set as the level of significance. SAS software, Version 9.4 (SAS Institute, Cary, North Carolina) was used for all analyses.

RESULTS

A total of 328 imaging studies were evaluated (118 patients with AD: median age, 78 years; interquartile range [IQR], 71–84 years; 172 patients with MCI: median age, 74 years; IQR, 69–78 years; and 38 patients with SCD: median age, 67 years; IQR, 54–78 years). The time from the MR imaging dementia protocol scan to the date of the ICD-10 diagnosis varied among the 3 groups (AD group: median time, 48 days; IQR, 15–98 days; MCI group: median time, 6 days; IQR, 3–62 days; and SCD group: median time, 20 days; IQR, 3–171 days).

Descriptive analyses indicated that only age at diagnosis, NTHV, MTA, and ERiCA scores were significantly different across the 3 outcome variables (Table 1 and Fig 3). In a post hoc analysis, patients with AD were older (median age, 78 years), had lower NTHVs (median, 0.35%), higher MTA score (median, 3), and higher ERiCA scores (median, 2) than those with SCD ($P < .001$) and MCI ($P < .001$).

There was a fairly strong positive linear correlation between MTA and ERiCA ($r = 0.82$), and a moderate negative linear correlation between NTHV and the visual scales (MTA and ERiCA). The correlation between MTA and NTHV ($r = -0.76$) was found to be significantly higher than that between ERiCA and NTHV ($r = -0.71$) ($P = .02$).

In multivariate logistic regression analyses, when we controlled for age at diagnosis, sex, race, highest educational level, history of arterial hypertension, and diabetes mellitus, only ERiCA remained as a significant predictor ($P = .02$) in discriminating AD from SCD. Regarding the differentiation of AD from MCI, NTHV was

Table 1: Descriptive statistics^a

Characteristic	AD	MCI	SCD	P Value
Sex				.93
Male (%)	39.8	41.9	42.1	
Female (%)	60.2	58.1	57.9	
Race				.23
Caucasian or white (%)	58.5	68.0	60.5	
Other (%)	41.5	32.0	39.5	
Highest education				.15
≤High school (%)	28.8	20.9	15.8	
>High school (%)	71.2	79.1	84.2	
Arterial hypertension				.45
Yes (%)	71.2	66.9	60.5	
No (%)	28.8	33.1	39.5	
Diabetes mellitus				.14
Yes (%)	18.6	23.3	34.2	
No (%)	81.4	76.7	65.8	
Age at diagnosis (yr)	78 (71–84)	74 (69–78)	67 (54–78)	<.001 ^b
NTHV (%)	0.35 (0.33–0.37)	0.41 (0.40–0.43)	0.48 (0.42–0.50)	<.001 ^b
Maximum MTA score	3.0 (2.0–3.0)	1.0 (0.0–2.0)	1.0 (0.0–2.0)	<.001 ^b
Maximum ERiCA score	2.0 (1.0–2.0)	1.0 (0.0–2.0)	1.0 (0.0–1.0)	<.001 ^b

^a 50% median and interquartile ranges (in parentheses) are shown for age at diagnosis, NTHV, maximum MTA and maximum ERiCA scores. Maximum MTA and maximum ERiCA refer to the higher scores of the right and left values of the respective parameters.

^b Denotes statistical significance at $\alpha = .05$.

the only significant predictor ($P = <.001$) in the adjusted model. In the discrimination of MCI from SCD, none of the predictors remained significant (Online Supplemental Data).

In the ROC analyses, the model containing ERiCA, MTA, NTHV, and age at diagnosis was used. All 3 predictors (NTHV, MTA, and ERiCA) were significantly better than chance in the discrimination of AD from SCD. Area under the curve values for each were the following: NTHV (0.83), ERiCA (0.83), and MTA (0.80) (Fig 4 and Online Supplemental Data). There was no statistically significant difference between NTHV versus MTA ($P = .37$), ERiCA versus MTA ($P = .28$), and NTHV versus ERiCA ($P = .90$). Regarding the differentiation of AD from MCI, all 3 predictors were significantly better than

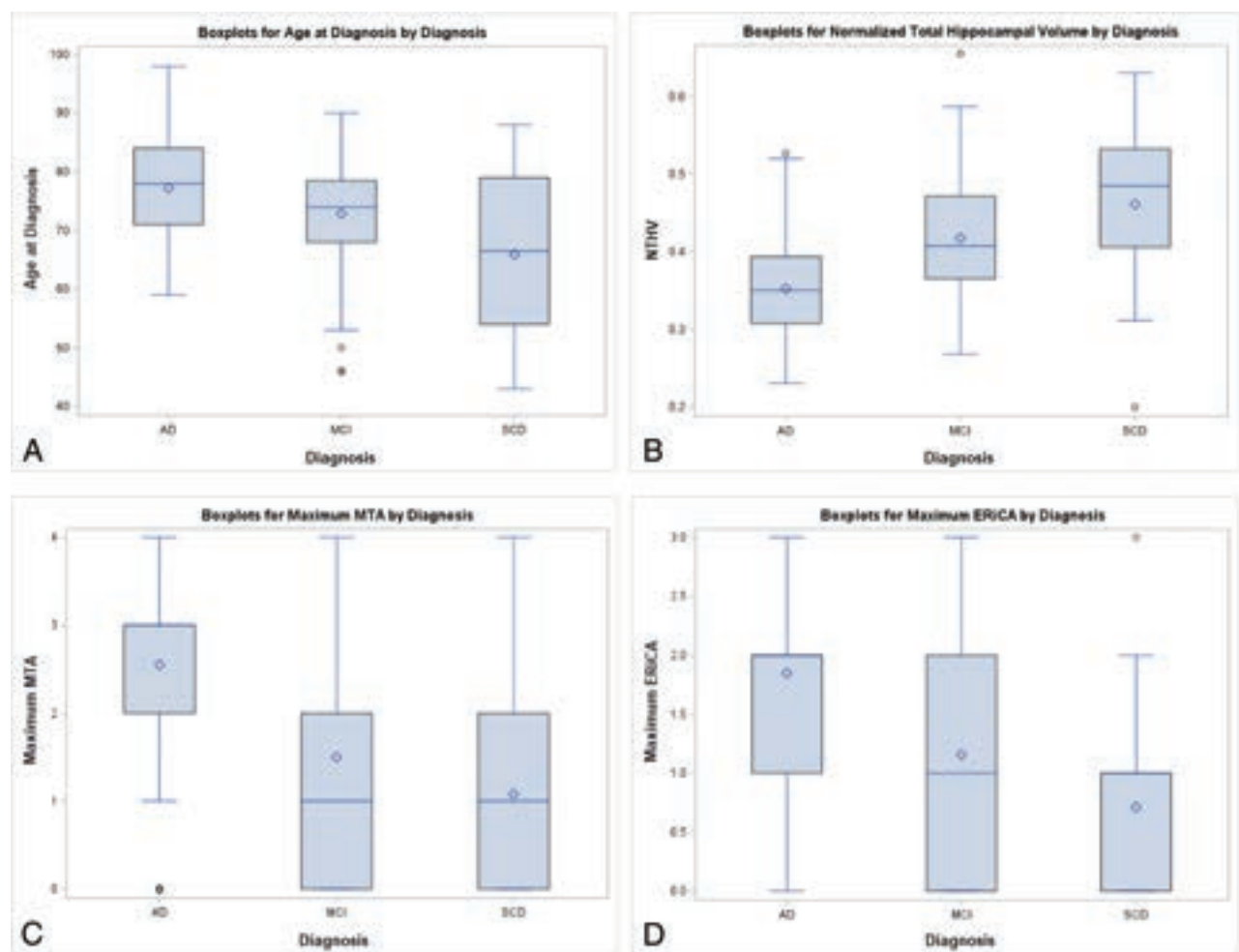


FIG 3. Boxplot graphs of the variables age at diagnosis (A), NTHV (B), maximum MTA (C), and maximum ERiCA (D) scores against the outcome variables AD, MCI, and SCD. The maximum and minimum values are represented at either end of the whiskers. The box represents the interquartile range (25th percentile to the 75th percentile), with the median represented by the line within the box, and the mean shown by the diamond. Outliers are shown by a circle. Maximum MTA and maximum ERiCA refer to the higher score of the right and left values of the respective parameters.

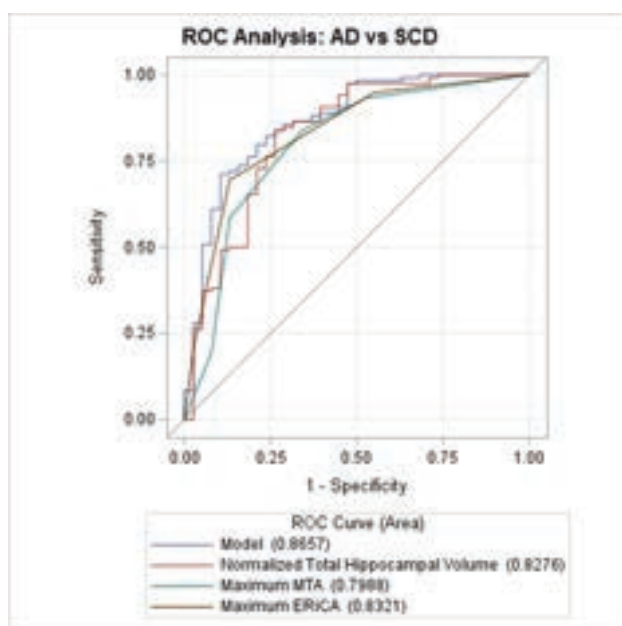


FIG 4. ROC curves for AD versus SCD. The overall model includes normalized total hippocampal volume, maximum MTA, maximum ERiCA, and age at diagnosis. Maximum MTA and maximum ERiCA refer to the higher score of the right and left values of the respective parameters.

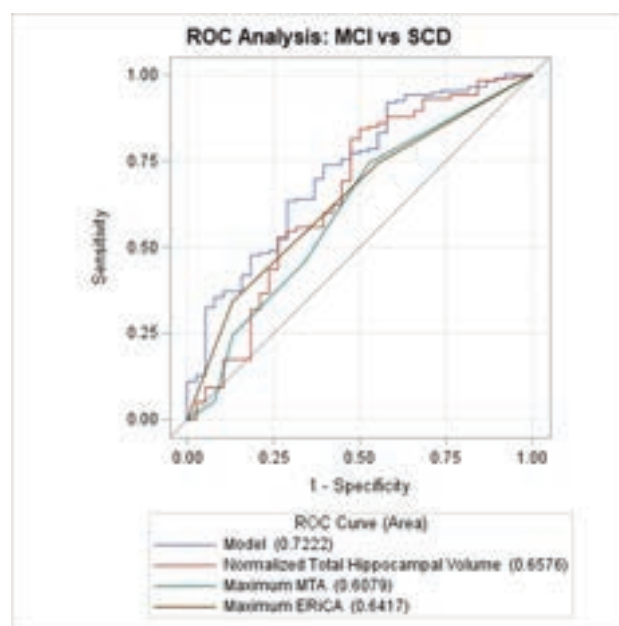


FIG 6. ROC curves for MCI versus SCD. The overall model includes NTHV, maximum MTA, maximum ERiCA, and age at diagnosis. Maximum MTA and maximum ERiCA refer to the higher scores of the right and left values of the respective parameters.

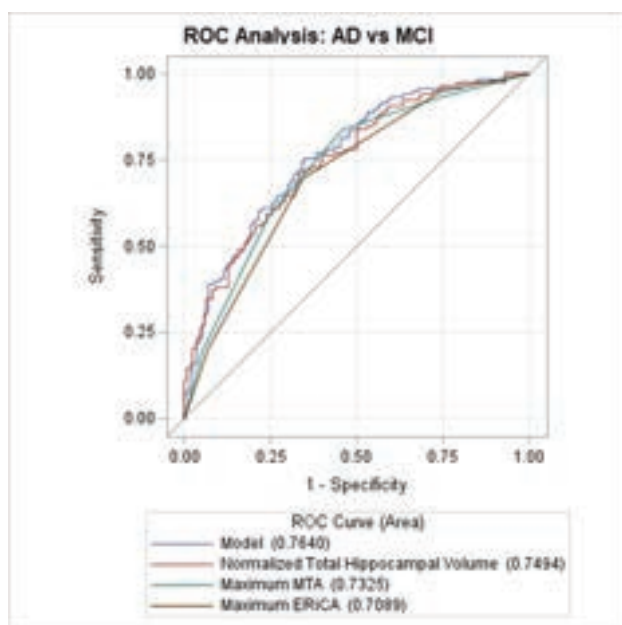


FIG 5. ROC curves for AD versus MCI. The overall model includes normalized total hippocampal volume, maximum MTA, maximum ERiCA, and age at diagnosis. Maximum MTA and maximum ERiCA refer to the higher score of the right and left values of the respective parameters.

chance. Area under the curve values for each were the following: NTHV (0.75), ERiCA (0.71), and MTA (0.73). There was no statistically significant difference between NTHV versus MTA ($P = .47$), ERiCA versus MTA ($P = .25$), and NTHV versus ERiCA ($P = .12$) (Fig 5 and Online Supplemental Data). When MCI was

compared with SCD, the confidence intervals of all 3 predictors included the value 0.5, implying that all 3 parameters are poor discriminators (Fig 6 and Online Supplemental Data).

In the discrimination of AD from SCD, an ERiCA cutoff value of 2 had a lower sensitivity (69%) compared with NTHV (84%) and MTA (84%) but had a higher specificity (87%) than NTHV (74%) and MTA (66%) (Table 2). When AD was compared with MCI, an ERiCA cutoff value of 3 had a sensitivity (69%) similar to that of NTHV (71%) but lower than that of MTA (84%); the ERiCA value had a specificity (66%) similar to that of NTHV (67%) but was higher than that of MTA (54%) (Table 3).

DISCUSSION

Our study compared the diagnostic performance of quantitative measurement (derived from automated volumetric assessment) and visual inspection scales in the discrimination of AD from SCD and MCI. The quantitative measure used was NTHV, while MTA and ERiCA scores were used as visual-inspection parameters. The interrater reliability analyses of the visual inspection parameters have been previously studied and have been shown to be good.^{7,9}

As expected, the correlation coefficient between MTA and NTHV was significantly higher than that between ERiCA and NTHV. This result is because MTA is a measure of hippocampal atrophy, whereas ERiCA is a measure of entorhinal cortical atrophy and not a direct assessment of hippocampal volume.^{6,8,10} This finding also explains why the OR of MTA in the prediction model differentiating AD from MCI loses statistical significance when NTHV is introduced into the model but is maintained when only ERiCA as a predictor variable is introduced in addition to other covariates. Statistically significant higher ORs were seen for ERiCA (OR, ≥ 2.0) in the unadjusted and adjusted AD-

Table 2: Predictor diagnostic performances—AD versus SCD^a

Parameter	Cutoff Value	Sensitivity	Specificity	Accuracy
NTHV (%)	0.41	99/118 (84) [76–90]	28/38 (74) [60–88]	127/156 (81) [75–87]
Max MTA score: all ages	2.0	99/118 (84) [77–91]	25/38 (66) [51–81]	124/156 (79) [73–86]
MTA score: <75 years	2.0	32/44 (73) [60–86]	23/27 (85) [72–99]	55/71 (77) [68–87]
MTA score: ≥75 years	3.0	50/74 (68) [57–78]	8/11 (73) [46–99]	58/85 (68) [58–78]
Max ERiCA score	2.0	82/118 (69) [61–78]	33/38 (87) [76–98]	115/156 (74) [67–81]

Note:—Max indicates maximum.

^aPatient numbers shown in sensitivity, specificity, and accuracy columns with percentage scores (in parentheses) and 95% confidence intervals [in brackets]. Maximum MTA and maximum ERiCA refer to the higher score of the right and left values of the respective parameters.

Table 3: Predictor diagnostic performances—AD versus MCI^a

Parameter	Cutoff Value	Sensitivity	Specificity	Accuracy
NTHV (%)	0.38	84/118 (71) [62–79]	115/172 (67) [59–74]	199/290 (69) [63–74]
Max MTA score: all ages	2.0	99/118 (84) [77–91]	93/172 (54) [47–62]	192/290 (66) [61–72]
MTA score: <75 years	2.0	32/44 (73) [60–86]	63/90 (70) [61–79]	95/134 (71) [63–79]
MTA score: ≥75 years	3.0	50/74 (68) [57–78]	51/82 (62) [52–73]	101/156 (65) [57–72]
Max ERiCA score	3.0	82/118 (69) [61–78]	113/172 (66) [59–73]	195/290 (67) [62–73]

Note:—Max indicates maximum.

^aPatient numbers shown in sensitivity, specificity, and accuracy columns with percentage scores (in parentheses) and 95% confidence intervals [in brackets].

versus-SCD prediction models, and a statistically significant OR (OR, 1.7) was demonstrated for MTA in the unadjusted AD-versus-MCI prediction model (MTA and ERiCA as predictors). Even though hippocampal atrophy (either by volume or MTA) is a hallmark of AD that has been demonstrated in multiple prior studies^{7,11–14} and also confirmed in our study, it is not as predictive as it should have been in the AD-versus-SCD group, but rather discriminative when the difference in atrophy was expected to be lower (AD versus MCI group). These overlapping results potentially help to re-emphasize the clinical relevance that SCD, MCI, and AD are not mutually exclusive states but exist with overlaps in a cognitive continuum. The entorhinal cortex has been identified as a distinct early marker of AD pathology before significant hippocampal atrophy,^{7,15–17} and this can be demonstrated in the ERiCA results obtained in the AD-versus-SCD models.

An ERiCA cutoff value of 2 produced a sensitivity of 69% and a specificity of 87%, which are lower than those reported by Enkirch et al.⁷ Our results do, however, show the higher specificity of ERiCA compared with MTA in discriminating AD and SCD, supportive of their findings. The lower diagnostic performance of ERiCA in our study reflects what can be expected in a larger cohort with clinical interpretation from multiple reporting neuroradiologists in a routine setting instead of dedicated research reviewers. The sensitivity and specificity of MTA scores in discriminating AD from controls varies across studies, with sensitivity ranges from 57% to 100% and specificity ranges from 67% to 100%.^{6,7,12,18–20} In our study, we calculated the sensitivity and specificity of the MTA cutoff point for all ages (MTA, 2) in discriminating AD from SCD to be 84% and 66%, respectively.

In discriminating AD and MCI, our study produced an area under the curve value of 0.71, which is the same as that calculated by Traschütz et al.²¹ and ERiCA also showed higher specificity but lower sensitivity in the differentiation of AD from MCI as estimated by Roberge et al.²² Even though the ROC analyses indicate that all 3 diagnostic tests (NTHV, MTA, and ERiCA) are

better than chance in differentiating AD from MCI, their sensitivity and specificity values as shown in the results indicate challenges in using only these parameters in the diagnosis of dementia.

Our study had limitations, including the retrospective study design and the small sample size of the SCD group. Also, the SCD group is not truly a healthy group because these individuals presented to the clinic with varied cognitive symptoms for which they underwent the MR imaging dementia protocol scan. Because our study relied on NeuroQuant, which we use only in the context of a referral for assessment of some form of cognitive impairment, we did not have NeuroQuant data on true healthy patients. Nevertheless, the SCD group may serve as a useful comparison group because it reflects a realistic sampling of the patient population who undergo the MR imaging dementia protocol. In addition, even though the brain MR imaging scan result is just one component used in the diagnosis of dementia, its impression could still possibly bias the final definitive diagnosis. Last, even though the NeuroQuant analyses were conducted at the time of performing the dementia scan protocol, interpreting neuroradiologists scored MTA and ERiCA on the basis of standardized criteria and a visual guide, independent of the NeuroQuant analyses and as per our institutional practice. However, because the reporting neuroradiologists were not completely blinded to the NeuroQuant analyses, the reported visual assessment scores could potentially have been influenced by the NeuroQuant results.

CONCLUSIONS

The structured scoring scale, ERiCA, had lower sensitivity but higher specificity compared with NTHV and MTA in the discrimination of AD from SCD. In a multivariable model, only ERiCA remained as an independent predictor. Our results support the inclusion of the ERiCA score in the radiologic assessment of MR imaging performed for suspected dementia, in addition to the more widely used MTA score because these 2 scores when used together may be helpful supplements to the

evaluation of dementia, especially if automated quantitative analysis is not available.

Disclosure forms provided by the authors are available with the full text and PDF of this article at www.ajnr.org.

REFERENCES

1. World Health Organization. *International statistical classification of diseases and related health problems*. 2016 (10th ed.). Available at: <https://icd.who.int/browse10/2016/en>. Accessed October 3, 2023
2. Alzheimer's Disease International. **Number of People with Dementia Around the World. 2017**. <https://www.alzint.org/u/numbers-people-with-dementia-2017.pdf>. Accessed April 25, 2023
3. Petersen RC. **Mild cognitive impairment as a diagnostic entity**. *J Intern Med* 2004;256:183–94 CrossRef Medline
4. Vernooij MW, Pizzini FB, Schmidt R, et al. **Dementia imaging in clinical practice: a European-wide survey of 193 centres and conclusions by the ESNR working group**. *Neuroradiology* 2019;61:633–42 CrossRef Medline
5. Pemberton HG, Zaki LA, Goodkin O, et al. **Technical and clinical validation of commercial automated volumetric MRI tools for dementia diagnosis: a systematic review**. *Neuroradiology* 2021;63:1773–89 CrossRef Medline
6. Scheltens P, van de Pol L. **Atrophy of medial temporal lobes on MRI in “probable” Alzheimer's disease and normal ageing: diagnostic value and neuropsychological correlates**. *J Neurol Neurosurg Psychiatry* 2012;83:1038–40 CrossRef Medline
7. Enkirsch SJ, Traschütz A, Müller A, et al. **The ERICA score: an MR imaging-based visual scoring system for the assessment of entorhinal cortex atrophy in Alzheimer disease**. *Radiology* 2018;288:226–333 CrossRef Medline
8. McKhann GM, Knopman DS, Chertkow H, et al. **The diagnosis of dementia due to Alzheimer's disease: recommendations from the National Institute on Aging-Alzheimer's Association workgroups on diagnostic guidelines for Alzheimer's disease**. *Alzheimers Dement* 2011;7:263–69 CrossRef Medline
9. Molinder A, Ziegelitz D, Maier SE, et al. **Validity and reliability of the medial temporal lobe atrophy scale in a memory clinic population**. *BMC Neurol* 2021;21:289 CrossRef Medline
10. Dubois B, Feldman HH, Jacova C, et al. **Revising the definition of Alzheimer's disease: a new lexicon**. *Lancet Neurol* 2010;9:1118–27 CrossRef Medline
11. Laakso MP, Soininen H, Partanen K, et al. **MRI of the hippocampus in Alzheimer's disease: sensitivity, specificity, and analysis of the incorrectly classified subjects**. *Neurobiol Aging* 1998;19:23–31 CrossRef Medline
12. Min J, Moon WJ, Jeon JY, et al. **Diagnostic efficacy of structural MRI in patients with mild-to-moderate Alzheimer disease: automated volumetric assessment versus visual assessment**. *AJR Am J Roentgenol* 2017;208:617–23 CrossRef Medline
13. Falgas N, Sanchez-Valle R, Bargallo N, et al. **Hippocampal atrophy has limited usefulness as a diagnostic biomarker on the early onset Alzheimer's disease patients: a comparison between visual and quantitative assessment**. *Neuroimage Clin* 2019;23:101927 CrossRef Medline
14. Wei M, Shi J, Ni J, et al. **A new age-related cutoff of medial temporal atrophy scale on MRI improving the diagnostic accuracy of neurodegeneration due to Alzheimer's disease in a Chinese population**. *BMC Geriatr* 2019;19:59 CrossRef Medline
15. Du AT, Schuff N, Kramer JH, et al. **Higher atrophy rate of entorhinal cortex than hippocampus in AD**. *Neurology* 2004;62:422–27 CrossRef Medline
16. Bottero V, Powers D, Yalamanchi A, et al. **Key disease mechanisms linked to Alzheimer's disease in the entorhinal cortex**. *Int J Mol Sci* 2021;22:3915 CrossRef Medline
17. Fagone P, Mangano K, Martino G, et al. **Characterization of altered molecular pathways in the entorhinal cortex of Alzheimer's disease patients and in silico prediction of potential repurposable drugs**. *Genes (Basel)* 2022;13:703 CrossRef Medline
18. Wahlund LO, Julin P, Lindqvist J, et al. **Visual assessment of medial temporal lobe atrophy in demented and healthy control subjects: correlation with volumetry**. *Psychiatry Res* 1999;90:193–99 CrossRef Medline
19. Bresciani LC, Rossi R, Testa C, et al. **Visual assessment of medial temporal atrophy on MR films in Alzheimer's disease: comparison with volumetry**. *Aging Clin Exp Res* 2005;17:8–13 CrossRef Medline
20. Claus JJ, Staekenborg SS, Holl DC, et al. **Practical use of visual medial temporal lobe atrophy cut-off scores in Alzheimer's disease: validation in a large memory clinic population**. *Eur Radiol* 2017;27:3147–55 CrossRef Medline
21. Traschütz A, Enkirsch SJ, Polomac N, et al. **The entorhinal cortex atrophy score is diagnostic and prognostic in mild cognitive impairment**. *J Alzheimers Dis* 2020;75:99–108 CrossRef Medline
22. Roberge X, Brisson M, Laforce RJ. **Specificity of entorhinal atrophy MRI scale in predicting Alzheimer's disease conversion**. *Can J Neurol Sci* 2023;50:112–14 CrossRef Medline

Cervical Osteomyelitis and Diskitis as a Complication of Neopharyngeal Breakdown: A Multisite Case Series Review

 Alok A. Bhatt,  Prasanna Vibhute,  Xin Cynthia Wu,  Edward J. Escott,  Charlotte Chung, and  Patricia A. Rhyner



ABSTRACT

SUMMARY: Laryngectomy and pharyngectomy are surgical options for advanced laryngeal or pharyngeal squamous cell carcinoma. Cervical osteomyelitis-diskitis, occurring when there is dehiscence of the posterior neopharyngeal wall, is an uncommon complication of laryngopharyngectomy. This case series describes imaging findings of pharyngoesophageal wall breakdown with subsequent cervical spine infection and demonstrates that most of these patients had undergone prior esophageal or neopharyngeal dilations for benign posttreatment stricture. Neck pain, fever, or serologic evidence of infection should prompt careful evaluation for osteomyelitis-diskitis and assessment for neopharyngeal breakdown and sinus tract formation, especially in the postdilation setting.

ABBREVIATION: SCCA = squamous cell carcinoma

Treatment of advanced or recurrent head and neck cancer usually involves multiple modalities, including surgical resection, radiation therapy, and/or chemotherapy. For advanced laryngeal and pharyngeal squamous cell carcinoma (SCCA), the surgical options are generally laryngectomy or pharyngectomy, which create defects that are managed by primary closure or flap reconstruction.¹ In addition to defect closure, a neopharynx is constructed to restore swallowing. A cutaneous fistula between the neopharynx and skin is a complication that is readily recognized by clinical examination of the treated neck. Neopharyngeal or pharyngoesophageal ulceration and anastomotic breakdown of the posterior wall, with subsequent sinus tract formation, are, however, uncommon and underrecognized complications.² Risk factors for perforation are those resulting in poor soft-tissue healing, including prior chemo-/radiation therapy, poor nutritional status, and continued tobacco and alcohol use.^{3,4} Ulceration and perforation most commonly occur on the posterior neopharyngeal wall.⁵ Such perforations or microperforations establish conditions under which cervical osteomyelitis and diskitis can result.

The purpose of this retrospective, multisite clinical series is to describe 11 patients who developed osteomyelitis-diskitis following laryngopharyngectomy for tumor resection, pharyngeal reconstruction, and adjuvant radiation.⁶

Case Series

Institutional review board approval from each institution (Mayo Clinic Jacksonville, Emory University, University of Kentucky) was obtained. A total of 11 patients comprised the study population. Seven of 11 patients were identified at the time of imaging performed for “neck pain” or possible infection. Additional cases were identified retrospectively; databases were searched for “laryngectomy,” “pharyngectomy,” “diskitis” or “osteomyelitis.” Electronic medical records were reviewed to confirm cervical osteomyelitis-diskitis after laryngectomy or pharyngectomy. Imaging was reviewed by group consensus.

There were 9 male and 2 female patients (age range, 60–78 years, with an average age of 65.5 years). All patients had undergone surgical resection for SCCA of the larynx (10/11) or hypopharynx (1/11). All were also treated with adjuvant radiation. All patients had flap reconstruction after laryngopharyngectomy, either as the initial surgery or after recurrent tumor. The average time between initial treatment and the diagnosis of osteomyelitis-diskitis was 7 years; range, 3–12 years. Patients presented years after the operation with new pathologic compression fractures, neck pain, or arm pain. All had serologic evidence (elevated white blood cell count, C-reactive protein, and/or erythrocyte sedimentation rate) of infection. The time between symptom onset and diagnosis was not available for all, but the delay in diagnosis was as long as 18 months.

A barium swallow in our series was used when patients had new or worsening dysphagia to evaluate stenosis or aspiration; only 1 examination showed a leak. Nine patients had ≥ 1 posttreatment esophageal or neopharyngeal stricture dilation for dysphagia, obstruction, and an inability to take oral nutrition. Two had no history available regarding dilation. The onset of symptoms after dilation was not immediate and ranged from several weeks to months.

Received August 9, 2023; accepted after revision September 27.

From the Department of Radiology (A.A.B., P.V., P.A.R.), Mayo Clinic, Jacksonville, Florida; Department of Radiology (X.C.W.), University of California, San Francisco, San Francisco, California; Department of Radiology (E.J.E.), University of Kentucky, Lexington, Kentucky; and Department of Radiology (C.C.), New York University Langone Health, New York, New York.

Please address correspondence to Alok A. Bhatt, MD, Mayo Clinic Jacksonville, Department of Radiology, 4500 San Pablo Rd S, Jacksonville, FL 32224; e-mail: Bhatt.alok@mayo.edu
<http://dx.doi.org/10.3174/ajnr.A8042>



FIG 1. A 51-year-old man with a history of laryngeal SCCA, treated with total laryngectomy and myocutaneous flap reconstruction. Sagittal contrast-enhanced CT demonstrates marked prevertebral soft-tissue thickening from C4 to T1 and chronic fracture/dislocation at C6–C7. A bulky myocutaneous flap reconstructs the anterior pharyngeal wall; note how lumen tapers, terminating at C7. A tiny locule of extraluminal air is present in the prevertebral soft tissues just anterior to the T1 superior endplate (arrow).

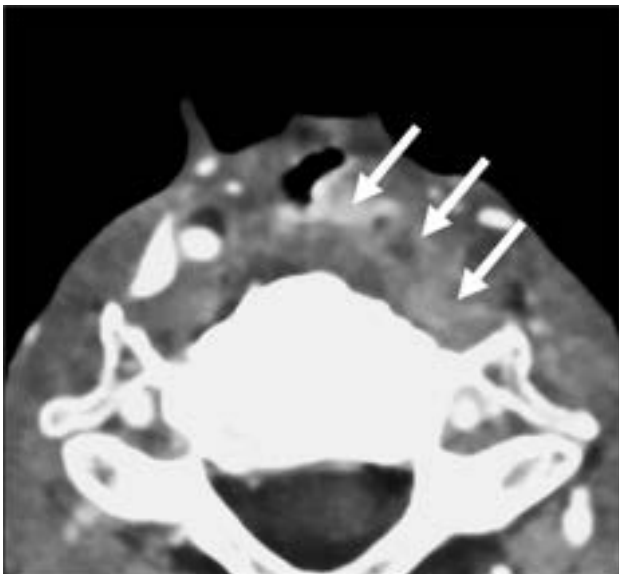


FIG 2. A 67-year-old man with a history of laryngeal SCCA, status post laryngectomy and radiation, and dilation of multiple sites of neopharyngeal and esophageal stenosis presented with obstruction and severe neck pain. An axial contrast-enhanced image demonstrates a fluid-filled sinus tract from the neopharyngeal posterior wall, extending to thickened prevertebral soft tissues (arrows). MR imaging of the cervical spine revealed characteristic cervical diskitis/osteomyelitis at multiple levels (not shown).

Cross-sectional imaging was performed for routine surveillance or because of neck pain, dysphagia, or concern for infection. Both CT and MR imaging were performed in 9 patients; CT only in 1 patient; and MR imaging only in 1 patient. Both CT and MR imaging showed edema and phlegmonous changes around the neopharynx. An incomplete air column from the oropharynx to the cervical esophagus was present in all cases. Extraluminal air was frequently misinterpreted as neopharyngeal air. Extraluminal air was either a relatively large, isolated pocket of air or small bubbles around the reconstruction (Fig 1) and was seen in 4 of 11 patients. A defect in the posterior neopharynx with a fluid- and/or air-filled fistulous tract extending to the cervical spine was visible in 10 of 11 patients (Figs 2 and 3A). Multiplanar reformations performed at the workstation in oblique planes facilitated recognizing that air or gas was not in the lumen and the presence of a fistulous tract.

Characteristic CT and MR imaging findings of osteomyelitis and diskitis were present in all cases (Fig 3B). Diskitis was at C5–6 in 4/11, C6–7 in 2/11, and 1 each at C2–3, C3–4, and C4–5. Two patients had multilevel diskitis from C4 to C7.

DISCUSSION

Dysphagia reportedly occurs in up to 70%–75% of patients in the posttreatment setting of head and neck cancer with a negative impact on the quality of life.⁷ Neopharyngeal or esophagopharyngeal strictures are common causes of dysphagia. In this patient population, strictures may be due to recurrent tumor, but, more commonly, are benign.^{8,9} Multimodality treatment—surgery, radiation, and chemotherapy—increases the risk of pharyngeal or neopharyngeal benign strictures, reportedly occurring as frequently as 33% of the time.⁸

After chemoradiation, soft-tissue chronic inflammation causes collagen deposition and fibrin production, resulting in fibrosis and stricture. Patients may undergo endoscopy with dilation to relieve such strictures. Endoscopic dilation of a neopharyngeal or pharyngoesophageal stricture is a safe and effective treatment for stricture-related dysphagia. Complications of this procedure include bleeding and perforation.⁹ In this setting, infectious organisms can gain access to the vertebral bodies by either perforation or microtrauma.⁵

In patients who have not undergone laryngopharyngectomy, perforation in the cervical region most commonly occurs at the triangular area in the posterior wall of the pharynx between the transverse and oblique bundles of the inferior pharyngeal constrictor muscles, termed the Killian triangle.⁴ This area is adjacent to the C4–C6 vertebral bodies, separated by only a thin layer of fascia. In patients undergoing laryngectomy or pharyngectomy, the Killian triangle does not exist and is replaced by a neopharyngeal anastomosis, an anatomic site of weakness but also, commonly, the site of stricture.⁸

All patients in this series had flap reconstruction of the defect, either as part of the initial treatment or after failure and tumor recurrence. Flap failure is a serious complication for the patient with treated head and neck malignancy. MR imaging or CT perfusion may help predict free flap failure from vascular compromise.¹⁰ Evaluation for stricture and possible leak following dilation may be diagnosed by fluoroscopic barium swallow examination.¹¹

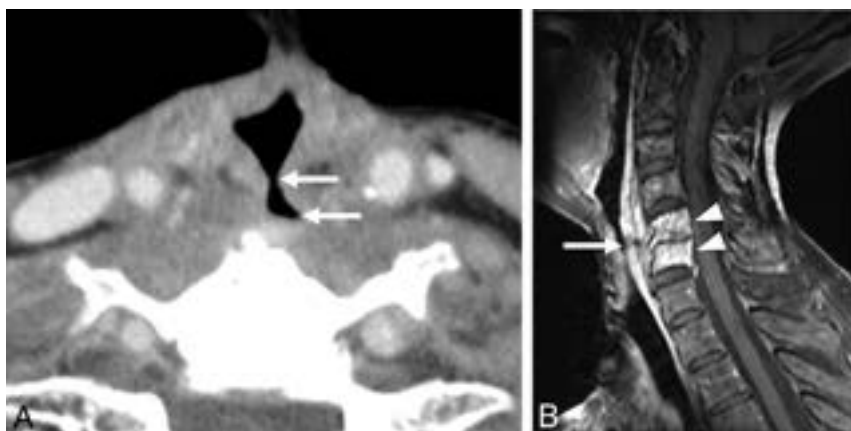


FIG 3. A 74-year-old woman with a history of laryngeal carcinoma, status post total laryngectomy and radiation, and recent esophageal dilation presented with neck pain and fever. A, An axial postcontrast CT image demonstrates a sinus tract extending to the vertebral body (arrows). B, Sagittal T1 postcontrast fat-saturated MR image demonstrates thickening of the prevertebral soft tissue with a focal defect (arrow) and enhancement of the C5 and C6 vertebral bodies (arrowheads) and loss of disk height with enhancement, consistent with diskitis/osteomyelitis.

Our series showed esophageal or neopharyngeal stenosis, and subsequent dilation should prompt attention to the cervical spine, looking for infection if a patient presents with neck pain. In the absence of cord compromise or spine instability, surgical management of diskitis/osteomyelitis with debridement and spine stabilization and repair of the neopharyngeal defect should be considered after failure of medical therapy.¹²

In conclusion, diskitis/osteomyelitis should be a consideration in a patient previously treated for laryngeal or hypopharyngeal carcinoma who presents with neck pain or signs of infection, especially if imaging reveals posterior neopharyngeal breakdown and sinus tract formation. While CT is often the first imaging performed in this setting, MR imaging of the cervical spine is more sensitive for spine infection. In our series, most patients with neopharyngeal perforation and spinal infection had undergone prior esophageal or neopharyngeal dilations for benign posttreatment stricture.

Disclosure forms provided by the authors are available with the full text and PDF of this article at www.ajnr.org.

REFERENCES

- Anderson G, Ebadi M, Vo K, et al. **An updated review on head and neck cancer treatment with radiation therapy.** *Cancers (Basel)* 2021;13:4912 CrossRef Medline
- Clifton WE, Gupta V, Prause C, et al. **Cervical spine osteomyelitis in head and neck cancer patients: looking twice for posterior hypopharyngeal dehiscence.** *Radiol Infect Dis* 2018;5:81–84 CrossRef
- Timmermans AJ, Lansaat L, Theunissen EA, et al. **Predictive factors for pharyngocutaneous fistulization after total laryngectomy.** *Ann Otol Rhinol Laryngol* 2014;123:153–61 CrossRef Medline
- Kim DH, Kim SW, Hwang SH. **Predictive value of risk factors for pharyngocutaneous fistula after total laryngectomy.** *Laryngoscope* 2023;133:742–54 CrossRef Medline
- Zamparini E, Seng P, Bardou M, et al. **Cervical osteomyelitis: a new identity of dreaded complication following pharyngeal cancer treatment.** *Int J Infect Dis* 2019;80:118–21 CrossRef Medline
- Bhatt AA, Vibhute PG, Wu XC, et al. **Osteomyelitis/discitis after treatment for head & neck cancer.** In: *Proceedings of the Annual Meeting of the American Society of Neuroradiology*. April 29 to May 3, 2023. Chicago, Illinois
- Harshitha N, Mohiyuddin SM. **Functional endoscopic evaluation of swallowing in patients treated by total laryngectomy and adjuvant treatment for advanced laryngeal and hypopharyngeal malignancies.** *Indian J Otolaryngol Head Neck Surg* 2021;73:413–18 CrossRef Medline
- Vu KN, Day TA, Gillespie MB, et al. **Proximal esophageal stenosis in head and neck cancer patients after total laryngectomy and radiation.** *ORL J Otorhinolaryngol Relat Spec* 2008;70:229–35 CrossRef Medline
- Stoner PL, Fullerton AL, Freeman AM, et al. **Endoscopic dilatation of refractory postlaryngectomy strictures: a case series and literature review.** *Gastroenterol Res Pract* 2019;2019:8905615 CrossRef Medline
- Ota Y, Moore AG, Spector ME, et al. **Prediction of wound failure in patients with head and neck cancer treated with free flap reconstruction: utility of CT perfusion and MR perfusion in the early postoperative period.** *AJNR Am J Neuroradiol* 2022;43:585–91 CrossRef Medline
- Carbo AI, Brown M, Nakroun N. **Fluoroscopic swallowing examination: radiologic findings and analysis of their causes and pathophysiologic mechanisms.** *Radiographics* 2021;41:1733–49 CrossRef Medline
- D'Souza JN, Luginbuhl AJ, Goldman RA, et al. **Cervical spine spondylodiscitis after esophageal dilatation in patients with a history of laryngectomy or pharyngectomy and pharyngeal irradiation.** *JAMA Otolaryngol Head Neck Surg* 2016;142:467–71 CrossRef Medline

CT of the Larynx: Is an Additional High-Resolution Acquisition Necessary for Diagnostic Accuracy?

Eva Chau, Katie S. Traylor, and Barton F. Branstetter



ABSTRACT

BACKGROUND AND PURPOSE: Diagnostic CT of the larynx is historically performed with a protocol that combines a standard neck CT with dedicated imaging through the larynx. Multichannel CT scanners, however, allow high-resolution reformatted images of the larynx to be created directly from the initial neck acquisition data. The purpose of this study was to determine whether reformatted laryngeal images derived from a standard neck CT acquisition provide information comparable with that of separate dedicated high-resolution laryngeal images.

MATERIALS AND METHODS: The CT protocol for suspected laryngeal masses at our institution consists of a standard neck acquisition followed by a second acquisition focused on the larynx. We enrolled 200 patients who had undergone this protocol for a suspected laryngeal mass. Two head and neck radiologists independently reviewed each of the 200 scans twice. In one session, the entire scan was available, while in the other session, only images derived from the standard neck acquisition were available. The main outcome variable was the frequency of discrepant tumor staging between the interpretation sessions. No pathologic reference standard was used.

RESULTS: Radiologist A had discrepant staging in 45 of the 200 scans (23%; 95% CI, 17%–29%). Radiologist B had discrepant staging in 42 of the 200 scans (21%; 95% CI, 16%–27%). Fifty-three of the 87 discrepancies (61%) reflected improper downstaging of the laryngeal tumor on standard images alone, while the other 34 (39%) had improper upstaging on standard images alone.

CONCLUSIONS: Reformatted images from our institution's standard neck CT acquisition were less accurate than dedicated images of the larynx for analysis of laryngeal tumor extension. Focused images of the larynx were needed to optimize interpretation.

ABBREVIATION: AJCC = American Joint Committee on Cancer

Diagnostic CT of the larynx is historically performed using a protocol that combines a standard neck CT with additional, dedicated imaging through the larynx. Multidetector CT scanners, however, allow high-resolution multiplanar reformatted images of the larynx to be created directly from the initial neck acquisition. If the additional dedicated larynx acquisition is unnecessary, there are potential benefits to the patient (reduced radiation and reduced time in the scanner), the radiologist (fewer images resulting in reduced interpretation time), and the institution (improved scanner throughput and decreased contrast costs).

While there is literature comparing the use of CT versus MR imaging,^{1–4} as well as the diagnostic accuracy of CT overall^{2,5–7} in the staging of laryngeal carcinoma, there is limited literature

regarding the use of dedicated imaging through the larynx in conjunction with a standard neck CT. One preliminary study in 2010 found no substantial difference in the comparison of standard neck CT with dedicated breath-maneuver laryngeal CT in 27 patients.⁸ With the improvements in CT technology in the past decade, however, it is possible that standard high-resolution images are more useful now than before. Therefore, the purpose of this study was to determine whether reformatted laryngeal images derived from a standard neck CT acquisition can replace a separate dedicated high-resolution laryngeal acquisition.

MATERIALS AND METHODS

Patient Selection

Our institutional review board approved this retrospective study. Patients who had undergone neck CT using the larynx protocol for the evaluation of a suspected laryngeal mass were eligible. A power analysis was performed using a clinically significant threshold for a difference in the discrepancy rate of 5% and an α threshold of .05. This finding indicated that 200 patients were

Received July 26, 2023; accepted after revision October 3.

From the University of Pittsburgh Medical Center, Pittsburgh, Pennsylvania.

Please address correspondence to Barton F. Branstetter, MD, University of Pittsburgh Medical Center, 200 Lothrop St, Pittsburgh, PA 15213; e-mail: BFB1@pitt.edu; @CharBranstetter

<http://dx.doi.org/10.3174/ajnr.A8048>

needed for the study, so consecutive patients were enrolled from 2017 to 2021. Inclusion was based on the clinical suspicion of a laryngeal mass, not the final diagnosis of a laryngeal mass, so some of the patients had CT examinations with negative findings. Patients were excluded if the 2 reviewers in consensus determined that motion artifacts rendered their scan nondiagnostic or if the larynx protocol was not performed correctly.

Image Acquisition

All imaging was performed on a LightSpeed 64-channel scanner (GE Healthcare). The neck acquisition was performed using Isovue 370 (Bracco), 75-mL IV, with an 80-second delay. Helical acquisition was performed with 120-kV(peak); milliamperage automated; FOV = 25 cm; pitch = 0.97; matrix = 512 × 512. Axial reconstructions were performed as stacked 2.5-mm-thick slices. Coronal and sagittal reformats were performed as stacked 1-mm-thick slices.

The larynx acquisition was performed using an additional bolus of Isovue 370, 75 mL, again with an 80-second delay. The helical acquisition was performed with 120 kV(p); milliamperage automated; FOV = 10 cm; pitch = 0.53; matrix = 512 × 512. Axial reconstructions were performed as stacked 1-mm-thick slices. Coronal and sagittal reformats were performed as stacked 1-mm-thick slices.

Patients were instructed to maintain shallow breathing and not swallow during the image acquisition.

Image Interpretation

Two Certificate of Added Qualification–certified neuroradiologists with head and neck imaging fellowship training with 20 and 3 years of post-training experience (radiologist A and radiologist B, respectively), working independently, retrospectively reviewed each of the 200 scans twice, in 2 separate sessions. In one session, the entire scan was available to the radiologist, while in the other session, only images derived from the standard neck acquisition were available. Half of the time, the full laryngeal protocol was presented in the first session, and half of the time, the limited scan was presented first. During the second session, the radiologists were blinded to their interpretations from their first session. The interpretation sessions were separated by at least 3 months to avoid recall bias, and the scans were presented in random order in each session. During both review sessions, the radiologists were blinded to all clinical data, including the results of endoscopy and the physical examination.

Involvement of laryngeal subsites was tabulated and used to calculate a radiologic stage based on the American Joint Committee on Cancer (AJCC) 8th edition schema.⁹ The subsites that were evaluated included the epiglottis, epiglottic petiole, aryepiglottic fold, false vocal cords, true vocal cords, anterior commissure, paraglottic fat, pre-epiglottic fat, postcricoid hypopharynx, inner table of the thyroid cartilage, outer table of the thyroid cartilage, cricoid cartilage, and arytenoid cartilage. Some patients had no radiologic evidence of tumor because the selection criterion was based on clinical suspicion of a laryngeal mass. The main outcome variable was the frequency of discrepant staging between the interpretation of the complete scan and the interpretation of the single-acquisition scan for each radiologist. For a



FIG 1. Axial CT images of a 65-year-old man with squamous cell carcinoma of the left true vocal cord. Standard 2.5-mm neck image (A) was interpreted as having normal findings. On a dedicated 1-mm larynx protocol image (B), the ulcerated enhancing tumor along the true vocal cord (arrows) was evident.

concordant interpretation, not every subsite had to be identically interpreted as long as the differences did not affect the overall staging. The staging was radiologic only. Clinical data such as vocal cord mobility were not incorporated into the staging.

χ^2 analysis was used to identify differences in discordance rates between the 2 radiologists and in their propensity to upstage or downstage tumor with the addition of the dedicated larynx acquisition. A Cohen κ statistic with linear rating for ordinal categorical variables was used to evaluate the interreader variability between radiologists in the interpretation of the full laryngeal protocol. No pathologic reference standard was used because this study was designed to evaluate the consistency of radiologic interpretations.

RESULTS

Two hundred patients were included in the study. One hundred thirty-eight (69%) were men, and sixty-two (31%) were women. The average patient age was 65 years, with a range of 20–100 years. One hundred thirty-five of the 200 patients (68%) were eventually diagnosed with squamous cell carcinoma of the larynx.

Radiologist A had discrepant staging in 45 of the 200 scans (23%; 95% CI, 17%–29%). Radiologist B had discrepant staging in 42 of the 200 scans (21%; 95% CI, 16%–27%). For radiologist A, 27 of the 45 discordant scans (60%) were upstaged by the additional dedicated imaging through the larynx. The remaining 18 of the 45 discordant scans (40%) were downstaged by the additional images. Similarly, for radiologist B, 28 of the 42 discordant scans (67%) were upstaged by the additional dedicated imaging through the larynx. The remaining 14 of the 42 discordant scans (33%) were downstaged by the additional images.

Overall, 53 of the 87 discrepancies (61%) resulted in upstaging of the tumor with the dedicated acquisition, while the other 34 (39%) reflected downstaging of the tumor. Most of the discordant interpretations involved distinguishing between true and false cord involvement, accounting for 33 of the total 87 discordances, approximately 38% (Fig 1). Determining thyroid cartilage invasion accounted for 31 of the total 87 discordant reads, approximately 36% (Fig 2).

Motion artifacts on one of the acquisitions contributed to some of the discrepant interpretations. Motion artifacts degraded the quality of standard neck images in 20 of the 200 patients

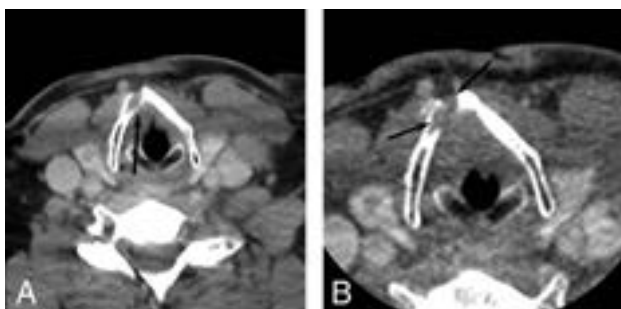


FIG 2. Axial images of a 58-year-old man with squamous cell carcinoma of the right true vocal cord. The thyroid cartilage was interpreted as intact on standard 2.5-mm neck imaging (A) because of a visible inner table (arrow). On a 1-mm larynx protocol image (B), tumor extension into the thyroid cartilage was identified (arrows).

(10%) and in 8 of the dedicated laryngeal sequences (4%). The 95% CI for the difference of proportions is 0.01–0.11, indicating statistical significance.

Abducted vocal cords (closed glottis) on one of the acquisitions also contributed to some of the discrepant interpretations. Abducted cords degraded the quality of standard neck images in 20 of the 200 patients (10%) and in 17 of the dedicated laryngeal sequences (9%). This difference was not statistically significant.

χ^2 analysis revealed no difference between observers in the overall concordance rate ($P=.72$) or in the propensity to upstage versus downstage ($P=.52$). The Cohen κ statistic for interrater variability was 0.67, which is considered “good” agreement between raters.

DISCUSSION

Reformatted images based on standard neck CT are often presumed to convey adequate diagnostic information for staging of laryngeal squamous cell carcinoma. In comparing interpretations made from standard neck CTs with those that included a dedicated laryngeal acquisition, however, this study found a discrepancy in nearly one-quarter of the interpretations. This discrepancy rate was consistent between head and neck radiologists with varying experience levels.

Staging errors made with our standard neck CT protocol alone were a mix of false-positive and false-negative findings. A slight majority of the errors were downstaging errors, but about one-third of cases were erroneously upstaged when only the conventional sequences were used. The errors were made in predictable locations, such as determining thyroid cartilage invasion or tumor spread across the laryngeal ventricle, but these determinations are critical in defining the optimal therapeutic approach. The AJCC staging guidelines outline how the radiologic extent of tumor spread may impact tumor staging and, therefore, treatment choice.⁹ For example, T3 lesions have extension into the pre-epiglottic space or the inner cortex of the thyroid cartilage. These patients can opt for organ-preservation surgery without compromising overall survival. For selected patients with extensive T3 or large T4a lesions that erode the outer cortex of the thyroid cartilage, however, better survival rates and quality of life are achieved with total laryngectomy.¹⁰

Thus, accurate T categorization may directly impact therapeutic decision-making and prognosis.

Our results differ from those of the preliminary study by Gilbert et al,⁸ which found no significant difference in accuracy between the interpretations of the standard neck CT and the additional laryngeal CT in 27 patients. Their study appears to be the only study comparing similar imaging protocols, to our knowledge, and it may be underpowered to detect substantial differences between protocols.

When evaluating the overall literature regarding the propensity for CT imaging to upstage-versus-downstage tumors, our results are consistent with the audit by Agada et al¹¹ comparing the accuracy of CT staging of advanced laryngeal tumor evaluated against the pathologic examination. Of their audit of 38 patients with laryngeal carcinoma, 11 had discordant staging, with 9 patients erroneously upstaged by CT imaging, while 2 were erroneously downstaged.¹¹ In this study, only thick axial slices, 5 mm through the neck and 3 mm through the larynx, were used. Similarly, Contrera et al¹² reported that clinical staging, using a combination of clinical examination, endoscopy, and imaging, can downstage or upstage a patient with laryngeal cancer nearly one-third of the time after pathologic confirmation in their cohort of 265 patients.

Concerns regarding additional radiation and contrast use with a dedicated larynx protocol require that we determine whether these images are necessary. As the American College of Radiology 2007 white paper on radiation dose in medicine recommends, the additional cases of cancer resulting directly from the radiation exposure from CT scans can likely be minimized by optimizing studies that are performed to obtain the best image quality with the lowest radiation dose.¹³ Furthermore, given the adverse effects of contrast media¹⁴ and the ongoing iodinated contrast media shortage,¹⁵ minimizing individual doses to reduce waste continues to be important. Nevertheless, dedicated images through the larynx may still be of benefit in the imaging for suspected laryngeal carcinoma.

Using a smaller FOV for dedicated laryngeal images has both potential benefits and potential drawbacks. A larger FOV gives us better contrast resolution by decreasing noise. As the FOV decreases, the pixel size decreases, resulting in a higher spatial resolution but an increase in noise.¹⁶ Given the small size of the larynx, this higher spatial resolution allows radiologists to better appreciate smaller structures that are located in close proximity to each other. While it is not immediately obvious which FOV is preferable, our results suggest that the increased spatial resolution is advantageous. Additionally, we found that 1 acquisition often contained a great deal of motion artifacts. The additional set of images provided by the dedicated larynx acquisition allowed better diagnostic interpretation in these situations despite the increase in noise.

Our study has several limitations. Our larynx protocol includes a second bolus of contrast for the high-resolution acquisition. It is unclear whether the benefits of the larynx protocol derive exclusively from the higher spatial resolution and thinner slices or whether having 2 contrast boluses given at different times played a role. We did not use dual-energy or perfusion techniques in our protocol; such advanced imaging might further

improve diagnostic accuracy. Furthermore, we did not incorporate clinical data into staging. Given that not all patients undergo laryngectomies to allow pathologic staging confirmation, this study also did not confirm which of the discrepant interpretations were ultimately concordant with pathologic staging. Future studies involving biopsy-confirmed subsite involvement and staging of laryngeal carcinoma will likely shed more light on these issues.

CONCLUSIONS

Radiologic staging of laryngeal tumors may be improved with the addition of focused images of the larynx produced with a second contrast bolus and a second acquisition sequence.

Disclosure forms provided by the authors are available with the full text and PDF of this article at www.ajnr.org.

REFERENCES

1. Cho SJ, Lee JH, Suh CH, et al. **Comparison of diagnostic performance between CT and MRI for detection of cartilage invasion for primary tumor staging in patients with laryngo-hypopharyngeal cancer: a systematic review and meta-analysis.** *Eur Radiol* 2020;30:3803–12 CrossRef Medline
2. Han MW, Kim SA, Cho KJ, et al. **Diagnostic accuracy of computed tomography findings for patients undergoing salvage total laryngectomy.** *Acta Otolaryngol* 2013;133:620–25 CrossRef Medline
3. Kuno H, Sakamaki K, Fujii S, et al. **Comparison of MR imaging and dual-energy CT for the evaluation of cartilage invasion by laryngeal and hypopharyngeal squamous cell carcinoma.** *AJNR Am J Neuroradiol* 2018;39:524–31 CrossRef Medline
4. Wu JH, Zhao J, Li ZH, et al. **Comparison of CT and MRI in diagnosis of laryngeal carcinoma with anterior vocal commissure involvement.** *Sci Rep* 2016;6:30353 CrossRef Medline
5. Li L, Krantz ID, Deng Y, et al. **Alagille syndrome is caused by mutations in human Jagged1, which encodes a ligand for Notch1.** *Nat Genet* 1997;16:243–51 CrossRef Medline
6. Imre A, Pinar E, Erdoğan N, et al. **Prevertebral space invasion in head and neck cancer: negative predictive value of imaging techniques.** *Ann Otol Rhinol Laryngol* 2015;124:378–83 CrossRef Medline
7. Ryu IS, Lee JH, Roh JL, et al. **Clinical implication of computed tomography findings in patients with locally advanced squamous cell carcinoma of the larynx and hypopharynx.** *Eur Arch Otorhinolaryngol* 2015;272:2939–45 CrossRef Medline
8. Gilbert K, Dalley RW, Maronian N, et al. **Staging of laryngeal cancer using 64-channel multidetector row CT: comparison of standard neck CT with dedicated breath-maneuver laryngeal CT.** *AJNR Am J Neuroradiol* 2010;31:251–56 CrossRef Medline
9. Amin MB, Edge SB, Greene FL, et al. *AJCC Cancer Staging Manual*. 8th ed. Springer-Verlag; 2017
10. Forastiere AA, Ismaila N, Lewin JS, et al. **Use of larynx-preservation strategies in the treatment of laryngeal cancer: American Society of Clinical Oncology Clinical Practice Guideline Update.** *J Clin Oncol* 2018;36:1143–69 CrossRef Medline
11. Agada FO, Nix PA, Salvage D, et al. **Computerised tomography vs. pathological staging of laryngeal cancer: a 6-year completed audit cycle.** *Int J Clin Pract* 2004;58:714–16 CrossRef Medline
12. Contrera KJ, Hair BB, Prendes B, et al. **Clinical versus pathologic laryngeal cancer staging and the impact of stage change on outcomes.** *Laryngoscope* 2021;131:559–65 CrossRef Medline
13. Amis ES Jr, Butler PF, Applegate KE, et al; American College of Radiology. **American College of Radiology white paper on radiation dose in medicine.** *J Am Coll Radiol* 2007;4:272–84 CrossRef Medline
14. Andreucci M, Solomon R, Tasanarong A. **Side effects of radiographic contrast media: pathogenesis, risk factors, and prevention.** *Biomed Res Int* 2014;2014:741018 CrossRef Medline
15. Eibschutz LS, Gholamrezaezhad A. **How low can we go? Strategies and recommendations to combat the iodinated contrast shortage.** *Emerg Radiol* 2022;29:925–28 CrossRef Medline
16. Seeram E. *Computed Tomography-E-Book: Physical Principles, Clinical Applications, and Quality Control*. 4th ed. Elsevier; 2015

Diagnostic Value of Multiparameter MRI-Based Radiomics in Pediatric Myelin Oligodendrocyte Glycoprotein Antibody–Associated Disorders

Ting Li, Xin Chen, Yang Jing, Haoru Wang, Ting Zhang, Li Zhang, Hao Ding, Mingye Xie, and Ling He



ABSTRACT

BACKGROUND AND PURPOSE: Myelin oligodendrocyte glycoprotein antibody-associated disorders (MOGAD) have a higher prevalence among children. For children undergoing the initial manifestation of MOGAD, prompt diagnosis has paramount importance. This study assessed the performance of multiparameter MRI-based radiomics in distinguishing patients with and without MOGAD with idiopathic inflammatory demyelinating diseases.

MATERIALS AND METHODS: We enrolled a cohort of 121 patients diagnosed with idiopathic inflammatory demyelinating diseases, including 68 children with MOGAD and 53 children without MOGAD. Radiomics models (T1WI, T2WI, FLAIR, and compound model) using features extracted from demyelinating lesions within the brain parenchyma were developed in the training set. The performance of these models underwent validation within the internal testing set. Additionally, we gathered clinical factors and MRI features of brain parenchymal lesions at their initial presentation. Subsequently, these variables were used in the construction of a clinical prediction model through multivariate logistic regression analysis.

RESULTS: The areas under the curve for the radiomics models (T1WI, T2WI, FLAIR, and the compound model) in the training set were 0.781 (95% CI, 0.689–0.864), 0.959 (95% CI, 0.924–0.987), 0.939 (95% CI, 0.898–0.979), and 0.989 (95% CI, 0.976–0.999), respectively. The areas under the curve for the radiomics models (T1WI, T2WI, FLAIR, and the compound model) in the testing set were 0.500 (95% CI, 0.304–0.652), 0.833 (95% CI, 0.697–0.944), 0.804 (95% CI, 0.664–0.918), and 0.905 (95% CI, 0.803–0.979), respectively. The areas under the curve of the clinical prediction model in the training set and testing set were 0.700 and 0.289, respectively.

CONCLUSIONS: Multiparameter MRI-based radiomics helps distinguish MOGAD from non-MOGAD in patients with idiopathic inflammatory demyelinating diseases.

ABBREVIATIONS: AUC = area under the ROC curve; IIDDs = idiopathic inflammatory demyelinating diseases; LASSO = least absolute shrinkage and selection operator; MOG = myelin oligodendrocyte glycoprotein; MOGAD = myelin oligodendrocyte glycoprotein antibody associated disorders; NMOs = neuromyelitis optica spectrum disorder; ROC = receiver operating characteristic

Myelin oligodendrocyte glycoprotein antibody-associated disorders (MOGAD) represent a collection of immune-mediated monophasic or multiphasic demyelinating diseases affecting the brain, optic nerve, and spinal cord.¹ This condition

falls under the umbrella of idiopathic inflammatory demyelinating diseases (IIDDs), with the distinguishing feature being the myelin oligodendrocyte glycoprotein (MOG) antibody as a unique biomarker. MOGAD is more prevalent in children than in adults. In children, about 13% of the antibodies that cause autoimmune encephalitis are MOG antibodies.² In contrast, MS occurs less frequently in children than in adults. In children experiencing the initial onset of MOGAD, early diagnosis is of utmost importance. During the acute phase, treatment primarily involves the use of glucocorticoids, high-dose IV immunoglobulin, or plasma exchange. Failure to correctly diagnose MOGAD can result in delayed treatment, progression, and recurrence, ultimately leading to irreversible damage to the CNS following multiple relapses.^{3,4}

The early diagnosis of MOGAD in children continues to pose challenges in both imaging and clinical practice. While the

Received July 6, 2023; accepted after revision September 28.

From the Department of Radiology (T.L., X.C., H.W., T.Z., L.Z., H.D., M.X., L.H.), Children's Hospital of Chongqing Medical University, National Clinical Research Center for Child Health and Disorders Ministry of Education Key Laboratory of Child Development and Disorders, Chongqing Key Laboratory of Pediatrics, Chongqing, China; and Huiying Medical Technology Co (Y.J.), Dongsheng Science and Technology Park, Beijing, China.

Please address correspondence to Ling He, MD, Department of Radiology, Children's Hospital of Chongqing Medical University, National Clinical Research Center for Child Health and Disorders, Ministry of Education Key Laboratory of Child Development and Disorders, Chongqing Key Laboratory of Pediatrics, Chongqing 400014, China, 136 Zhongshan Second Rd, Yuzhong District, Chongqing, China; e-mail: doctorheling@yeah.net



Indicates article with online supplemental data.

<http://dx.doi.org/10.3174/ajnr.A8045>

detection of MOG antibodies in serum or CSF samples serves as a crucial diagnostic indicator, it typically takes approximately 2 weeks and can be costly. Moreover, some primary hospitals lack the capability to perform such tests, leading to delays in a timely diagnosis.^{5,6} In MOGAD and other IIDDs, brain parenchymal lesions appear as high-signal demyelinating lesions on FLAIR and T2WI sequences. Although previous studies have identified certain MR imaging features associated with brain lesions in children with MOGAD, qualitative MR imaging features are insufficient for identifying these disorders.⁷

In recent years, radiomics has emerged as a novel discipline extensively used in tumor-related diseases. By analyzing the ROI in images, radiomics involves extracting and calculating first-order, second-order, and high-order features. This process enables the discovery of hidden pathology, prognostic indicators, and other features that may not be discernible to the naked eye.⁸ However, the application of radiomics in children with IIDDs has been limited.⁹ Currently, there are no reports on the use of MR imaging radiomics to differentiate IIDDs caused by MOG antibodies and those with other origins. In this study, we aimed to address this gap by constructing models using 3 conventional MRI sequences (T1WI, T2WI, and FLAIR) to distinguish MOGAD from non-MOGAD in patients with IIDDs. The validity and performance of these models were verified and compared, ultimately identifying the model with the most optimal performance. We anticipate that these models will serve as effective tools for computer-aided identification of patients with MOGAD, filling a critical need in the field of IIDDs.

MATERIALS AND METHODS

This retrospective, single-center study was approved by the institutional review board of Children's Hospital of Chongqing Medical University with a waiver of written informed consent.

Patients

We conducted a retrospective collection of clinical and MRI data from children admitted to our neurology department between February 2017 and December 2021. The study focused on children diagnosed with MOGAD and those with other IIDDs during their initial attack.

The inclusion criteria were as follows:

- 1) Acute or subacute onset characterized by single or multiple symptoms such as optic neuritis, encephalitis, meningoencephalitis, brainstem encephalitis, and myelitis.
- 2) Patients with a positive antibody for MOG (excluding other positive antibodies like glial fibrillary acidic protein, *N*-methyl-D-aspartate, and aquaporin-4). Confirmation of negative antibodies to MOG, glial fibrillary acidic protein, *N*-methyl-D-aspartate, and aquaporin-4 was achieved by detecting relevant neurologically autoimmune antibodies in CSF/serum samples using the cell-based assay method.
- 3) Brain MRI examination with clear and complete images showing demyelinating lesions in the brain parenchyma performed within a window of 15 days before or after the neurologically relevant autoimmune antibody test.

Exclusion criteria were as follows:

- 1) The presence of other possible diseases such as neurodegenerative, metabolic, or cerebrovascular.
- 2) Poor image quality that would impede further research.

The flow chart is depicted in the Online Supplemental Data. A total of 121 patients with IIDDs were enrolled in the study, comprising 68 patients with MOGAD and 53 patients without MOGAD. We collected clinical features including sex and age at the time of the initial attack. The study cohort was randomly sampled at a ratio of 7:3 and divided into a training set and a testing set. In the training set, there were 47 patients with MOGAD and 37 patients without MOGAD. The testing set included 21 patients with MOGAD and 16 patients without it.

MR Imaging Technique

The children were examined using a 3T MRI machine (Achieva 3T; Philips Healthcare) or a 1.5T MR imaging machine (Signa Horizon Lx; GE Healthcare). MR images mainly included axial sequences, T1WI (TR = 700 ms, TE = 30 ms), T2WI (TR = 3000 ms, TE = 100 ms), and T2-FLAIR (TR = 8000 ms, TE = 94 ms). Scanning parameters were the following: section number = 16, section thickness = 5 mm, spacing = 1 mm, FOV = 18 × 18 cm, number of excitations = 2–4. Patients who were unable to cooperate were sedated before undergoing MR imaging.

Radiomics Processing

Segmentation of ROIs. The T1WI, T2WI, and FLAIR sequences of brain MRIs from all patients were obtained in DICOM format from the PACS system. The ROI segmentation was performed using ITK-SNAP (Version 3.6.0; www.itksnap.org) software by radiologist 1 with >5 years of diagnostic experience. Radiologist 1 carefully segmented the ROI along the lesion edges on the T1WI, T2WI, and FLAIR images. The ROI encompassed demyelinating lesions in the brain parenchyma and perifocal edema while excluding CSF. Radiologist 2 with 10 years of diagnostic experience verified the segmentation. The agreement of the final selected radiomics features between 2 radiologists was evaluated using intra-class correlation coefficient. The result is depicted in the Online Supplemental Data.

Feature Extraction, Selection, and Model Establishment

Features were extracted from the T1WI, T2WI, and FLAIR sequences of the patient's brain MRIs. The extracted radiomics features encompassed first-order features, shape features, texture features, as well as Laplacian of Gaussian-filtered and wavelet transform features. The selection of radiomics features underwent 4 stages using Python software (PyRadiomics, Version 2.2.0; <https://github.com/AIM-Harvard/pyradiomics/blob/master/docs/index.rst>). In the first stage, features were chosen through variance thresholding, with features having a threshold value of >0.8 retained for further analysis. Subsequently, the features underwent downsampling using the univariate selection method, and features with a *P* value < .05 were retained. Next, the features were selected using a least absolute shrinkage and selection operator (LASSO) regression analysis with 10-fold cross-validation to determine the optimal λ value. Finally, a feature-correlation analysis was performed to select the most relevant features. For each patient, a Radscore was calculated using the

Table 1: Clinical and MR imaging features of patients with and without MOGAD^a

Patient Characteristic	MOGAD Group	Non-MOGAD Group	P Value
Age (mean) (median) (yr)	2.6 [SD, 3.1], 2.6	6.5 [SD, 3.7], 6.5	.045
Sex			.217
Male	27	27	
Female	41	26	
Cortex	22	8	.029
White matter	54	45	.437
Thalamus	41	17	.002
Pedunculus cerebri	23	7	.009
Cerebellar peduncles	13	7	.385
Multifoci	66	48	.129
Involvement of both cerebral hemispheres	57	46	.649

^aSignificant difference with *P* value <.05.

Table 2: Univariate and multivariate logistic analysis in the cohort

Variable	Univariate Analysis (<i>P</i> Value)	Multivariate Analysis (<i>P</i> Value)
Age	.041 ^a	.017 ^a
Sex	.753	
Cortex	.027 ^a	.021 ^a
White matter	.657	
Thalamus	.220	
Pedunculus cerebri	.072	
Cerebellar peduncles	.172	
Multifoci	.116	
Involvement of both cerebral hemispheres	.749	

^aSignificant difference with *P* value <.05.

equation, and Radscore models were developed for individual sequences as well as a compound of the 3 sequences.

$$\text{Radscore} = \text{Intercept} + \sum_{i=1}^n \text{coefficients}[i] \times \text{Feature}[i]$$

Patient Characteristics and Clinical Model Building

We collected clinical features including sex and age at the time of the initial attack. Additionally, the MRI presentations of the patient's brain lesions were evaluated, and consensus was reached through discussions by radiologist 1 and radiologist 2. The assessments included the following points: 1) determining the number of lesions (single or multiple); 2) identifying involvement of the cerebral cortex, white matter, thalamus, cerebral peduncle, and cerebellar peduncle; and 3) assessing whether the lesions involved the bilateral cerebral hemispheres. Univariate logistic analysis was performed on the collected clinical and imaging features, and the influencing factors with statistical significance (*P* < .05) were analyzed by multivariate logistic regression analysis to establish the clinical model.

Statistical Analysis

Statistical analysis for this study was conducted using R Studio software (Version 4.1.2; <http://rstudio.org/download/desktop>). Paired-samples *t* tests or nonparametric tests were used for the analysis of clinical and imaging data. To evaluate the efficacy of the models, we used various evaluation metrics, including the receiver operating characteristic (ROC) curve, area under the ROC curve (AUC), accuracy, sensitivity, and specificity, which were assessed

in both the training and testing sets. The DeLong test was applied to compare the effectiveness of different models within the training set. Statistical significance was defined as *P* < .05.

RESULTS

Patient Characteristics and Clinical Model Building

Among the patients with MOGAD, there were 27 males and 41 females, ranging in age from 1 year 7 months to 14 years, with a mean age of 2.6 years. In the non-MOGAD group, there were 27 males and 26 females, ranging from 1 to 13 years of age, with a mean age of 6.5 years. A comparison of the clinical features and MR imaging presentations of the patients is shown in Table 1. The analysis revealed no statistically significant differences in terms of sex, multiple lesions, involvement of lesions in the bilateral cerebral hemispheres, and involvement of the white matter and cerebellar peduncles between the 2 groups (*P* > .05). However, statistically significant differences were observed in

terms of age, involvement of the cortex, thalamus, and pedunculus cerebri (*P* < .05).

Characteristics, including age and involvement of the cortex, were identified as significant with *P* < .05 by univariate analysis. Both of them, age (OR = 1.1896, *P* = .017) and involvement of cortex (OR = 3.9862, *P* = .0207), were selected by multivariate logistic regression analysis (Table 2). The AUCs of the clinical prediction model in the training set and testing set were 0.700 and 0.289. The ROC curves depicting the clinical model are presented in Fig 1.

Feature Extraction and Selection

On the basis of the ROI segmentation performed by 2 radiologists, a total of 1688 features were extracted from the T1WI, T2WI, and FLAIR sequence images. Initially, redundant features were eliminated using the variance threshold method, resulting in the removal of 168, 128, and 127 features with thresholds of <0.8. Subsequently, the single-variable selection method was used, resulting in the selection of 30,233 and 395 features, which were further selected through LASSO regression analysis (Online Supplemental Data). The λ value was determined using 10-fold cross-validation. By applying feature-correlation analysis, a total of 15 features for the T1WI model, 22 features for the T2WI model, 19 features for the FLAIR model, and 32 features for the compound model were selected. The 10 most optimal features for each sequence, used for constructing the radiomics models, are presented in the Online Supplemental Data. By means of the equation, the Radscore was calculated for each patient, and radiomics models were developed for individual sequences as well as the combined analysis of all 3 sequences.

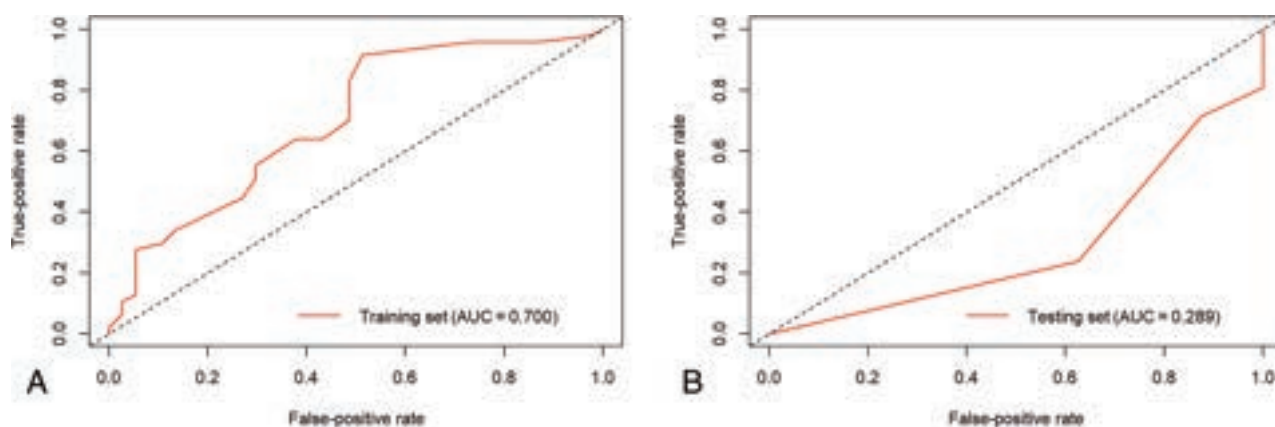


FIG 1. ROC curves of the clinical prediction model in the training and testing sets.

Table 3: Evaluation indexes of T1WI, T2WI, FLAIR, and compound models in the training and testing sets

Models	AUC (95% CI)	Accuracy	Sensitivity	Specificity
T1WI				
Training set	0.781 (0.689–0.864)	0.690	0.745	0.622
Testing set	0.500 (0.304–0.652)	0.459	0.571	0.312
T2WI				
Training set	0.959 (0.924–0.987)	0.857	0.894	0.811
Testing set	0.833 (0.697–0.944)	0.784	0.857	0.688
FLAIR				
Training set	0.939 (0.898–0.979)	0.845	0.851	0.838
Testing set	0.804 (0.664–0.918)	0.730	0.762	0.688
Compound				
Training set	0.989 (0.976–0.999)	0.940	0.936	0.946
Testing set	0.905 (0.803–0.979)	0.838	0.905	0.750

Efficacy of Radiomics Models to Identify MOGAD

The T1WI sequence model demonstrated an AUC of 0.781 (95% CI, 0.689–0.864), with accuracy, sensitivity, and specificity values of 69.0%, 74.5%, and 62.2% in the training set, respectively. In the testing set, the values were 0.500 (95% CI, 0.304–0.652) for AUC, 45.9% for accuracy, 57.1% for sensitivity, and 31.2% for specificity.

For the T2WI sequence model, the training set yielded an AUC of 0.959 (95% CI, 0.924–0.987), with accuracy, sensitivity, and specificity values of 85.7%, 89.4%, and 81.1%, respectively. In the testing set, the values were 0.833 (95% CI, 0.697–0.944) for AUC, 78.4% for accuracy, 85.7% for sensitivity, and 68.8% for specificity.

The FLAIR sequence model achieved an AUC of 0.939 (95% CI, 0.898–0.979) in the training set, along with accuracy, sensitivity, and specificity values of 84.5%, 85.1%, and 83.8%, respectively. In the testing set, the values were 0.804 (95% CI, 0.664–0.918) for AUC, 73.0% for accuracy, 76.2% for sensitivity, and 68.8% for specificity.

The compound model combining all 3 sequences had an AUC of 0.989 (95% CI, 0.976–0.999), with accuracy, sensitivity, and specificity values of 94.0%, 93.6%, and 94.6% in the training set, respectively. In the testing set, the values were 0.905 (95% CI, 0.803–0.979) for AUC, 83.8% for accuracy, 90.5% for sensitivity, and 75.0% for specificity (Table 3). The ROC curves depicting the models are shown in Fig 2.

The DeLong test indicated that the efficacy of the compound model, as well as the FLAIR and T2WI sequence models, was

superior to that of the T1WI model, with statistically significant differences. Additionally, the compound model showed higher efficacy than the FLAIR sequence model, while the differences between the compound model and the T2WI sequence model, as well as between the FLAIR sequence model and the T2WI sequence model, were not statistically significant (Table 4).

DISCUSSION

Although MOGAD was introduced as a new subtype of IIDD in 2018, our understanding of this condition has improved with time, revealing that the MOG antibody is the most common autoimmune antibody associated with IIDDs in children.¹⁰ MR imaging plays a crucial role in the clinical assessment of patients with MOGAD. In MOGAD, brain parenchymal lesions appear as high-signal demyelinating lesions in FLAIR and T2WI sequences.¹¹ These lesions resemble those seen in acute disseminated encephalomyelitis and typically manifest as asymmetrically distributed multiple lesions with indistinct borders, potentially accompanied by edema around larger lesions. MR imaging offers high soft-tissue resolution, multiple parameters, and diverse sequences, enabling the visualization of demyelinating lesions in IIDDs.¹²

Although previous studies have identified certain MR imaging features associated with brain lesions in children with MOGAD such as a higher involvement of the cortex, thalamus, and cerebral peduncle compared with those without MOGAD, these manifestations lack specificity, and accurate diagnosis cannot rely solely on imaging features.¹³ As in the clinical model based on

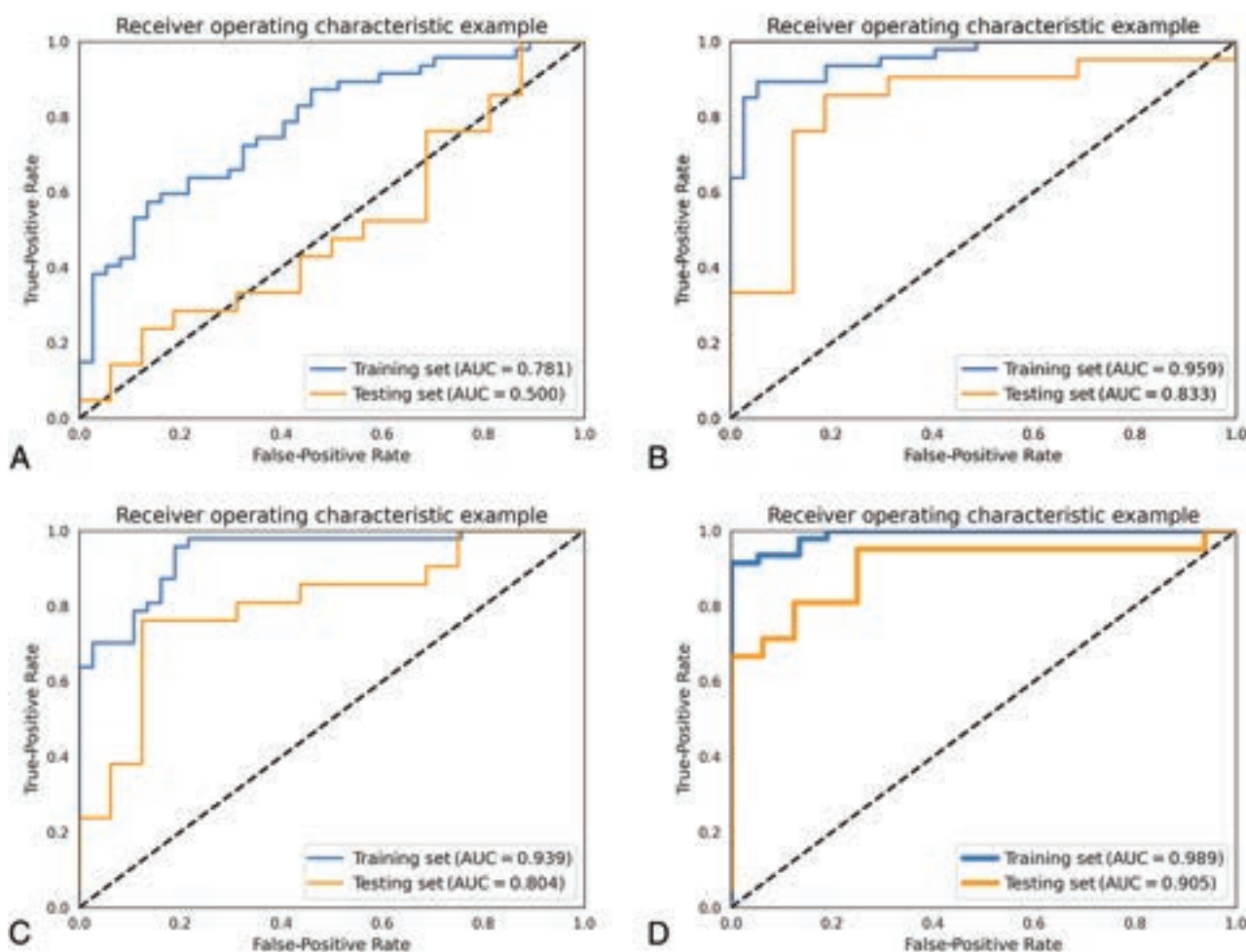


FIG 2. ROC curves of the radiomics models. TIWI (A), T2WI (B), FLAIR (C), and the compound model (D) of 3 sequences.

Table 4: DeLong test among TIWI, T2WI, FLAIR, and compound models in the training set

Models		DeLong Test (P value)
TIWI training set	T2WI training set	0.0018
	FLAIR training set	0.0041
T2WI training set	FLAIR training set	0.3317
	Compound training set	0.0502
FLAIR training set	Compound training set	0.0061
Compound training set	TIWI training set	<0.0001

clinical and imaging features in this study, efficacy was low in both the training and testing groups. The AUCs of the clinical prediction model in the training set and testing set were 0.700 and 0.289. The emergence of radiomics, a field that uses automated data-mining algorithms to extract high-throughput, non-visualized feature parameters from images, has shown great potential in elucidating the pathology, efficacy, and prognosis of various lesions.¹⁴ While radiomics is predominantly used in tumor-related diseases, its application in IIDDs in children, particularly using MR imaging radiomics, remains unexplored.

To date, only a limited number of studies have investigated the application of MR imaging radiomics in IIDDs, particularly in MS. These studies have demonstrated the potential of MR

imaging radiomics in the diagnosis and prediction of MS progression.⁹ For instance, research has shown that radiomics based on T2WI sequences in brain MRIs can effectively differentiate MS from central small-vessel disease.¹⁵ Moreover, a compound MR imaging model using T1WI and T2WI sequences has been shown to successfully distinguish white matter lesions between MS and neuromyelitis optica spectrum disorder (NMOSD).¹⁶ Furthermore, MR imaging radiomics has proved effective in predicting the progression of MS, with certain studies establishing models based on the T2WI sequence to predict the progression of unenhanced MS lesions.¹⁷ Existing MR imaging radiomics studies in MS have predominantly focused on a single sequence or compound modeling of 2 sequences, leading to a biased selection. Due to the absence of standardized criteria for sequence selection, choosing the most appropriate MRI sequence for radiomics modeling can effectively enhance diagnostic performance.¹⁸

This study used the imaging data from our center to extract features from 3 conventional MR imaging sequences, enabling the establishment of robust radiomics models for differentiating MOGAD and non-MOGAD. Most interesting, 2 of the most crucial features identified in previous MRI-based radiomics research to differentiate MS from NMOSD were texture

features.¹⁹ In our prediction models, a large portion of the 4 models comprised texture features. Previous reports have indicated that texture heterogeneity is associated with the severity of histopathologic injury.²⁰ Another MRI-based radiomics discrimination study between MS and NMOSD discovered differences in Gln values within the gray-level run length matrix features of patients with MS and NMOSD. It potentially reflecting varying degrees of tissue damage between the 2 conditions.²¹ Gln measures the similarity of gray level values throughout the ROI. If the gray level values are similar, the value is small. In our study, the gray-level run length matrix is included within the texture features of the models, suggesting the presence of differences in tissue damage between MOGAD and non-MOGAD. Additionally, some valuable features extracted in this study were derived from wavelet transform. Wavelet transform encompasses intensity and texture information and applies a linear or radial wave matrix to the image. It can capture the spatial relationship among ≥ 3 pixels, potentially uncovering more nuanced information regarding the pathologic level of the lesions. However, further research is necessary to confirm these findings.

Moreover, while most radiomics studies on MS primarily use T2WI sequences, our study demonstrates that both T2WI and FLAIR models have excellent performance. The classification efficiency of the T2WI and FLAIR sequence models is significantly superior to that of the T1WI sequence model. This heightened classification efficiency in the T2WI and FLAIR sequence models may stem from the higher ability to distinguish demyelinating lesions. Additionally, it is possible that the features extracted from T2WI and FLAIR sequences more effectively capture the underlying pathology of demyelinating lesions. Notably, in this study, the compound model that combines features from all 3 sequences demonstrates higher diagnostic efficiency compared with the single-sequence models of T1WI and FLAIR.

However, this study has several limitations. First, it is a retrospective study, which may introduce selection bias and limit the generalizability of the findings. Therefore, further confirmation of these results is warranted through prospective studies. Second, the present study used only conventional sequences of brain MRIs for modeling purposes. In future investigations, incorporating additional imaging techniques such as quantitative MRI and fMRI features could potentially enhance the efficiency of our radiomics model. Previous studies have shown that incorporating magnetization transfer imaging features from quantitative MRI can improve the performance of models in identifying MS.²² Third, the original image-layer thickness in this study was 5 mm, and although the spatial resolution was improved to 1 mm during preprocessing, the improvement may have resulted in lower accuracy in delineating boundaries of small lesions. Therefore, the 5-mm image-layer thickness was used in this study, but this might have an impact on the diagnostic performance of radiomic features. Last, the sample size in this study is relatively small. MOGAD is a newly proposed subtype of IIDDs, and previous cases are limited. Hence, in future studies, a multicenter prospective design should be established to expand the sample size and further validate the findings.

CONCLUSIONS

In this study, we have demonstrated that radiomics models based on T2WI, FLAIR sequences, and a compound model of 3 conventional sequences in brain MR imaging can effectively and early on distinguish children with unknown causes of IIDDs during their initial onset. We have also identified the important role of textural features in the differential diagnosis. Notably, both the T2WI and FLAIR models exhibited exceptional performance as single-sequence models. Moreover, the compound model showed superior diagnostic capability compared with the T1WI and FLAIR models individually, thereby addressing the gap in radiomics application for IIDDs beyond MS. We believe that radiomics holds great potential for extension to other subtypes of IIDDs in the future and will find widespread use in the diagnosis, evaluation, and prognosis of demyelinating diseases in children.




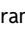
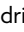




Disclosure forms provided by the authors are available with the full text and PDF of this article at www.ajnr.org.

REFERENCES

- Wynford-Thomas R, Jacob A, Tomassini V. **Neurological update: MOG antibody disease.** *J Neurol* 2019;266:1280–86 CrossRef Medline
- Jarius S, Ruprecht K, Kleiter I, et al; in cooperation with the Neuromyelitis Optica Study Group (NEMOS). **MOG-IgG in NMO and related disorders: a multicenter study of 50 patients. Part 2: Epidemiology, clinical presentation, radiological and laboratory features, treatment responses, and long-term outcome.** *J Neuroinflammation* 2016;13:280 CrossRef Medline
- Bruijstens AL, Lechner C, Flet-Berliac L, et al; E.U. Paediatric MOG Consortium. **E.U. Paediatric MOG Consortium consensus, Part 1: classification of clinical phenotypes of paediatric myelin oligodendrocyte glycoprotein antibody-associated disorders.** *Eur J Paediatr Neurol* 2020;29:2–13 CrossRef Medline
- Armangue T, Olive-Cirera G, Martinez-Hernandez E, et al; Spanish Pediatric anti-MOG Study Group. **Associations of paediatric demyelinating and encephalitic syndromes with myelin oligodendrocyte glycoprotein antibodies: a multicentre observational study.** *Lancet Neurol* 2020;19:234–46 CrossRef Medline
- Narayan R, Simpson A, Fritsche K, et al. **MOG antibody disease: a review of MOG antibody seropositive neuromyelitis optica spectrum disorder.** *Mult Scler Relat Disord* 2018;25:66–72 CrossRef Medline
- Hennes EM, Baumann M, Lechner C, et al. **MOG spectrum disorders and role of MOG-antibodies in clinical practice.** *Neuropediatrics* 2018;49:3–11 CrossRef Medline
- Baumann M, Grams A, Djurdjevic T, et al. **MRI of the first event in pediatric acquired demyelinating syndromes with antibodies to myelin oligodendrocyte glycoprotein.** *J Neurol* 2018;265:845–55 CrossRef Medline
- Mayerhoefer ME, Materka A, Langs G, et al. **Introduction to radiomics.** *J Nucl Med* 2020;61:488–95 CrossRef Medline
- Eichinger P, Zimmer C, Wiestler B. **AI in radiology: where are we today in multiple sclerosis imaging?** *Rofo* 2020;192:847–53 CrossRef Medline
- Fernandez-Carbonell C, Vargas-Lowy D, Musallam A, et al. **Clinical and MRI phenotype of children with MOG antibodies.** *Mult Scler* 2016;22:174–84 CrossRef Medline
- Mao L, Yang L, Kessi M, et al. **Myelin oligodendrocyte glycoprotein (MOG) antibody diseases in children in central south China: clinical features, treatments, influencing factors, and outcomes.** *Front Neurol* 2019;10:868 CrossRef Medline
- Borisow N, Mori M, Kuwabara S, et al. **Diagnosis and treatment of NMO spectrum disorder and MOG-encephalomyelitis.** *Front Neurol* 2018;9:888 CrossRef Medline

13. Cross H, Sabiq F, Ackermans N, et al. **Myelin oligodendrocyte glycoprotein (MOG) antibody positive patients in a multi-ethnic Canadian cohort.** *Front Neurol* 2020;11:525933 CrossRef Medline
14. Fornacon-Wood I, Faivre-Finn C, O'Connor JP, et al. **Radiomics as a personalized medicine tool in lung cancer: separating the hope from the hype.** *Lung Cancer* 2020;146:197–208 CrossRef Medline
15. He T, Zhao W, Mao Y, et al. **MS or not MS: T2-weighted imaging (T2WI)-based radiomic findings distinguish MS from its mimics.** *Mult Scler Relat Disord* 2022;61:103756 CrossRef Medline
16. Huang J, Xin B, Wang X, et al. **Multi-parametric MRI phenotype with trustworthy machine learning for differentiating CNS demyelinating diseases.** *J Transl Med* 2021;19:377 CrossRef Medline
17. Peng Y, Zheng Y, Tan Z, et al. **Prediction of unenhanced lesion evolution in multiple sclerosis using radiomics-based models: a machine learning approach.** *Mult Scler Relat Disord* 2021;53:102989 CrossRef Medline
18. Kang D, Park JE, Kim YH, et al. **Diffusion radiomics as a diagnostic model for atypical manifestation of primary central nervous system lymphoma: development and multicenter external validation.** *Neuro Oncol* 2018;20:1251–61 CrossRef Medline
19. Bathla G, Priya S, Liu Y, et al. **Radiomics-based differentiation between glioblastoma and primary central nervous system lymphoma: a comparison of diagnostic performance across different MRI sequences and machine learning techniques.** *Eur Radiol* 2021;31:8703–13 CrossRef Medline
20. Huh SY, Min JH, Kim W, et al. **The usefulness of brain MRI at onset in the differentiation of multiple sclerosis and seropositive neuromyelitis optica spectrum disorders.** *Mult Scler* 2014;20:695–704 CrossRef Medline
21. Ma X, Zhang L, Huang D, et al. **Quantitative radiomic biomarkers for discrimination between neuromyelitis optica spectrum disorder and multiple sclerosis.** *J Magn Reson Imaging* 2019;49:1113–21 CrossRef Medline
22. Lavrova E, Lommers E, Woodruff HC, et al. **Exploratory radiomic analysis of conventional vs. quantitative brain MRI: toward automatic diagnosis of early multiple sclerosis.** *Front Neurosci* 2021;15:679941 CrossRef Medline

Automatic Quantification of Normal Brain Gyrfication Patterns and Changes in Fetuses with Polymicrogyria and Lissencephaly Based on MRI

 Bossmat Yehuda,  Aviad Rabinowich,  Daphna Link-Sourani,  Netanell Avisdris,  Ori Ben-Zvi, Bella Specktor-Fadida,  Leo Joskowicz,  Liat Ben-Sira,  Elka Miller, and  Dafna Ben Bashat



ABSTRACT

BACKGROUND AND PURPOSE: The current imaging assessment of fetal brain gyrfication is performed qualitatively and subjectively using sonography and MR imaging. A few previous studies have suggested methods for quantification of fetal gyrfication based on 3D reconstructed MR imaging, which requires unique data and is time-consuming. In this study, we aimed to develop an automatic pipeline for gyrfication assessment based on routinely acquired fetal 2D MR imaging data, to quantify normal changes with gestation, and to measure differences in fetuses with lissencephaly and polymicrogyria compared with controls.

MATERIALS AND METHODS: We included coronal T2-weighted MR imaging data of 162 fetuses retrospectively collected from 2 clinical sites: 134 controls, 12 with lissencephaly, 13 with polymicrogyria, and 3 with suspected lissencephaly based on sonography, yet with normal MR imaging diagnoses. Following brain segmentation, 5 gyrfication parameters were calculated separately for each hemisphere on the basis of the area and ratio between the contours of the cerebrum and its convex hull. Seven machine learning classifiers were evaluated to differentiate control fetuses and fetuses with lissencephaly or polymicrogyria.

RESULTS: In control fetuses, all parameters changed significantly with gestational age ($P < .05$). Compared with controls, fetuses with lissencephaly showed significant reductions in all gyrfication parameters ($P \leq .02$). Similarly, significant reductions were detected for fetuses with polymicrogyria in several parameters ($P \leq .001$). The 3 suspected fetuses showed normal gyrfication values, supporting the MR imaging diagnosis. An XGBoost-linear algorithm achieved the best results for classification between fetuses with lissencephaly and control fetuses ($n = 32$), with an area under the curve of 0.90 and a recall of 0.83. Similarly, a random forest classifier showed the best performance for classification of fetuses with polymicrogyria and control fetuses ($n = 33$), with an area under the curve of 0.84 and a recall of 0.62.

CONCLUSIONS: This study presents a pipeline for automatic quantification of fetal brain gyrfication and provides normal developmental curves from a large cohort. Our method significantly differentiated fetuses with lissencephaly and polymicrogyria, demonstrating lower gyrfication values. The method can aid radiologic assessment, highlight fetuses at risk, and may improve early identification of fetuses with cortical malformations.

ABBREVIATIONS: AUC = area under the curve; GA = gestational age; GI = gyrfication index; GIA = gyrfication index by area; GIC = gyrfication index by contour; LIS = lissencephaly; MCC = Matthews correlation coefficient; max = maximum; MCD = malformation of cortical development; PMG = polymicrogyria; SI = symmetry index

Fetal cortical development is a complex process that relies on adequate cell differentiation, proliferation, neuronal migration, and organization.¹ Gyrfication starts gradually from the second trimester and continues during postnatal life.² The spatiotemporal pattern of normal fetal gyrfication

is correlated with gestational age (GA) and is used to evaluate brain development.³⁻⁶


Disruption of this organized process can cause malformations of cortical development (MCDs). Two common MCDs are lissencephaly (LIS) and polymicrogyria (PMG). In LIS, the brain appears smooth with complete or partial gyral loss,⁶ while PMG is characterized by excessive, irregular small gyri that can be focal,

Received May 3, 2023; accepted after revision September 23.

From the Sagol Brain Institute (B.Y., A.R., D.L.-S., N.A., O.B.-Z., D.B.B.) and Division of Radiology (A.R., L.B.-S.), Tel Aviv Sourasky Medical Center, Tel Aviv, Israel; Sagol School of Neuroscience (B.Y., L.B.-S., D.B.B.) and Sackler Faculty of Medicine (A.R., L.B.-S., D.B.B.), Tel Aviv University, Tel Aviv, Israel; School of Computer Science and Engineering (N.A., B.S.-F., L.J.), The Hebrew University of Jerusalem, Jerusalem, Israel; and Department of Medical Imaging (E.M.), Children's Hospital of Eastern Ontario, University of Ottawa, Ottawa, Ontario, Canada.

This work was supported by the Yoran Institute of Human Genome Research and the Israel Innovation Authority.

Please address correspondence to Dafna Ben Bashat, PhD, Sagol Brain Institute, Tel Aviv Sourasky Medical Center, 6 Weizman St, Tel Aviv, 64239, Israel; e-mail: dafnab@tlvmc.gov.il

 Indicates open access to non-subscribers at www.ajnr.org


 Indicates article with online supplemental data.
<http://dx.doi.org/10.3174/ajnr.A8046>

Table 1: MR imaging data included in this study

Vendor/System (Magnetic Field)	Sequence	No.	TE (Milliseconds [SD])	TR (Milliseconds [SD])	Spacing (mm [SD])
GE Healthcare Discovery MR450 (1.5T) Signa (1.5T)	FRFSE	40	121.7 [SD, 2.3]	9946.5 [SD, 1984.5]	3.8 [SD, 0.8]
	FIESTA	10	1.7 [SD, 0.09]	3.9 [SD, 0.2]	4.6 [SD, 0.9]
	SS-FSE	3	111.7 [SD, 0.6]	2517.4 [SD, 835.9]	3.9 [SD, 0.65]
Siemens Magnetom Aera (1.5T) Magnetom Prisma (3T) Skyra (3T) Magnetom Vida (3T)	HASTE	4	94 [SD, 0]	1200 [SD, 0]	3.05 [SD, 0.7]
	HASTE	2	96 [SD, 16.9]	2000 [SD, 0]	3.3 [SD, 1.8]
	TRUFI	4	2.5 [SD, 0.01]	4.9 [SD, 0.02]	3.15 [SD, 0.3]
	HASTE	31	92.4 [SD, 21.7]	1839.1 [SD, 325.1]	3.5 [SD, 0.6]
	TRUFI	7	2.5 [SD, 0.04]	4.9 [SD, 0.08]	3.9 [SD, 0.7]
	TRUFI	1	2.5 [SD, 0]	4.9 [SD, 0]	3 [SD, 0]

Note:—SS-FSE indicates single-shot, fast spin-echo; TRUFI, true fast imaging with steady-state free precession; FRFSE, fast recovery fast spin echo; HASTE, Half-Fourier acquisition single-shot turbo spin-echo.

multifocal, unilateral, or bilateral.⁷ MCDs are associated with a wide range of clinical outcomes and neurodevelopment disorders later in life.⁸

Fetal development is assessed primarily by using sonography, with MR imaging as a complementary tool to support its findings or when clinically indicated,^{9–13} and was shown to have significant advantages in diagnosing brain malformations.^{14–16} Clinical assessment of fetal brain gyrification using both sonography and MR imaging is qualitative through visual inspection of the cortical global appearance and specific sulci such as the Sylvian fissure, and it requires special expertise and experience.^{7,17,18}

The gyrification index (GI) was first introduced in histologic images of adult brains,¹⁷ defined as the ratio between the outer cortical contour and the cerebral hull contour tightly wrapping the brain. Additional quantitative parameters such as curvature, surface area, and the 3D GI have been proposed for the 3D-reconstructed cortical surface.^{18–21} Global and local 3D GIs were found to correlate with age (in children),²² sex,²³ and cognitive functions (in adults).²⁴ Furthermore, parameters from other research fields have been applied to adults.^{4,19,25–28} However, these methods are less applicable to fetal brain MR imaging, due to changes in GA; high variability in scanning planes, resolutions, and contrasts, as well as changes in fetal position and motion artifacts.

Some studies proposed methods to quantify fetal gyrification on the basis of the 3D MR imaging–reconstructed cortical surface.^{20,28–32} However, these methods require unique data acquisition, with a few volumes acquired in different spatial planes, and they are time-consuming and sensitive to fetal motion and require high computational power. In addition, these methods were developed in small cohorts (<40, except as in Wright et al²⁰) based on specific MR imaging sequences with only a few proposed developmental curves for a narrow GA range (except in Wright et al²⁰).

Our aims were the following: 1) to develop an automatic pipeline for quantitatively assessing fetal cortical folding on the basis of clinical 2D MR imaging data; 2) to quantify normal gyrification and symmetry on a large cohort of control fetuses; and 3) to measure gyrification in fetuses with LIS and PMG and evaluate the machine learning classification models for control fetuses and fetuses with LIS or PMG based on quantitative gyrification parameters.

MATERIALS AND METHODS

This retrospective study was approved by the local ethics committees of 2 institutions, which waived the need for informed consent.

MR Imaging Data and Study Population

The data set included coronal T2-weighted MR imaging, acquired between 2007 and 2022 from 2 clinical sites, Tel Aviv Sourasky Medical Center, Tel Aviv, Israel, and the Children's Hospital of Eastern Ontario, Ottawa, Ontario, Canada, using 6 MR imaging scanners from 2 vendors and different sequences and parameters, as shown in Table 1.

Control fetuses were chosen according to GA for a wide and well-represented range of weeks with normal MR imaging findings, no chromosomal abnormalities, and no evidence of fetal cytomegalovirus infection or chronic maternal disease. Pregnancies were dated according to the first-trimester crown-rump length. Clinical indications for MR imaging in controls included a suspected fetal abnormality on sonography, maternal cytomegalovirus seroconversion, a family history of genetic disease, and previous pregnancy with confirmed abnormalities. Fetuses with MCD were diagnosed by an expert fetal MR imaging neuroradiologist (L.B.-S. with > 20 years' experience or E.M. with >15 years).

Poor-quality images, including severe motion or artifacts, were excluded.

Image Analysis

The image-processing pipeline (Fig 1) includes 4 stages:

A) Brain detection as previously described in Dudovitch et al³³ using an anisotropic 3D U-Net classifier for initial segmentation and computing a tight bounding box around it.

B) Brain component segmentation,³⁴ using a 2D multiclass segmentation network, dividing the fetal brain into 6 components: left/right hemispheres, left/right lateral ventricles, extra-axial cerebrum-spinal fluid, and cerebellum (including the brainstem). Anatomic left and right classifications were based on the inferior-superior direction (cerebellum) and anterior-posterior direction (eyes, automatically identified using another deep learning network). Manual segmentation corrections were performed when needed to ensure accurate GI calculation.

Next, the cerebral contour was defined as the boundary between the cerebrum and the extra-axial cerebrum-spinal fluid, and the convex-hull was computed as the smallest convex that contains the contour of the hemisphere. GI parameters were calculated for each slice, separately for the right and left side as follows:

C) GI by area (GIA) was defined as the ratio of the bounded area between the cerebral cortex and convex hull contours and the hemisphere area.

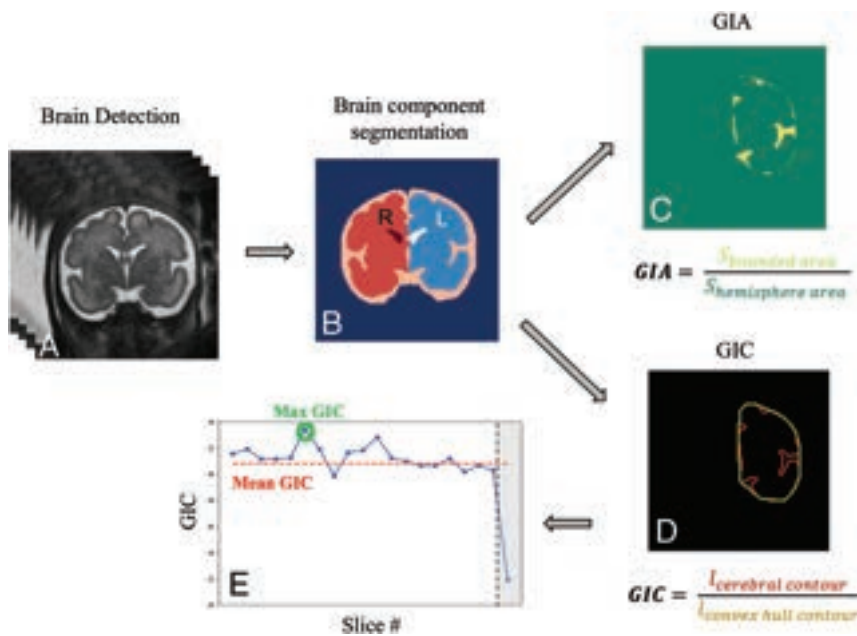


FIG 1. Image-analysis pipeline: A, Brain detection. B, Brain component segmentation. C, GIA calculation based on the bounded area (yellow) between the cerebral cortex and its convex hull and the hemisphere area (green, surrounded by the yellow area). D, GIC calculation based on contour extraction of the cerebral hemisphere (red) and its convex hull (yellow). E, Example of GIC values in all slices of a single fetus. Outliers are marked in gray and were not included in the mean GIC.

Equation 1
$$GIA = \frac{S_{\text{bounded area}}}{S_{\text{hemisphere area}}}.$$

D) GI by contour (GIC) was defined as the ratio of the cerebral and convex hull contour lengths.

Equation 2
$$GIC = \frac{L_{\text{cerebral contour}}}{L_{\text{convex hull contour}}}.$$

We extracted 5 gyrification parameters: 1) mean GIA, the mean value from all slices excluding outliers. A predefined threshold was used and slices located at the most anterior or posterior parts with the GI below this threshold were excluded; 2) maximum (max) GIA, the maximum value from all slices, hypothesized to represent the Sylvian fissure level; 3) bounded volume, the bounded volume between the hemisphere and its convex hull, normalized by the hemisphere volume. Similarly, 4) mean GIC and 5) max GIC were extracted on the basis of the GIC defined above.

In addition, the symmetry index (SI) was calculated for each parameter, where R and L are the GIs of the right and left hemispheres, respectively:

Equation 3
$$SI_{\text{parameter}} = \frac{\text{Parameter}_R - \text{Parameter}_L}{\text{Parameter}_R + \text{Parameter}_L}.$$

Statistical Analysis

Statistical analysis was performed using R Studio, Version 022.07.2 (<http://rstudio.org/download/desktop>).

Changes with GA in the control group were assessed by fitting a second-degree polynomial using a parametrical Generalized Additive Models for Location, Scale, and Shape (GAMLSS; <https://www.gamlss.com/>) with a Box-Cox power exponential

distribution, as recommended by the World Health Organization.³⁵ All *P* values were adjusted for multiple comparisons as described by Benjamini and Yekutieli.³⁶ The 95% nonparametric confidence intervals³⁷ were adjusted to a false coverage rate of 0.05.³⁸

MCD Classification

Differences between control fetuses and MCDs were first assessed using Wilcoxon rank-sum tests while controlling for GA. Next, a machine learning classifier was developed to differentiate between fetuses with normal gyrification and those with MCDs, separately for LIS and PMG, based on all the gyrification parameters presented in this study: right and left GIA max, GIA mean, GIC max, GIC mean, and bounded volume. The control group included fetuses older than 24 weeks' GA (*n* = 86) to match the MCD group, because MCDs can only be diagnosed after 24 weeks' GA.^{39,40} Seven models were tested, including random forests⁴¹ (*n* = 100), linear and radial basis

function kernel Support Vector Machine (SVM),⁴² Extreme Gradient Boosting (XGBoost; <https://www.nvidia.com/en-us/glossary/data-science/xgboost/>)⁴³ using 2 different objectives, logistic and linear k-nearest neighbors (*k* = 5), and multilayer perceptron. To compensate for the inherent imbalance between control and pathologic cases, the Synthetic Minority Oversampling Technique (SMOTE; <https://arxiv.org/abs/1106.1813>)⁴⁴ was used in model training. The training phase was performed using a 3-fold cross-validation scheme, randomly splitting the data into training data sets (LIS: *n* = 66, fifty-eight controls and 8 cases of LIS; PMG: *n* = 66, fifty-eight controls and 8 cases of PMG) and validation data sets (LIS: *n* = 32, twenty-eight controls and 4 cases of LIS; PMG: *n* = 33, twenty-eight controls and 5 cases of PMG). The performance of the models was evaluated using several metrics, including accuracy (Equation 4), F1 score (Equation 5), Matthews correlation coefficient (MCC) (Equation 6),⁴⁵ area under the curve (AUC) of the receiver operating characteristic curve, precision, and recall (Equations 7 and 8):

Equation 4
$$\text{Accuracy} = \frac{t_p + t_n}{t_p + f_p + t_n + f_n},$$

Equation 5
$$F1 - \text{Score} = \frac{2}{\text{recall}^{-1} + \text{precision}^{-1}} = \frac{t_p}{t_p + \frac{1}{2}(f_p + f_n)},$$

Equation 6
$$MCC = \frac{t_p * t_n - f_p * f_n}{\sqrt{(t_p + f_p)(t_p + f_n)(t_n + f_p)(t_n + f_n)}},$$

Equation 7
$$\text{Precision} = \frac{t_p}{t_p + f_p},$$

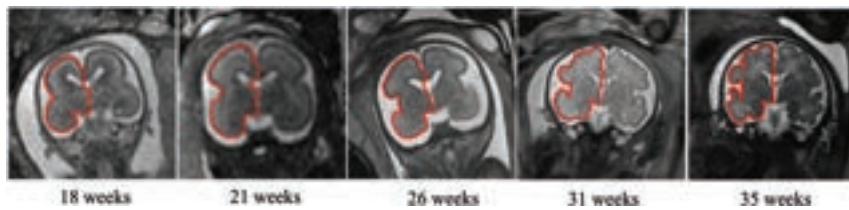


FIG 2. T2-weighted MR imaging of coronal views for control fetuses demonstrating gyrification development of the right hemisphere (red, *hemisphere contour*) at the Sylvian fissure level with gestation.

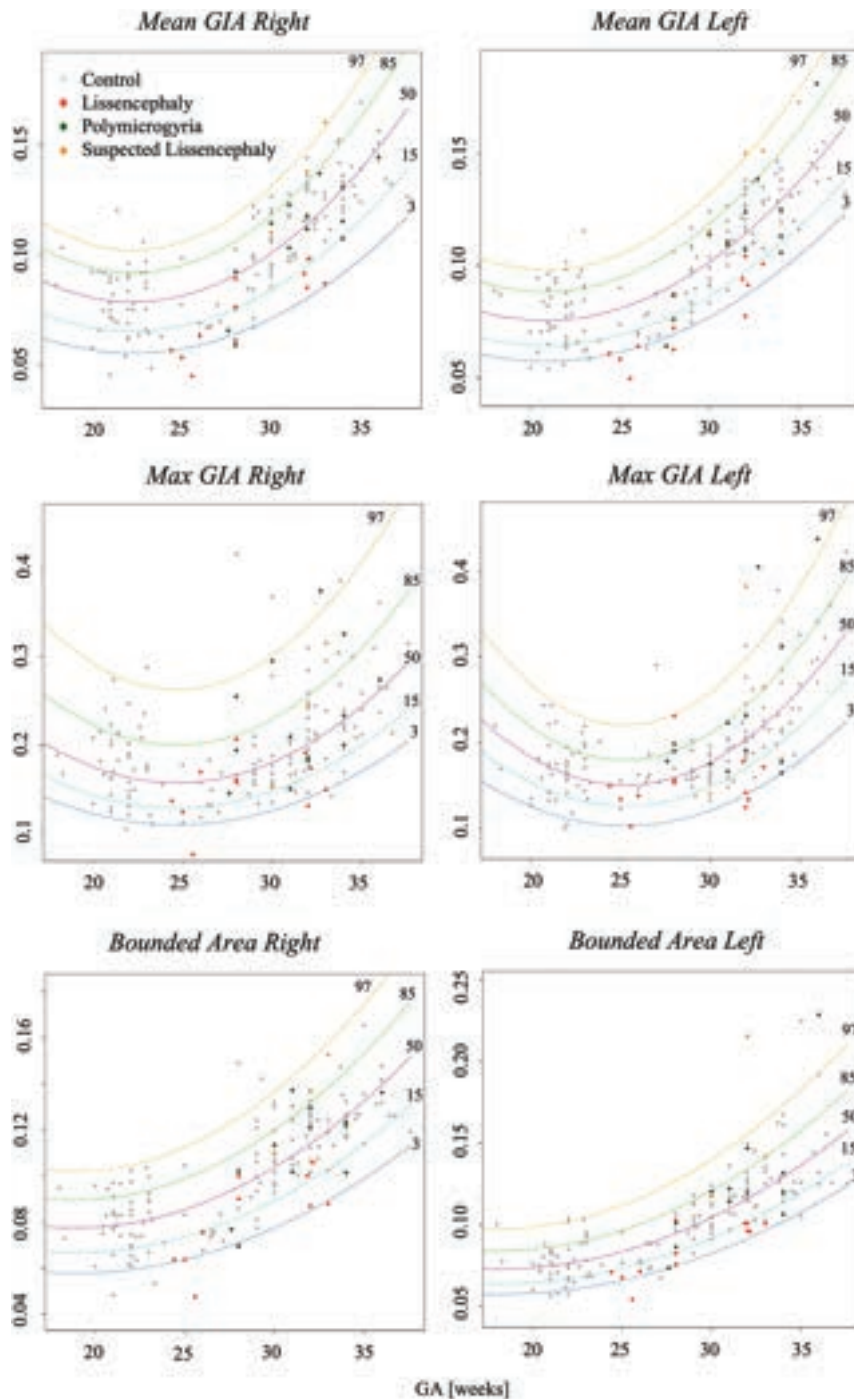


FIG 3. Development curves with GA of area-based gyrification parameters. Curve percentile lines 3, 15, 50, 85, and 97 are presented as blue, light blue, purple, green, and yellow, respectively. Note control fetuses (gray), PMG (green), LIS (red), and suspected LIS (orange).

$$\text{Equation 8} \quad \text{Recall} = \frac{t_p}{t_p + f_n},$$

where t_p is true-positive, t_n is true-negative, f_p is false-positive, and f_n is false-negative.

RESULTS

A data set of 200 fetuses was collected, with 9 fetuses excluded due to poor image quality and 29 for genetic or abnormal MR imaging findings. Of the 162 fetuses finally included, there were 134 controls (mean GA, 27.9 [SD, 5.3] weeks; range, 18–36 weeks); 12 with LIS (mean GA, 28.3 [SD, 3.2] weeks; range, 33–24 weeks); 13 with PMG (mean GA, 31.5 [SD, 2.7] weeks; range, 27–37 weeks); and 3 fetuses suspected of having LIS on the basis of sonography (mean GA, 31.3 [SD, 1.1] weeks; range, 30–32.5 weeks), but with normal MR imaging findings.

Controls

Figure 2 shows 5 control fetuses at different GAs with right hemisphere contours at the Sylvian fissure level, demonstrating the advancement in gyrification with gestation. Developmental curves for GIA and GIC parameters are presented in Figs 3 and 4, respectively, separated by the right and left hemispheres. All GI parameters change significantly throughout gestation ($P < .05$).

Most parameters increased throughout gestation, mainly from 23 weeks onward. The max GIA exhibited a U-shaped parabolic curve, reaching a minimum around the 25th week of GA, possibly due to changes in the Sylvian fissure.

Symmetry indices with GA are shown in Fig 5, demonstrating homogeneous dispersion, indicating no brain asymmetry.

MCD

Fetuses with MCD exhibited underdeveloped gyrification compared with controls. All GI parameters were significantly lower in fetuses with LIS ($P < .02$) highlighted at late GA, as seen in Figs 3 and 4, and Table 2. Representative MR imaging of controls and fetuses with LIS and PMG of equivalent ages are demonstrated in Fig 6.

Three fetuses suspected of having LIS based on sonography but diagnosed with normal MR imaging, findings showed normal GI values, supporting the MR imaging diagnosis.

Fetuses with PMG had significantly lower GICs ($P < .001$), with no significant difference in GIAs compared with controls (Table 2).

Brain asymmetry was not significant in fetuses with MCD, with homogeneous dispersion and no change in GA (Fig 5). However, 2 fetuses with PMG showed extreme asymmetry,

confirming the radiologic diagnosis. One fetus (34 GA) had PMG only in the right hemisphere, while the other fetus (36 weeks' GA) had PMG focused anteriorly, with an abnormal shape of the right operculum.

MCD Classification

Using machine learning classifiers based on GIC and GIA parameters, we evaluated 7 models. The performance of all models is

shown in the Online Supplemental Data. The best results for classification of controls and fetuses with LIS were achieved using XGBoost-logic, with the F1 score = 0.60, accuracy = 0.87, AUC = 0.90, MCC = 0.56, precision = 0.48, and recall = 0.83. The best classifier used for PMG was random forest with an F1 score = 0.59, accuracy = 0.89, AUC = 0.84, MCC = 0.53, precision = 0.57 and recall = 0.61.

DISCUSSION

In this study, we developed a method for automatic quantification of fetal gyrification based on clinical heterogeneous 2D MR imaging data, demonstrating high robustness, and we proposed 5 parameters. We found significant changes in gyrification with GA in control fetuses, with no asymmetry. We also found significantly reduced gyrification in fetuses with MCD compared with controls.

Five quantitative gyrification parameters were extracted for each hemisphere, including the contour-based parameters GIC and area-based parameters of GIA. Previous studies used different methods, including ridge detection,²⁸ local tensor-based morphometry,²⁹ and curvature-based^{20,30} and sulcal pattern similarities with fetal brain atlas.³¹ However, all these methods require 3D reconstruction, are

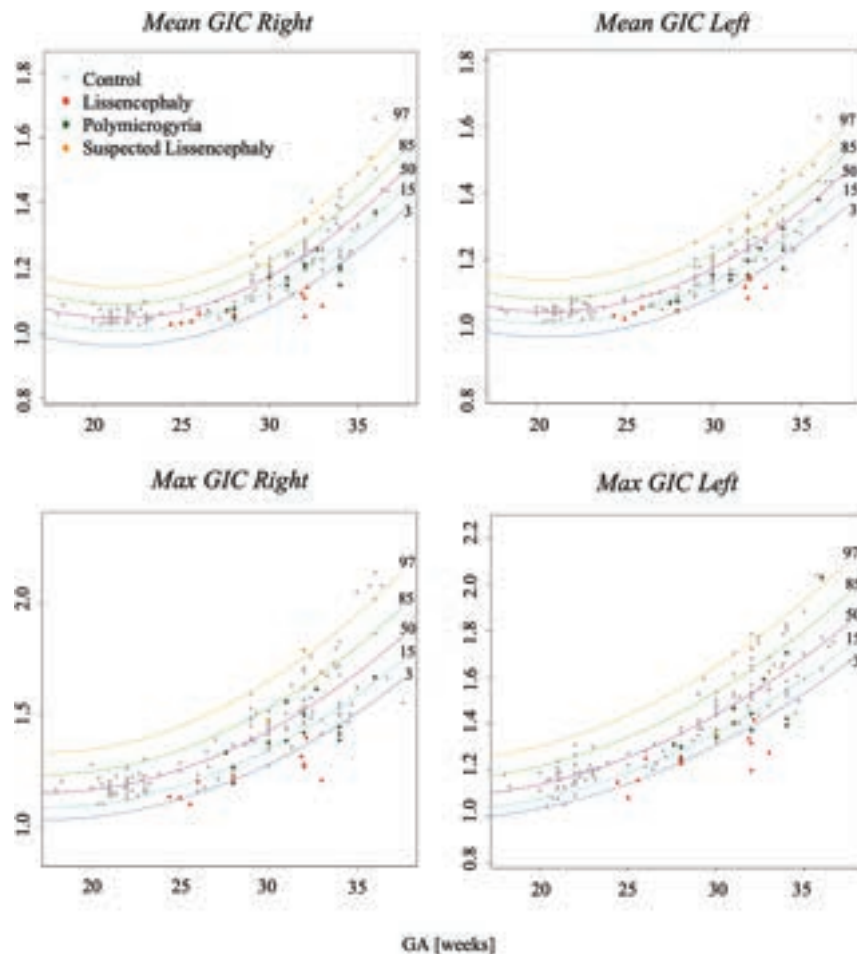


FIG 4. Development curves with GA of contour-based gyrification parameters. Curve percentile lines 3, 15, 50, 85, and 97 are presented as blue, light blue, purple, green, and yellow, respectively. Note control fetuses (gray), PMG (green), LIS (red), and suspected LIS (orange).

Table 2: Comparisons between LIS or PMG with control fetuses—the adjusted *P* values and CIs

Parameter	LIS		PMG	
	<i>P</i> Value	(CI Lower, CI Upper)	<i>P</i> Value	(CI Lower, CI Upper)
Mean GIC right	.002 ^a	(0.001–0.007)	<.001 ^a	(0.002–0.008)
Mean GIC left	.002 ^a	(0.001–0.007)	<.001 ^a	(0.002–0.008)
Max GIC right	<.001 ^a	(0.004–0.01)	<.001 ^a	(0.003–0.008)
Max GIC left	<.001 ^a	(0.004–0.009)	.001 ^a	(0.002–0.007)
Bounded volume right	.01 ^a	(0.0003–0.001)	.994	(–0.0004–0.0004)
Bounded volume left	<.001 ^a	(0.0003–0.009)	.366	(–0.0006–0.0002)
Mean GIA right	<.001 ^a	(0.0006–0.001)	.46	(–0.0002–0.0006)
Mean GIA left	<.001 ^a	(0.0006–0.001)	.46	(–0.0003–0.0005)
Max GIA right	.02 ^a	(0.0002–0.002)	.88	(–0.001–0.001)
Max GIA left	<.001 ^a	(0.0008–0.003)	.994	(–0.001–0.001)

^a *P* value < .05.

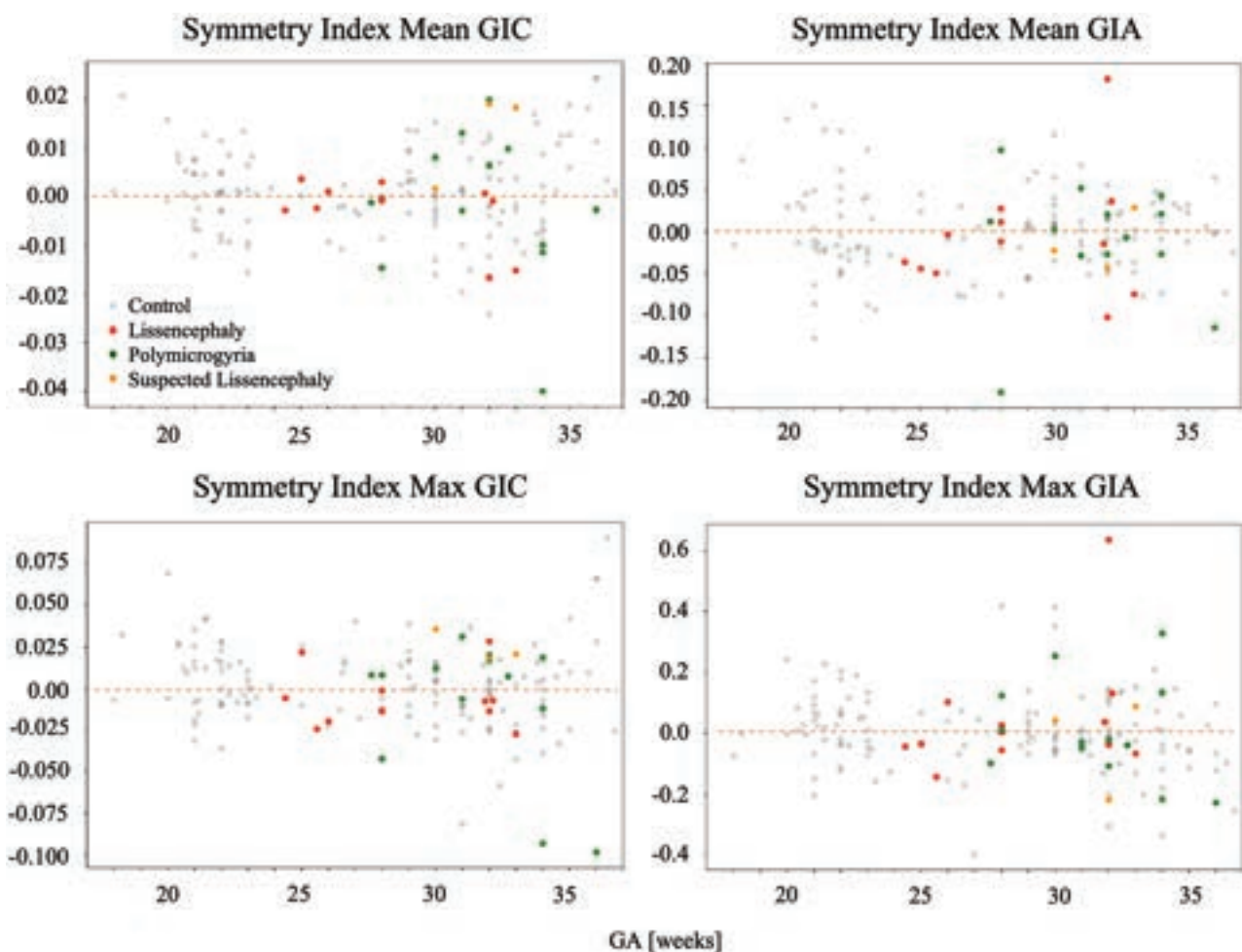


FIG 5. Symmetry indices for GI parameters with GA. All are close to zero, with homogeneous dispersion, indicating no brain asymmetry.

time-consuming, and are not easily applicable to clinical data. Our proposed method presents simple quantifying parameters that can be used in routine clinical practice and applied to retrospective data of large cohorts.

Developmental Curves

In this study, growth curves were calculated as recommended by the World Health Organization.³⁵ Our results indicate that gyrification in control fetuses increases in a second-degree polynomial curve after the 23rd week of gestation. Our findings corroborate previous studies by Dubois et al⁴⁶ who described cortical development in preterm infants across a similar range, demonstrating an accelerated gyrification measured by the cortical surface area and its GI after 28 weeks. In addition, Wright et al²⁰ showed nonlinear increased values in several global curvature-based parameters. Similarly, Rajagopalan et al²⁸ found that the GI development based on 3D reconstruction was best described with a second-order polynomial curve. Only 1 study demonstrated a linear gyrification increase with GA, probably due to the narrow range of GAs.²⁹

Brain Symmetry

Our study did not find evidence of gyrification asymmetry, consistent with previous studies that quantified global gyrification on the

basis of a 3D reconstructed cortical surface.^{18,20,22,23,25,26,28-30,47} While there is known asymmetry in specific sulci, such as the superior temporal gyrus,^{3,46,48} our results suggest that global gyrification measurements may not be sensitive enough to detect subtle regional differences.

MCD

Our results demonstrate significantly reduced gyrification in fetuses with LIS, with greater deviations at advanced GA. Notably, our results showed values within the normal range in 3 fetuses suspected of having LIS on the basis of sonography, yet with a normal MR imaging diagnosis.

Reduced gyrification was also detected in fetuses with PMG, but only in the GIC parameters. One previous study³¹ quantified gyrification in PMG and normally developing fetuses using 3D GI measurements yet did not find differences between the 2 groups. This was a small-scale study ($N_{\text{control}} = 17$, $N_{\text{PMG}} = 3$). To our knowledge, no additional studies quantified LIS and PMG fetal gyrification patterns with gestation or developed classifiers on the basis of control fetuses and fetuses with MCD. The classifiers trained in this study, both for LIS and for PMG, showed good performance in several metrics; however, the F1 score was improved when using SMOTE for

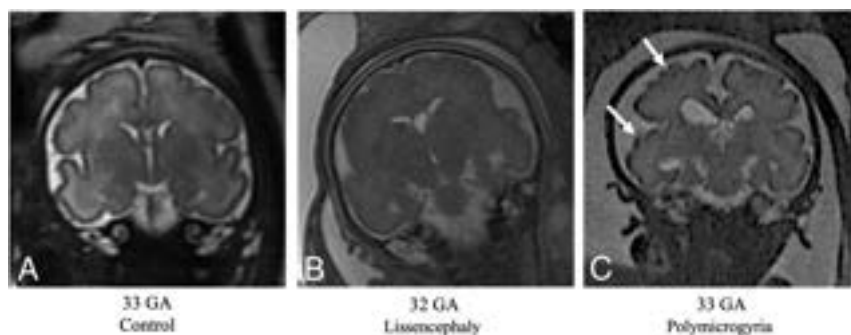


FIG 6. T2-weighted MR imaging of coronal views for controls and fetuses with LIS and PMG of equivalent ages. A, Control fetus, 33 weeks' GA. B, Fetus diagnosed with LIS at 32 weeks' GA, characterized by undeveloped gyrification patterns. C, Fetus diagnosed with PMG at 33 weeks' GA, with abnormal excessive gyri (white arrows).

imbalanced data and showed low values. These results are expected due to the overlap of MCDs and healthy fetuses in some of our gyrification parameters. Our findings support the use of quantitative analysis for fetal brain assessment in fetuses with MCD, to highlight fetuses at risk and to aid radiologic interpretation and diagnosis.

Limitations

Our study limitations include the potential impact of section acquisition symmetry on 2D gyrification parameters. However, analyzing each hemisphere separately may address this issue. This study focused on global parameters and did not analyze specific sulci. Future studies should develop automatic 2D methods to assess local parameters in different regions. Additionally, our gyrification parameters may pseudonormalize the multiple and shallow gyri in PMGs, leading to values within the normal range. The outcomes of the MCD fetuses were unavailable, and our criterion standard was the radiologist's diagnosis based on MR imaging. Finally, our cohort included 25 fetuses with MCD, representing the largest study to date that quantifies gyrification in MCD, yet the number is relatively small, especially when developing an automatic classifier. Therefore, due to the small cohort size, the classifiers developed in this study were only validated and not tested on a separate test set. Moreover, higher recall is needed and other parameters should be included in the model such as brain volume, brain biometrics, and so forth, to develop a method for clinical use.

CONCLUSIONS

This study presents an automatic quantification of fetal brain gyrification based on 2D routinely acquired MR imaging data and suggests the use of 5 parameters. The method successfully detected changes in normal gyrification with GA and showed reduced gyrification in fetuses with MCD compared with controls. These findings suggest that quantifying gyrification can aid in assessing fetal brain maturation and identifying MCDs.

ACKNOWLEDGMENTS

This research was supported by the Israel Innovation Authority and the Yoran Institute of Human Genome Research. Mr Yair

Wexler, School of Neurobiology, Biochemistry and Biophysics, Faculty of Life Sciences, Tel Aviv University, Tel Aviv, Israel, provided statistical advice for this study.

Disclosure forms provided by the authors are available with the full text and PDF of this article at www.ajnr.org.

REFERENCES

1. Fogliarini C, Chaumoitte K, Chapon F, et al. **Assessment of cortical maturation with prenatal MRI, Part I: normal cortical maturation.** *Eur Radiol* 2005;15:1671–85 CrossRef Medline
2. Dubois J, Dehaene-Lambertz G. **Fetal and postnatal development of the cortex: MRI and genetics.** *Brain Mapping: An Encyclopedic Reference* 2015;2:11–19 CrossRef
3. Garel C, Chantrel E, Brisse H, et al. **Fetal cerebral cortex: normal gestational landmarks identified using prenatal MR imaging.** *AJNR Am J Neuroradiol* 2001;22:184–89 Medline
4. Dubois J, Lefèvre J, Angleys H, et al. **The dynamics of cortical folding waves and prematurity-related deviations revealed by spatial and spectral analysis of gyrification.** *Neuroimage* 2019;185:934–46 CrossRef Medline
5. Dubois J, Benders M, Borradori-Tolsa C, et al. **Primary cortical folding in the human newborn: an early marker of later functional development.** *Brain* 2008;131:2028–41 CrossRef Medline
6. Garel C. *MRI of the Fetal Brain Normal Development and Cerebral Pathologies.* Springer-Verlag; 2004
7. Barkovich AJ. **MRI analysis of sulcation morphology in polymicrogyria.** *Epilepsia* 2010;51:17–22 CrossRef Medline
8. Schmitt S, Ringwald KG, Meller T, et al. **European Archives of Psychiatry and Clinical Neuroscience. Associations of gestational age with gyrification and neurocognition in healthy adults.** *Eur Arch Psychiatry Clin Neurosci* 2023;273:467–79 CrossRef Medline
9. Cassart M, Garel C. **European overview of current practice of fetal imaging by pediatric radiologists: a new task force is launched.** *Pediatr Radiol* 2020;50:1794–98 CrossRef Medline
10. Garel C. **Fetal cerebral biometry: normal parenchymal findings and ventricular size.** *Eur Radiol* 2005;15:809–13 CrossRef Medline
11. Epstein KN, Kline-Fath BM, Zhang B, et al. **Prenatal evaluation of intracranial hemorrhage on fetal MRI: a retrospective review.** *AJNR Am J Neuroradiol* 2021;42:2222–28 CrossRef Medline
12. Wilson M, Muir K, Reddy D, et al. **Prognostic accuracy of fetal MRI in predicting postnatal neurodevelopmental outcome.** *AJNR Am J Neuroradiol* 2020;41:2146–54 CrossRef Medline
13. Jaimes C, Rofeberg V, Stopp C, et al. **Association of isolated congenital heart disease with fetal brain maturation.** *AJNR Am J Neuroradiol* 2020;41:1525–31 CrossRef Medline
14. Papaioannou G, Klein W, Cassart M, et al. **Indications for magnetic resonance imaging of the fetal central nervous system: recommendations from the European Society of Paediatric Radiology Fetal Task Force.** *Pediatr Radiol* 2023;53:297–312 CrossRef Medline
15. Rima Valevicöien N, Varyt G, Zakarevicöien J, et al. **Use of magnetic resonance imaging in evaluating fetal brain and abdomen malformations during pregnancy.** *Medicina (B Aires)* 2019;55:55 CrossRef
16. Raafat M, Hosny SM, Sheta GA, et al. **Role of fetal MRI to diagnose abnormal cerebral ventricular system and associated fetal brain anomalies.** *Egypt J Radiol Nucl Med* 2022;53:85 CrossRef
17. Zilles K, Armstrong E, Schleicher A, et al. **The human pattern of gyrification in the cerebral cortex.** *Anat Embryol (Berl)* 1988;179:173–79 CrossRef Medline

18. Shimony JS, Smyser CD, Wideman G, et al. **Comparison of cortical folding measures for evaluation of developing human brain.** *Neuroimage* 2016;125:780–90 CrossRef Medline
19. Luders E, Thompson PM, Narr KL, et al. **A curvature-based approach to estimate local gyrification on the cortical surface.** *Neuroimage* 2006;29:1224–30 CrossRef Medline
20. Wright R, Kyriakopoulou V, Ledig C, et al. **Automatic quantification of normal cortical folding patterns from fetal brain MRI.** *Neuroimage* 2014;91:21–32 CrossRef Medline
21. Lefèvre J, Germanaud D, Dubois J, et al. **Are developmental trajectories of cortical folding comparable between cross-sectional datasets of fetuses and preterm newborns?** *Cereb Cortex* 2016;26:3023–35 CrossRef Medline
22. Raznahan A, Shaw P, Lalonde F, et al. **How does your cortex grow?** *J Neurosci* 2011;31:7174–77 CrossRef Medline
23. Duvernoy CS, Smith DE, Manohar P, et al. **Gender differences in adverse outcomes after contemporary percutaneous coronary intervention: an analysis from the Blue Cross Blue Shield of Michigan Cardiovascular Consortium (BMC2) percutaneous coronary intervention registry.** *Am Heart J* 2010;159:677–83.e1 CrossRef Medline
24. Luders E, Narr KL, Bilder RM, et al. **Mapping the relationship between cortical convolution and intelligence: effects of gender.** *Cereb Cortex* 2008;18:2019–26 CrossRef Medline
25. Lohmann G. **Extracting line representations of sulcal and gyral patterns in MR images of the human brain.** *IEEE Trans Med Imaging* 1998;17:1040–48 CrossRef Medline
26. Chen H, Li Y, Ge F, et al. **Gyral net: a new representation of cortical folding organization.** *Med Image Anal* 2017;42:14–25 CrossRef Medline
27. Im K, Pienaar R, Paldino MJ, et al. **Quantification and discrimination of abnormal sulcal patterns in polymicrogyria.** *Cereb Cortex* 2013;23:3007–15 CrossRef Medline
28. Rajagopalan V, Scott J, Habas PA, et al. **Quantitative in vivo MRI measurement of cortical development in the fetus.** *Brain Struct Funct* 2012;217:127–39 CrossRef Medline
29. Rajagopalan V, Scott J, Habas PA, et al. **Local tissue growth patterns underlying normal fetal human brain gyrification quantified in utero.** *J Neurosci* 2011;31:2878–87 CrossRef Medline
30. Habas PA, Scott JA, Roosta A, et al. **Early folding patterns and asymmetries of the normal human brain detected from in utero MRI.** *Cereb Cortex* 2012;22:13–25 CrossRef Medline
31. Im K, Guimaraes A, Kim Y, et al. **Quantitative folding pattern analysis of early primary sulci in human fetuses with brain abnormalities.** *AJNR Am J Neuroradiol* 2017;38:1449–55 CrossRef Medline
32. Wu J, Awate SP, Licht DJ, et al. **Assessment of MRI-based automated fetal cerebral cortical folding measures in prediction of gestational age in the third trimester.** *AJNR Am J Neuroradiol* 2015;36:1369–74 CrossRef Medline
33. Dudovitch G, Link-Sourani D, Ben Sira L, et al. **Deep learning automatic fetal structures segmentation in MRI scans with few annotated datasets.** In: *Proceedings of the International Conference on Medical Image Computing and Computer-Assisted Intervention*, October 4–8, 2020; Virtual: 365–74
34. Ori Ben Z, Netanel A, Bossmat Y, et al. **Automatic segmentation of fetal brain components from MRI using deep learning.** In: *Annual Meeting and Exhibition of the International Society for Magnetic Resonance in Medicine and the Society of MR Radiographers and Technologists*, May 15–20, 2021; Virtual
35. Borghi E, de Onis M, Garza C, et al; WHO Multicentre Growth Reference Study Group. **Construction of the World Health Organization child growth standards: selection of methods for attained growth curves.** *Stat Med* 2006;25:247–65 CrossRef Medline
36. Benjamini Y, Yekutieli D. **The control of the false discovery rate in multiple testing under dependency.** *Ann Statist* 2001;29:1165–88 CrossRef
37. Benjamini Y, Yekutieli D. **False discovery rate: adjusted multiple confidence intervals for selected parameters.** *J Am Stat Assoc* 2005;100:71–81 CrossRef
38. Rigby RA, Stasinopoulos DM. **Generalized additive models for location, scale and shape.** *Appl Statist* 2005;54:507–54
39. Righini A, Zirpoli S, Mrakic F, et al. **Early prenatal MR imaging diagnosis of polymicrogyria.** *AJNR Am J Neuroradiol* 2004;25:343–46 Medline
40. Dhombres F, Nahama-Allouche C, Gelot A, et al. **Prenatal ultrasonographic diagnosis of polymicrogyria.** *Ultrasound Obstet Gynecol* 2008;32:951–54 CrossRef Medline
41. Breiman L. *Random Forests*. Springer Link; 2001
42. Chang CC, Lin CJ. **LIBSVM: A Library for Support Vector Machines.** *ACM Transactions on Intelligent Systems and Technology*. Vol 2. 2001
43. Chen T, He T. **XGBoost: Extreme Gradient Boosting.** R package version 0.4-2 1.4 (2015): 1–4.
44. Chawla NV, Bowyer KW, Hall LO, et al. **SMOTE: Synthetic Minority Over-Sampling Technique.** *J Artif Intell Res* 2002;16:321–57
45. Chicco D, Jurman G. **The advantages of the Matthews correlation coefficient (MCC) over F1 score and accuracy in binary classification evaluation.** *BMC Genomics* 2020;21:6 CrossRef Medline
46. Dubois J, Benders M, Cachia A, et al. **Mapping the early cortical folding process in the preterm newborn brain.** *Cereb Cortex* 2008;18:1444–54 CrossRef Medline
47. Janssen J, Díaz-Caneja CM, Alloza C, et al. **Dissimilarity in sulcal width patterns in the cortex can be used to identify patients with schizophrenia with extreme deficits in cognitive performance.** *Schizophr Bull* 2021;47:552–61 CrossRef Medline
48. Kasprian G, Langs G, Brugger PC, et al. **The prenatal origin of hemispheric asymmetry: an in utero neuroimaging study.** *Cereb Cortex* 2011;21:1076–83 CrossRef Medline

Fetal Brain Growth in the Early Second Trimester

Maria Camila Cortes-Albornoz,¹ Camilo Calixto,² M. Alejandra Bedoya,³ Ryne A. Didier,⁴ Judy A. Estroff,⁵ and Camilo Jaimes⁶



ABSTRACT

BACKGROUND AND PURPOSE: Recent advances in fetal MR imaging technology have enabled acquisition of diagnostic images in the early second trimester. Interpretation of these examinations is limited by a lack of familiarity with the developmental changes that occur during these early stages of growth. This study aimed to characterize normal fetal brain growth between the 12th and 20th weeks of gestational age.

MATERIALS AND METHODS: This study was conducted as an observational retrospective analysis. Data were obtained from a tertiary care center's PACS database. All fetuses included had late fetal MR imaging (>20 weeks) or postnatal MR imaging, which confirmed normality. Each MR image was manually segmented, with ROIs placed to calculate the volume of the supratentorial parenchyma, brainstem, cerebellum, ventricular CSF, and extra-axial CSF. A linear regression analysis was used to evaluate gestational age as a predictor of the volume of each structure.

RESULTS: Thirty-one subjects with a mean gestational age of 17.23 weeks (range, 12–19 weeks) were studied. There was a positive, significant association between gestational age and intracranial, supratentorial parenchyma; brainstem cerebellum; intraventricular CSF; and extra-axial CSF volumes ($P < .001$). Growth was fastest in the supratentorial parenchyma and extra-axial CSF. Fetal sex was not associated with the volume in any of the ROIs.

CONCLUSIONS: This study demonstrates distinct trajectories for the major compartments of the fetal brain in the early second trimester. The fastest growth rates were observed in the supratentorial brain and extra-axial CSF.

ABBREVIATION: GA = gestational age

Extensive literature has demonstrated the usefulness of fetal MR imaging in assessing CNS abnormalities during the late second and third trimesters.^{1–4} Due to the small size of the fetus

and the high prevalence of motion artifacts, imaging is generally deferred until after 20 weeks' gestational age (GA).⁵ However, advancements in MR imaging technology, including receiving coils and the use of 3T scanners now allow imaging with sufficient spatial and temporal resolution to acquire diagnostic images in the early second trimester.^{6–8} This growing practice has highlighted the relative void of information regarding normal brain development in vivo in these early stages.

Evaluating brain growth and neurologic well-being in the early second trimester is of great interest to developmental neuroscience and fetal neurology. This period is characterized by the formation of the subplate, intense neuronal proliferation in the germinal centers, extensive neuronal migration, early synaptic sprouting, and axonal growth.⁹ In clinical practice, patients with pregnancies with fetal abdominal wall defects, chromosomal abnormalities detected on screening tests, major CNS abnormalities, and complications related to multiple pregnancies frequently seek diagnostic imaging and prognostication at earlier time points. Information obtained from early second-trimester fetal MR imaging can be tremendously useful in counseling these families.

Received July 6, 2023; accepted after revision October 2.

From the Department of Radiology (M.C.C.-A., C.C., M.A.B., R.A.D., J.A.E., C.J.) and Maternal Fetal Care Center (M.A.B., R.A.D., J.A.E.), Boston Children's Hospital, Boston, Massachusetts; Department of Radiology (M.C.C.-A., C.J.) and Pediatric Imaging Research Center (M.C.C.-A., C.J.), Massachusetts General Hospital, Boston, Massachusetts; and Harvard Medical School (M.C.C.-A., C.C., M.A.B., R.A.D., J.A.E., C.J.), Boston, Massachusetts.

J.A. Estroff and C. Jaimes are co-senior authors.

This work was supported by the American Roentgen Ray Society Scholarship; Career Development Award from the Office of Faculty Development at Boston Children's Hospital; National Institute of Neurological Disorders and Stroke, grant/award Nos. R01EB031849, R01EB032366, R01HD109395, R01NS106030; National Institutes of Health Office of the Director, grant/award No. S10OD025011; Rosamund Stone Zander Translational Neuroscience Center, Boston Children's Hospital; National Institute of Biomedical Imaging and Bioengineering; Eunice Kennedy Shriver National Institute of Child Health.

Please address correspondence to Camilo Jaimes, MD, Boston Children's Hospital, Radiology, 300 Lognwood Ave, Boston, MA, 02115; e-mail: cjaimescobos@partners.org; @PIRC_MGH



Indicates article with online supplemental data.

<http://dx.doi.org/10.3174/ajnr.A8051>

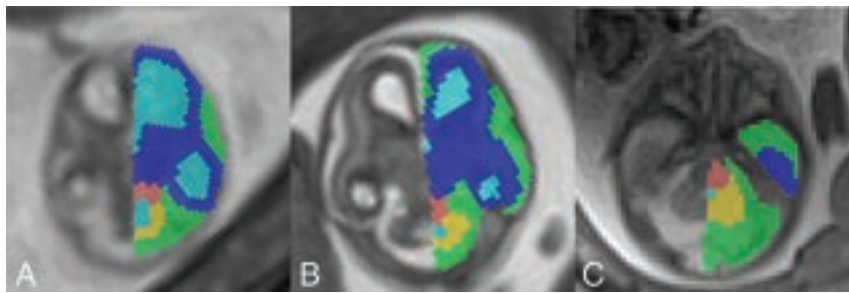


FIG 1. Representative example of ROIs in the brain of 12-week (A), 15-week (B), and 19-week-old fetuses (C). The supratentorial brain is labeled in dark blue; the ventricular CSF, in light blue; the extra-axial CSF, in green; the brainstem, in salmon; and the cerebellum, in yellow.

The purpose of this study was to characterize normal fetal brain development in vivo between the 12th and 20th weeks of gestation by performing a retrospective analysis at a large tertiary maternal and fetal care center. We hypothesized that while all structures in the fetal brain will grow during this period, our volumetric analysis will demonstrate distinct trajectories for the major constituents of the fetal brain at these early GAs.

MATERIALS AND METHODS

The institutional review board (Boston Children's Hospital) approved this observational retrospective study. All data were obtained from the PACS database at a tertiary children's hospital. Inclusion criteria were as follows: 1) fetal MR imaging performed between January 1, 2014, and December 30, 2022, in a pregnancy with <20 weeks' GA, 2) non-neurologic indication for the examination, and 3) the availability of a high-quality (fully diagnostic), late fetal (>20 weeks' GA), or postnatal MR imaging confirming a structurally normal brain. Exclusion criteria included the following: 1) fetal abnormalities that may affect neurodevelopment (eg, syndromic diseases, congenital infections, multiple gestations, chromosomal abnormalities), 2) twin pregnancies, and 3) MR imaging examinations with insufficient quality for manual segmentations. At least 1 series covering the fetal brain had to be devoid of motion in every single section to be considered of sufficient quality.

Data Acquisition

All images were acquired on 3T scanners (Magnetom Skyra and Magnetom Vida; Siemens). Institutional protocols were followed for image acquisition, consisting of HASTE or balanced steady-state free precession images. The parameters of the HASTE sequences were the following: TR = 1400–4000 ms, TE = 100–102 ms, FOV = 230 × 230 or 256 × 256, 1-mm in-plane resolution, 2- to 2.5-mm section thickness, acquisition matrix size = 208 × 208 or 256 × 256. For the balanced steady-state free precession sequences parameters were the following: TR = 4.3–5.2 ms, TE = 1.8–2.6 ms, FOV = 230 × 230–300 × 300, 1-mm in-plane resolution, 2- to 2.5-mm section thickness, acquisition matrix size = 256 × 320.

Image Processing

DICOM data of fetuses meeting the criteria were converted to the NIFTI format. Data were visualized and segmented using ITK-

SNAP (Version 4.0.0; www.itksnap.org) (Fig 1). We performed manual segmentations, placing ROIs in the fetal supratentorial brain parenchyma (the portion of the brain above the tentorium cerebelli), brainstem, cerebellum, extra-axial CSF, and intraventricular CSF using a high-resolution (1080p) Wacom Cintiq Tablet (<https://www.wacom.com/en-us/products/pen-displays/wacom-cintiq>). Given that fetal MR imaging at such an early GA is prone to motion degradation and that either sequence provides sufficient tissue contrast to out-

line the desired anatomy, we chose the sequence with the highest SNR and lowest artifact degradation (shadowing, motion, banding). This choice was determined subjectively by an experienced neuroradiologist. We performed an intraobserver variability analysis for 4 randomly chosen fetuses; the second set of segmentations was completed >4 months after the original segmentation.

Statistical Analysis

The volume of each label was calculated for all subjects. Intracranial volume was calculated as the sum of all ROIs. A linear regression analysis was used to evaluate GA as a predictor of the volume of each structure. We also controlled for sex on the basis of previously reported findings on sexual dimorphism by Machado-Rivas et al.⁷ The relative volume of each structure was calculated as the ratio of the absolute volume of the structure to the intracranial volume. We performed an intraobserver reliability analysis for the manual segmentations by randomly choosing 4 fetuses, performing new volumetric segmentations, and estimating the percentage change of the results relative to the index segmentation. Descriptive statistics were used to summarize the data from relative volume estimations. All calculations were performed using R (Version 4.2.1; <http://www.r-project.org/>) with a significance level of .05. Plots were designed using the ggplot2 package (Version 3.4.0; <https://www.rdocumentation.org/packages/ggplot2/versions/3.4.4>).

RESULTS

Population

We retrieved a total of 270 early second-trimester fetal MRIs. The examinations of 51 subjects met the criteria for inclusion, and 20 of these were subsequently excluded due to low image quality that precluded accurate segmentations (Fig 2). The final sample consisted of 31 subjects (13 female) with a mean GA of 17.23 weeks (range, 12–19 weeks). For 26 subjects, the follow-up examination consisted of a second fetal MR imaging obtained at a mean age of 27.2 weeks (range, 21–36 weeks), and for 5 subjects, the follow-up consisted of a postnatal MR imaging obtained 8.2 months postdelivery (range, 1–24 months). The average interval between the index study and the follow-up study was 13.32 weeks (range, 3–57 weeks). Table 1 summarizes the indications for fetal MRIs.

Volumetric Analysis

Intracranial Volume and Parenchyma. There were significant positive associations between GA and intracranial volume,

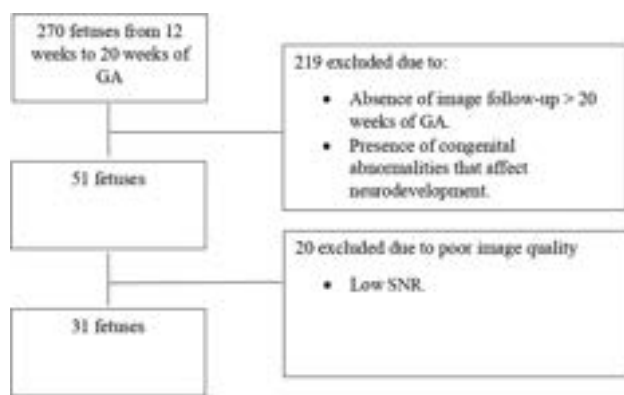


FIG 2. Application of inclusion and exclusion criteria in a flow diagram.

Table 1: Demographics and clinical characteristics

Population Characteristics	Median (Range)
Maternal age (yr)	32 (18–41)
Median GA (weeks)	18 (12–19)
Mean fetal growth percentile	44.62 (10.6–96.3)
Sex ^a	
Female	12 (38.70%)
Male	19 (61.29%)
Fetal diagnosis	
Congenital diaphragmatic hernia	7 (21.87%)
Normal	7 (21.87%)
Omphalocele	4 (12.5%)
Congenital pulmonary airway malformation	3 (9.37%)
Cleft lip	2 (6.25%)
Congenital heart disease	2 (6.25%)
Patent urachus	2 (6.25%)
Lymphatic malformation	1 (3.12%)
Occipital subcutaneous mass	1 (3.12%)
Hepatic hemangioma	1 (3.12%)
Hepatic pseudocyst	1 (3.12%)
Cardiac rhabdomyoma	1 (3.12%)

^a Data from this point down are No. of subjects (%).

supratentorial parenchymal volume, brainstem volume, and cerebellar volume. Fetal sex was not significantly associated with the volume of any of the ROIs ($P > .05$). The Online Supplemental Data summarize the mean volume and weekly change of the individual structures across the study period. The Online Supplemental Data present the mean volume of the individual structures per week.

CSF Spaces. We observed significant associations between GA and intraventricular CSF volume and extra-axial CSF. Fetal sex was not significantly associated with either ROI ($P > .05$, both). The Online Supplemental Data summarize the change in volume per week and present the mean volume per week.

The result of our intraobserver variability analysis showed high concordance between segmentations. The average percentage difference across all ROIs was 7.71%, and it was highest for the brainstem and intraventricular CSF ROIs. The highest concordance was found for the extra-axial CSF. The Online Supplemental Data summarize the data for this analysis.

Relative Volumetry

There was a significant GA-related increase in the relative volume of the supratentorial brain and extra-axial CSF ($P < .02$).

Conversely, there was a significant decrease in the relative volume of the brainstem, cerebellum, and intraventricular CSF ($P < .001$) (Table 2). Figure 3 provides a graphical comparison of the absolute and relative growth of each structure per GA. Fetal sex was not significantly associated with relative volume growth ($P > .05$).

DISCUSSION

Advancements in MR imaging technology have expanded the clinical applications of fetal MR imaging, enabling the acquisition of diagnostic images in the early second trimester. This study aimed to address the scarcity of data on in vivo fetal brain development in pregnancies between the 12th and 20th weeks' GA by performing a retrospective analysis of brain growth in subjects whose subsequent neuroradiologic studies confirmed normality. Our results demonstrate rapid growth of all intracranial structures with distinct trajectories for individual regions. Awareness of normative and relative volumetry of structures can inform the interpretation of fetal MRIs and contribute to understanding the selective vulnerability and physiopathology of abnormalities that could arise at these early developmental stages.

Most MR imaging literature pertaining to fetal brain development in the early second trimester is based on ex vivo studies.^{10–14} The absolute volumetric estimates for the cerebellum and total brain volume from our study align with those reported by Zhan et al¹⁰ and Xu et al.¹¹ The analysis performed by Zhan et al used sub-millimeter acquisitions at 7T in conjunction with atlas techniques. In addition to having similar growth trajectories, their approach enabled them to identify a clear anterior-to-posterior gradient in these developmental changes.¹⁰ Xu et al also used sub-millimeter acquisitions at 7T to study cerebellar growth, and while the trends they reported are consistent with our observations, their work delved deeper into the regional patterns of individual cerebellar lobules.¹¹ Most important, our study is the only one that has addressed these challenges using in vivo MR imaging, demonstrating the feasibility of this approach and facilitating translation. Furthermore, the use of in vivo data minimizes the effects of biases related to tissue damage, swelling, and tissue preparation that are inherent in ex vivo analyses.¹⁵

The supratentorial brain was the dominant compartment, and it also displayed the highest growth rate. At 12 weeks, it constituted about one-third of the intracranial volume, which increased to nearly one-half by the 19 weeks. Active neuronal proliferation and migration, the formation of the subplate, and the rapid expansion of the latter likely drive this exuberant growth.¹⁶ As these processes halt or slow down, growth does the same, leading to a more modest growth rate reported later in pregnancy by Machado-Rivas et al.⁷ Despite moderately high rates of growth, the brainstem and cerebellum were outpaced by the supratentorial brain, which resulted in a slight decrease in their relative percentage of intracranial volume between the 12th and 19th weeks. At later GAs, the rate of growth of the supratentorial brain decreases and the cerebellum becomes the fastest-growing compartment.^{7,17}

The ventricles constitute a dominant structure in early pregnancy, accounting for nearly one-quarter of intracranial volume at 12 weeks. Ventricular growth is slow, a finding previously

Table 2: Relative volume change per week based on linear regression analyses^a

Structure	Initial Relative Volume	Final Relative Volume	Change in Relative Volume per Week (95% CI)	P Value
Intraventricular CSF	23.52% (20.912%–26.12%)	8.64% (7.45%–9.84%)	–2.12 (–2.58 to –1.66)	.001
Supratentorial parenchyma	38.06% (34.25%–41.87%)	48.15% (46.39%–49.90%)	1.44 (0.77–2.11)	.001
Extra-axial CSF	32.26% (27.65%–36.86%)	39.62% (37.50%–41.74%)	1.05 (0.24–1.87)	.02
Brainstem	3.57% (2.97%–4.18%)	1.93% (1.66%–2.21%)	–0.23 (–0.34 to –0.13)	.001
Cerebellum	2.57% (2.16%–2.98%)	1.63% (1.44%–1.82%)	–0.13 (–0.21 to –0.06)	.001

^aRelative volume is expressed in terms of percentage. Data in parentheses are 95% CIs. ROIs are sorted in descending order based on the magnitude of the change of relative volume. The initial relative volume represents an estimate of 12 weeks' GA, and the final relative volume represents an estimate of 19 weeks' GA.

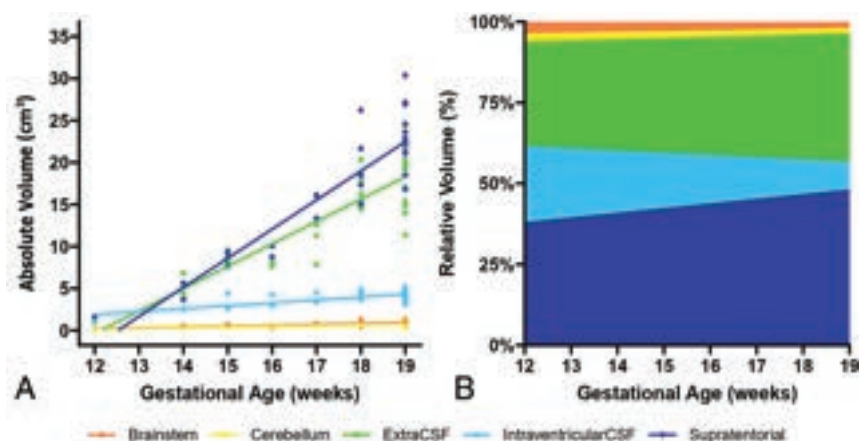


FIG 3. Absolute and relative volume growth per week. For each structure, absolute volume growth per week of GA (A) and relative volume growth per week (B) demonstrate relatively larger supratentorial growth during these early GAs.

corroborated by sonography and fetal MR imaging studies across a wide range of GAs.^{7,18} It is crucial to note that this slow growth results in a substantial decrease in the proportion of intracranial volume of the ventricles with advancing GA. The expansion of the extra-axial CSF emerged as another key finding in our analysis. Its growth rate was second only to that of the supratentorial parenchyma, reaching almost 40% of intracranial volume by 19 weeks' GA. The role of the extra-axial CSF as a marker of normal neurologic development is often underestimated. For instance, an increase in volume has been reported in cases of congenital heart disease, and a reduced volume is a hallmark of open neural tube defects.^{19,20}

Fetal neuroimaging in pregnancies of <20 weeks' GA, though uncommon, is an area of increasing interest. The desire to counsel families as early as possible, monitor vulnerable pregnancies, and triage patients for a growing number of fetal interventions has fueled this trend. One relatively common indication in our cohort was the characterization of abdominal wall defects. While not the primary malformation, the neurologic well-being of these fetuses is a pivotal point in counseling because multiorgan system malformations necessitate specialized counseling, particularly in regard to the potential for genetic or syndromic etiologies. Monochorionic diamniotic twins represent another vulnerable population; these fetuses are at risk of unbalanced vascular and placental sharing (eg, twin-twin transfusion syndrome) and resultant complications, have a high risk of cerebrovascular events, and frequently are eligible for fetoscopic interventions.^{16,21} Last, sociopolitical factors, such as the evolving

legal landscape surrounding pregnancy termination, could serve as an incentive to image fetuses at an earlier GA to provide prognostic information. The availability of normative volumetric data can enhance the interpretation of imaging findings in these early pregnancies.

The limitations of this study include its retrospective nature, which may introduce bias, and the relatively small sample size of 31 subjects. The exclusion of 20 subjects due to low image quality underscores the challenges of acquiring high-quality images during the early second trimester. The segmentations used for analysis were based on 2D images rather than 3D reconstructed volumes. Although previous work has

pioneered the use of super-resolved 3D volumes for fetal images, these tools are not available for the GA range analyzed in this study. Consequently, the reported volumes of structures in the fetal brain might be underestimated or overestimated compared with a 3D volume estimation. Future studies with larger sample sizes, prospective designs, and improved image analysis pipelines may help refine and expand the normative data generated in this study.

CONCLUSIONS

This study provides essential normative data on fetal brain development in vivo between the 12th and 20th weeks of gestation. During this period, there is substantial absolute and relative growth in the brain parenchyma and extra-axial CSF volume relative to the intraventricular CSF, cerebellum, and brainstem. As the clinical footprint of fetal MR imaging continues to expand to the early second trimester, these data can aid in interpreting these examinations.

Disclosure forms provided by the authors are available with the full text and PDF of this article at www.ajnr.org.

REFERENCES

1. Hulshof HM, Slot EM, Lequin M, et al; EPISTOP consortium. **Fetal brain magnetic resonance imaging findings predict neurodevelopment in children with tuberous sclerosis complex.** *J Pediatr* 2021;233:156–62. e2 CrossRef Medline
2. Griffiths PD, Bradburn M, Campbell MJ, et al; MERIDIAN collaborative group. **Use of MRI in the diagnosis of fetal brain abnormalities**

- in utero (MERIDIAN): a multicentre, prospective cohort study. *Lancet* 2017;389:538–46 CrossRef Medline
3. Yinon Y, Katorza E, Nassie DI, et al. **Late diagnosis of fetal central nervous system anomalies following a normal second trimester anatomy scan: late diagnosis of fetal CNS anomalies.** *Prenat Diagn* 2013;33:929–34 CrossRef Medline
 4. Jaimes C, Machado-Rivas F, Chen K, et al. **Brain injury in fetuses with vein of Galen malformation and nongalenic arteriovenous fistulas: static snapshot or a portent of more?** *AJNR Am J Neuroradiol* 2022;43:1036–41 CrossRef Medline
 5. The American College of Radiology. **ACR-SPR Practice Parameter for The Safe And Optimal Performance of Fetal Magnetic Resonance Imaging (MRI).** 2020. <https://www.acr.org/-/media/ACR/Files/Practice-Parameters/mr-fetal.pdf>. Accessed May 5, 2023
 6. Machado-Rivas F, Cortes-Albornoz MC, Afacan O, et al. **Fetal MRI at 3 T: principles to optimize success.** *Radiographics* 2023;43:e220141 CrossRef Medline
 7. Machado-Rivas F, Gandhi J, Choi JJ, et al. **Normal growth, sexual dimorphism, and lateral asymmetries at fetal brain MRI.** *Radiology* 2022;303:162–70 CrossRef Medline
 8. Jarvis DA, Finney CR, Griffiths PD. **Normative volume measurements of the fetal intra-cranial compartments using 3D volume in utero MR imaging.** *Eur Radiol* 2019;29:3488–95 CrossRef Medline
 9. Ackerman S. **The Development and Shaping of the Brain.** In: Ackerman S. *Discovering the Brain*. Vol 6. National Academies Press; 1992
 10. Zhan J, Dinov ID, Li J, et al. **Spatial-temporal atlas of human fetal brain development during the early second trimester.** *Neuroimage* 2013;82:115–26 CrossRef Medline
 11. Xu F, Ge X, Shi Y, et al. **Morphometric development of the human fetal cerebellum during the early second trimester.** *Neuroimage* 2020;207:116372 CrossRef Medline
 12. Brisse H, Fallet C, Sebag G, et al. **Supratentorial parenchyma in the developing fetal brain: in vitro MR study with histologic comparison.** *AJNR Am J Neuroradiol* 1997;18:1491–97 Medline
 13. Kinoshita Y, Okudera T, Tsuru E, et al. **Volumetric analysis of the germinal matrix and lateral ventricles performed using MR images of postmortem fetuses.** *AJNR Am J Neuroradiol* 2001;22:382–88 Medline
 14. Chong BW, Babcook CJ, Salama MS, et al. **A magnetic resonance template for normal neuronal migration in the fetus.** *Neurosurgery* 1996;39:110–16 CrossRef Medline
 15. D'Hondt A, Cassart M, De Maubeuge R, et al. **Postmortem fetal magnetic resonance imaging: where do we stand?** *Insights Imaging* 2018;9:591–98 CrossRef Medline
 16. Akkermans J, Peeters SH, Klumper FJ, et al. **Twenty-five years of fetoscopic laser coagulation in twin-twin transfusion syndrome: a systematic review.** *Fetal Diagn Ther* 2015;38:241–53 CrossRef Medline
 17. Clouchoux C, Guizard N, Evans AC, et al. **Normative fetal brain growth by quantitative in vivo magnetic resonance imaging.** *Am J Obstet Gynecol* 2012;206: 173.e1–8 CrossRef Medline
 18. Salomon LJ, Bernard JP, Ville Y. **Reference ranges for fetal ventricular width: a non-normal approach.** *Ultrasound Obstet Gynecol* 2007;30:61–66 CrossRef Medline
 19. Nagaraj UD, Bierbrauer KS, Stevenson CB, et al. **Myelomeningocele versus myelocele on fetal MR images: are there differences in brain findings?** *AJR Am J Roentgenol* 2018;211:1376–80 CrossRef Medline
 20. Brossard-Racine M, Du Plessis AJ, Vezina G, et al. **Prevalence and spectrum of in utero structural brain abnormalities in fetuses with complex congenital heart disease.** *AJNR Am J Neuroradiol* 2014;35:1593–99 CrossRef Medline
 21. Kocaoglu M, Kline-Fath BM, Calvo-Garcia MA, et al. **Magnetic resonance imaging of the fetal brain in monochorionic diamniotic twin gestation: correlation of cerebral injury with ultrasound staging and survival outcomes.** *Pediatr Radiol* 2020;50:1131–33 CrossRef Medline

Diagnostic Performance of Decubitus Photon-Counting Detector CT Myelography for the Detection of CSF-Venous Fistulas

Ajay A. Madhavan, Jeremy K. Cutsforth-Gregory, Waleed Brinjikji, Girish Bathla, John C. Benson, Felix E. Diehn, Laurence J. Eckel, Ian T. Mark, Pearse P. Morris, Melissa A. Payne, Jared T. Verdoorn, Nikkole M. Weber, Lifeng Yu, Francis Baffour, Joel G. Fletcher, and Cynthia H. McCollough



ABSTRACT

BACKGROUND AND PURPOSE: CSF-venous fistulas are a common cause of spontaneous intracranial hypotension. Lateral decubitus digital subtraction myelography and CT myelography are the diagnostic imaging standards to identify these fistulas. Photon-counting CT myelography has technological advantages that might improve CSF-venous fistula detection, though no large studies have yet assessed its diagnostic performance. We sought to determine the diagnostic yield of photon-counting detector CT myelography for detection of CSF-venous fistulas in patients with spontaneous intracranial hypotension.

MATERIALS AND METHODS: We retrospectively searched our database for all decubitus photon-counting detector CT myelograms performed at our institution since the introduction of the technique in our practice. Per our institutional workflow, all patients had prior contrast-enhanced brain MR imaging and spine MR imaging showing no extradural CSF. Two neuroradiologists reviewed pre-procedural brain MRIs, assessing previously described findings of intracranial hypotension (Bern score). Additionally, 2 different neuroradiologists assessed each myelogram for a definitive or equivocal CSF-venous fistula. The yield of photon-counting detector CT myelography was calculated and stratified by the Bern score using low-, intermediate-, and high-probability tiers.

RESULTS: Fifty-seven consecutive photon-counting detector CT myelograms in 57 patients were included. A single CSF-venous fistula was definitively present in 38/57 patients. After we stratified by the Bern score, a definitive fistula was seen in 56.0%, 73.3%, and 76.5% of patients with low-, intermediate-, and high-probability brain MR imaging, respectively.

CONCLUSIONS: Decubitus photon-counting detector CT myelography has an excellent diagnostic performance for the detection of CSF-venous fistulas. The yield for patients with intermediate- and high-probability Bern scores is at least as high as previously reported yields of decubitus digital subtraction myelography and CT myelography using energy-integrating detector scanners. The yield for patients with low-probability Bern scores appears to be greater compared with other modalities. Due to the retrospective nature of this study, future prospective work will be needed to compare the sensitivity of photon-counting detector CT myelography with other modalities.

ABBREVIATIONS: CTM = CT myelography; CVF = CSF-venous fistula; DSM = digital subtraction myelography; EID = energy-integrating detector; EVVP = external vertebral venous plexus; IVVP = internal vertebral venous plexus; PC = photon-counting detector; SIH = spontaneous intracranial hypotension; SR = standard resolution; T3D = low-energy threshold; UHR = ultra-high resolution; VMI = virtual monoenergetic image

Spontaneous intracranial hypotension (SIH) is a clinical syndrome caused by a spinal CSF leak. Although the hallmark symptom of SIH is an orthostatic headache, patients may present

with myriad symptoms that are frequently debilitating and occasionally life-threatening. Currently recognized are 3 types of spinal CSF leaks: dural tears (type 1a [ventral tears], type 1b [posterolateral tears]), leaking meningeal diverticula (type 2), and CSF-venous fistulas [CVFs, type 3]).^{1,2} Among these, CVFs are the most recently recognized and most challenging to diagnose.³ Patients with CVFs do not have evidence of extradural CSF on spine imaging (neither MR imaging nor CT myelography [CTM]), because leaked CSF and myelographic contrast are rapidly washed away by draining veins without accumulating in the epidural space. Furthermore, characteristic brain MR imaging abnormalities may be absent in some patients with spinal CSF leaks.⁴ A scoring system (Bern Score) assigning points to various

Received August 22, 2023; accepted after revision September 24.

From the Departments of Radiology (A.A.M., W.B., G.B., J.C.B., F.E.D., L.J.E., I.T.M., P.P.M., J.T.V., N.M.W., L.Y., F.B., J.G.F., C.H.M.), and Neurology (J.K.C.-G., M.A.P.), Mayo Clinic, Rochester, Minnesota.

Drs McCollough and Fletcher receive research support from Siemens Healthineers through a research grant paid to our institution.

Please address correspondence to Ajay Madhavan, MD, Division of Neuroradiology, Department of Radiology, Mayo Clinic, 200 First St SW, Rochester, MN 55905; e-mail: madhavan.ajay@mayo.edu



Indicates article with online supplemental data.

<http://dx.doi.org/10.3174/ajnr.A8040>

brain MR imaging findings was previously shown to predict the probability of finding a spinal CSF leak on myelography, initially being validated in patients with dural tears and subsequently used in the assessment of patients with CVFs.⁵⁻⁷

Digital subtraction myelography (DSM) and CTM are currently the preferred modalities for detecting CVFs at most centers with experience in the diagnosis of spinal CSF leaks, with the latter sometimes being performed in a dynamic (multiphase) fashion.^{8,9} Both modalities have been shown to be effective, especially as techniques for DSM and dynamic CTM have been refined in recent years. In particular, it is now known that performing myelography with the patient in the lateral decubitus position and imaging immediately after intrathecal contrast injection increase the likelihood of detecting CVFs.⁹ Despite many advances, however, neither technique is perfectly sensitive, with some CVFs being missed in patients with clear clinical symptoms of SIH and/or brain MR imaging abnormalities consistent with that diagnosis.^{6,7} Thus, there is a need for continued improvement in imaging techniques to detect CVFs.

In collaboration with another institution, Madhavan et al¹⁰ recently reported a small series of 6 patients in whom CVFs were detected using photon-counting detector CT myelography (PC-CTM). Three of those patients had negative findings on DSM, and 2 had negative findings on dynamic CTM using a conventional energy-integrating detector (EID) CT scanner before the positive findings on PC-CTM. We thus hypothesized that PC-CTM may be an effective technique with a high diagnostic yield for the detection of CVFs. Here, we describe the first large series of patients with SIH studied by PC-CTM, focusing on the diagnostic yield of this examination in patients without extradural CSF on initial spine imaging.

MATERIALS AND METHODS

Patient Selection

This Health Insurance Portability and Accountability Act-compliant retrospective study was approved by our institutional review board. We retrospectively identified all patients who underwent PC-CTM at our institution between February 1, 2023, and June 30, 2023. Clinical information, including indications for the PC-CTM, patient age and sex at the time of the examination, the presence of prior brain and spine MR imaging, and the presence of any prior myelographic studies, were obtained from the medical record. Inclusion criteria were the following: 1) patient meeting the International Classification of Headache Disorders (ICHD-3) criteria for SIH, 2) the presence of at least 1 contrast-enhanced brain MR imaging before PC-CTM, and 3) the absence of spinal extradural fluid on spine MR imaging or conventional CT myelography before PC-CTM. Exclusion criteria were a technically unsuccessful or incomplete PC-CTM or lack of documented consent to use medical information for retrospective research.

Imaging Technique

All PC-CTMs at our institution were performed using the same technique. The patient was placed on the PC-CT scanner (NAEOTOM Alpha; Siemens) in the right lateral decubitus Trendelenburg position. A 20-ga Quincke spinal needle was

advanced into the subarachnoid space at L2-L3 or a lower spinal level under CT guidance. Five milliliters of Omnipaque 300 (GE Healthcare) were injected intrathecally. Low-dose monitoring scans at C7-T1 were performed every 5 seconds to dynamically monitor contrast flow. A series of 3-6 scans of the entire spine was initiated manually when intrathecal contrast reached C7-T1, with the number of scans varying depending on the radiologist's preference and patient-specific factors. All scans were performed during slow inspiration with a 5-second interval between scans. The needle was removed, the patient was rotated to the left lateral decubitus position, and the process was repeated after placing a new spinal needle. Note that a same-day bilateral technique keeping the initial spinal needle in place has been reported, which is likely a viable option for many patients but was not done in this study.¹¹

Among the 3-6 scans in each position, the first 2-4 scans were performed with standard resolution (SR) mode (144×0.4 mm detector collimation), and the last 1-2 scans, with ultra-high-resolution (UHR) mode (120×0.2 mm detector collimation). The order of SR and UHR scans occasionally varied. All scans had a rotation time of 0.5 seconds and a CARE keV IQ level of 200. Automatic exposure control was used, with a manual tube potential of 140 kV. All scans were reconstructed separately as virtual monoenergetic images (VMIs) at 40 keV and a low-energy threshold (referred to as T3D by the manufacturer and including photon energies from 25 to 140 keV to exclude electronic noise), all with a Br40 kernel (quantum iterative reconstruction strength setting of 3). SR scans were reconstructed at 0.4 mm, and UHR scans were reconstructed at 0.2 mm. Pitch was 1.2 (SR) or 1.0 (UHR), and the approximate time per scan was 5.0 seconds (SR) and 12.0 seconds (UHR).

Imaging Review

For each patient, the most recent pre-PC-CTM brain MR imaging was reviewed by 2 blinded neuroradiologists and assigned a Bern score, which is calculated on the basis of the presence of pachymeningeal enhancement (2 points), venous sinus engorgement (2 points), effacement of the suprasellar cistern of <4 mm (2 points), the presence of subdural fluid collections (1 point), effacement of the prepontine cistern of <5 mm (1 point), and reduction of the mamillopontine distance of <6.5 mm (1 point). Venous sinus engorgement was assessed specifically in the dominant transverse sinus at a paramidline sagittal section on postgadolinium MPRAGE images. Any discrepancy between the 2 reviewers (either in total Bern score or individual components of the score) was resolved by a third adjudicating neuroradiologist.

PC-CTM images were reviewed by 2 neuroradiologists in consensus, both different from the brain MR imaging reviewers. Reviewers specifically assessed the following: 1) the presence or absence of a CVF, 2) whether the CVF was definitive or equivocal, 3) the maximal attenuation of the draining vein, and 4) the scan number on which the finding was first visible. Reviewers were blinded to imaging reports and patient history. Each case was reviewed on a standard PACS workstation capable of generating multiplanar reformats from source axial images. Venous attenuation was determined by placing a circular ROI over the

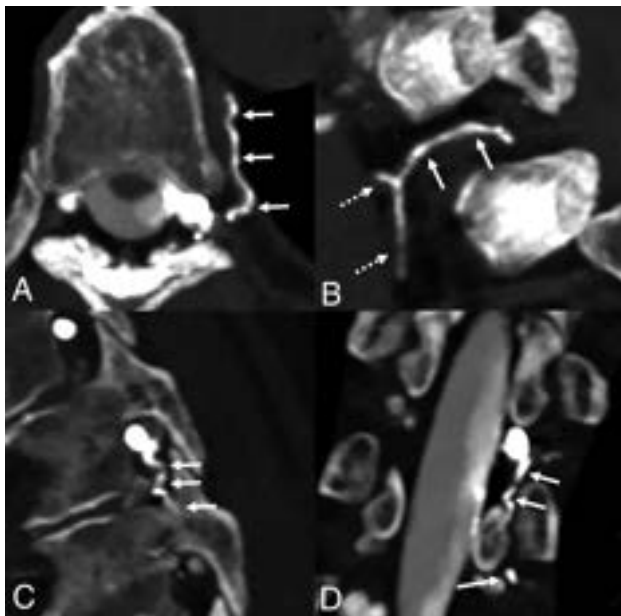


FIG 1. Definitive CVF on PC-CTM involving both the IVVP and EVVP in a patient meeting the ICHD-3 criteria for SIH. Axial MIP images derived from 0.4-mm 40-keV slices demonstrate a left T6 CVF involving the paraspinal segmental vein (A and B, *solid arrows*) and extending into the hemiazygos system (B, *dashed arrows*). Sagittal and coronal 40-keV images (C and D) obtained at a different time point show additional involvement of the IVVP, with contrast extending down to the level of T7 (C and D, *arrows*).

most visually attenuated draining vein on an axial image and reporting the highest value in the ROI. Definitive CVFs had a maximal venous attenuation of >200 HU on T3D images, while equivocal CVFs had a maximal venous attenuation of 100–199 HU on T3D images. These cutoffs were chosen to be at least as stringent as previously proposed Hounsfield unit cutoffs for CVFs, with 1 prior study suggesting a cutoff of 70 HU.¹²

The side and spinal level of the CVF were recorded. Additionally, the most proximal draining vein of each CVF was identified and recorded, specifically noting whether drainage was to the internal vertebral venous plexus (IVVP, medial to the midpoint of the pedicle, Figs 1–3) or the external vertebral venous plexus (EVVP, lateral to the midpoint of the pedicle, Fig 1 and Online Supplemental Data). If no CVF was present, the 2 reviewers also determined whether there was evidence of a type 1 or type 2 leak (dural tear or leaking meningeal diverticulum). Finally, the same 2 neuroradiologists who reviewed the PC-CTMs also reviewed, in consensus, any decubitus DSM or decubitus dynamic EID CTM performed before the PC-CTM, again assessing the presence or absence of a CVF and whether the CVF was definite or equivocal (EID CTMs) or simply whether a definitive CVF was present (DSMs). Only DSMs and EID CTMs that included decubitus positioning and imaging in that same position within 2 minutes of intrathecal contrast injection were included in this review.

The radiation dose of each examination was obtained from the medical record by a single neuroradiologist. Finally, any subsequent treatment based on PC-CTM findings was documented by a single neuroradiologist.¹³

Data Analysis

Mean patient ages and sex distribution were calculated. The mean Bern score of all patients was calculated. The positivity rate (diagnostic yield) of definitive and equivocal CVFs on PC-CTM was calculated and stratified by the Bern score (using previously described low, medium, and high pretest probability tiers). The diagnostic yield of PC-CTM was also stratified by the presence or absence of a previously negative decubitus DSM or decubitus EID CTM.

RESULTS

Patient Characteristics

A total of 63 patients underwent 63 PC-CTMs during the study period. One patient was excluded because she was unable to complete the myelogram secondary to nausea. Five patients were excluded due to lack of documented consent to use medical information for research purposes. Thus, 57 patients having undergone 57 PC-CTMs were included in the final cohort (Online Supplemental Data). Of these, 42 patients were women and 15 were men. The mean age of all patients was 51.2 years (Online Supplemental Data).

Brain MR Imaging Findings

Among the 57 reviewed brain MRIs, there were discrepant findings between the 2 initial reviewers in 2 cases. In the first case, one reviewer noted pachymeningeal enhancement and the other did not. The third adjudicating reviewer deemed pachymeningeal enhancement to be present. In the second case, one reviewer noted venous sinus engorgement and the other did not. The third adjudicating reviewer deemed venous sinus engorgement to be present. There were no other discrepancies among the reported Bern scores (total score or individual components) among the 2 reviewers.

The mean Bern score in the 57 patients was 3.53, with a range of 0–8. Twenty-five of 57 (43.9%) patients had a low-probability Bern score of 0–2, 15/57 (26.3%) patients had an intermediate-probability Bern score of 3–4, and 17/57 (29.8%) patients had a high-probability Bern score of 5–8. No patients had a Bern score of 9.

PC-CTM Findings

A single CVF was identified definitively in 38/57 (66.7%) patients and equivocally in 11/57 (19.3%) patients. No CVF was identified in the remaining 8/57 (14.0%) patients, and none of these 8 patients had a type 1 or 2 leak identified on their PC-CTM. No patients had more than a single CVF. Stratification by Bern score revealed the following:

- 1) In patients with low-probability brain MRIs (Bern score of 0–2, $n = 25$), a single CVF was identified definitively in 14/25 (56.0%) patients and equivocally in 8/25 (32.0%) patients.
- 2) In patients with intermediate-probability brain MRIs (Bern score of 3–4, $n = 15$), a single CVF was identified definitively in 11/15 (73.3%) patients and equivocally in 1/15 (6.7%) patients.
- 3) In patients with a high-probability brain MRI (Bern score of 5–8, $n = 17$), a single CVF was identified definitively in 13/17 (76.5%) patients and equivocally in 2/17 (11.8%) patients.

Definitive CVFs occurred on the right in 25/38 (65.8%) patients and on the left in 13/38 (34.2%) patients, with the most

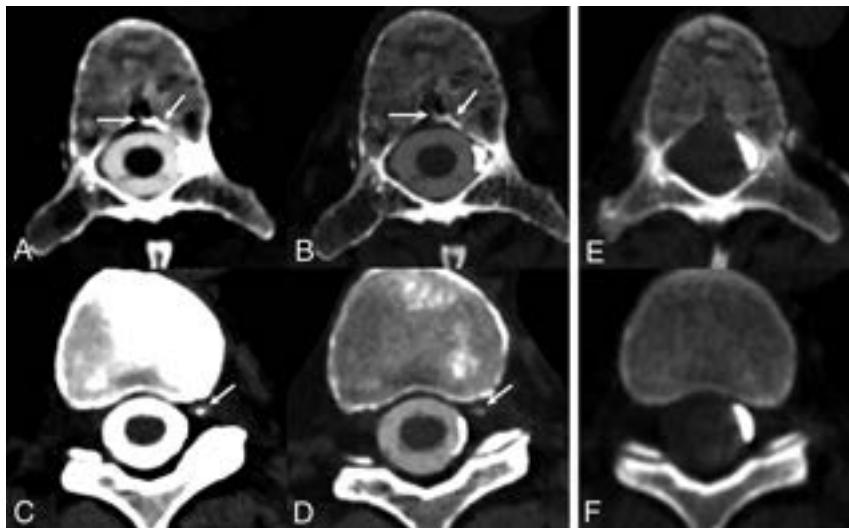


FIG 2. Definitive left T10 CVF involving the ventral IVVP and basivertebral vein in a patient with previously negative findings on decubitus dynamic EID CTM. Axial 40-keV 0.4-mm (A) and T3D 0.2-mm (B) images from PC-CTM, both at the same window/level setting, demonstrate contrast opacification of the T10 basivertebral vein (A and B, arrows), which is most conspicuous on the 40-keV image but defined with better resolution on the T3D image. Axial 40-keV 0.4-mm (C) and T3D 0.2-mm (D) images at the same window/level setting from an adjacent slice at an earlier time point show additional involvement of the ventral IVVP (C and D, arrows). This subtle finding is best seen on the 40-keV image. Neither finding was seen on retrospective review of the patient's dynamic EID CTM (E and F).

frequent spinal level being T10 ($n = 7$, Online Supplemental Data). Equivocal CVFs occurred on the right in 5/11 (46.0%) patients and on the left in 6/11 (54.0%) patients. Regarding venous drainage in the 49 patients with definitive or equivocal CVFs, 17/49 (34.7%) CVFs involved the IVVP only, 28/49 (57.1%) CVFs involved the EVVP only, and 4/49 (8.2%) involved both the IVVP and EVVP. Among the 38 definitive CVFs, 13/38 (34.2%) CVFs involved the IVVP only, 21/38 (55.3%) CVFs involved the EVVP only, and 4/38 (10.5%) involved both the IVVP and EVVP. Among the 38 definitive CVFs, the imaging finding was initially on first scan in 20/38 (52.6%) patients, on the second scan in 5/38 (13.2%) patients, on the fourth scan in 5/38 (13.2%) patients, on the fifth scan in 6/38 (15.8%) patients, and on the sixth scan in 2/38 (5.3%) patients. Among the 11 equivocal CVFs, the imaging finding was seen initially on the first scan in 8/11 (72.7%) patients and on the fifth scan in 3/11 (27.3%) patients. The mean radiation dose (dose-length product) per scan for all included PC-CTMs was 340 mGy-cm. The mean number of scans performed (accounting for both the left and right sides) was 10.

With regard to myelographic studies before PC-CTM, 39/57 (68.4%) patients had a previous DSM. In all cases, this DSM was deemed negative for CVF by both reviewers. On PC-CTM in these patients, a single CVF was identified in 33/39 (84.6%) patients with a negative DSM (Fig 3 and Online Supplemental Data). The CVF was definitive in 22/39 (56.4%) patients and equivocal in 11/39 (28.2%) patients. The mean time interval between DSM and PC-CTM was 57 days, with 15 patients having undergone a nontargeted blood patch between the DSM and PC-CTM.

Eight of 57 (14.0%) patients had undergone a prior decubitus dynamic EID CTM. In all cases, this EID CTM was deemed

negative for CVF by both reviewers. On PC-CTM, a single definitive CVF was identified in 8/8 (100%) patients (Figs 2 and 3 and Online Supplemental Data). The mean time interval between EID CTM and PC-CTM was 30 days, with 4 patients having undergone a nontargeted blood patch between the EID CTM and PC-CTM.

Treatment

All 38 patients with definitive CVFs localized on PC-CTM underwent transvenous Onyx (Medtronic) embolization of the fistula. Among the 11 patients with equivocal CVFs, 6 underwent transvenous Onyx embolization and 5 underwent a targeted transforaminal epidural blood patch. Review of post-treatment images confirmed treatment of the correct spinal level and side.

DISCUSSION

We describe the largest cohort to date of patients with SIH having undergone dynamic decubitus PC-CTM, allowing

several meaningful conclusions. PC-CTM identified a definitive CVF in 66.7% of consecutive patients presenting with SIH in the absence of an extradural CSF. When stratified by the pretest probability of finding a CSF leak on the basis of brain MR imaging Bern score, PC-CTM identified a definitive CVF in 56.0%, 73.3%, and 76.5% of patients with low, intermediate, and high probabilities, respectively. PC-CTM was effective in detecting CVFs draining to the IVVP, EVVP, or a combination of both.

The high diagnostic yield of PC-CTM for detecting CVFs in patients with intermediate and high pretest probability Bern scores is consistent with that in previous studies on decubitus DSM and CTM.^{6,8,9} The yield of PC-CTM in patients with low-probability Bern scores is greater than that reported for other modalities. For example, a prior study on decubitus DSM found that no CVFs were detected in 9 patients with low-probability Bern scores.⁶ Other studies have reported a yield of typically under 20% in patients with low-probability Bern scores when using DSM or EID CTM, though large studies on the yield of EID CTM are lacking.^{4,14} Importantly, we do continue to consider DSM and EID CTM to be excellent modalities for CVF detection. While our findings are interesting, particularly regarding the high yield in patients with low-probability Bern scores, this is a retrospective study with some selection bias, and it does not prove that PC-CTM is more sensitive than DSM or EID CTM. Also, patients with transvenous Onyx embolization may, in particular, be best served with DSM due to extensive streak artifacts caused by Onyx on CT. Many complex factors must be considered because different institutions determine the modalities of choice for CVF detection. Still, our study does provide evidence that PC-CTM has a high yield in patients with SIH and

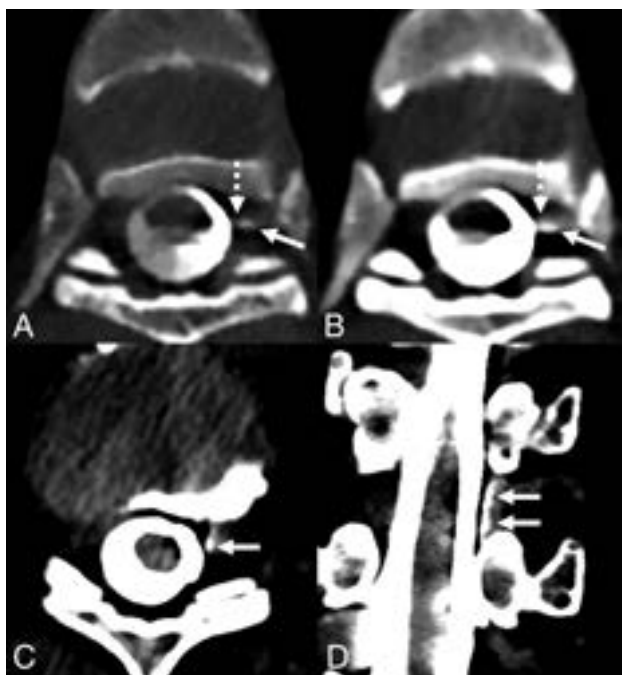


FIG 3. Definitive CVFs involving the IVVP in 2 separate patients, illustrating the complementary benefits of high-spatial-resolution and low kiloelectron volt VMIs. Both patients had a Bern score of 1. The first patient had no prior decubitus myelographic studies, while the second patient initially underwent negative decubitus DSM and negative decubitus EID CTM (not shown). In the first patient (A and B), an axial 0.2-mm T3D image (A) from PC-CTM demonstrates a left T6 CVF involving the IVVP (A, *solid arrow*). The draining vein is clearly separate from the thecal sac (A, *dashed arrow*), distinguishing it from a direct epidural leak. Concurrent axial 40-keV VMI reconstructed at the minimum allowed slice thickness of 0.4 mm with identical window/level settings demonstrates higher attenuation of the same finding (B, *arrow*), but the lower spatial resolution less clearly distinguishes the vein from the thecal sac (B, *dashed arrow*). In the second patient (C and D), axial (C) and coronal (D) 40-keV 0.4-mm VMIs from PC-CTM demonstrate a left T10 CVF of the IVVP (C and D, *arrows*). In this case, the 0.4-mm slice thickness was sufficient to distinguish the vein from the thecal sac. In both patients, the venous contrast washed away on subsequently obtained images (not shown).

low Bern scores, which is promising and worthy of further investigation.

PC-CT has many advantages that make it beneficial for the detection of CVFs.^{10,15} First, PC-CT has excellent temporal resolution. In our protocol including 3–6 scans of the spine in each decubitus position, the approximate duration of each scan is 3–5 seconds for SR scans and 10–12 seconds for UHR scans (depending on patient body habitus). The interval between scans is approximately 5 seconds. This permits rapid sampling of multiple time points while maintaining a scan speed that is conducive to minimizing respiratory and other motion artifacts. Second, PC-CT has higher spatial resolution compared with EID CT. The minimum section thickness achieved with PC-CT varies between 0.2 mm with the UHR mode and 0.4 mm with the SR mode. Thin-section imaging is invaluable for detecting contrast within tiny veins, or even a thin column of contrast within a larger vein (Online Supplemental Data). High spatial resolution also helps to distinguish small internal epidural veins from the adjacent thecal

sac or veins adjacent to diverticula (Online Supplemental Data). Our protocol included up to 2 UHR scans and 4 SR scans. Although it would be optimal to perform all 6 scans in the UHR mode, in our experience, this practice resulted in too much reduction in temporal resolution.

Finally, PC-CT has inherent spectral imaging capabilities that allow VMIs to be reconstructed without the need for dual-energy/dual-source techniques. VMIs with a kiloelectron volt closer to the K-edge of iodine have the benefit of increasing the iodine signal, which has been shown to increase the conspicuity of subtle CSF leaks, with the main trade-off being an impaired SNR.^{16,17} We found that VMIs as low as 40 keV retained a visually acceptable SNR while maximizing the iodine signal.¹⁰ Although EID-based techniques such as dual-energy CT can also produce low kiloelectron volt VMIs, dual energy scan modes usually require slower scan speeds compared with PC-CT. In our experience, it is the combination of high spatial resolution, high temporal resolution, and VMIs that allows the detection of the most subtle CVFs (Online Supplemental Data).

Radiation dose is an important concern for all types of myelography. In general, PC-CT has a lower radiation dose compared with EID CT with similar or improved image quality.¹⁸ In our study, the mean dose-length product per scan was 340 mGy-cm, with the mean number of scans being 10. Thus, the dose is certainly not trivial. However, we also found that at least 5 scans were needed to identify the imaging finding in 7 cases of definitive CVF and 3 cases of equivocal CVF, suggesting some added value in multiple scans. In our practice, some proceduralists have recently opted to split the contrast injection over multiple scans and review images between scans so that the examination can be stopped if a definitive CVF is identified. This procedure may be an effective means to limit the radiation dose in the future. Alternatively, if a patient has had a previously negative CTM performed with an early scan (immediately after contrast injection), subsequent CT examinations could, instead, start with a slightly delayed scan of several minutes.

Our study has limitations. First and most important, it was not possible to directly compare PC-CTM with other imaging modalities. Although many patients in our study had previously negative DSMs or EID CTMs and subsequently positive PC-CTMs, there is selection bias in the retrospective study design. Future prospective studies directly comparing PC-CTM, DSM, and EID CTM with consistent examination techniques and close timing between the examinations will be needed. Second, our PC-CTMs were reviewed in consensus rather than independently, due to the complexity of the examinations and subtlety of findings in some cases. Reviewers were also aware that they were viewing a PC-CTM, which could introduce bias. Independent review should be considered in future studies when possible.

Finally, our study did not assess treatment response. The scope of this study was to evaluate the diagnostic performance of PC-CTM for detecting CVFs, and future studies focusing on clinical outcomes after treatment will be needed. This limitation is particularly applicable to the equivocal CVFs in our study, in which treatment response would be helpful to determine whether the radiographic findings were clinically relevant. The efficacy of Onyx embolization and other techniques for CVF treatment has

been demonstrated previously, and response to treatment could help confirm radiographically indeterminate findings.¹⁹⁻²¹ As more patients with indeterminate findings are found, future studies discussing treatment response in this patient population, as well as defining better radiographic criteria for definitive versus equivocal CVFs, will be helpful.

Despite its limitations, this is the first study to assess the diagnostic performance of PC-CTM for the detection of CVFs. PC-CTM has a high diagnostic yield for CVF detection. Its potential advantage over DSM and EID CTM warrants further investigation as PC-CT becomes more widely available.

CONCLUSIONS

We describe the first large cohort of consecutive patients with SIH having undergone PC-CTM, showing that it has a high diagnostic yield for detection of CVFs. This study suggests that the yield of PC-CTM compared with decubitus DSM and EID CTM is at least as high for patients with intermediate and high Bern scores and the yield may be higher in those with low Bern scores.

Disclosure forms provided by the authors are available with the full text and PDF of this article at www.ajnr.org.

REFERENCES

- Schievink WI, Maya MM, Jean-Pierre S, et al. **A classification system of spontaneous spinal CSF leaks.** *Neurology* 2016;87:673–79 CrossRef Medline
- Callen AL, Timpone VM, Schwertner A, et al. **Algorithmic multimodality approach to diagnosis and treatment of spinal CSF leak and venous fistula in patients with spontaneous intracranial hypotension.** *AJR Am J Roentgenol* 2022;219:292–301 CrossRef Medline
- Schievink WI, Moser FG, Maya MM. **CSF-venous fistula in spontaneous intracranial hypotension.** *Neurology* 2014;83:472–73 CrossRef Medline
- Schievink WI, Maya M, Prasad RS, et al. **Spontaneous spinal cerebrospinal fluid-venous fistulas in patients with orthostatic headaches and normal conventional brain and spine imaging.** *Headache* 2021;61:387–91 CrossRef Medline
- Dobrocky T, Grunder L, Breiding PS, et al. **Assessing spinal cerebrospinal fluid leaks in spontaneous intracranial hypotension with a scoring system based on brain magnetic resonance imaging findings.** *JAMA Neurol* 2019;76:580–87 CrossRef Medline
- Kim DK, Carr CM, Benson JC, et al. **Diagnostic yield of lateral decubitus digital subtraction myelogram stratified by brain MRI findings.** *Neurology* 2021;96:e1312–18 CrossRef Medline
- Callen AL, Pattee J, Thaker AA, et al. **Relationship of Bern score, spinal elastance, and opening pressure in patients with spontaneous intracranial hypotension.** *Neurology* 2023;100:e2237–46 CrossRef Medline
- Kranz PG, Gray L, Amrhein TJ. **Decubitus CT myelography for detecting subtle CSF leaks in spontaneous intracranial hypotension.** *AJNR Am J Neuroradiol* 2019;40:754–56 CrossRef Medline
- Mamlouk MD, Ochi RP, Jun P, et al. **Decubitus CT myelography for CSF-venous fistulas: a procedural approach.** *AJNR Am J Neuroradiol* 2021;42:32–36 CrossRef Medline
- Madhavan AA, Yu L, Brinjikji W, et al. **Utility of photon-counting detector CT myelography for the detection of CSF-venous fistulas.** *AJNR Am J Neuroradiol* 2023;44:740–44 CrossRef Medline
- Carlton Jones L, Goadsby PJ. **Same-day bilateral decubitus CT myelography for detecting CSF-venous fistulas in spontaneous intracranial hypotension.** *AJNR Am J Neuroradiol* 2022;43:645–48 CrossRef Medline
- Kranz PG, Amrhein TJ, Gray L. **CSF venous fistulas in spontaneous intracranial hypotension: imaging characteristics on dynamic and CT myelography.** *AJR Am J Roentgenol* 2017;209:1360–66 CrossRef Medline
- Brinjikji W, Savastano LE, Atkinson JLD, et al. **A novel endovascular therapy for CSF hypotension secondary to CSF-venous fistulas.** *AJNR Am J Neuroradiol* 2021;42:882–87 CrossRef Medline
- D'Antona L, Merchan MA, Vassiliou A, et al. **Clinical presentation, investigation findings, and treatment outcomes of spontaneous intracranial hypotension syndrome: a systematic review and meta-analysis.** *JAMA Neurol* 2021;78:329–37 CrossRef Medline
- Schwartz FR, Malinzak MD, Amrhein TJ. **Photon-counting computed tomography scan of a cerebrospinal fluid venous fistula.** *JAMA Neurol* 2022;79:628–29 CrossRef Medline
- Houk JL, Marin DM, Malinzak MD, et al. **Dual energy CT for the identification of CSF-venous fistulas and CSF leaks in spontaneous intracranial hypotension: report of four cases.** *Radiol Case Rep* 2022;17:1824–2 CrossRef Medline
- Albrecht MH, Vogl TJ, Martin SS, et al. **Review of clinical applications for virtual monoenergetic dual-energy CT.** *Radiology* 2019;293:260–71 CrossRef Medline
- Marth AA, Marcus RP, Feuerriegel GC, et al. **Photon-counting detector CT versus energy-integrating detector CT of the lumbar spine: comparison of radiation dose and image quality.** *AJR Am J Roentgenol* 2023 Aug 30. [Epub ahead of print] CrossRef Medline
- Brinjikji W, Garza I, Whealy M, et al. **Clinical and imaging outcomes of cerebrospinal fluid-venous fistula embolization.** *J Neurointerv Surg* 2022;14:953–56 CrossRef Medline
- Kononov A, Gadzhiagaev V, Vinogradov E, et al. **Surgical treatment efficacy of CSF-venous fistulas: systematic review.** *World Neurosurg* 2022;161:91–96 CrossRef Medline
- Mamlouk MD, Shen PY, Sedrak MF, et al. **CT-guided fibrin glue occlusion of cerebrospinal fluid-venous fistulas.** *Radiology* 2021;299:409–18 CrossRef Medline

T1-Weighted, Dynamic Contrast-Enhanced MR Perfusion Imaging Can Differentiate between Treatment Success and Failure in Spine Metastases Undergoing Radiation Therapy

Mark Behar, Kyung K. Peck, Onur Yildirim, Jamie Tisnado, Atin Saha, Julio Arevalo-Perez, Eric Lis, Yoshiya Yamada, Andrei I. Holodny, and Sasan Karimi



ABSTRACT

BACKGROUND AND PURPOSE: Current imaging techniques have difficulty differentiating treatment success and failure in spinal metastases undergoing radiation therapy. This study investigated the correlation between changes in dynamic contrast-enhanced MR imaging perfusion parameters and clinical outcomes following radiation therapy for spinal metastases. We hypothesized that perfusion parameters will outperform traditional size measurements in discriminating treatment success and failure.

MATERIALS AND METHODS: This retrospective study included 49 patients (mean age, 63 [SD, 13] years; 29 men) with metastatic lesions treated with radiation therapy who underwent dynamic contrast-enhanced MR imaging. The median time between radiation therapy and follow-up dynamic contrast-enhanced MR imaging was 62 days. We divided patients into 2 groups: clinical success ($n = 38$) and failure ($n = 11$). Failure was defined as PET recurrence ($n = 5$), biopsy-proved ($n = 1$) recurrence, or an increase in tumor size ($n = 7$), while their absence defined clinical success. A Mann-Whitney U test was performed to assess differences between groups.

RESULTS: The reduction in plasma volume was greater in the success group than in the failure group (-57.3% versus $+88.2\%$, respectively; $P < .001$). When we assessed the success of treatment, the sensitivity of plasma volume was 91% (10 of 11; 95% CI, 82%–97%) and the specificity was 87% (33 of 38; 95% CI, 73%–94%). The sensitivity of size measurements was 82% (9 of 11; 95% CI, 67%–90%) and the specificity was 47% (18 of 38; 95% CI, 37%–67%).

CONCLUSIONS: The specificity of plasma volume was higher than that of conventional size measurements, suggesting that dynamic contrast-enhanced MR imaging is a powerful tool to discriminate between treatment success and failure.

ABBREVIATIONS: DCE = dynamic contrast-enhanced; ΔV_p = change in plasma volume; k^{trans} = vessel permeability; ROC = receiver operating characteristic; RT = radiation therapy; V_p = plasma volume

The skeletal system is the third most common location for metastatic lesions, following the lungs and liver. Within the skeleton, the spine is the most prevalent site of metastasis. Up to 10% of all patients with cancer will develop spinal osseous metastases, leading to increased morbidity and mortality.¹ Vertebral body metastases can effectively be detected using conventional MR imaging, including T1-weighted and STIR sequences. However, routine MR

imaging techniques are rather limited in assessing treatment response versus disease progression following radiation therapy (RT).^{2,3} Currently, progression is suggested by an increase in lesion size on conventional MR imaging, while lesion stability suggests treatment success.⁴ However, lesion size often fluctuates after both successful and unsuccessful treatment, limiting the utility of conventional MR imaging in evaluating the response to therapy. This limitation can lead to delayed detection of tumor recurrence, which, in turn, may adversely impact patient outcomes.

Dynamic contrast-enhanced (DCE) MR imaging is an advanced imaging technique that can noninvasively analyze vascular microenvironment and hemodynamics, which is not possible with conventional MR imaging.⁵ DCE-MR imaging involves rapid IV injection of a contrast agent, which is subsequently measured by a dynamic T1-weighted imaging sequence. The extended Tofts dual-compartment pharmacokinetic model is then applied to calculate the reduction of intravascular volume, reduction in plasma volume (V_p), and the rate of contrast leakage from the intravascular to interstitial space (k^{trans}).⁶ V_p is an indicator of tumor vascularity,

Received March 11, 2023; accepted after revision October 5.

From the Departments of Radiology (M.B., K.K.P., O.Y., J.T., A.S., J.A.-P., E.L., A.I.H., S.K.), Medical Physics (K.K.P.), and Radiation Oncology (Y.Y.), Memorial Sloan Kettering Cancer Center, New York, New York; Department of Radiology (A.I.H.), Weill Medical College of Cornell University, New York, New York; and Department of Neuroscience (A.I.H.), Weill-Cornell Graduate School of the Medical Sciences, New York, New York.

This study was funded, in part, through an industrial grant (Bayer HealthCare: study No: DI-2013-003) and the National Institutes of Health/National Cancer Institute Cancer Center Support Grant P30 CA008748.

Please address correspondence to Andrei I. Holodny, MD, Department of Radiology, Memorial Sloan Kettering Cancer Center, 1275 York Ave, NY, NY 10065; e-mail: holodnya@mskcc.org



Indicates article with online supplemental data.

<http://dx.doi.org/10.3174/ajnr.A8057>

while K^{trans} reflects vessel permeability. In essence, a voxelwise tracer kinetic analysis of the ROI offers insight into the pathophysiologic status of the tumor microenvironment.⁷

Previous work has demonstrated the superiority of DCE-MR imaging in assessing tumor vascularity compared with conventional techniques.⁸ The results of DCE-MR imaging can then be applied to evaluate treatment response in patients with spinal metastases treated with high-dose RT.⁹ Other work has shown that changes in perfusion parameters, most notably V_p , reflect tumor response to RT in spinal osseous metastases and serve as a predictor of tumor recurrence in lumbar metastases.^{2,10} DCE-MR imaging parameters additionally have been demonstrated to change quickly after other treatment modalities, including stereotactic radiosurgery.¹¹ DCE-MR imaging is emerging as a powerful tool for estimating tissue permeability and enables the assessment of tumor angiogenesis, which is not possible with conventional MR imaging and traditional dynamic susceptibility contrast perfusion methods. However, DCE-MR imaging output parameters can be influenced by numerous factors including age, sex, and lesion location.¹² Relative CBV measured by traditional dynamic susceptibility contrast can be influenced by the presence of susceptibility artifacts and contrast leakage from tumor vessels.

We hypothesized that a reduction in V_p would correlate with treatment success and, therefore, improve clinical outcomes and that DCE-MR imaging could predict tumor recurrence more successfully than traditional size measurements on conventional MR imaging. Therefore, the objective of this retrospective study was to evaluate the validity of using perfusion parameters to predict treatment success or failure regarding spinal osseous metastases. Additionally, the study aimed to show that analysis using perfusion parameters was concordant and, in some cases, surpassed lesion-size measurements in the determination of treatment success or failure.

MATERIALS AND METHODS

This retrospective study was conducted under a waiver of authorization from the Institutional Review Board at Memorial Sloan Kettering Cancer Center.

Study Patients

We collected patients who underwent DCE-MR imaging before and after receiving RT between March of 2013 and December of 2020. Exclusion criteria included technically limited and therefore nondiagnostic DCE perfusion studies and DCE perfusion MR imaging obtained >1 year post-RT, resulting in the inclusion of 49 patients. Of the remaining patients, the median time between RT and the first available DCE-MR imaging was 62 days (Online Supplemental Data). We then separated the patients into 2 distinct groups reflecting their clinical outcomes: clinical response ($n = 38$) and persistent disease ($n = 11$). Patients were assessed within 18 months after the second DCE-MR imaging, with persistent disease defined as PET recurrence at the same spine level ($n = 5$), size increase recorded by a radiologist ($n = 7$), or biopsy-proved recurrence ($n = 1$). Some patients met multiple conditions. The patients in this study had limited spinal disease, and some had oligometastases to the spine with well-controlled primaries or without evidence of local disease at the primary site. The goal of radiation therapy in this patient population was a cessation of disease progression. The patients were treated with a

single dose or a hypofractionated regimen as follows: 24 Gy in 1 fraction, 27 Gy in 3 fractions, or 30 Gy in 3 fractions, depending on location, histology, age, and the patient's ability and availability to return and complete his or her treatment.

MR Imaging Acquisition

We performed MR imaging of the spine with a 1.5T scanner (Discovery 450W; GE Healthcare), using an 8-channel cervical-thoracic-lumbar surface coil. All patients underwent routine MR imaging sequences, including sagittal T1 (FOV, 32–36 cm; section thickness, 3 mm; TR, 400–650 ms; and flip angle, 90°), sagittal T2 (FOV, 32–36 cm; section thickness, 3 mm; TR, 3500–4000 ms; and flip angle, 90°), and sagittal STIR images (FOV, 32–36 cm; section thickness, 3 mm; TR, 3500–6000 ms; and flip angle, 90°).

DCE-MR imaging of the spine was then performed. Gadobutrol (Gadavist; Bayer) was administered at 0.1 mmol/kg of body weight and a rate of 2–3 mL/s. Kinetic enhancement of the tissue during and after injection of gadopentetate dimeglumine was obtained via a 3D T1-weighted fast spoiled gradient-echo sequence (TR, 4–5 ms; TE, 1–2 ms; section thickness, 5 mm; flip angle, 25°; FOV, 32 cm; and temporal resolution, 5–6 seconds) and consisted of 10–12 images in the sagittal plane. The 3D fast-spoiled gradient echo sequences generated phase images in addition to standard magnitude images. The duration of the DCE sequence was 300 seconds. Sagittal and axial T1-weighted MR images with gadopentetate dimeglumine were acquired after DCE perfusion.

Data Analysis

Data were processed and analyzed by a single trained researcher (M.B.) using US FDA-approved commercial software (NordicICE, Version 2.3; NordicNeuroLab). Preprocessing steps included background noise removal, spatial and temporal smoothing, and automatic detection of the arterial input function from the aorta. The aorta was selected on the basis of prior literature. The arterial input function was individually computed and visually verified in every section, and arterial input function curves with a rapid increase in signal enhancement and a sharp peak followed by minimal temporal noise were selected for further DCE analysis. Arterial input function curves were shifted manually to account for delayed blood flow to the spine.

We applied the extended Tofts dual-compartment pharmacokinetic model, which assumes that the contrast agent is either in the interstitial space or in the intravascular compartment, to calculate the DCE perfusion MR imaging parameter, V_p .⁶ ROIs were manually defined around the spinal lesions with careful consideration, to exclude venous structures, hemangiomas, disk spaces, cortical bone, and spondylotic changes on each T1-weighted DCE perfusion MR imaging section. Structures of interest included vertebral bodies, lamina, spinous processes, and paraspinal soft tissues. ROIs were then superimposed onto corresponding perfusion maps to guide calculations. When the lesions appeared to extend beyond the osseous structure into paraspinal soft tissues, we included both the bony and soft structures in our ROI analysis. A fellowship-trained neuroradiologist (O.Y.) used conventional MR imaging, including T1- and T2-weighted images, to measure the size of the lesion. Correlation was determined between these sequences to ensure the accuracy of the lesion margin. The largest bidimensional size of the lesions was measured on the axial plane. The measurement was performed in the pre-

and posttreatment scans closest to the time of RT, with careful consideration to avoid adjacent treatment-related changes and normal bone marrow. The axial and sagittal images were

Patient demographics and cancer type

	Total	Clinical Response	Persistent Disease
Patients and age (y)			
No. of patients	49	38	11
Age (mean) (yr)	63 (SD, 13)	61 (SD, 13)	68 (SD, 7)
Sex			
No. of men	29	24	5
No. of women	20	14	6
Lesion location			
Cervical	2	2	0
Thoracic	27	20	7
Lumbar	16	13	3
Sacral	4	3	1
Metastatic source			
Lung	12	9	3
RCC	9	8	1
Breast	5	3	2
Prostate	4	4	0
Thyroid	4	4	0
Melanoma	3	3	0
Other	12	7	5

Note:—RCC indicates renal cell carcinoma.

chosen for the assessment and measurement of the extraosseous tumor extension. The tridimensional measurement of the extraosseous component of the tumor is calculated by measuring the extraosseous spread from the adjacent normal bony cortex, which is defined as the line connecting the tumor and normal bony cortex at the unilateral margins. Measurement from an estimated normal bony cortex surface line may also be useful in high-volume tumoral lesions. The contralateral margins of the bony cortex are used to draw this line.

Measurements of all lesions were performed by a neuroradiologist (O.Y.). Two senior neuroradiologists (A.I.H., with 25 years of experience, and S.K., with 20 years of experience) were consulted for size measurements in specific cases. To account for background variations among different DCE perfusion MR imaging studies, we normalized fractional plasma volume by obtaining the ratio between the lesion ROI and an adjacent healthy vertebra (ie, V_p normalization). The normalized V_p values were then used for statistical analyses.

Statistical Analysis

We performed Mann-Whitney U tests, in which P values $\leq .05$ indicated statistical significance, on V_p , K^{trans} , and signal intensity to evaluate differences between clinical response and clinical failure. We performed receiver operating characteristic (ROC) analysis using

software (Johns Hopkins online ROC curve calculator; <http://www.rad.jhmi.edu/jeng/javarad/roc/JROCFITi.html>) to determine the optimal cutoff with the highest Youden index.

RESULTS

Study Patients

After exclusion criteria were applied, 49 patients remained, 29 men and 20 women with similar age distributions (Table). The mean age for all patients was 63 (SD, 13) years. All patients had metastatic disease, with the most prevalent primary cancers being lung, kidney, breast, prostate, and thyroid. Metastatic lesions were present at all spinal levels, with thoracic (32.7%; 27 of 49) and lumbar (55.1%; 16 of 49) lesions comprising most. Of all included patients, 11 demonstrated persistent disease, while the remaining 38 demonstrated clinical response.

Tumor Perfusion Analysis

Qualitatively, metastatic spinal lesions appeared hypointense on T1-weighted images. Perfusion maps of malignant spinal lesions demonstrate marked signal intensity changes that are easily distinguishable from healthy spinal tissue. This signal intensity change is most pronounced in lesions with increased vascularity and metabolic activity.

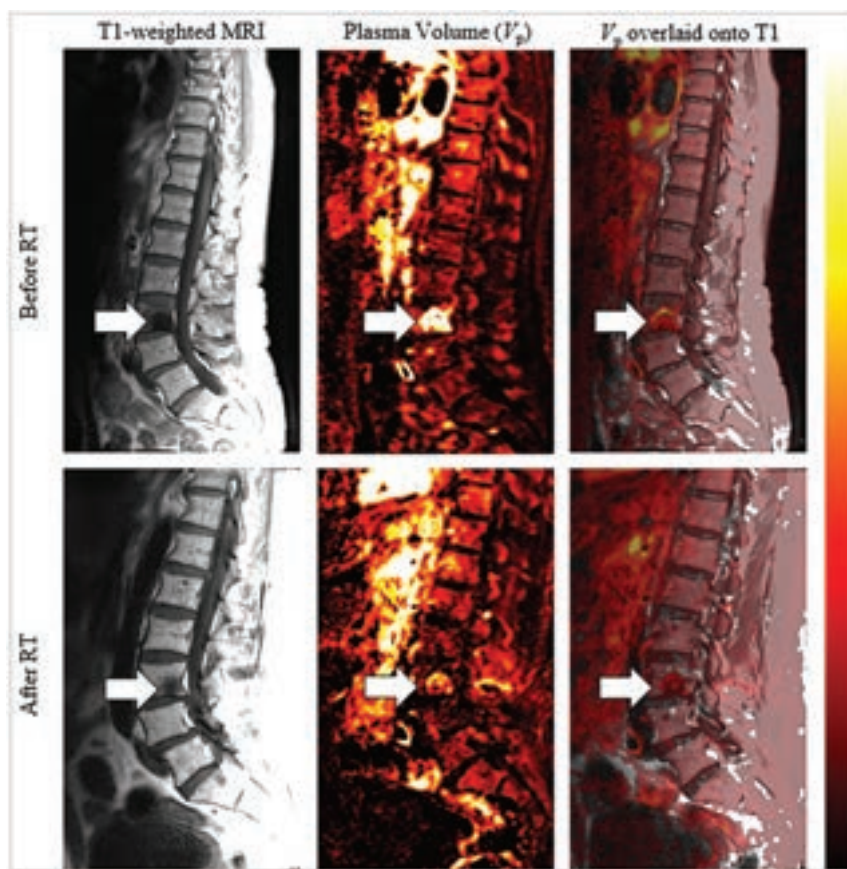


FIG 1. Example of a 64-year-old male patient with metastatic pancreatic neuroendocrine cancer demonstrating a successful treatment response at L3. The *left column* shows sagittal T1-weighted MR imaging of the lower spine. The hypointense area corresponds to vertebral lesions. The *middle column* shows plasma volume (V_p) maps of the lesions. The normalized V_p of the lesion was 9.26 before RT, and 1.13 after RT, a reduction of 87.8%. The *right column* is a T1-weighted MR imaging merged with the perfusion V_p map. The arrows indicate the lesions of interest.

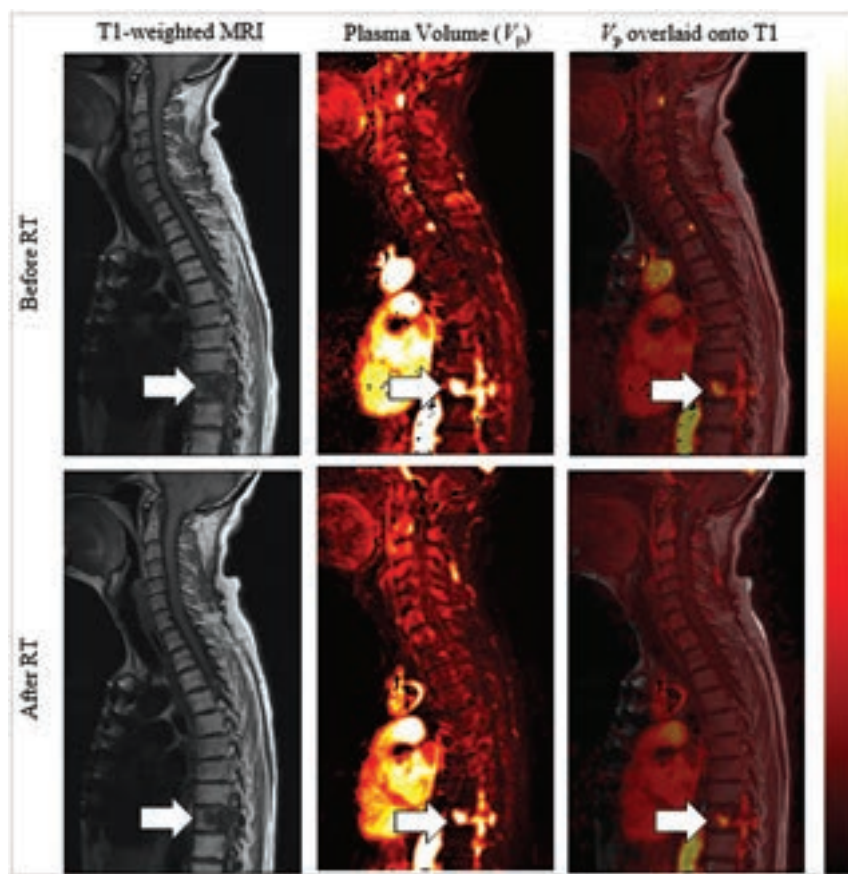


FIG 2. Example of a 63-year-old female patient with metastatic thymoma demonstrating an unsuccessful treatment response at T9 and the associated epidural area. The *left column* shows sagittal T1-weighted MR imaging of the cervical and thoracic spine. The hypointense area corresponds to vertebral lesions. The *middle column* shows plasma volume (V_p) maps of the lesions. Although tumor size decreased 19.4%, the normalized V_p of the lesion was 5.48 before RT and 9.03 after RT, an increase of 64.8%. The patient experienced progression of disease, particularly in the epidural-associated portion of the tumor. Additional RT therapy was required from T8–T10 14 months after the secondary imaging study. The *right column* is a T1-weighted MR imaging merged with the perfusion V_p map. The arrows indicate the lesions of interest.

Overlaying V_p maps on T1-weighted images reveals active lesion locations (Fig 1).

As seen in Fig 1, normalized V_p was 9.26 before RT and 1.13 after RT. This 87.8% reduction represents a decrease in tumor vascularity. Overwhelmingly, this decrease in V_p correlated with treatment success and clinical response. However, not all patients demonstrated this extent of reduction in V_p following RT (Fig 2).

As seen in Fig 2, the normalized V_p was 5.48 before RT and 9.03 after RT, an increase of 64.8%. This increase in V_p correlated with disease progression, particularly in the epidural component of the tumor. The patient in Fig 2 required additional radiation at the same spinal levels 14 months after the secondary imaging study. Additional observation shows a decrease in lesion size of –19.4%. Despite this decrease in size, disease progression occurred. Figure 2 exemplifies the ways in which DCE perfusion MR imaging can detect progression, while conventional MR imaging cannot.

Overall, there was a statistically significant difference in the change of V_p (ΔV_p) before and after RT (Fig 3) between

the clinical response and persistent disease groups ($P = .0002$). The median percentage ΔV_p following RT for clinical response was –81.1%. Correspondingly, the median ΔV_p was +1.43% for the persistent disease group. A statistically significant difference existed for the change in K^{trans} ($P = .037$), as well.

Lesion contrast uptake curves also revealed a difference between clinical groups (Fig 4). Within the clinical response group, there was a reduction in signal intensity following RT ($P = .0021$). In contrast, there was an increase in signal intensity following RT in the persistent disease group ($P = .0317$).

Finally, we conducted an ROC analysis to determine the validity of using perfusion parameters to predict clinical outcomes (Fig 5) and compared predictions with traditional size measurements obtained by a neuroradiologist. The optimal ΔV_p cutoff was –40%, which yielded a sensitivity of 91% (10 of 11; 95% CI, 82%–97%) and a specificity of 87% (33 of 38; 95% CI, 73%–94%) (ΔV_p ; area under the ROC curve, 0.86; 95% CI, 0.717–1). The optimal Δ area cutoff was –10%, which yielded a sensitivity of 82% (9 of 11; 95% CI, 67%–90%) and a specificity of 47% (18 of 38; 95% CI, 37%–67%) (Δ area; area under the ROC curve, 0.68; 95% CI, 0.505–0.846). By means of the cutoff values

above, 20 false-positives of persistent disease were identified in the 49 patients in this study via conventional size measurements. Conversely, only 5 false-positives were identified via perfusion.

DISCUSSION

Prior studies in the literature have characterized the use of DCE perfusion MR imaging in metastatic spinal disease. However, much of this work had limitations, such as small sample sizes and niche patient populations, therefore limiting the utility of results and their application across broad patient populations. Despite these limitations, it has been demonstrated that DCE perfusion MR imaging parameters; namely, plasma volume (V_p), can aid in the detection of viable spinal neoplasms. The earliest work applying DCE-MR imaging to the spine demonstrated the ability to assess metastatic bone marrow from prostate and hematologic malignancies.^{13,14} Recent work by Guan et al¹⁵ demonstrated that DCE-MR imaging perfusion can differentiate benign and malignant spinal lesions, specifically using the V_p parameter. Other groups showed that infectious etiologies of spinal disease can also be

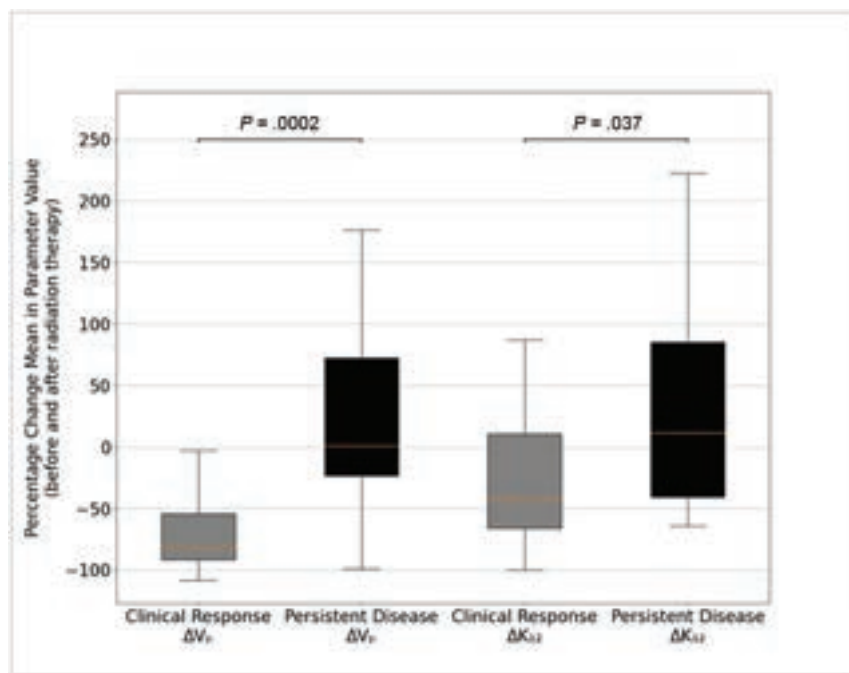


FIG 3. Box-and-whisker plot of the ΔV_p and the change in mean vessel permeability (ΔK^{trans}) by group. The mean ΔV_p is -57.3% in the clinical response group and $+88.2\%$ in the persistent disease group. The mean ΔK^{trans} is -11.7% in the clinical response group and $+51.4\%$ in the persistent disease group. There is a statistically significant difference in ΔV_p between the persistent disease and clinical response groups as evidenced by a Mann-Whitney U test ($P < .001$). ΔK_{12} indicates ΔK^{trans} .

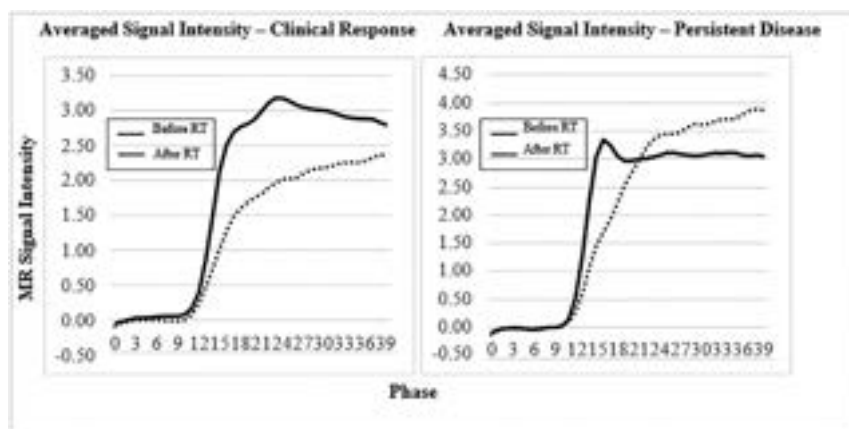


FIG 4. Graphs of the averaged MR signal intensity separated by the clinical outcome group. There is a reduction in averaged signal intensity following RT within the clinical response group. However, averaged signal intensity remains elevated within the persistent disease group.

distinguished from malignancy using perfusion parameters.^{16,17} Lang et al¹⁸ provided further insight into malignant disease. Their work demonstrated that DCE-MR imaging could potentially distinguish metastatic disease and local malignancy, including myelomas. Additionally, Kumar et al⁹ determined that perfusion parameters following radiosurgery could predict tumor recurrence for metastatic lesions in the lower spine.⁹ The goals of this study were to expand on the work of Kumar et al, to demonstrate that perfusion parameters can indeed detect viable tumor throughout all spinal levels, and to show that perfusion data are a better predictor of clinical outcomes than traditio-

nal radiologist-conducted anatomic size measurements performed on conventional MR imaging.

Our results showed significant differences in ΔV_p following RT between the clinical response and persistent disease groups, with medians of -81% and $+1.43\%$, respectively. With an optimal ΔV_p of -40% , perfusion parameters can predict persistent disease with a sensitivity of 91% and a specificity of 87% (area under the curve = 0.86).

This study expands on previous works that have established the ability of DCE perfusion MR imaging to characterize spinal lesions accurately. For example, Chu et al² and Lis et al¹⁰ demonstrated that V_p could be used to determine a successful response of spinal lesions to RT. Other groups demonstrated the ability to accurately assess the treatment of native spinal tumors, improve surveillance of metastatic spinal lesions,¹⁹ as well as to differentiate benign and malignant spinal fractures, hypovascular and hypervascular metastases, and hemangiomas and metastases.²⁰⁻²² Our study is rooted in the idea that malignant lesions lead to new vasculature formation.^{23,24} New vessel networks allow the contrast agent to accumulate, leading to a measurable increase in V_p . As a corollary, this vasculature will regress if RT is successful, leading to a decrease in V_p . Conversely, if RT is unsuccessful, V_p would remain elevated.

Despite these promising data, our study had several limitations. One such limitation is the potential existence of methodologic circularity. We used size measurements to assign patients to clinical groups, which were then compared using the results of DCE-MR imaging. Subsequently, we compared DCE-MR imaging with conventional radiologist-completed size measurements in assessing clinical failure. This approach is not

ideal. However, the size assessments were conducted differently. Radiologists' impressions were assessed in the 18-month interval following the post-RT DCE-MR imaging to assign groups, while quantitative measurements before and after RT were used for the comparison with traditional radiologist-completed size measurements. As discussed in the materials and methods, these measurements were taken using the closest imaging to the date of RT. Although we foresaw this limitation, the decision to use the conventional size measurement as a criterion was based on its established relevance and widespread use in similar studies within our field. We believe future studies that

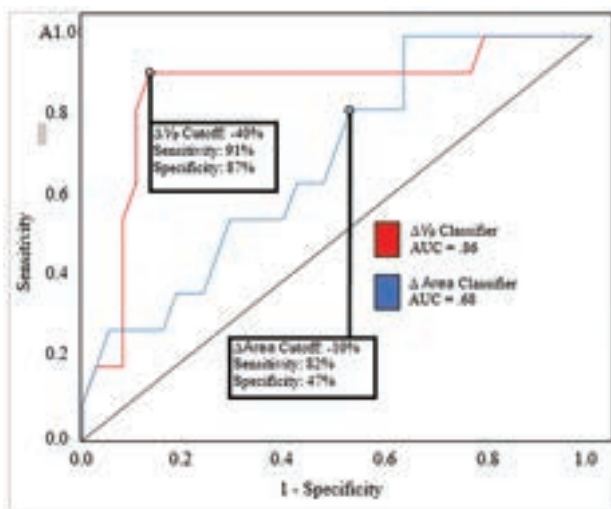


FIG 5. ROC curve of the ΔV_p (area under the ROC curve, 0.86; 95% CI, 0.717–1) and change in lesion area (Δarea ; area under the ROC curve, 0.68; 95% CI, 0.505–0.846). The optimal ΔV_p cutoff is -40% , which yields a sensitivity of 91% and a specificity of 87%. The optimal Δarea cutoff is -10% , which yields a sensitivity of 82% and a specificity of 47%. AUC indicates area under the curve.

explore alternative criteria or methodologies would complement our findings.

Additional limitations exist. First, perfusion parameters can be influenced by factors other than malignancy. Local injuries and benign fractures can lead to angiogenesis and corresponding increases in V_p .²⁵ Additionally, defining clinical response and persistent disease is somewhat problematic. Our categoric assignment would ideally be replaced with solely biopsy-proved recurrence, though even biopsies can be falsely negative. Currently, an increase in standardized uptake values in FDG-PET is part of persistent disease criteria. Increased FDG uptake on PET can be suggestive of tumor recurrence, but false-positives are also seen using this technique.²⁶ Nevertheless, DCE perfusion may be more sensitive and specific than the imperfect criteria of the present study. Further studies are therefore needed to elucidate this point. Finally, our study included some technical limitations. The DCE processing and arterial input function selection and shift were performed manually. Although this process was standardized, automation would be ideal for consistency.

Significant work remains in the field of spine imaging, and this study should be further expanded to validate the dynamic contrast-enhanced perfusion MR imaging model of assessing the response of metastatic spinal lesions to RT.

CONCLUSIONS

Our study results provide strong evidence in favor of incorporating DCE-MR perfusion imaging into routine clinical practice when assessing metastatic spinal lesions. Perfusion imaging allows more accurate differentiation between treatment success and persistent disease. Conventional imaging techniques rely on lesion size and signal characteristics, which can commonly be indeterminate or inaccurate in evaluating tumor recurrence. The use of perfusion parameters offers greater specificity and should be considered when determining whether to pursue a new course of treatment.

Further studies applying DCE-MR imaging to spinal metastases are warranted to validate and explore this line of reasoning.

ACKNOWLEDGMENTS

We would like to thank Cecile Berberat (Department of Radiology) for the editing assistance.





Disclosure forms provided by the authors are available with the full text and PDF of this article at www.ajnr.org.

REFERENCES

1. Togawa D, Lewandrowski KU. The pathophysiology of spinal metastases. In: McLain RF. *Cancer in the Spine*. Humana Press; 2006:17–23
2. Chu S, Karimi S, Peck KK, et al. Measurement of blood perfusion in spinal metastases with dynamic contrast-enhanced magnetic resonance imaging: evaluation of tumor response to radiation therapy. *Spine (Phila Pa 1976)* 2013;38:E1418–24 CrossRef Medline
3. Norman D, Mills CM, Brant-Zawadzki M, et al. Magnetic resonance imaging of the spinal cord and canal: potentials and limitations. *AJR Am J Roentgenol* 1983;141:1147–52 CrossRef Medline
4. Thibault I, Chang EL, Sheehan J, et al. Response assessment after stereotactic body radiotherapy for spinal metastasis: a report from the SPIne response assessment in Neuro-Oncology (SPINO) group. *Lancet Oncol* 2015;16:e595–603–603 CrossRef Medline
5. Saha A, Peck KK, Lis E, et al. Magnetic resonance perfusion characteristics of hypervascular renal and hypovascular prostate spinal metastases: clinical utilities and implications. *Spine (Phila Pa 1976)* 2014;39:E1433–40 CrossRef Medline
6. Tofts PS, Brix G, Buckley DL, et al. Estimating kinetic parameters from dynamic contrast-enhanced T(1)-weighted MRI of a diffusible tracer: standardized quantities and symbols. *J Magn Reson Imaging* 1999;10:223–32 CrossRef Medline
7. Tofts PS. T1-weighted DCE imaging concepts: modelling, acquisition and analysis. *Magnetom Flash* 2010;500:400 http://paul-tofts-phd.org.uk/DCE-MRI_siemens.pdf. Accessed July 1, 2022
8. Meng X, Zhang Y, Liao H, et al. Dynamic contrast-enhanced MRI for the assessment of spinal tumor vascularity: correlation with angiography. *Eur Spine J* 2016;25:3952–61 CrossRef Medline
9. Kumar KA, Peck KK, Karimi S, et al. A pilot study evaluating the use of dynamic contrast-enhanced perfusion MRI to predict local recurrence after radiosurgery on spinal metastases. *Technol Cancer Res Treat* 2017;16:857–65 CrossRef Medline
10. Lis E, Saha A, Peck KK, et al. Dynamic contrast-enhanced magnetic resonance imaging of osseous spine metastasis before and 1 hour after high-dose image-guided radiation therapy. *Neurosurg Focus* 2017;42:E9 CrossRef Medline
11. Chen Y, Zhang E, Wang Q, et al. Use of dynamic contrast-enhanced MRI for the early assessment of outcome of CyberKnife stereotactic radiosurgery for patients with spinal metastases. *Clin Radiol* 2021;76:864–e1 CrossRef Medline
12. Hillengass J, Stieltjes B, Bäuerle T, et al. Dynamic contrast-enhanced magnetic resonance imaging (DCE-MRI) and diffusion-weighted imaging of bone marrow in healthy individuals. *Acta Radiol* 2011;52:324–30 CrossRef Medline
13. Zha Y, Li M, Yang J. Dynamic contrast enhanced magnetic resonance imaging of diffuse spinal bone marrow infiltration in patients with hematological malignancies. *Korean J Radiol* 2010;11:187–94 CrossRef Medline
14. Michoux N, Simoni P, Tombal B, et al. Evaluation of DCE-MRI post-processing techniques to assess metastatic bone marrow in patients with prostate cancer. *Clin Imaging* 2012;36:308–15 CrossRef Medline
15. Guan Y, Peck KK, Lyo J, et al. T1-weighted dynamic contrast-enhanced MRI to differentiate nonneoplastic and malignant vertebral body lesions in the spine. *Radiology* 2020;297:382–89 CrossRef Medline

16. Verma M, Sood S, Singh B, et al. **Dynamic contrast-enhanced magnetic resonance perfusion volumetrics can differentiate tuberculosis of the spine and vertebral malignancy.** *Acta Radiol* 2022;63:1504–12 CrossRef Medline
17. Qiao P, Zhao P, Gao Y, et al. **Differential study of DCE-MRI parameters in spinal metastatic tumors, brucellar spondylitis and spinal tuberculosis.** *Chin J Cancer Res* 2018;30:425–31 CrossRef Medline
18. Lang N, Su MY, Hon JY, et al. **Differentiation of myeloma and metastatic cancer in the spine using dynamic contrast-enhanced MRI.** *Magn Reson Imaging* 2013;31:1285–91 CrossRef Medline
19. Kayhan A, Yang C, Soyly FN, et al. **Dynamic contrast-enhanced MR imaging findings of bone metastasis in patients with prostate cancer.** *World J Radiol* 2011;3:241–45 CrossRef Medline
20. Santos P, Peck KK, Arevalo-Perez J, et al. **T1-weighted dynamic contrast-enhanced MR perfusion imaging characterizes tumor response to radiation therapy in chordoma.** *AJNR Am J Neuroradiol* 2017;38:2210–16 CrossRef Medline
21. Arevalo-Perez J, Peck KK, Lyo JK, et al. **Differentiating benign from malignant vertebral fractures using T1-weighted dynamic contrast-enhanced MRI.** *J Magn Reson Imaging* 2015;42:1039–47 CrossRef Medline
22. Morales KA, Arevalo-Perez J, Peck KK, et al. **Differentiating atypical hemangiomas and metastatic vertebral lesions: the role of T1-weighted dynamic contrast-enhanced MRI.** *AJNR Am J Neuroradiol* 2018;39:968–73 CrossRef Medline
23. Kerbel RS. **Tumor angiogenesis.** *N Engl J Med* 2008;358:2039–49 CrossRef Medline
24. Carmeliet P, Jain RK. **Molecular mechanisms and clinical applications of angiogenesis.** *Nature* 2011;473:298–307 CrossRef Medline
25. Loi F, Córdova LA, Pajarinen J, et al. **Inflammation, fracture and bone repair.** *Bone* 2016;86:119–30 CrossRef Medline
26. Rosenbaum SJ, Lind T, Antoch G, et al. **False-positive FDG PET uptake: the role of PET/CT.** *Eur Radiol* 2006;16:1054–65 CrossRef Medline

Accuracy of Noncontrast T2 SPACE in Active MS Cord Lesion Detection

 Anousheh Sayah,  Elias Khayat,  Earn-Chun C. Lee, and  Erini V. Makariou

ABSTRACT

BACKGROUND AND PURPOSE: The diagnosis of active MS lesions is often based on postgadolinium T1-weighted MR imaging. Recent studies suggest a risk of IV gadolinium to patients, predominantly based on gadolinium deposition in tissue. Noncontrast sequences have shown promise in MS diagnosis, but none differentiate acute from chronic MS lesions. We hypothesized that 3D T2 sampling perfection with application-optimized contrasts by using different flip angle evolution (SPACE) MR imaging can help detect and differentiate active-versus-chronic MS lesions without the need for IV contrast.

MATERIALS AND METHODS: In this single-center retrospective study, 340 spinal MR imaging cases of MS were collected in a 24-month period. Two senior neuroradiologists blindly and independently reviewed postcontrast T1-weighted sagittal and T2-SPACE sagittal images for the presence of MS lesions, associated cord expansion/atrophy on T2-SPACE, and enhancement on postcontrast T1WI. Discrepancies were resolved by consensus between the readers. Sensitivity, specificity, and accuracy of T2-SPACE compared with postcontrast T1WI were computed, and interobserver agreement was calculated.

RESULTS: The sensitivity of lesion detection on T2-SPACE was 85.71%, 95% CI, 63.66%–96.95%; with a specificity of 93.52%, 95% CI, 90.06%–96.05%; and an accuracy of 92.99%, 95% CI, 89.58%–95.56. Additionally, 16/21 (84.2%) acute enhancing cord lesions showed cord expansion on T2-SPACE. The interobserver agreement was 92%.

CONCLUSIONS: Our study shows that T2-SPACE facilitates noncontrast detection of acute MS lesions with high accuracy compared with postcontrast T1WI and with high interobserver agreement. The lack of gadolinium use provides an advantage, bypassing any potential adverse effects of repetitive contrast administration.

ABBREVIATIONS: AP = anterior-posterior; MOGAD = MOG antibody-associated disease; NPV = negative predictive value; PPV = positive predictive value; SPACE = sampling perfection with application-optimized contrasts by using different flip angle evolution

MS is a neurologic autoimmune disorder marked by the demyelination of neurons in the brain and spinal cord.^{1,2} MS diagnosis is based on the McDonald criteria, which require the detection of at least 1 lesion by neuroimaging, often via MR imaging T2-weighted sequences and postcontrast T1-weighted sequences.^{3–6} The use of gadolinium-based contrast agents for MS diagnosis is ubiquitous but adds extra cost, time, and potential contrast reactions to the imaging studies. Additionally, studies have shown tissue accumulation of gadolinium despite renal function after multiple doses of gadolinium-based contrast agents, notably with linear contrast agents, though the clinical significance

of this is not fully understood.^{7–13} For patients with MS, this constellation of concerns regarding gadolinium is relevant because >70% will receive at least 25 doses of IV gadolinium in their lifetimes, making the search for noncontrast imaging modalities crucial in MS lesion evaluation.¹⁴

Many gadolinium-free MR imaging sequences have shown promise in the diagnosis of MS, such as 3D phase-sensitive inversion recovery, double-inversion recovery, and FLAIR.^{4–6} Yet, none of these techniques have been capable of discerning the different types of MS lesions without the use of a gadolinium-based contrast, a critical step needed to define the disease and its progression.³ Generally, MS lesions are divided into 2 categories: acute and chronic. Acute MS lesions are characterized by inflammation, demyelination, and vasogenic edema. With time, as the acute active lesion resolves, it becomes chronic, inactive, or nonenhancing, and the associated inflammation and edema resolve.¹

In this study, we examine the role of the 3D T2 sampling perfection with application-optimized contrasts by using different

Received March 28, 2023; accepted after revision October 6.

From the Department of Radiology (A.S., E.-C.C.L., E.V.M.), MedStar Georgetown University Hospital, Washington, DC; and Georgetown University School of Medicine (E.K.), Washington, DC.

Please address correspondence to Anousheh Sayah, MD, MedStar Georgetown University Hospital, Department of Radiology, 3800 Reservoir Rd, NW, CG 201, Washington, DC, 20007; e-mail: anousheh.sayah@gunet.georgetown.edu; @AnoushehSayah

<http://dx.doi.org/10.3174/ajnr.A8060>

flip angle evolution (SPACE sequence; Siemens) in MS spinal cord lesion detection and differentiation. Generally, the T2-SPACE sequence is good for evaluation of the anatomy/pathology of the spinal cord and nearby structures due to its excellent spatial resolution.¹⁵ Although this sequence tends to have relatively low sensitivity for detecting intramedullary cord lesions, it can demonstrate intramedullary lesions with high water content.¹⁶ This latter property of T2-SPACE is of interest to us in evaluating MS lesions. Acute MS lesions are characterized by vasogenic edema with a high water-diffusion coefficient, whereas chronic lesions have significant regression of this edema with a low diffusion coefficient.¹⁷⁻¹⁹ As a result, we hypothesized that the T2-SPACE sequence can differentiate active, edematous MS lesions from chronic lesions without the need for IV gadolinium administration.

MATERIALS AND METHODS

Patient Selection

This retrospective study was approved by the Medstar Georgetown University Hospital institutional review board via an expedited review process. We searched the institutional PACS database for studies performed between January 2017 to December 2018, with the following as inclusion criteria: 1) older than 18 years of age; 2) having undergone cervical and/or thoracic MR spine imaging; and 3) had a diagnosis of MS. From this group of studies, any noncontrast studies were excluded, as were any studies with significant motion artifacts or those not including a sagittal T2-SPACE sequence.

Image Acquisition

All MR imaging examinations were performed on either 1.5T or 3T magnets (Siemens, Erlangen, Germany; Aera & Verio). All studies consisted of the following set of sequences: T1 sagittal 3 mm, T2 sagittal 3 mm, STIR sagittal 3 mm, T2-SPACE sagittal 1 mm, axial T2 3 mm, and postcontrast T1 sagittal and axial 3 mm. For this study, only postcontrast T1 sagittal (3-mm matrix = 256/0/0/230; TR = 701 ms; TE = 11 ms), and T2-SPACE sagittal (1-mm matrix = 256/0/0/261; TR = 1200 ms; TE = 132 ms) stacks were examined. T2-SPACE images were acquired before the administration of gadolinium contrast in all cases. No reconstructions were reviewed for this study.

Lesion Detection

The entirety of the spinal cord imaged on T1 postcontrast sagittal and T2-SPACE sagittal sequences from each study was evaluated separately and in a blinded fashion by 2 attending neuroradiologists, one with 23 years of experience (E.V.M.) and the second with 11 years of experience (E.-C.C.L.) in the field postfellowship. T1 postcontrast images were evaluated for contrast-enhancing lesions in the spinal cord. Later, T2-SPACE sequences were reviewed for hyperintense cord lesions as well as cord dimensions at the level of the lesions. To determine focal cord dimensions, we evaluated the anterior-posterior (AP) length of the cord and each lesion. If the AP dimension was larger than that of the normal-appearing cord on the same study, the lesion was recorded with increased cord volume. If there was no difference in the AP dimension between the abnormal lesion and the normal cord, the lesion was recorded with no change in volume. Accordingly, if

the lesion demonstrated an AP dimension lower than that of the normal cord, it was recorded as low volume. Results were collected via an Excel (Microsoft) spreadsheet by each of the investigators. Data values from the 2 readers were merged if nondiscrepant; any discrepancies in lesion enhancement, T2 hyperintensity, or cord volume between the readers were resolved by consensus between the 2 readers.

Statistical Analysis

Interreader reliability between the 2 neuroradiologists was computed as the percentage agreement between the raters. Using contrast enhancement on T1-weighted sequences as the criterion standard for active MS lesions, we computed the sensitivity, specificity, negative predictive value (NPV), positive predictive value (PPV), and accuracy for signal hyperintensity on T2-SPACE sequences. Each of these measures is reported with a 95% CI. We computed the same measures for hyperintense lesions on T2-SPACE with increased focal cord parenchymal volume, again using enhancement as the criterion standard. Statistical analyses were performed using MedCalc for Windows, Version 20 (MedCalc Software).

RESULTS

Of the 338 cases identified for this study, 314 met the inclusion criteria. Of the 24 studies excluded, 19 had no IV contrast administration, 2 did not include T2-SPACE imaging, 2 were dismissed due to motion artifacts, and one had imaging findings related to compressive myelopathy. The remaining 314 cases were from unique patients. The prevalence of acute MS lesions in this study was 6.69% (95% CI, 4.19%–10.04%). The percentage agreement between the raters for this study was 92%.

The first test evaluated the efficacy of T2-SPACE hyperintensity to detect acute MS lesions on the basis of postcontrast T1 as the criterion standard. Of the 314 total cases, 18 lesions from 18 separate studies showed both contrast enhancement on T1-weighted imaging and hyperintensity on T2-SPACE imaging. Nineteen lesions from 19 studies were hyperintense on T2-SPACE and had no enhancement on postcontrast T1 imaging; 3 lesions from 3 studies showed contrast enhancement without T2 hyperintensity; and 274 cases showed neither contrast enhancement nor T2 hyperintensity (the latter is depicted in Fig 1). When the presence of lesion hyperintensity on T2-SPACE was used as a diagnostic tool to detect acute MS lesions, the sensitivity was 85.71% (95% CI, 63.66%–96.95%); specificity, 93.52% (95% CI, 90.06%–96.05%); PPV, 48.65% (95% CI, 37.22%–60.22%); NPV, 98.92% (95% CI, 96.97%–99.62%); and accuracy, 92.99% (95% CI, 89.58%–95.56%).

To further evaluate findings from the T2-SPACE sequence, we next tested the presence of signal hyperintensity within lesions combined with an increased AP dimension of the cord against enhancement. Among all lesions that were T2-hyperintense, 16 lesions had an increased focal cord AP dimension, all of which had corresponding enhancement on postcontrast T1 sequences (Figs 2 and 3). Combining both T2 hyperintensity and increased lesional volume on T2-SPACE imaging yielded a sensitivity of 88.89% (95% CI, 65.29%–98.62%), a specificity of 100.00% (95% CI, 82.35%–100.00%), a PPV of 100.00% (95% CI, 80.64%–100%), an NPV of 99.21% (95% CI, 97.14%–99.78%), and an accuracy of

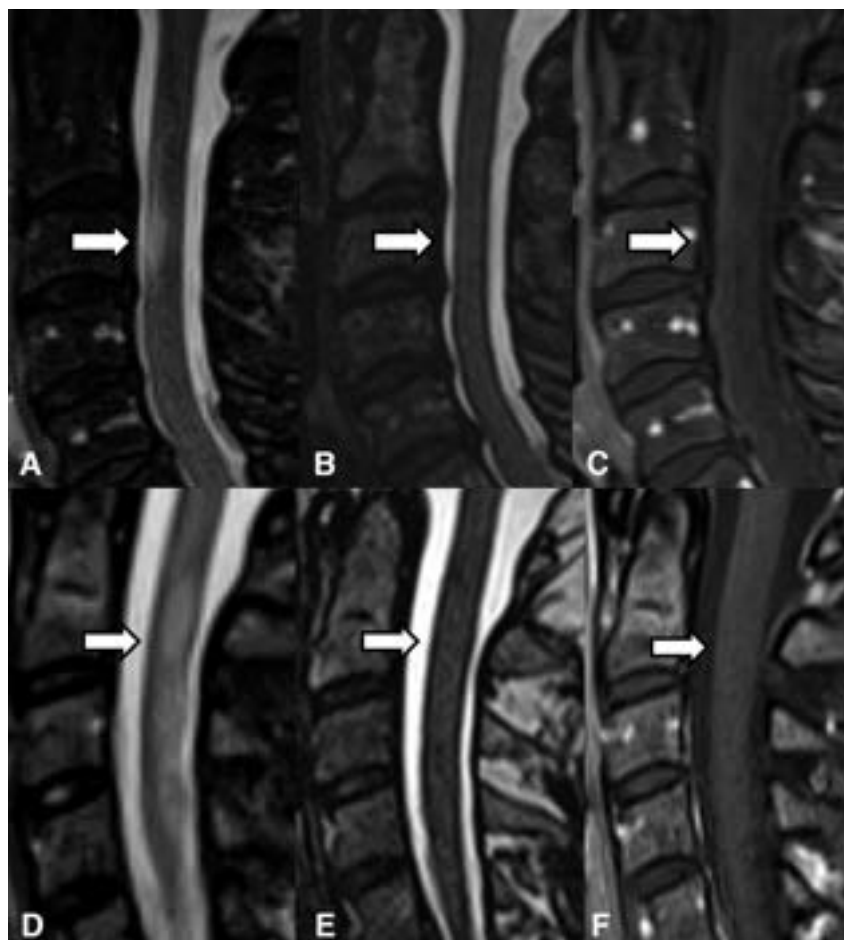


FIG 1. MR imaging of 2 patients with MS. A 62-year-old woman in the top row (A–C) and a 52-year-old woman in the bottom row (D–F). The first panel (A and D) shows a sagittal STIR image of an MS lesion (arrow) in the cervical spine in both patients, which is not conspicuous on sagittal T2-SPACE (B and E) or sagittal postcontrast T1WI (C and F).



FIG 2. MR imaging of a 38-year-old woman with MS. Sagittal T2-SPACE (left) shows focal T1–T3 hyperintensity (arrow) with focally increased volume corresponding to an active cord lesion on sagittal T1 postcontrast (right).

99.26% (95% CI, 89.12%–100.00%). Furthermore, of 21 lesions with T2 hyperintensity and normal or atrophied focal cord parenchymal volume, 19 of them showed no lesional enhancement on postcontrast T1 (Fig 4).

DISCUSSION

Our findings suggest that hyperintensity of an MS lesion on T2-SPACE, best used in addition to increased lesional cord volume, is a strong indicator of the presence of an active MS spinal cord lesion without the need for IV gadolinium. These findings are compatible with the known pathophysiology of active MS lesions. In the early stages of an acute MS attack, an abundant amount of T-cells disrupt the BBB²⁰ and break down myelin.²¹ They release chemotactic factors and inflammatory mediators and recruit cytokines, plasma cells, macrophages, and destructive proteins further breaking down the BBB.²¹ This process results in leakage of extracellular fluid into the lesion and focal vasogenic edema and cord swelling.²² Furthermore, biophysical studies have demonstrated that active MS lesions have a higher water ADC compared with chronic lesions and normal-appearing white matter.^{17–19}

Comparison of hyperintensity on T2-SPACE and enhancement on postcontrast T1 in MS lesions suggests that the former finding provides precise detection of active MS lesions with high sensitivity (85.71%), high specificity (93.52%), and high accuracy (92.99%). Furthermore, when combining the presence of increased cord volume of the

lesion with T2 hyperintensity, the specificity, sensitivity, and accuracy increase to 100%, 88.89%, and 99.26%, respectively. The sensitivity of 89% for this evaluation still leads to about 11% of active lesions being incorrectly labeled as chronic and is a limitation in the use of a noncontrast-only evaluation of MS lesions (Fig 5). On further review of these instances, we found that the lesions were relatively small in comparison with others in the subset. We postulate that lesion size may affect the sensitivity of noncontrast evaluations and could be examined in future studies.

Further ad hoc investigation into the prior and subsequent images of patients in our study with acute MS plaques did show a progression of imaging findings with time. We observed that lesions with enhancement on postcontrast T1 and hyperintensity and cord expansion on T2-SPACE later progressed across months to years into lesions that were nonenhancing and isointense on T2-SPACE with normal-to-decreased cord volume (Fig 6). This observation supports the findings in our current study but certainly needs further investigation for validity.

Additionally, not all acute MS lesions may have gadolinium enhancement and have been described as “chronic active” or “smoldering” lesions with ongoing disease activity in the absence of enhancement.²³ Thus, lesions in our study that were T2-positive but negative on postgadolinium sequences ($n = 19$) could still

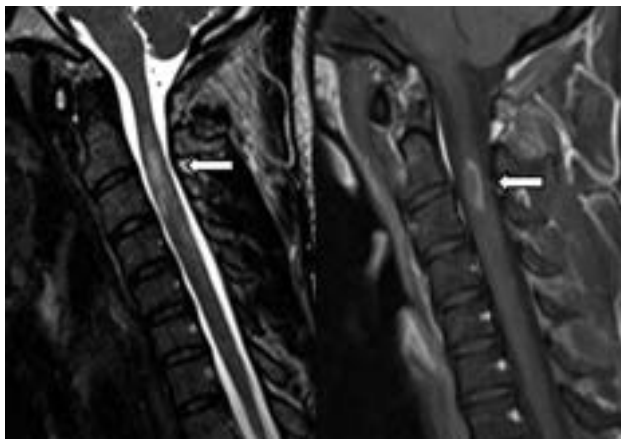


FIG 3. MR imaging of a 25-year-old man with relapsing-remitting MS. Sagittal T2-SPACE (left) shows focal C2-C3 hyperintensity (arrow), with focal increased cord volume corresponding to an enhancing, active lesion on sagittal T1 postcontrast (right) image.



FIG 4. MR imaging of a 32-year-old woman with relapsing-remitting MS. Sagittal T2-SPACE (left) shows focal T2 hyperintensity (arrow) with normal/decreased cord volume. No active lesion/enhancement is seen on the sagittal T1 postcontrast image (right).

represent active lesions. In this case, if this scenario is suspected, serial noncontrast T2-SPACE imaging could be performed to show reduction in the size of such lesions as a sign of decreased disease activity in clinical practice.

The high NPV of 98.92% for T2-SPACE hyperintensity in determining an active plaque presents imaging centers with the opportunity to screen patients with MS via noncontrast protocols, in that this offers the option to subsequently add IV contrast in patients with T2-SPACE hyperintense lesions either in real-time or on return imaging. This option could significantly reduce the amount of IV gadolinium to which patients with MS are exposed and mitigate the risk of potential adverse effects, including entities such as nephrogenic systemic fibrosis in patients with impaired kidney function.^{24,25} Additionally, our findings of high interreader reliability suggest that this sequence could provide

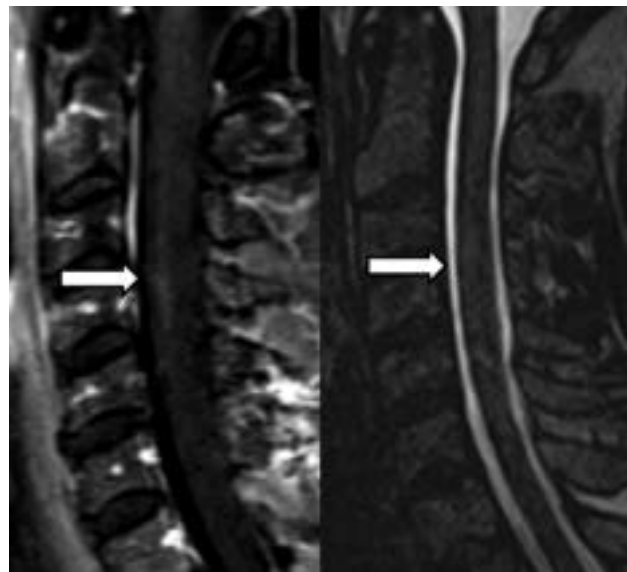


FIG 5. MR imaging of a 51-year-old woman with MS. Sagittal T1 postcontrast imaging shows an enhancing lesion (arrow) in the C3-C4 cord (left) without associated hyperintensity on T2-SPACE (right).

consistent results among readers for this purpose in clinical practice.

Our study has several limitations. Although many examinations were entered into this study, the percentage of acute lesions identified was low. A larger sample size with increased power would provide stronger statistical significance to our results. This study was retrospective, and all cases were from a single center, leading to inherent bias in the group/patient population and, therefore, in the data analyzed. The studies were performed on 1.5T or 3T magnet strengths, which could contribute to inconsistency in lesion characterization, though studies have shown that 1.5T and 3T yield comparable results.²⁶ Of note, every study included T2-SPACE and T1 postcontrast sequences acquired from the same MR imaging machine; no one sequence should have a Tesla strength advantage within the same case. Lesions were not pathologically correlated—an impractical expectation in this clinical evaluation but introduces a confounding variable because lesions could have an etiology other than MS. All studies were from patients with documented clinical diagnoses of MS. Finally, the neuroradiologists in this study could not be blinded to the sequence type they were assessing (T2-SPACE versus T1 postcontrast), possibly having added inherent bias in the reads.

Future directions in the use of this noncontrast protocol include differentiating various demyelinating diseases from one another. For example, a higher proportion of active lesions may suggest myelin oligodendrocyte glycoprotein antibody-associated disease (MOGAD) over MS, because MOGAD often only manifests with acute lesions, with older lesions resolving with time.²⁷ Additionally, using noncontrast imaging to understand the active disease burden in MS may impact future treatment decisions, including the use of more aggressive therapies earlier in the disease. Prospectively, in case the determination of active lesions becomes incorporated into the diagnostic MS criteria, having a noncontrast method to evaluate these lesions will be crucial. Other promising directions in the use of noncontrast imaging

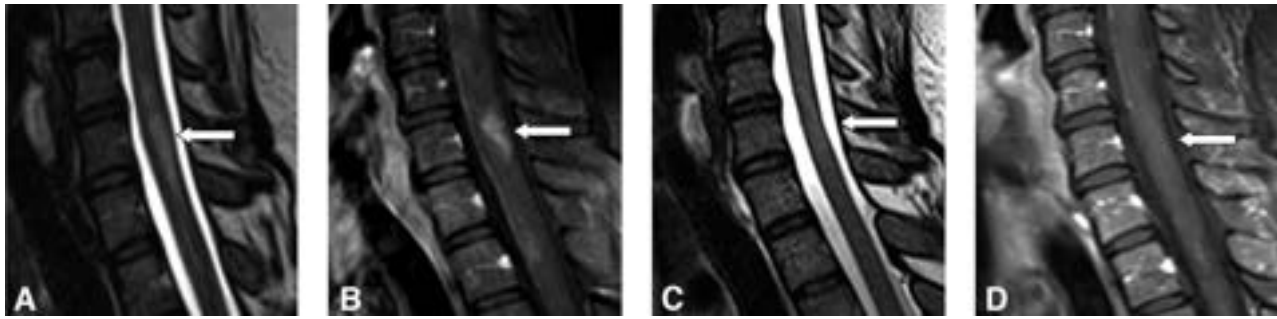


FIG 6. Observational imaging progression of an active MS lesion in the C6 spinal cord across time to a chronic lesion in a 36-year-old woman with MS. Sagittal T2-SPACE (A) and sagittal postcontrast T1WI (B) show a T2-hyperintense lesion with cord expansion and enhancement compatible with an active lesion. Follow-up T2-SPACE (C) and postcontrast T1 (D) after 2 years demonstrate no T2 hyperintensity at the same site, with mild cord volume loss, and no enhancement, suggestive of a chronic lesion.

for the detection of active MS plaques include application of DWI and quantitative susceptibility mapping protocols currently studied in the brain.^{28,29}

CONCLUSIONS

The purpose of this study was to evaluate the use of T2-SPACE MR imaging for the detection of active MS plaques without IV gadolinium. We found high sensitivity, specificity, and accuracy for the presence of hyperintensity on T2-SPACE in diagnosing active plaques, which improved further when combined with focal cord expansion at the level of the lesions. These findings suggest that sagittal T2-SPACE imaging could play a role in routine follow-up spine MR imaging of patients with MS without the need for the routine use of IV gadolinium, with high correlation among interpreting readers.

Disclosure forms provided by the authors are available with the full text and PDF of this article at www.ajnr.org.

REFERENCES

1. Frohman EM, Racke MK, Raine CS. **Medical Progress Multiple Sclerosis-The Plaque and Its Pathogenesis.** 2006. <https://www.nejm.org/doi/pdf/10.1056/NEJMra052130>. Accessed July 8, 2021
2. Gh Popescu BF, Pirkio I, Lucchinetti CF. **Pathology of multiple sclerosis: where do we stand?** *Continuum (Minneapolis)* 2013;19(4 Multiple Sclerosis):901–21 CrossRef Medline
3. Thompson AJ, Banwell BL, Barkhof F, et al. **Diagnosis of multiple sclerosis: 2017 revisions of the McDonald criteria.** *Lancet Neurol* 2018;17:162–73 CrossRef Medline
4. Mattay RR, Davtayan K, Bilello M, et al. **Do all patients with multiple sclerosis benefit from the use of contrast on serial follow-up MR imaging? A retrospective analysis.** *AJNR Am J Neuroradiol* 2018;39:2001–06 CrossRef Medline
5. Fechner A, Savatovsky J, El Methni J, et al. **A 3T phase-sensitive inversion recovery MRI sequence improves detection of cervical spinal cord lesions and shows active lesions in patients with multiple sclerosis.** *AJNR Am J Neuroradiol* 2019;40:370–75 CrossRef Medline
6. Eichinger P, Schön S, Pongratz V, et al. **Accuracy of unenhanced MRI in the detection of new brain lesions in multiple sclerosis.** *Radiology* 2019;291:429–35 CrossRef Medline
7. McDonald RJ, McDonald JS, Kallmes DF, et al. **Intracranial gadolinium deposition after contrast-enhanced MR imaging.** *Radiology* 2015;275:772–82 CrossRef Medline
8. Kanda T, Fukusato T, Matsuda M, et al. **Gadolinium-based contrast agent accumulates in the brain even in subjects without severe renal dysfunction: evaluation of autopsy brain specimens with inductively coupled plasma mass spectroscopy.** *Radiology* 2015;276:228–32 CrossRef Medline
9. Gulani V, Calamante F, Shellock FG, et al; International Society for Magnetic Resonance in Medicine. **Gadolinium deposition in the brain: summary of evidence and recommendations.** *Lancet Neurol* 2017;16:564–70 CrossRef Medline
10. Iyad N, Ahmad M S, Alkhatib SG, et al. **Gadolinium contrast agents-challenges and opportunities of a multidisciplinary approach: literature review.** *Eur J Radiol Open* 2023;11:100503 CrossRef Medline
11. Bi Q, Li H, Du J, et al. **Gadolinium deposition in the brain is related to various contrast agents: a matched case-control study.** *Clin Radiol* 2022;77:299–306 CrossRef Medline
12. Dogra S, Borja MJ, Lui YW. **Impact of kidney function on CNS gadolinium deposition in patients receiving repeated doses of gadobutrol.** *AJNR Am J Neuroradiol* 2021;42:824–30 CrossRef Medline
13. Traboulsee S, Kolind DK, Li H, et al. **Gadolinium deposition in deep brain structures: relationship with dose and ionization of linear gadolinium-based contrast agents.** *AJNR Am J Neuroradiol* 2018;39:1597–603 CrossRef Medline
14. Leray E, Moreau T, Fromont A, et al. **Epidemiology of multiple sclerosis.** *Rev Neurol (Paris)* 2016;172:3–13 PMC/CrossRef Medline
15. Chokshi FH, Sadigh G, Carpenter W, et al. **Diagnostic quality of 3D T2-SPACE compared with T2-FSE in the evaluation of cervical spine MRI anatomy.** *AJNR Am J Neuroradiol* 2017;38:846–50 CrossRef Medline
16. Vargas MI, Dietemann JL. **3D T2-SPACE versus T2-FSE or T2 gradient recalled-echo: which is the best sequence?** *AJNR Am J Neuroradiol* 2017;38:E48–49 CrossRef Medline
17. Castriota-Scanderbeg A, Sabatini U, Fasano F, et al. **Diffusion of water in large demyelinating lesions: a follow-up study.** *Neuroradiology* 2002;44:764–67 CrossRef Medline
18. Filippi M, Iannucci G, Cercignani M, et al. **A quantitative study of water diffusion in multiple sclerosis lesions and normal-appearing white matter using echo-planar imaging.** *Arch Neurol* 2000;57:1017–21 CrossRef Medline
19. Tievsky AL, Ptak T, Farkas J. **Investigation of apparent diffusion coefficient and diffusion tensor anisotropy in acute and chronic multiple sclerosis lesions.** *AJNR Am J Neuroradiol* 1999;20:1491–99 Medline
20. Haase S, Linker RA. **Inflammation in multiple sclerosis.** *Ther Adv Neurol Disord* 2021;14:17562864211007687 CrossRef Medline
21. Compston A, Coles A. **Multiple sclerosis.** *Lancet* 2002;359:1221–31 CrossRef Medline
22. Claudio L, Raine CS, Brosnan CF. **Evidence of persistent blood-brain barrier abnormalities in chronic-progressive multiple sclerosis.** *Acta Neuropathol* 1995;90:228–38 CrossRef Medline
23. Wenzel N, Wittayer M, Weber CE, et al. **MRI predictors for the conversion from contrast-enhancing to iron rim multiple sclerosis lesions.** *J Neurol* 2022;269:4414–20 CrossRef Medline

24. Thomsen HS. **Nephrogenic systemic fibrosis: history and epidemiology.** *Radiology Clin North Am* 2009;47:827–31, vi CrossRef Medline
25. Thomsen HS, Morcos SK, Almén T, et al; ESUR Contrast Medium Safety Committee. **Nephrogenic systemic fibrosis and gadolinium-based contrast media: updated ESUR Contrast Medium Safety Committee guidelines.** *Eur Radiol* 2013;23:307–18 CrossRef Medline
26. Laader A, Beiderwellen K, Kraff O, et al. **1.5 versus 3 versus 7 Tesla in abdominal MRI: A comparative study.** *PLoS One* 2017;12: e0187528 CrossRef Medline
27. Kitley J, Waters P, Woodhall M, et al. **Neuromyelitis optica spectrum disorders with aquaporin-4 and myelin-oligodendrocyte glycoprotein antibodies: a comparative study.** *JAMA Neurol* 2014;71:276–83 CrossRef Medline
28. Zhang Y, Gauthier SA, Gupta A, et al. **Longitudinal change in magnetic susceptibility of new enhanced multiple sclerosis (MS) lesions measured on serial quantitative susceptibility mapping (QSM).** *J Magn Reson Imaging* 2016;44:426–32 CrossRef Medline
29. Droogan AG, Clark CA, Werring DJ, et al. **Comparison of multiple sclerosis clinical subgroups using navigated spin echo diffusion-weighted imaging.** *Magn Reson Imaging* 1999;17:653–61 CrossRef Medline

Automated Determination of the H3 K27-Altered Status in Spinal Cord Diffuse Midline Glioma by Radiomics Based on T2-Weighted MR Images

Junjie Li, Yongzhi Wang, Jinyuan Weng, Liying Qu, Minghao Wu, Min Guo, Jun Sun, Geli Hu, Xiaodong Gong, Xing Liu, Yunyun Duan, Zhizheng Zhuo, Wenqing Jia, and Yaou Liu

ABSTRACT

BACKGROUND AND PURPOSE: Conventional MR imaging is not sufficient to discern the H3 K27-altered status of spinal cord diffuse midline glioma. This study aimed to develop a radiomics-based model based on preoperative T2WI to determine the H3 K27-altered status of spinal cord diffuse midline glioma.

MATERIALS AND METHODS: Ninety-seven patients with confirmed spinal cord diffuse midline gliomas were retrospectively recruited and randomly assigned to the training ($n = 67$) and test ($n = 30$) sets. One hundred seven radiomics features were initially extracted from automatically-segmented tumors on T2WI, then 11 features selected by the Pearson correlation coefficient and the Kruskal-Wallis test were used to train and test a logistic regression model for predicting the H3 K27-altered status. Sensitivity analysis was performed using additional random splits of the training and test sets, as well as applying other classifiers for comparison. The performance of the model was evaluated through its accuracy, sensitivity, specificity, and area under the curve. Finally, a prospective set including 28 patients with spinal cord diffuse midline gliomas was used to validate the logistic regression model independently.

RESULTS: The logistic regression model accurately predicted the H3 K27-altered status with accuracies of 0.833 and 0.786, sensitivities of 0.813 and 0.750, specificities of 0.857 and 0.833, and areas under the curve of 0.839 and 0.818 in the test and prospective sets, respectively. Sensitivity analysis confirmed the robustness of the model, with predictive accuracies of 0.767–0.833.

CONCLUSIONS: Radiomics signatures based on preoperative T2WI could accurately predict the H3 K27-altered status of spinal cord diffuse midline glioma, providing potential benefits for clinical management.

ABBREVIATIONS: AUC = area under the curve; CE = contrast-enhanced; DMG = diffuse midline glioma; HR = hazard ratio; LR = logistic regression; NPV = negative predictive value; OS = overall survival; PPV = positive predictive value; SC-DMG = spinal cord diffuse midline glioma; WHO = World Health Organization

Diffuse midline glioma (DMG), which occurs in both children and young adults, is a rare type of glioma first recognized as a new entity in the 2016 World Health Organization (WHO) Classification of CNS Tumors as DMG H3 K27M-mutant. Recently,

it has been renamed DMG H3 K27-altered status in the 2021 WHO Classification.^{1–4} Previous evidence demonstrated that H3 K27-altered was a poor prognostic biomarker for DMG, while a recent clinical trial showed that GD2-directed chimeric antigen receptor T-cell therapy had a promising value in reducing tumor volume of DMG H3 K27-altered tumors.^{3,5–11}

Currently, the criterion standard techniques to accurately determine the H3 K27-altered status rely on gene sequencing or immunohistochemistry through invasive biopsy or surgical resection.¹² Tissue sampling bias due to intertumoral heterogeneity may reduce the sensitivity and accuracy of H3 K27-altered status determination. Therefore, a noninvasive method using whole-tumor information is warranted to accurately predict the H3 K27-altered status preoperatively.

MR imaging can provide various morphologic and physiologic features to comprehensively characterize glioma heterogeneity.¹³ Recently, radiomics based on medical images has become a promising tool for noninvasively assessing the molecular genotypes of gliomas in several studies, providing potential benefits

Received May 8, 2023; accepted after revision October 8.

From the Departments of Radiology (J.L., L.Q., M.W., M.G., J.S., Y.D., Z.Z., Y.L.), Neurosurgery (Y.W., W.J.), and Pathology (X.L.), Beijing Tiantan Hospital, Capital Medical University, Beijing, People's Republic of China; Department of Medical Imaging Products (J.W., X.G.), Neusoft, Group Ltd, Shenyang, People's Republic of China; and Clinical and Technical Support (G.H.), Philips Healthcare, Beijing, People's Republic of China.

J. Li, Y. Wang, and J. Went are first authors who contributed equally to this work. Z. Zhuo, W. Jia, and Y. Liu are senior authors who contributed equally to this work.

This work was supported by the Beijing Municipal Natural Science Foundation for Distinguished Young Scholars (No. JQ20035), the Capital Health Development Research Project (No. 2022-1-2042), and the Radiographic Standard Database Construction Project (NO. YXFSC2022JJSJ004).

Please address correspondence to Yaou Liu, MD, PhD, No.119, the West Southern 4th Ring Rd, Fengtai District, Beijing, 100070, China; e-mail: liuyaou@bjtth.org

Indicates article with online supplemental data.

<http://dx.doi.org/10.3174/ajnr.A8056>

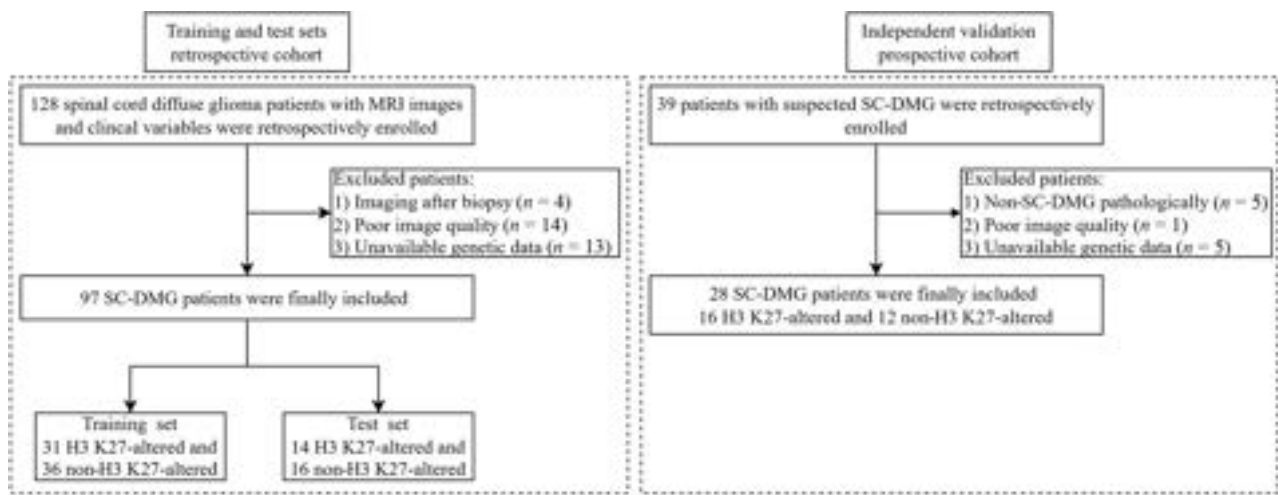


FIG 1. Flowchart of the included patients in this study.

for personalized and effective treatment plans.^{14,15} Several studies have efficiently predicted the H3 K27-altered status by using radiomics in diffuse midline gliomas in the brainstem.^{16,17} However, few studies have focused on spinal cord diffuse midline glioma (SC-DMG) due to its rarity. Conventional features such as hemorrhage and syringohydromyelia appear to have limited predictive value for SC-DMG H3 K27-altered status.^{18,19} Developing an accurate, accessible, robust, and noninvasive radiomics approach for detecting the H3 K27-altered status in SC-DMG remains clinically feasible. This study aimed to predict the H3 K27-altered status of SC-DMG by using radiomics from retrospective and prospective cohorts based on T2WI.

MATERIALS AND METHODS

Study Design and Patients

This study was approved by the institutional review board of Beijing Tiantan Hospital, Capital Medical University, and written informed consent was obtained from all patients or their legal guardians.

A total of 128 patients with histopathologic diagnosis of diffuse glioma in the spinal cord from December 2013 to October 2019 were retrospectively enrolled. A total of 97 patients was finally included on the basis of the following inclusion criteria: 1) preoperative sagittal T2WI scans with adequate image quality; 2) available H3 K27-altered status. Exclusion criteria were the following: 1) a history of biopsy or an operation before MR imaging; 2) poor image quality (eg, obvious motion artifacts, distortion, and signal loss); 3) unknown H3 K27-altered status (Fig 1). From November 2019 to June 2022, thirty-nine patients with suspected SC-DMG were prospectively recruited for independent validation. Inclusion criteria were the following: 1) SC-DMG pathologically confirmed by biopsy or surgical resection; 2) no treatment history before MR imaging; 3) available H3 K27-altered status. Exclusion criteria were the following: 1) pathologic confirmation of other diseases; 2) poor image quality; 3) unknown H3 K27-altered status (Fig 1). MR images, including sagittal T2WI, T1WI, and contrast-enhanced (CE) T1WI, as well as clinical variables, including patient demographics, treatment information, survival status, and detailed pathologic data, were obtained.

After applying the inclusion and exclusion criteria, the final study cohort consisted of 97 patients in the retrospective cohort who were divided into a training set ($n = 67$, including 31 H3 K27-altered and 36 non-H3 K27-altered cases) and a test set ($n = 30$, including 14 H3 K27-altered and 16 non-H3 K27-altered cases) to build a H3 K27-altered predictive model. Then, an independent prospective cohort of 28 patients, including 16 H3 K27-altered and 12 non-H3 K27-altered cases, was enrolled to validate the predictive model. Further survival analysis was performed to confirm the clinical prognostic prediction value of the H3 K27-altered status of SC-DMG.

Neuropathology Analysis

All tumor histopathologic grading was evaluated following the 2016 WHO Classification using formalin-fixed/paraffin-embedded samples with H&E staining. The H3 K27-altered (H3 K27M mutation) status was assessed through immunohistochemistry using the corresponding specific antibody (ABE419; MilliporeSigma; 1:800).

MR Imaging Acquisition

Spinal cord MR images were acquired using 6 MR imaging scanners: SIGNA HD and Discovery 750 (GE Healthcare), Ingenia CX (Philips Healthcare), and Verio, Magnetom Trio, and Magnetom Prisma (Siemens). MR imaging protocols (T2WI, T1WI, and CE-T1WI) for intramedullary spinal cord lesions and parameters are found in the Online Supplemental Table 1.

MR Image Preprocessing

For all patients whose images were used with tumor segmentation, T2WI was first corrected for N4 bias using the SimpleITK python package (<https://pypi.org/project/SimpleITK/>). The image signal intensities were normalized by subtracting the mean value and dividing by the SD of the signal intensity.

Assessment of MR Imaging Characteristics

Conventional MR imaging features, including tumor location, length, edema, cystic/necrosis, contrast-enhancement status, and syringohydromyelia, were assessed by a senior neuroradiologist (Y.D., with >13 years of experience in neuroradiology) and a

junior neuroradiologist (M.G., with >4 years of experience in neuroradiology) who were blinded to clinicopathologic data. Because there were high interrater agreements (K-values ranged from 0.71 to 1) on the MR imaging assessments, we presented the MR imaging assessments by the senior neuroradiologist in the main text and provided those by the junior neuroradiologist in the Online Supplemental Table 2. Tumor location was classified as cervical, cervicothoracic, thoracic, thoracolumbar, or lumbar vertebral, on the basis of the area involving the main component of the tumor. Tumor length was defined as the number of tumor-involved vertebrae. Edema was reflected by greater signal intensity than in the tumor noncontrast portion, lower signal intensity than in the CSF, and unclear boundaries on the T2WI.²⁰ The presentation of cystic or necrosis was well-defined as high-T2WI and low-T1WI signals essentially matching the CSF signals and nonenhanced wall. Compared with T1WI, the tumor CE pattern was classified as no enhancement (including mild enhancement) and obvious enhancement on CE-T1WI. Syringohydromyelia was defined as cystic dilation of the central portion of the spinal cord on T2WI without wall enhancement.^{20,21}

Radiomics Feature Extraction

Tumor segmentation on T2WI was automatically performed by a deep learning model developed by our research team (the mean Dice score of tumor segmentation was 0.852) and visually checked by a senior neuroradiologist (Y.D.) (8 of 97 patients in the retrospective cohort required additional manual review and correction).^{22,23} Radiomics features of tumors were then extracted using Feature Analysis Explorer (FAE, Version 0.5.2; <https://github.com/salan668/FAE>) software. One hundred seven original radiomics features, including 14 shape-based features, 18 first-order features, 24 gray-level co-occurrence matrix features, 14 gray-level dependence matrix features, 16 gray-level run length matrix features, 16 gray-level size zone matrix features, and 5 neighboring gray tone difference matrix features, from T2WI were extracted.

Feature Processing and Selection

Using FAE, we adopted an up-sampling strategy to balance the H3 K27-altered and non-H3 K27-altered cases in the training set. Z score transformation was used for feature normalization. The Pearson correlation coefficient assessment was performed for feature-dimension reduction by randomly removing one of the paired features with high similarity (Pearson correlation coefficient > 0.99), followed by the Kruskal-Wallis method for selection of the optimal features.

Model Development

Logistic regression (LR) was used to determine the H3 K27-altered status by using the selected radiomics features. Five-fold cross-validation was performed for model parameter optimization in the training set. Then, we evaluated the performance of the model in the test set, by determining the classification accuracy, sensitivity, specificity, positive predictive value (PPV), negative predictive value (NPV), and area under the curve (AUC).

Sensitivity Analysis

Sensitivity analysis was performed to support the main findings using the LR radiomics model in the test set: 1) We compared the

other 2 conventional MR imaging radiomic features, T1WI and CE-T1WI, to assess whether this additional information could improve the performance of the model. 2) To exclude potential bias in separating the training and test sets, we repeated the pipeline with 4 additional random splits of the training and test sets. 3) We included 4 classifiers, including support vector machine, least absolute shrinkage, and selection operator regression; linear discriminant analysis; and the Gaussian process for comparison to support the performance of the LR model. 4) We evaluated the predictive performance of combined original radiomics features and their variant features in comparison with the original radiomic features.

Survival Analysis

The overall survival (OS) of a subset of 79 patients was finally available, including 33 H3 K27-altered and 46 non-H3 K27-altered cases. The therapeutic regimen (eg, extent of tumor resection and postoperative treatment) was obtained from the medical records and follow-up visits. The extent of tumor resection was classified as total, subtotal, partial resection, or biopsy on the basis of medical records. Postoperative treatment included chemotherapy and radiation therapy.

Statistical Analysis

Statistical analysis was performed with SPSS (SPSS for Windows, Version 26.0; IBM) and the R statistical and computing software (Version 4.2.1; <http://www.r-project.org/>). Categorical variables were expressed as frequency and compared using the χ^2 test or Fisher exact test. Continuous variables were expressed as mean (SD) and compared using the Student *t* test or Mann-Whitney *U* test. $P < .05$ was considered statistically significant. Classification accuracy, sensitivity, specificity, PPV, NPV, and AUC were calculated to evaluate the performance of the model. OS was estimated by Kaplan-Meier survival curve analysis and the logrank test using the survminer package in R (<https://cran.r-project.org/web/packages/survminer/index.html>). Using the coxph package (<https://www.rdocumentation.org/packages/survival/versions/3.5-7/topics/coxph>), the univariate and multivariate Cox proportional hazards models were used to evaluate the model's performance with the WHO grade that integrating the H3 K27-altered status and histologic grade, and other clinical variables in predicting OS. $P < .05$ was considered statistically significant.

RESULTS

Demographic and MR Imaging Characteristics

Detailed demographic and MR imaging characteristics are shown in Online Supplemental Data. In the retrospective cohort, no differences were observed between the H3 K27-altered and non-H3 K27-altered groups in age, sex, tumor location, tumor length, and tumor enhancement. As for MR imaging characteristics, non-H3 K27-altered SC-DMG cases exhibited higher rates of edema, cystic/necrosis, and syringohydromyelia compared with the H3 K27-altered group ($P < .05$). There were no significant differences in terms of demographic and MR imaging features in the prospective set.

Prediction of H3 K27-Altered Status by Radiomics. Figure 2 shows 6 representative cases (4 correctly predicted cases and 2 wrongly predicted cases) and their corresponding predicted probability

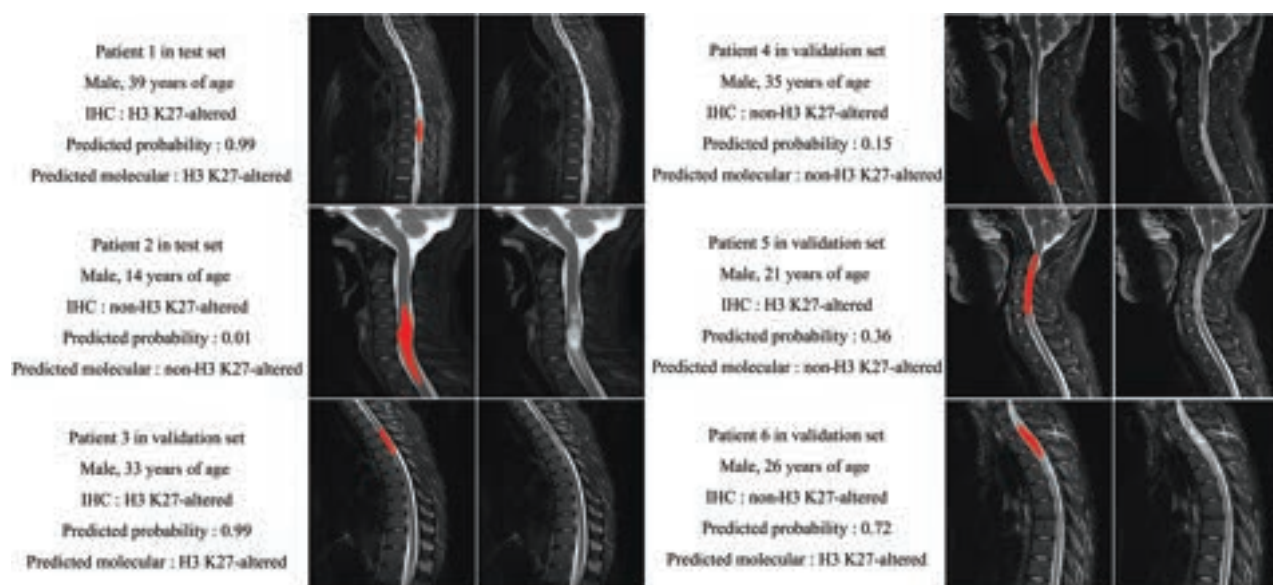


FIG 2. Six representative patients with SC-DMG in the test and validation sets, including 4 correctly predicted cases and 2 wrongly predicted cases. Immunohistochemistry (IHC) showed the H3 K27-altered status of each patient. The predicted probability and predicted molecular status were calculated by using the LR model. *Red overlay* indicates the tumor segmentation.

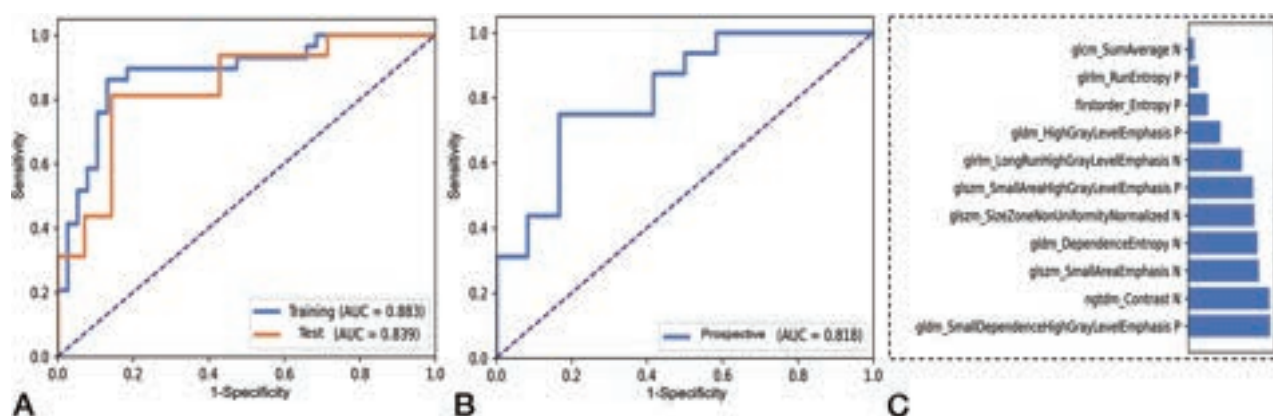


FIG 3. A and B, Receiver operating characteristic curve analysis of the LR model for predicting the H3 K27-altered status in the retrospective cohort (A) and in the independent prospective cohort (B). C, The 11 selected radiomics features with the highest average importance.

calculated by the cutoff value of the LR model. The LR predictive model based on 11 radiomics features achieved an accuracy of 0.833, a sensitivity of 0.813, a specificity of 0.857, a PPV of 0.867, a NPV of 0.800, and an AUC of 0.839 in the test set (Fig 3A and Online Supplemental Data). In the independent prospective set, the predictive model achieved an accuracy of 0.786, a sensitivity of 0.750, a specificity of 0.833, a PPV of 0.857, a NPV of 0.714, and an AUC of 0.818 (Fig 3B and Online Supplemental Data). The 11 important radiomics features are shown in Fig 3C and the Online Supplemental Table 3.

Sensitivity Analysis

The predictive performance of other conventional models (T1WI and CE-T1WI) was lower than that of the LR model (accuracy range of 0.553–0.700) (Online Supplemental Data and Online Supplemental Table 4). Another 4 random splits of the training and test sets demonstrated comparable predictive abilities (accuracy

range of 0.767–0.833) (Online Supplemental Data). Other classifiers had comparable performance to predict SC-DMG H3 K27-altered status with accuracies ranging from 0.767 to 0.800 (Online Supplemental Data). Different age and field strength subgroups had comparable performance, with accuracies ranging from 0.750 to 0.818 (Online Supplemental Table 5). The combined original radiomics features and their variant features had comparable performance with an accuracy of 0.821 in the test set (Online Supplemental Table 6).

Survival Analysis

Kaplan-Meier curve analysis revealed that patients with SC-DMG H3 K27-altered status had worse OS than those with non-H3 K27-altered tumors (logrank test, $P < .001$) (Fig 4), with a median OS in non-H3 K27-altered cases of 40.7 (SD, 26.4) months versus 24.3 (SD, 17.6) months in H3 K27-altered cases (Online Supplemental Table 7). Univariate Cox regression analysis showed

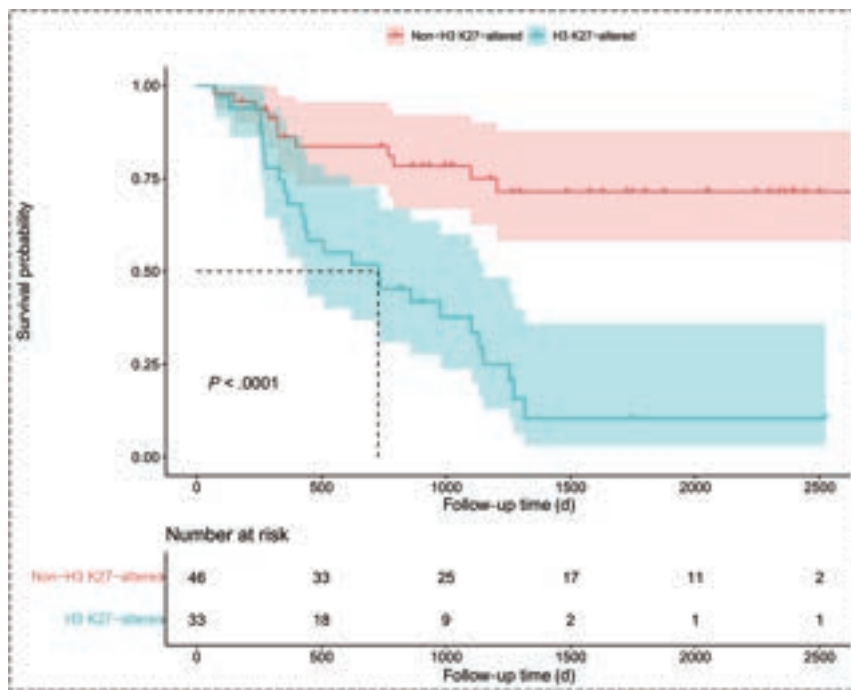


FIG 4. Kaplan-Meier survival curves for H3 K27-altered and non-H3 K27-altered SC-DMG.

that sex, age, syringohydromyelia, extent of resection, and WHO grades were risk factors for OS, with hazard ratios (HRs) of 0.44 (95% CI, 0.23–0.86; $P = .016$), 1.02 (95% CI, 1.00–1.05; $P = .010$), 0.14 (95% CI, 0.03–0.592; $P = .007$), 1.93 (95% CI, 1.21–3.09; $P = .006$), and 3.19 (95% CI, 1.97–5.16; $P = .001$), respectively. Multivariate Cox regression analysis showed the WHO grade as an independent risk factor for OS (HR = 4.48, 95% CI, 1.90–10.59; $P = .001$). We also analyzed the H3 K27-altered status and histologic grade factors by Cox analysis (Online Supplemental Tables 8 and 9).

DISCUSSION

In the current study, we constructed an LR predictive model on the basis of T2WI-based radiomics features in SC-DMG for preoperatively and accurately predicting the H3 K27-altered status. This model using only T2WI showed a robust performance in predicting the H3 K27-altered status, with an accuracy of 0.833 in the test set and 0.767 in the independent prospective cohort.

Age and sex showed no differences between H3 K27-altered and non-H3 K27-altered SC-DMG, which corroborated previous reports.^{9,18,19,24} The conventional MR imaging presentations of H3 K27-altered or non-H3 K27-altered SC-DMG are still unclear due to limited sample sizes ($n < 25$) in most previous studies.^{3,10,25–29} Compared with non-H3 K27-altered SC-DMG, only a few studies reporting H3 K27-altered SC-DMG showed more hemorrhage and less syringohydromyelia.^{18,19} In this study, conventional MR imaging presentations, including edema, cyst/necrosis, and syringohydromyelia, showed differences between H3 K27-altered SC-DMG and non-H3 K27-altered SC-DMG in the retrospective cohort, but they had an insufficient predictive ability with a low accuracy of 53.5%. In addition, no difference in

these features was observed in the prospective validation cohort. These findings indicated that the conventional MR imaging features may have limited value for the determination of the H3 K27-altered SC-DMG. Further studies with large samples are warranted to confirm the current findings and identify specific MR imaging features of H3 K27-altered SC-DMG.

Previous studies have focused on predicting the H3 K27-altered status in brain gliomas by MR imaging.^{16,17,25,30,31} Our study predicted the H3 K27-altered status of SC-DMG using MR imaging-based radiomics, which demonstrated superior performance compared with conventional features. The predictive model had an accuracy of 0.833 and an AUC of 0.839 in the test set. This finding was further supported by an accuracy of 0.786 and an AUC of 0.818 in an independent prospective set. The high diagnostic performance based on 11 radiomics features extracted from T2WI

associated with the distribution of pixel intensity, the relative position of the various gray levels, and the description of patterns or the spatial distribution of voxel intensities may help determine SC-DMG H3 K27-altered status. These findings showed that T2WI may be the most helpful imaging technique, because it could clearly depict high-signal lesions, swelling, cavities, and edema features, while, presumably, enhancement characteristics may play little role, as indicated by the lower value of CE-T1WI in the determination of H3K27-altered SC-DMG.

Sensitivity analysis demonstrated the robustness of the LR predictive model. The primary results (accuracy of 0.833 in the test set) were better than those in other models using conventional MR imaging features and radiomics features from T1WI and CE-T1WI (accuracies ranging from 0.533 to 0.700 in the test set). Comparable predictive performance (accuracies ranging from 0.767 to 0.833) using random splits of the training and test sets indicated the absence of sample bias for the training and test splits in the primary findings. The predictive performance of other classifiers (accuracies ranging from 0.767 to 0.800) was comparable with that of our LR radiomics model, which indicated little model selection bias and the robustness of the MR imaging features for predicting H3 K27-altered status. Subgroup analyses in children and adults (accuracies ranging from 0.750 to 0.773) and the analysis of field strength (accuracies ranging from 0.737 to 0.818) demonstrated its generalizability for clinical practice. The combined original radiomics features and their variant features achieved a predictive accuracy of 0.821 in the test set, with performance comparable with that of the main results.

H3 K27-altered status in SC-DMG initiates tumorigenesis by affecting epigenetic regulation, transcriptional changes, and oncogenic activation.³² In the current study, a relatively large sample size of 79 SC-DMG cases with grades 2–4 was included, and SC-

DMG H3 K27-altered status was identified as a poor prognostic factor, consistent with several previous studies confirming the deleterious role of H3 K27-altered status in SC-DMG.^{10,19} However, some studies have shown that patients with SC-DMG with H3 K27-altered status have a better prognosis.^{7,9} This discrepancy may be explained by potential sample selection bias in their smaller samples ($n < 30$) and the effects of other unreported genetic alterations in addition to the H3 K27-altered status.²⁴

The present study had several limitations. First, all patients were from a single center in this study. More extensive studies and external validations are required in prospective and multi-institutional settings. Second, the main variants of histone H3, the H3.1 (HIST1H3B/C) and H3.3 (H3F3A) mutations, which represent distinct subgroups with different prognostic and phenotypic patterns in glioma, were not analyzed.³³ Only H3 K27M mutation and wild-type status were assessed in the current study, and the H3 K27-altered status of some patients before 2016 was analyzed according to the 2016 WHO Classification, which may have introduced a potential selection bias. Third, the pathophysiologic processes underlying T2WI-based radiomics features and their mechanisms need to be determined for reasonable interpretation. Last, the reproducibility of the radiomics method and the heterogeneity across various MR imaging devices and sequences, such as spectral presaturation with inversion recovery (SPIR), STIR, and Dixon, should be considered.

CONCLUSIONS

The radiomics signatures based on T2WI could noninvasively predict H3 K27-altered status of SC-DMG. These could serve as a noninvasive tool providing reliable molecular information to aid in the clinical treatment of SC-DMG.

ACKNOWLEDGMENT

We acknowledge all the colleagues who helped with the patient recruitment and MR imaging.

Disclosure forms provided by the authors are available with the full text and PDF of this article at www.ajnr.org.

REFERENCES

- Fakhreddine MH, Mahajan A, Penas-Prado M, et al. **Treatment, prognostic factors, and outcomes in spinal cord astrocytomas.** *Neuro Oncol* 2013;15:406–12 CrossRef Medline
- Abd-El-Barr MM, Huang KT, Moses ZB, et al. **Recent advances in intradural spinal tumors.** *Neuro Oncol* 2018;20:729–42 CrossRef Medline
- Meyronet D, Esteban-Mader M, Bonnet C, et al. **Characteristics of H3 K27M-mutant gliomas in adults.** *Neuro Oncol* 2017;19:1127–34 CrossRef Medline
- Louis DN, Perry A, Wesseling P, et al. **The 2021 WHO Classification of Tumors of the Central Nervous System: a summary.** *Neuro Oncol* 2021;23:1231–51 CrossRef Medline
- Louis DN, Giannini C, Capper D, et al. **cIMPACT-NOW update 2: diagnostic clarifications for diffuse midline glioma, H3 K27M-mutant and diffuse astrocytoma/anaplastic astrocytoma, IDH-mutant.** *Acta Neuropathol* 2018;135:639–42 CrossRef Medline
- Aquilanti E, Miller J, Santagata S, et al. **Updates in prognostic markers for gliomas.** *Neuro Oncol* 2018;20:vii17–26 CrossRef Medline
- Yi S, Choi S, Shin DA, et al. **Impact of H3.3 K27M mutation on prognosis and survival of grade IV spinal cord glioma on the basis of new 2016 World Health Organization Classification of the Central Nervous System.** *Neurosurgery* 2019;84:1072–81 CrossRef Medline
- Chai RC, Zhang YW, Liu YQ, et al. **The molecular characteristics of spinal cord gliomas with or without H3 K27M mutation.** *Acta Neuropathol Commun* 2020;8:40 CrossRef Medline
- Akinduro OO, Garcia DP, Higgins DM, et al. **A multicenter analysis of the prognostic value of histone H3 K27M mutation in adult high-grade spinal glioma.** *J Neurosurg Spine* 2021;35:834–43 CrossRef Medline
- Karremann M, Gielen GH, Hoffmann M, et al. **Diffuse high-grade gliomas with H3 K27M mutations carry a dismal prognosis independent of tumor location.** *Neuro Oncol* 2018;20:123–31 CrossRef Medline
- Majzner RG, Ramakrishna S, Yeom KW, et al. **GD2-CAR T cell therapy for H3K27M-mutated diffuse midline gliomas.** *Nature* 2022;603:934–41 CrossRef Medline
- Gielen GH, Gessi M, Buttarelli FR, et al. **Genetic analysis of diffuse high-grade astrocytomas in infancy defines a novel molecular entity.** *Brain Pathol* 2015;25:409–17 CrossRef Medline
- Thust SC, Heiland S, Falini A, et al. **Glioma imaging in Europe: a survey of 220 centres and recommendations for best clinical practice.** *Eur Radiol* 2018;28:3306–17 CrossRef Medline
- Rudie JD, Rauschecker AM, Bryan RN, et al. **Emerging applications of artificial intelligence in neuro-oncology.** *Radiology* 2019;290:607–18 CrossRef Medline
- Bhandari AP, Liong R, Koppen J, et al. **Noninvasive determination of IDH and 1p19q status of lower-grade gliomas using MRI radiomics: a systematic review.** *AJNR Am J Neuroradiol* 2021;42:94–101 CrossRef Medline
- Su X, Chen N, Sun H, et al. **Automated machine learning based on radiomics features predicts H3 K27M mutation in midline gliomas of the brain.** *Neuro Oncol* 2020;22:393–401 CrossRef Medline
- Zhuo Z, Qu L, Zhang P, et al. **Prediction of H3K27M-mutant brainstem glioma by amide proton transfer-weighted imaging and its derived radiomics.** *Eur J Nucl Med Mol Imaging* 2021;48:4426–36 CrossRef Medline
- Jung JS, Choi YS, Ahn SS, et al. **Differentiation between spinal cord diffuse midline glioma with histone H3 K27M mutation and wild type: comparative magnetic resonance imaging.** *Neuroradiology* 2019;61:313–22 CrossRef Medline
- Cheng L, Wang L, Yao Q, et al. **Clinicoradiological characteristics of primary spinal cord H3 K27M-mutant diffuse midline glioma.** *J Neurosurg Spine* 2021;36:1–12 CrossRef Medline
- Kim DH, Kim JH, Choi SH, et al. **Differentiation between intramedullary spinal ependymoma and astrocytoma: comparative MRI analysis.** *Clin Radiol* 2014;69:29–35 CrossRef Medline
- Timponi VM, Patel SH. **MRI of a syrinx: is contrast material always necessary?** *AJR Am J Roentgenol* 2015;204:1082–85 CrossRef Medline
- Lemay A, Gros C, Zhuo Z, et al. **Automatic multiclass intramedullary spinal cord tumor segmentation on MRI with deep learning.** *Neuroimage Clin* 2021;31:102766 CrossRef Medline
- Sun T, Wang Y, Liu X, et al. **Deep learning based on preoperative magnetic resonance (MR) images improves the predictive power of survival models in primary spinal cord astrocytomas.** *Neuro Oncol* 2023;25:1157–65 CrossRef Medline
- Wang L, Li Z, Zhang M, et al. **H3 K27M-mutant diffuse midline gliomas in different anatomical locations.** *Hum Pathol* 2018;78:89–96 CrossRef Medline
- Piccardo A, Tortora D, Mascelli S, et al. **Advanced MR imaging and 18F-DOPA PET characteristics of H3K27M-mutant and wild-type pediatric diffuse midline gliomas.** *Eur J Nucl Med Mol Imaging* 2019;46:1685–94 CrossRef Medline
- Qiu T, Chanchotisation A, Qin Z, et al. **Imaging characteristics of adult H3 K27M-mutant gliomas.** *J Neurosurg* 2019;133:1662–70 CrossRef Medline
- Schulte JD, Buerki RA, Lapointe S, et al. **Clinical, radiologic, and genetic characteristics of histone H3 K27M-mutant diffuse midline gliomas in adults.** *Neurooncol Adv* 2020;2:vdaa142 CrossRef Medline

28. Schreck KC, Ranjan S, Skorupan N, et al. **Incidence and clinicopathologic features of H3 K27M mutations in adults with radiographically-determined midline gliomas.** *J Neurooncol* 2019;143:87–93 CrossRef Medline
29. Wang YZ, Zhang YW, Liu WH, et al. **Spinal cord diffuse midline gliomas with H3 K27m-mutant: clinicopathological features and prognosis.** *Neurosurgery* 2021;89:300–07 CrossRef Medline
30. Kandemirli SG, Kocak B, Naganawa S, et al. **Machine learning-based multiparametric magnetic resonance imaging radiomics for prediction of H3K27M mutation in midline gliomas.** *World Neurosurg* 2021;151:e78–85 CrossRef Medline
31. Pan CC, Liu J, Tang J, et al. **A machine learning-based prediction model of H3K27M mutations in brainstem gliomas using conventional MRI and clinical features.** *Radiother Oncol* 2019;130:172–79 CrossRef Medline
32. Nagaraja S, Quezada MA, Gillespie SM, et al. **Histone variant and cell context determine H3K27M reprogramming of the enhancer landscape and oncogenic state.** *Mol Cell* 2019;76:965–80.e12 CrossRef Medline
33. Castel D, Philippe C, Calmon R, et al. **Histone H3F3A and HIST1H3B K27M mutations define two subgroups of diffuse intrinsic pontine gliomas with different prognosis and phenotypes.** *Acta Neuropathol* 2015;130:815–27 CrossRef Medline

“Best of” ASNR 2023 (Chicago) and “Sneak Peek” of ASNR 2024 (Las Vegas)

The ASNR held its 61st Annual Meeting from April 29 to May 3, 2023, in the organization’s hometown of Chicago, Illinois. As underscored by the ASNR 2023 Program Chair and President-Elect, Yvonne Lui, the 2023 meeting theme, “Transforming the Future of Neuroradiology,” reflected the rapidly evolving landscape of the field and the ongoing advancements that are shaping its trajectory. Attendees, both in-person and virtually, had the opportunity to learn about cutting-edge research, practice innovations, and technological advancements through educational sessions, subspecialty society symposia, study groups, scientific presentations, education exhibits, and social events.

ASNR 2023 showcased the breadth and depth of diagnostic and therapeutic neuroimaging with diverse topics spanning the gamut of its subspecialty societies. The content not only covered functional and advanced (American Society of Functional Neuroradiology [ASFNR]), head and neck (American Society of Head and Neck Radiology [ASHNR]), pediatric (American Society of Pediatric Neuroradiology [ASPNR]), spine (American Society of Spine Radiology [ASSR]), and neurointerventional imaging (Society of NeuroInterventional Surgery [SNIS]) but also included sessions on diversity and inclusion, education, professional development, artificial intelligence (AI), clinical workflow advances, multidisciplinary collaboration, and more.

Although ASNR 2023 only recently concluded, exciting plans are already in motion for the 62nd Annual Meeting in Las Vegas, Nevada, occurring May 18–22, 2024. The theme for ASNR 2024

is “Celebrating Neuroradiologists,” and the event will showcase and celebrate the accomplishments of neuroradiologists in all aspects of practice. In addition to the top-notch invited lectures, oral and electronic research presentations, exhibits, and social activities to which ASNR attendees are accustomed, the ASNR 2024 Program Chair and President-Elect, Max Wintermark, also plans to include “how-to” sessions and expert discussions of clinical vignettes among other innovative content.

The purpose of this article is to provide a day-by-day, image-rich summary of just some of the highlights of ASNR 2023, based on the clinical interests and subjective biases of our small group of coauthors, each representing a different neuroimaging subspecialty, as well as a sneak peek of what to look forward to in Las Vegas for ASNR 2024.

Day 1: Saturday April 29, 2023 (Weekend Symposium)

The meeting “kicked off” with welcome remarks and announcements from the Program Chair Yvonne Lui, who emphasized the process of transformation and the importance of community. A remarkable “Virtual and Augmented Reality Symposium” session followed, which explored the disruptive potential of these technologies through various clinical and educational applications. For example, the use of patient-specific 3D models for surgical planning has been associated with increased technical success rates and decreased complication rates in a variety of settings,¹ and holographic navigation for placement of external ventricular drains has been associated with improved targeting compared with freehand insertion.² In the context of education, “digital twinning” of human anatomy allows realistic holograms that can be used to effectively teach anatomy more efficiently compared with cadaveric dissection.^{3,4}

Following an excellent session discussing innovations in neuroradiology education, day 1 also highlighted “Advances in Multidisciplinary Head and Neck Imaging” through a simulated head and neck cancer tumor board (Fig 1). With each speaker focusing on a specific site of primary head and neck cancer (ie, oropharynx, David Zander; larynx, Alok Bhatt; paranasal sinuses, Tabby Kennedy), this session emphasized the importance of understanding clinical context. The speakers showed that by maintaining an awareness of the relevant management paradigm, radiologists are better equipped to report the specific imaging features most pertinent to the patient’s care. Attendees left feeling inspired to fully participate as valued members of the multidisciplinary team.

Day 2: Sunday April 30, 2023 (Weekend Symposium)

On the second day of the weekend symposium, 2 compelling innovation-focused sessions were well-received by participants. The first, entitled “Pushing the Boundaries of AI Innovations,” included



FIG 1. David Zander conducts a simulated head and neck tumor board while lecturing on the oropharynx in Saturday’s Advances in Multidisciplinary Head and Neck Imaging session.



FIG 2. Kim Seifert and Risto Filippi participate in the Neurorad Password Game Show.



FIG 3. Attendees socialize with friends and colleagues in the exhibit hall while also having the opportunity to visit with meeting exhibitors during the Opening Reception and Reunion Night.

compelling talks on worklist prioritization (David Kim), health equity (Noushin Yahyavi), research trends (Evan Calebrese), and FDA regulations regarding AI monitoring (Gabriela Rodal). In the second session, entitled “Innovations in Image-Guided Therapeutics,” attendees learned about innovations across a broad range of topics, including theranostics (Michael Veronesi) and multiple applications of focused ultrasound (neuro-oncology, Kazim Narsinh; movement disorders, Timothy Kaufmann; and back pain, Lubdha Shah).

Sunday also featured the “Neurorad Password Game Show,” an entertaining and educational session hosted by Rick Wiggins and Yvonne Lui that challenged participants’ radiologic knowledge through a game show format (Fig 2). Four pairs of

contestants (Risto Filippi/Kim Seifert, Pat Rhyner/Sachin Gujar, Mislá Yuhasz/Doug Phillips, and Tanya Rath/Sohil Patel) faced off against one another with impressive displays of teamwork and radiology acumen.

Immediately following the Neurorad Password Game Show, the Opening Reception and Reunion Night was held in the exhibit hall among the vendor booths. The turnout was great, and the exhibit hall location allowed attendees to not only socialize with friends and colleagues, both old and new, but also to learn about many of the latest and greatest products offered by the meeting exhibitors (Fig 3). Finally, a new addition to the exhibit hall for ASNR 2023 was an assortment of lawn games, including Cornhole and Lifesize Connect 4.

Day 3: Monday May 1, 2023

Monday morning’s plenary session, “Unpacking the Stars: Luminaries Share Their Cases and Analyses,” featured eminent neuroradiologists discussing their diagnostic approaches to some of their favorite cases. The case mix spanned the spectrum from bread and butter to dramatic and exceedingly rare, with each presented case including multiple practical teaching points. Speakers included Pam Schaefer (brain, Fig 4A), David Hackney (spine), Laurie Loevner (head and neck), and Ellen Grant (pediatric neuroradiology, Fig 4B). This packed session was a favorite of many attendees.

Following the weekend symposium and the Monday morning plenary session, day 3 of ASNR 2023 transitioned to the first day of parallel sessions. Two noteworthy, standing-room-only parallel

sessions were “DECT in Neuroradiology: Where We Are and What Lies Ahead” and “Imaging and the Glymphatic System.”

In the dual-energy CT (DECT) session, Aaron Sodickson summarized the basic principles and underlying physics, Shobhit Mathur discussed specific applications (20+) in neuroradiology, and Nicolas Murray summarized implementation challenges and potential solutions. With the advent of photon-counting CT, which will be highlighted at ASNR 2024, interest in and applications of multienergy CT are expected to increase.

The glymphatic system session featured Maiken Nedergaard, one of the scientists who first described this system,⁵ who explained the basic functions of the system. Subsequently, Risto Filippi summarized imaging of glymphatic flow, Giuseppe



FIG 4. Pam Schaefer (A) and Ellen Grant (B) share some of their favorite cases and provide associated teaching points in Monday morning's plenary session, Unpacking the Stars: Luminaries Share Their Cases and Analyses.



FIG 5. Selected photos from Monday evening's Committee Orientation and Meet-Up Reception.

Barisano discussed approaches to perivascular space quantification and the associated clinical relevance, and Meng Law outlined the various disease states for which the perivascular spaces and glymphatics have implications (eg, neurodegeneration, traumatic brain injury, stroke, epilepsy, sleep apnea, coronavirus disease 2019 [COVID-19], and demyelinating and autoimmune diseases).

The social event of Monday evening was the Committee Orientation and Meet-Up Reception. New for ASNR 2023, this gathering was held to acknowledge and thank committee volunteers for their service. Tables designated for each ASNR committee were arranged throughout the event space, where committee chairs and vice-chairs welcomed new members and reconnected with continuing members in a fun, relaxed environment. Some selected photos from the Meet-Up Reception are shown in Fig 5.

Day 4: Tuesday May 2, 2023

Following the J. Arliss Pollock Memorial Award Lecture plenary session ("Rethinking US Health Care: Facts and Fallacies" delivered by Amy Finkelstein), parallel sessions resumed Tuesday morning.

The highlight of the day was "Women in Neuroradiology: Improving Diversity and Achieving Success." Organized by Aparna Singhal and Niky Farid, this first-of-its-kind, standing-room-only session included inspiring talks from 5 accomplished neuroradiologists, including 2 ASNR Presidents (Tina Young Poussaint, Erin Simon Schwartz) and 1 Department Chair (Vijay Rao). Attendees ranged from trainees to luminaries in the field, including the first 2 female ASNR Presidents, Anne Osborne and Pat Rhyner. The session tackled important topics relevant to both sexes, including sex diversity, becoming a leader, creating a Women in Radiology group, advice for the young neuroradiologist, and work-life balance. Attendees left with a sense of how far neuroradiology has come with respect to sex equity and of the work left to make neuroradiology and the ASNR a welcoming place for all.⁶

The President's Appreciation Gala was held Tuesday evening and featured live music from a local Chicago band (Fig 6) and honored the recipients of the ASNR 2023 Annual Awards, including Gordon Sze (Gold Medal, Fig 7A), Pedro Lylyk (Honorary Member, Fig 7B), Ric Harnsberger (Outstanding Contributions in Neuroradiology Education, Fig 7C), and Greg Zaharchuk (Outstanding Contributions in Research, Fig 7D), among others. Outgoing *American Journal of Neuroradiology* (AJNR) Editor Jeff Ross (Fig 8) was also recognized for his dedicated service to the journal. New this year, the event was open to all attendees who purchased a ticket. Some selected additional photos from the gala are shown in Fig 9.

Day 5: Wednesday May 3, 2023

The final day of ASNR 2023 kicked off with a plenary session entitled "Innovations of Our Field: Historical Perspectives and Where We Are Headed," which featured

neuroradiology superstars reflecting on challenges and rewards of an academic career (Bill Dillon), global health and neuroradiology outreach (Anne Osborn), health policy (Josh Hirsch),



FIG 6. Local Chicago musicians providing live music at Tuesday evening's President's Appreciation Gala.

medical journalism (Jeff Ross), and education (Rick Wiggins). This engaging session simultaneously offered reflections on the past as well as strategies for meeting current and future challenges.

Among Wednesday's parallel sessions, one highlight was "The Changing Neuroradiology Practice: Opportunities and Challenges." Organized by the Diversity and Inclusion Committee, this session focused on the shift to hybrid workflow (ie, mix of on-site and remote work). When considered through the lens of diversity, equity, and inclusion, the secular trend toward hybrid models affects all neuroradiologists and offers opportunities to build better, more equitable systems if thoughtfully designed and executed. Following talks from Sean Pierce ("Neuroradiology Workforce Changes: A Leadership Worldview"), Ashley Aiken ("Medical Education and Radiology Training in the Hybrid Environment"), Haris Sair ("Challenges and Pitfalls of Hybrid Neuroradiology"), and Alex Norbash ("Hybrid Neuroradiology: How It Can Work"), attendees participated in a lively discussion and productive question-and-answer session.



FIG 7. Recipients of ASNR 2023 Annual Awards, including Gordon Sze (A, pictured with Erin Simon Schwartz), Gold Medal; Pedro Lylyk (B, pictured with Yvonne Lui), Honorary Member; Ric Harnsberger (C, pictured with Tina Young Poussaint), Outstanding Contributions in Neuroradiology Education; and Greg Zaharchuk (D, pictured with Tina Young Poussaint), Outstanding Contributions in Research.

ASNR 24 Sneak Peek

With ASNR 2023 behind us, we now eagerly look forward to ASNR 2024, which will take place May 18–22 in Las Vegas. Plans are actively underway and continue to evolve; however, we are excited to offer a sneak peek of some of what to expect, noting that part of what follows may be subject to change. Specifically, the weekend symposium will feature several cutting-edge topics, including but not limited to AI ("We're All In"), genetic therapies (emerging novel treatments, varied delivery routes such as cisterna magna puncture, and future impact), health policy commission programming (ie, "New Frontiers in Work Models," such as remote interpretation, staffing shortages, and the Relative Value Scale Update Committee [RUC]), and international attendee sessions. Furthermore, members of the neuroradiology community have submitted their own ideas for ASNR 2024 didactic sessions in addition to research abstracts.

A plenary session highlighting dementia ("New Era of Dementia Therapy") will include topics such as the following: 1) "Imaging and Blood-Based Biomarkers in Dementia," 2) "Brief History of Alzheimer Disease Treatment with a Focus on Recent Pivotal Clinical Trials," and 3) "Rehearsing your ARIA: How to Prepare for Imaging Patients on Anti-Amyloid Therapies."



FIG 8. ASNR President (2022–2023) Erin Simon Schwartz honors outgoing *AJNR* Editor-in-Chief Jeff Ross for his service to the Journal at Tuesday evening's President's Appreciation Gala.



FIG 9. Selected photos of attendees at Tuesday evening's President's Appreciation Gala.

Additional sessions will focus on psychiatry ("Toward Personalized Measures of Psychiatric Disease Using Advanced Neuroimaging"); novel technologies, such as photon-counting CT and magnetic particle imaging (a new noninvasive imaging method that detects iron oxide nanoparticles to produce 2D and 3D images, more sensitive and substantially faster than MR imaging or PET); and virtual reality. ASNR 2024 will also again highlight study groups for DTI/fMRI, PET, and vessel wall imaging.

Joint sessions from ASNR-affiliated societies (eg, ASFNR, ASHNR, ASPNR, ASSR) and other related societies (Sociedad Ibero Latino Americana de Neurorradiología Diagnóstica y Terapéutica [SILAN]; Asian-Oceanian Society of Neuroradiology and Head & Neck Radiology [AOSNHNR]; and, for the first time, the American Society of Emergency Radiology [ASER]) will also be featured, as well as sessions on computer science and

informatics (including the "hot topic" of Chat Generative Pre-trained Transformer [Chat-GPT]), epilepsy, section chief sessions on economics and recruitment, and sessions covering diversity, equity, and inclusion.

Finally, participants should expect the following: 1) sessions on emerging topics such as cryptogenic stroke, head and neck, and spine, 2) "pitch your idea" interactive sessions for facilitating innovative neuroimaging approaches, and 3) educational case vignettes.

CONCLUSIONS

ASNR 2023 attendees learned about the latest clinical innovations, technological advancements, and cutting-edge research. Perhaps as important, the meeting also provided ample opportunities for reconnecting with old friends and fostering new social bonds, within the backdrop of the organization's "hometown."

We know that the ASNR's brightest days are ahead, and we look forward to Celebrating Neuroradiologists with you in Las Vegas at ASNR 2024!

Disclosure forms provided by the authors are available with the full text and PDF of this article at www.ajnr.org.

REFERENCES

1. Tack P, Victor J, Gemmel P, et al. **3D-printing techniques in a medical setting: a systematic literature review.** *Biomed Eng Online* 2016;15:115 CrossRef Medline
2. Li Y, Chen X, Wang N, et al. **A wearable mixed-reality holographic computer for guiding external ventricular drain insertion at the bedside.** *J Neurosurg* 2018 Oct 1 [Epub ahead of Print] CrossRef Medline
3. Ruthberg JS, Tingle G, Tan L, et al. **Mixed reality as a time-efficient alternative to cadaveric dissection.** *Med Teach* 2020;42:896–901 CrossRef Medline
4. Stojanovska M, Tingle G, Tan L, et al. **Mixed reality anatomy using Microsoft hololens and cadaveric dissection: a comparative effectiveness study.** *Med Sci Educ* 2020;30:173–78 CrossRef Medline
5. Iliff JJ, Wang M, Liao Y, et al. **A paravascular pathway facilitates CSF flow through the brain parenchyma and the clearance of interstitial solutes, including amyloid β .** *Sci Transl Med* 2012;4:147ra111 CrossRef Medline
6. Bunch PM, Loevner LA, Bhala R, et al. **The American Society of Neuroradiology: cultivating a diverse and inclusive culture to build a stronger organization.** *AJNR Am J Neuroradiol* 2021;42:2127–29 CrossRef Medline

● Paul M. Bunch

Department of Radiology
Wake Forest University School of Medicine
Winston Salem, North Carolina

● Birgit B. Ertl-Wagner

Department of Diagnostic Imaging
The Hospital for Sick Children
Toronto, Ontario, Canada

Department of Medical Imaging
University of Toronto
Toronto, Ontario, Canada

● **Wende N. Gibbs**
Department of Neuroradiology
Barrow Neurological Institute
Phoenix, Arizona

● **Steven Lev**
Department of Radiology
Nassau University Medical Center
East Meadow, New York

● **Michael H. Lev**
Department of Radiology
Massachusetts General Hospital/Harvard Medical School
Boston, Massachusetts

<http://dx.doi.org/10.3174/ajnr.A8061>

Robert D. Zimmerman, MD

A long-time senior member of the American Society of Neuroradiology (ASNR) and my dearest friend Robert D. Zimmerman, MD, passed away after a prolonged illness, in the presence of his beloved wife Ellen and his 2 children, Max and Molly, on October 5, 2023.

A magna cum laude, Phi Beta Kappa graduate of Rutgers University, he received his MD degree from the Albert Einstein College of Medicine. I met Bob in the residency program at Montefiore Medical Center in the Bronx. When Bob returned as faculty after his fellowship with Dr David O. Davis at George Washington University, recruited by the Division Chief Dr Norman Leeds, a founding member of the ASNR, I was the chief resident, and we hit it off. His infectious love for his specialty and his clinical excellence and dedication to teaching led me to follow him, and we remained the closest of friends for more than 40 years.

Bob went on to a stellar career in 1983 at what was then New York Hospital, currently NewYork-Presbyterian/Weill Cornell Medical Center. He was a highly sought-after expert for his consummate clinical skills because referring physicians trusted his opinion and judgment. At the time, New York Hospital had just installed one of the first superconducting MR imaging scanners in the country, allowing Dr Zimmerman and his colleagues the unprecedented opportunity to explore and publish early articles on the full gamut of neurologic diseases, including meningiomas, head trauma, intracranial hemorrhage, and periventricular signal changes. He was a productive researcher, with 118 peer-reviewed publications, 15 book chapters, and more than 150 visiting professorships and invited lectures.

His enduring interest in and aptitude for teaching and education led to many important roles at Cornell and established a career direction that guided him throughout his professional and administrative work. Some of his key leadership roles included program director of the radiology residency and the neuroradiology fellowship, vice chair for education and faculty development, and executive vice chair of the Department of Radiology. He also served as the radiology representative on the NewYork-Presbyterian Hospital Graduate Medical Education Committee for more than 15 years. He was a recipient of the Robin Watson Award for Excellence in Radiology Teaching, the Annual Teaching Award from the neurosurgical residents, and the Teaching Excellence Award from Cornell Medical College. His residents chose to honor his excellence as a mentor, role model, and teacher, with the Robert D. Zimmerman Outstanding Educator Award given yearly at Cornell.

As Bob became involved in service to organized neuroradiology, he was recognized for his intellect, accomplishments, and interpersonal skills by society leaders. He served as president of the Eastern Neuroradiological Society (1992–1993) and president of the New York Roentgen Society (2003–2004).

ASNR leadership also recognized his attributes, not the least of which was his engaging personality and pithy sense of humor,



and over the years, apart from his numerous scientific presentations, he provided notable service and leadership on many ASNR committees. Bob was a member of the Education Committee for 15 years. Leadership roles also included chair of the Fellowship Program Director's Committee (1991–1998), chair of Publications Committee (2005–2008), and chair of the Continuing Medical Education Subcommittee on Electronic Education (2001–2004).

Bob's dedication to and expertise in educational issues led him to take on a leading role in the revision of the neuroradiology fellowship training standards for the ASNR. He had been a long-term advocate of the fellowship match and worked closely with others at ASNR, including David Yousem, in its successful implementation. He chaired the Association of Program Directors in Radiology Subcommittee that developed a "Resident Core Curriculum and Delineation of Resident Responsibilities and Training Goals for Neuroradiology."

Bob served for more than 20 years in one capacity or another as a member of the ASNR Executive Committee, and he served as secretary of the ASNR (1998–2000).

As president-elect and then as president of the ASNR (2008–2009), he worked on a number of issues that had a lasting positive impact on the ASNR and our specialty. Bob had an ambitious agenda and brought his involvement in other organizations to bear. As a member of the Radiology Residency Review Committee (RRC) of the Accreditation Council for Graduate Medical Education (ACGME), he believed that the

ASNR should serve as the major vehicle for our members' ability to meet the requirements of the developing American Board of Radiology (ABR) program for maintenance of certification, and he worked hard on this during his tenure. He also began discussions with the ABR, along with Pat Hudgins, to allow the neuroradiology recertification test to be given at the annual meeting (reducing cost and inconvenience for members).

As 1 of 8 members of the RRC representing neuroradiology (2004–2012), he spent countless hours reviewing and monitoring radiology programs across the country, as well as working tirelessly to define training requirements for radiology residents, neuroradiology fellows, and endovascular surgical neuroradiology fellows. He made important contributions to the revision of training standards in accordance with new ACGME requirements, while limiting additional administrative burdens on program directors.

His considerable work for the RRC and ABR was a natural outgrowth of his educational bent and dedication to neuroradiology. He served for 20 years as an ABR oral board examiner, during the time when we brought our own test cases to display on view boxes.

As a trustee of the ABR, he served as chair of the Neuroradiology Subspecialty Examination Committee during a period of rapid change in board certification and examination methodology. As chair of the Subspecialty Certification Committee, he helped develop an entirely new examination. He served as neuroradiology section chair for the Examination of the Future Committee and worked with the Maintenance of Certification Committees, the

Interventional Radiology Implementation Task Force, and an ACGME committee on radiology milestones. With the inception of the DR Neuroradiology Online Longitudinal Assessment Committee in 2017, he served as a senior reviewer until his untimely passing.

As written in a tribute by his department at Cornell following his passing, Bob achieved the pinnacle of success as a neuroradiologist, researcher, educator, and servant leader. He elevated the view of the neuroradiologist in the larger radiology and medical and patient communities by virtue of his clinical and investigative endeavors, his mentoring, his development of interdisciplinary cooperative projects, and, most important, his seriousness of purpose, sense of humor, and personal integrity.

Bob was a unique and exemplary servant leader for organized radiology, but his most important and lasting contribution was his caring nature and his unbridled enthusiasm for his specialty and for our trainees. He imprinted generations of residents and fellows with his passion, leading them to follow him. These are his “scientific children,” his lasting legacy. He will be sorely missed by so many of us who knew him well.

E. Russell, with contributions from Drs

V. Mathews

J. Tsiouris

C. Wood

T Naidich

<http://dx.doi.org/10.3174/ajnr.A8054>